Mantle Xenoliths from SE China and SE Australia: Nature and Evolution of the Lithospheric mantle

Jiang-Gu Lu

ARC Centre of Excellence for CCFS and GEMOC National Key Centre, Department of Earth and Planetary Sciences, Macquarie University, Australia

School of Earth Sciences, China University of Geosciences (Wuhan), China

This thesis is presented for the degree of Doctor of Philosophy
Macquarie University

June 2017

TABLE OF CONTENTS

Abstract i

Declaration iii

Acknowledgements v

List of figures vii

List of tables xiii

Chapter 1. Introduction 1

1.1 Research significance 1

1.2 An overview of previous studies of mantle-derived peridotite xenoliths 2

1.2.1 Mantle peridotite xenoliths on- and off-craton 2

1.2.2 Peridotite xenoliths in Eastern China 4

1.3 Overview previous work on mantle pyroxenite xenoliths 5

1.3.1 Mantle pyroxenite 5

1.3.2 Pyroxenite xenoliths in the South China Craton and southeastern Australia 9

1.4 Research targets and aims of this study 12

1.5 Thesis outline 13

Chapter 2. Geological settings 15

2.1 Geological setting of southeastern Australia 16

2.1.1 Paleozoic continental accretion 17

2.1.1.1 Delamerian orogenic belt 17

2.1.1.2 Lachlan orogenic belt 17

2.1.1.3 Tectonic history 19

2.1.2 Mesozoic rifting 20

2.1.3 Cenozoic volcanics and mantle xenoliths 20

2.2 Geological setting of the South China block 23

2.2.1 Paleozoic Wuyi-Yunkai Orogen and associated magmatism 25

2.2.2 Mesozoic Indosinian and Yanshanian orogeny and associated

magmatism 25
2.2.3 Cenozoic basalt and mantle xenoliths 26

Chapter 3. Analytical methods 29
3.1 Sample preparation and mineral separates 29
3.2 Optical and Scanning Electronic Microscopy (SEM) imaging 30
3.3 Major- and trace-element analyses of whole-rock samples 30
3.4 Major- and trace-element analyses of minerals 31
3.4.1 Electron microprobe: Major-element analysis 31
3.4.2 LA-ICPMS: Trace-Element analysis 31
3.5 Radiogenic isotope analysis 32
3.5.1 Sr-Nd-Hf solution analysis 32
3.5.2 **In situ** *Sr isotopes of minerals* 33
3.6 *In situ* **O-isotopic analysis of garnet** 34

Chapter 4. Nature and evolution of the lithospheric mantle beneath the Yangtze Craton, SE China 35
4.1 Introduction 35
4.2 Petrography 36
4.3 Results 37
4.3.1 Mineral chemistry 37
4.3.2 Equilibration temperatures 40
4.3.3 Whole-rock major and trace element compositions 40
4.3.4 Sr-Nd isotopes 42
4.4 Discussion 43
4.4.1 Melting history of Lianshan peridotites 43
4.4.2 Mantle metasomatism 44
4.4.3 Nature and evolution of the SCLM beneath the lower Yangtze block 46
4.5 Conclusions 48

Chapter 5. Microscale effects of melt infiltration into the lithospheric mantle: Peridotite xenoliths from Xilong, South China 51
5.1 Introduction 51
5.2 Petrograph of xenoliths 52

5.3 Results **56**
5.3.1 Major elements **56**
5.3.1.1 Primary minerals 56
5.3.1.2 Na-rich melts and spongy rims of clinopyroxene and spinel 57
5.3.1.3 K-rich melts and associated minerals 58
5.3.2 Trace-element compositions **59**
5.4 Discussion **61**
5.4.1 Early metasomatic event **61**
5.4.2 Later metasomatic event **62**
5.4.2.1 Infiltration of Na-melts 62
5.4.2.2 Infiltration of K-melts 63
5.4.3 Evolution of the lithospheric mantle beneath the Xilong area **65**
5.5 Conclusions **65**

Chapter 6. Garnet pyroxenite xenoliths from southeastern Australia: Tracing a deep lithospheric event **67**
6.1 Introduction **67**
6.2. Petrography **68**
6.2.1 Coarse equant textures **69**
6.2.2 Porphyroblastic textures **71**
6.2.2.1 Exsolution lamellae zones 71
6.2.2.2 Granoblastic mosaic zones 73
6.2.2.3 Relationship between the lamellar and mosaic zones 73
6.2.3 Spinel-cored texture **76**
6.2.4 Origin and mode determination **76**
6.3 Results **78**
6.3.1 Mineral compositions **78**
6.3.1.1 Major-element compositions 78
6.3.2.2 Trace-element compositions 84
6.3.2 Reconstructed whole rock **93**
6.3.3 Reconstructed clinopyroxene **100**
6.3.4 P-T estimates of the garnet pyroxenites **102**
6.3.4.1 P-T conditions of re-equilibration after the exsolution 102
6.3.4.2 P-T conditions before the exsolution 102
6.3.5 Isotopic geochemistry **103**

6.3.5.1 Sr-Nd-Hf solution analyses 103
6.3.5.2 *In situ* Sr-isotope analyses 105
6.3.4.3 *In situ* O isotope analyses 106
6.4. Discussion 106
6.4.1 Primary mineral phases 106
6.4.2 High-pressure cumulates and the source of parental melts 111
6.4.2.1 High-MgO garnet pyroxenites are cumulates from hydrous basaltic melts 111
6.4.2.2 Low-MgO garnet pyroxenites are cumulates from evolved magmas 114
6.4.2.3 Extraneous metasomatism in pyroxenites 116
6.4.3 Constraints on the ages of pyroxenites 117
6.4.4 Thermal-tectonic implications 121
6.5 Conclusions 124

Chapter 7. Summary of conclusions 126

References 131

Appendices:

Tables A1
Sample descriptions A61
Publications A83

ABSTRACT

Volcanism brings up mantle xenoliths that provide insights into the composition, structure and tectonic evolution of the ambient mantle. Peridotite and subordinate pyroxenite are the main rock types in the continental lithospheric mantle. In this study, peridotite xenoliths from the South China Craton and pyroxenite xenoliths from southeastern Australia have been investigated using petrographic and geochemical techniques to constrain their origins, evolution and relationships to geodynamic processes in each region.

Peridotite xenoliths from the South China Craton are divided into two groups. *Group 1* has olivine Mg# ~90-92 (relatively refractory) and shows the trace-element signature of "old" carbonatitic metasomatism. *Group 2* is fertile with olivine Mg# mainly ~89-90, and represents recently accreted lithospheric mantle. The residual refractory lithospheric mantle is inferred to be irregularly eroded by upwelling asthenosphere, leading to its replacement by newly accreted, fertile lithosphere. Peridotite xenoliths of both groups show sequential infiltration by Na-rich and K-rich silicate melts shortly before eruption. The lithospheric-mantle replacement may have been triggered by paleo-Pacific subduction and roll-back during late Mesozoic-Cenozoic time.

Garnet pyroxenite xenoliths from southeastern Australia record partial melting of the convective mantle wedge and represent crystallization products of the earliest recognized episodes of lithospheric mantle infiltration by mafic melts in this region. Paleozoic subduction of the proto-Pacific plate triggered melting of the convective mantle wedge beneath southeastern Australia and generated hydrous tholeiitic melts that crystallized high-MgO garnet pyroxenites at ~1420-1460 °C and 75-100 km. Subsequently, fluid-fluxed melting of the mantle wedge metasomatized by subducted sediments generated melts that precipitated low-MgO garnet pyroxenites at 1280-1400°C and ~53-66 km. Finally, all garnet pyroxenites were uplifted by at least 10~20 km at 40 Ma due to back-arc lithospheric extension; they finally equilibrated at ~950-1100°C and 40-60 km. The timing of these mantle events coincides with tectonism recorded in the overlying crust.

DECLARATION

This thesis is based on work carried out in the ARC Centre of Excellence for CCFS and GEMOC National Key Centre, Department of Earth and Planetary Sciences of Macquarie University (Australia) and in the China University of Geosciences (Wuhan), over the period from December 2013 to June 2017. I hereby declare that all data and interpretations in this thesis are all my own work, except for the information cited from published or unpublished sources which have been indicated and acknowledged.

No part of this thesis has ever been submitted for any other degree in any university or education institute. This thesis is submitted to both Macquarie University (Australia) and China University of Geosciences (Wuhan), under the conditions of the Cotutelle agreement for this PhD program between these two universities.

Jiang-Gu Lu

Date: **June 1, 2017**

ACKNOWLEDGEMENTS

I would like to acknowledge the people who have helped me on my way to getting my PhD. Without their support I simply would not have gotten to this point in my career.

My greatest thanks go to my supervisors Sue O'Reilly, Bill Griffin and Norm Pearson in Macquarie University and my Chinese supervisor Jian-Ping Zheng. They are all international experts on mantle geochemistry. Jian-Ping is my guide into the road of scientific research. Sue is my 'big boss' and she has a broad view on the scientific issues, which is helpful for me to get the key point on my work. Bill is a very kind person who always makes time to discuss with me about any breakthrough and problems I encountered, and he also has spent lot of time on my thesis of discussion and corrections to the draft. I benefited a lot from their wisdom, ideas and experience. I also truly appreciate that they provided me opportunities to use the state-of-the-art analytical facilities, and to study in a nice and efficient workplace.

Also, the analyses were accomplished with much help from Will Powell, Dave Adam, Peter Wieland, Steve Craven, Manal Bebbington, Yoann Greau, Rosanna Murphy, Hadrien Henry, Takako Satsukawa and Laure Martin.

Furthermore, I wish to thank Qing Xiong, Jin-Xiang Huang, John Adam, Montgarri Castillo Oliver, Romain Tilhac for their knowledge and advice for my work that has been published and presented in this thesis. I also thank my fellow PhD students, visitors and post-docs (Mei Li, Zhen Guo, Cheng-Xin Jiang, Bo Xu, …) who helped me to live and work well in Australia.

Third, I also wish to express my appreciation to Hua-Yun Tang, Chun-Mei Yu, Yun-Hai Zhu, Shan-Rong Zhao, Ming Chen, Bin Xia for their support and help when I was in Wuhan.

Last but not least, I must thank my husband (Tao Wu) for his unconditional and full support and understanding. I also thank my parents for giving me life and bringing me up. Special thanks should be given my sister. She is always with my parents and looks after my ailing dad with my mum. I love them so much, and I would not have made it this far without them.

Thanks all in my life!

LIST OF FIGURES

Chapter 1

Fig. 1-1 Representative Archean, Proterozoic and Phanerozoic subcontinental lithospheric mantle sections. 4

Fig. 1-2 Major element concentration of natural pyroxenite samples with different proposed origins. 7

Fig. 1-3 Normative compositions of natural mantle pyroxenites with different origins in the pesudoternary system of Fo-CaTs-Qz projected from Di 7

Fig. 1-4 Trace element concentrations and ratios plot in whole-rock mantle pyroxenite with different origins. 8

Fig. 1-5 Chondrite-normalised REE patterns for mantle pyroxenite with different origins ... 8

Fig. 1-6 Sr-Nd isotope variations in mantle pyroxenite with different origins 9

Chapter 2

Fig. 2-1 Possible reconstruction of Rodinia supercontinent at ~ 1Ga 15

Fig. 2-2 (a) Major tectonic divisions of Australia and relationship to the Antarctica. (b) Map of the Delamerian and Lachlan orogen belts, SE Australia 16

Fig. 2-3 Geological sketch map of western Victoria showing the Lachlan orogenic belt, Delamerian orogenic belt and Otway Basin 23

Fig. 2-4 (a) Map of major tectonic units in eastern China; (b) Map of Phanerozoic magmatic activity and representative peridotite xenolith localities in South China. (c, d) Cenozoic basalts and sample locations in Subei basin and Zhejiang province, respectively. 24

Chapter 4

Fig. 4-1 Photomicrographs of Lianshan xenoliths illustrating some key petrographic features 37

Fig. 4-2 Frequency distribution of Mg# in olivine from Lianshan peridotite xenoliths and other relevant samples from eastern China 38

Fig. 4-3 Chondrite-normalized REE patterns and primitive mantle-normalized trace element spidergrams in clinopyroxene of the Lianshan peridotites 39

Fig. 4-4 Mg# in clinopyroxene vs. Cr# in spinel in the Lianshan peridotite xenoliths 41
Fig. 4-5 Mg# (a) and CaO (b) vs. Al_2O_3 contents of the whole-rock Lianshan peridotite xenoliths. 41
Fig. 4-6 Chondrite-normalized REE patterns and primitive mantle-normalized trace element spidergrams of the whole-rock samples from the Lianshan area. 42
Fig. 4-7 $^{87}Sr/^{86}Sr$ vs. $^{143}Nd/^{144}Nd$ of the whole-rock compositions of Lianshan xenoliths. . 43
Fig. 4-8 Comparison of batch partial melting model (a) and fractional partial melting models (b). 44
Fig. 4-9 $(La/Yb)_N$ vs. Ti/Eu of clinopyroxenes from the Lianshan peridotites ..... .45
Fig. 4-10 Modal olivine contents vs. Mg# in olivine from Lianshan peridotite xenoliths.. . 47
Fig. 4-11 Equilibration temperature vs. Mg# in olivine from Lianshan peridotite xenoliths. 47

Chapter 5

Fig. 5-1 Photomicrographs showing the relationships between xenocryst/peridotitic minerals and the host basalt (a-d, BSE) and the textures (e-f)..... 52
Fig. 5-2 Spongy rims of clinopyroxene (a-d) and spinel (e-h) related to Na-rich and K-rich melts 54
Fig. 5-3 Dissolution and reaction of Opx (a-d) and Ol (e-f) related to reaction patches 55
Fig. 5-4 Variation of NiO (a) and CaO (b) vs Mg# in primary and secondary olivines. Al_2O_3 *vs.* TiO_2 (c) and Mg# *vs.* Cr# (d) in primary and secondary spinels 57
Fig. 5-5 Compositional variation of primary and secondary clinopyroxenes in Xilong peridotites 58
Fig. 5-6 Compositional traverse across reaction patches and clinopyroxene in XL-22 59
Fig. 5-7 Chondrite-normalized REE and primitive-mantle-normalized trace-element patterns of clinopyroxenes from Xilong peridotite xenoliths 60
Fig. 5-8 Chondrite-normalized REE and primitive-mantle-normalized trace-element patterns of K-melt 61
Fig. 5-9 (a) Fractional melting model based on Y_N *vs* Yb_N in primary clinopyroxene within the spinel stability field. (b) $(La/Yb)_N$ *vs* Ti/Eu in primary clinopyroxenes from the Xilong peridotite xenoliths..... 62

Chapter 6

Fig. 6-1 Hand specimen of representive garnet-pyroxenite xenoliths from Lakes Bullenmerri and Gnotuk 69

Fig. 6-2 Scanned images of thin sections of garnet websterites (BM96-3 (a), BM99-4 (b), GN35 (c)) and garnet clinopyroxenites (DR10162 (e), BM99X2 (f), BMC-1 (g)) 70
Fig. 6-3 Coarse equant microstructure in garnet pyroxenites 71
Fig. 6-4 Backscattered electron (BSE) photomicrographs of pyroxene megacrysts with exsolution products 72
Fig. 6-5 Petrographic illustration of representative minerals in the recrystallized texture ... 74
Fig. 6-6 Microstructure of samples BM99X2 and BMC-1 revealed by electron backscatter diffraction (EBSD) analysis 75
Fig. 6-7 Sp-cored textural variations in pyroxenite xenoliths..... 77
Fig. 6-8 Major-element traverses across the lamellar, recrystallized, and coarse zones in sample BM99X2 79
Fig. 6-9 Compositional variations of clinopyroxene and orthopyroxene in the garnet pyroxenite xenoliths from Lakes Bullenmerri and Gnotuk..... 80
Fig. 6-10 Compositional variations of garnet in the garnet pyroxenite xenoliths from Lakes Bullenmerri and Gnotuk..... 81
Fig. 6-11 Compositional variations of spinel in the garnet pyroxenite xenoliths from Lakes Bullenmerri and Gnotuk..... 82
Fig. 6-12 Compositional variations of amphibole (Amp) in the garnet pyroxenite xenoliths from Lakes Bullenmerri and Gnotuk. 83
Fig. 6-13 Cl versus F of apatite in the garnet pyroxenite xenoliths from Lakes Bullenmerri and Gnotuk 84
Fig. 6-14 REE zoning in individual garnets of sample BM99X2 (a, b) and DR11017c (c, d) from Lakes Bullenmerri and Gnotuk. 85
Fig. 6-15 Compositional profiles of Y (a, c) and REE (b, d) across the lamellar, recrystallized and coarse equant zones in BM99X2 for garnet and clinopyroxene. 86
Fig. 6-16 Compositional variations of Y (a, c, e) and REE (b, d, f) across the lamellar A, recrystallized B and recrystallized C zones in DR10165 for garnet, clinopyroxene and amphibole, respectively..... 86
Fig. 6-17 REE variations in garnet and clinopyroxene of recrystallized zone A, reaction zones B and C of sample BMC-1..... 87
Fig. 6-18 Chondrite-normalized REE and primitive mantle normalized multiple-element patterns of clinopyroxene in the garnet pyroxenite xenoliths from Lakes Bullenmerri and Gnotuk..... 88

Fig. 6-19 Chondrite-normalized REE and primitive mantle normalized multiple-element patterns of orthopyroxene in the garnet pyroxenite xenoliths from Lakes Bullenmerri and Gnotuk..... 89
Fig. 6-20 Chondrite-normalized REE and primitive mantle normalized multiple-element patterns of garnet in the garnet pyroxenite xenoliths from Lakes Bullenmerri and Gnotuk. 90
Fig. 6-21 Variations of Yb vs Nd (a) and Ybn vs (Gd/Yb)n (b) of garnet in the garnet pyroxenite xenoliths from Lakes Bullenmerri and Gnotuk..... 91
Fig. 6-22 Chondrite-normalized REE and primitive mantle normalized multiple-element patterns of amphibole in the garnet pyroxenite xenoliths from Lakes Bullenmerri and Gnotuk 92
Fig. 6-23 Chondrite-normalized REE (a) and primitive mantle normalized multiple-element (b) patterns of apatite in the garnet pyroxenite xenoliths from Lakes Bullenmerri and Gnotuk. 93
Fig. 6-24 Variations of whole-rock major oxides relative to wt% MgO of the garnet pyroxenite, spinel pyroxenite and peridotite xenoliths from Lakes Bullenmerri and Gnotuk95
Fig. 6-25 Normative compositions of the pyroxenite xenoliths from Lakes Bullenmerri and Gnotuk in the pesudoternary sustem Fo-CaTs-Qz projected from Di 96
Fig. 6-26 Compositional variations of whole-rock MgO versus trace element diagrams for garnet pyroxenite xenoliths in Lakes Bullenmerri and Gnotuk 96
Fig. 6-27 Chondrite-normalized REE and primitive mantle normalized multiple-element patterns of the garnet pyroxenite xenoliths in Lakes Bullenmerri and Gnotuk 98
Fig. 6-28 Variations of whole-rock Nb/Yb vs Th/Yb (a), Ti/1000 vs V (b), Zr vs Y (c) and Ce vs Ce/Pb (d) of the garnet pyroxenite xenoliths in Lakes Bullenmerri and Gnotuk. 99
Fig. 6-29 Compositional variations of the reconstructed clinopyroxene in the garnet pyroxenite xenoliths from Lakes Bullenmerri and Gnotuk..... 100
Fig. 6-30 Sr-Nd-Hf isotope variation of clinopyroxene and minor garnet in garnet pyroxenites from Lakes Bullenmerri and Gnotuk..... 104
Fig. 6-31 (a) Comparison of $^{87}Sr/^{86}Sr$ in clinopyroxene analyzed by LA-MC-ICPMS and by TIMS. (b) Covariations of *in situ* $^{87}Sr/^{86}Sr$ of clinopyroxene, amphibole, apatite and plagioclase by LA-MC-ICPMS..... 105
Fig. 6-32 Chondrite-normalized REE patterns of Cpx (a) and Gt (b) from a two-stage fractional crystallization..... 109
Fig. 6-33 Variation diagrams illustrating geochemical relationships between garnet pyroxenites, cumulate compositions from high-pressure crystallization experiments of

hydrous basalts, melt compositions and solid residues from partial melting of anhydrous MORB-like eclogite 113
Fig. 6-34 Normalized REE patterns and spider diagrams for melts in equilibrium with Type I and Type II garnet pyroxenites from Lakes Bullenmerri and Gnotuk 116
Fig. 6-35 Sm-Nd (a) and Lu-Hf (b) internal isochrons defined by garnet and clinopyroxene. (c) Sm-Nd isochron defined by whole-rock data. (d) Sr-Nd isotopic variation at t=300 Ma in the garnet pyroxenites from Lakes Bullenmerri and Gnotuk 119
Fig. 6-36 P-T diagram illustrating the thermal evolution of garnet pyroxenites from Lake Bullenmerri and Gnotuk……..... 123

LIST OF TABLES

Chapter 3

Table 3-1 Major-element compositions of Chinese standards GBW07102 and GBW07113 measured in this thesis and reference values by XRF A-1

Table 3-2 Trace element analysis of USGS basalt (BHVO-2 and BCR-2) and Chinese national standards (GSR-1) A-2

Table 3-3 Trace-element compositions of USGS BCR-2G, BHVO-2, BIR-1G and natural Mongol garnet measured in this thesis and their recommended values A-3

Chapter 4

Table 4-1 Microstructure and modal of the Lianshan xenoliths from the Yangtze craton A-4

Table 4-2 LA-ICPMS analyses (wt%) of minerals from the Lianshan peridotite xenoliths A-5

Table 4-3 Trace element compositions of olivines in the Lianshan xenoliths A-7

Table 4-4 Trace element compositions of orthopyroxenes in the Lianshan xenoliths A-8

Table 4-5 Trace element compositions of clinopyroxenes in the Lianshan xenoliths A-9

Table 4-6 Trace element compositions of spinels in the Lianshan xenoliths (ppm) A-10

Table 4-7 Major element compositions of the whole rocks from the Lianshan peridotite xenoliths (wt%) A-11

Table 4-8 Trace element compositions of the whole rocks from the Lianshan peridotite xenoliths (ppm) A-12

Table 4-9 Sr and Nd isotopic data for the Lianshan peridotite xenoliths A-13

Table 4-10 Equilibration temperature estimation for the Lianshan peridotite xenoliths A-14

Chapter 5

Table 5-1 Summary of petrological and geochemical data for Xilong xenoliths A-15

Table 5-2 Representative major element analyses (wt%) of primary minerals in Xilong peridotites A-16

Table 5-3 Major element analyses (wt%) of melts in spongy-textured minerals from Xilong peridotites by EDS. A-18

Table 5-4 Major element compositions analyses (wt%) of secondary clinopyroxene (Cpx2-A, Cpx2-B, Cpx2-C) by EMP in Xilong peridotites A-19

Table 5-5 Major element compositions analyses (wt%) of secondary spinel (Sp2-A, Sp2-B, Sp2-C) by EDS in Xilong peridotites.....A-20
Table 5-6 Major element compositions analyses (wt%) of K-melt by EMP in Xilong peridotites.....A-21
Table 5-7 Major element compositions analyses (wt%) of secondary olivine (Ol2) by EMP in Xilong peridotites.....A-22
Table 5-8 Major element composition variation of clinopyroxene in a profile AB from sample LS-22. .....A-23
Table 5-9 Representative trace element analyses (ppm) of clinopyroxene in Xilong peridotites by LA-ICPMS A-24
Table 5-10 Representative trace element analyses (ppm) of K-melt in Xilong peridotites by LA-ICPMS A-25

Chapter 6

Table 6-1 Point counted and calculated modal compositions (wt%) of garnet pyroxenites from Lakes Bullenmerri and Gnotuk A-26
Table 6-2 Major-element compositional profile of BM99X2 .....A-27
Table 6-3 Major-element compositions of clinopyroxene in the garnet pyroxenites from Lakes Bullenmerri and Gnotuk A-28
Table 6-4 Major-element compositions of orthopyroxene in the garnet pyroxenites from Lakes Bullenmerri and Gnotuk A-29
Table 6-5 Major-element compositions of garnet in the garnet pyroxenites from Lakes Bullenmerri and Gnotuk.....A-30
Table 6-6 Major-element compositions of spinel in the garnet pyroxenites from Lakes Bullenmerri and Gnotuk.....A-31
Table 6-7 Major-element compositions of amphibole in the garnet pyroxenites from Lakes Bullenmerri and Gnotuk.....A-32
Table 6-8 Major-element compositions of olivine, ilmenite, phlogopite, apatite and plagioclase in the garnet pyroxenites from Lakes Bullenmerri and Gnotuk.....A-33
Table 6-9 Trace-element compositional profile of BM99X2 by LA-ICPMS A-34
Table 6-10 Trace-element compositional profile of garnet around spinel in DR11017c by LA-ICPMS A-36
Table 6-11 Trace-element composition of clinopyroxene, garnet and amphibole from different textures in DR10165 by LA-ICPMS A-37

Table 6-12 Trace-element composition of clinopyroxene and garnet from different textures in BMC-1 by LA-ICPMS A-40
Table 6-13 Trace-element compositions (ppm) of clinopyroxene in the garnet pyroxenites from Lakes Bullenmerri and Gnotuk A-42
Table 6-14 Trace-element compositions (ppm) of orthopyroxene in the garnet pyroxenites from Lakes Bullenmerri and Gnotuk A-44
Table 6-15 Trace-element compositions (ppm) of garnet in the garnet pyroxenites from Lakes Bullenmerri and Gnotuk A-45
Table 6-16 Trace-element compositions (ppm) of amphibole in the garnet pyroxenites from Lakes Bullenmerri and Gnotuk A-47
Table 6-17 Trace-element compositions (ppm) of phlogopite (Phl), apatite (Ap) and plagioclase (Pl) in the garnet pyroxenites from Lakes Bullenmerri and Gnotuk A-48
Table 6-18 Major-element compositions of the reconstructed whole rock of the garnet pyroxenites from Lakes Bullenmerri and Gnotuk A-49
Table 6-19 Trace-element compositions (ppm) of reconstructed whole rock in the garnet pyroxenites from Lakes Bullenmerri and Gnotuk A-50
Table 6-20 Major- and Trace-element compositions of reconstructed clinopyroxene in the garnet pyroxenites from Lakes Bullenmerri and Gnotuk A-51
Table 6-21 Pressure-Temperature-Depth (P-T-D) results of re-equilibrated mineral assemblages and reconstructed clinopyroxene A-52
Table 6-22 Sr-Nd-Hf isotopes of clinopyroxene, amphibole, garnet and whole rock of garnet pyroxenites from Lakes Bullenmerri and Gnotuk A-53
Table 6-23 *In situ* Sr isotopic compositions of clinopyroxene, amphibole, apatite and plagioclase from garnet pyroxenite in Lakes Bullenmerri and Gnotuk A-54
Table 6-24 Mean Sr isotopic compositions of clinopyroxene, amphibole, apatite and plagioclase from garnet pyroxenite in Lakes Bullenmerri and Gnotuk A-58
Table 6-25 Mean O isotopic compositions of garnets from garnet pyroxenites in Lakes Bullenmerri and Gnotuk A-59
Table 6-26 The compositions of melts in equilibrium with the reconstructed clinopyroxene from garnet pyroxenites in Lakes Bullenmerri and Gnotuk A-60

CHAPTER 1
INTRODUCTION

1.1 Research significance

The solid Earth has three layers of significantly different composition (the core, the mantle and the crust); the mantle is further differentiated into the lithospheric mantle with a conductive thermal regime, and the convecting mantle. The whole mantle makes up ~82% by volume and ~65% by mass of the Earth, and is an important reservoir of material and energy. Understanding the structure, composition, origin and evolution of the mantle is a long-standing theme in solid-Earth science (e.g., Zindler and Hart, 1986; Nixon, 1987; McDonough and Sun, 1995; Hofmann, 1997; O'Reilly et al., 2001; Walter, 2003; Carlson, 2005). However, most of Earth's interior is 'sampled' only remotely – by geophysical data sets, such as the velocity of seismic waves, the slight variations in surface gravity due to density variations, and for those regions at lower temperatures than the Curie point, the variations in the magnetic field by convection in the electrically conductive fluid outer core (Mussett and Aftab Khan, 2000; Dziewonski and Romanowicz, 2015). However, these physical parameters are mainly sensitive to only the four most abundant elements in Earth's interior – oxygen, magnesium, silicon, and iron. Most of the elements in the periodic table have relatively little effect on the remotely measureable properties of Earth's interior, but they contain a record of the chemical constitution of the mantle and the mechanisms and time scales through which differentiation of Earth's interior created the planet we know today (Carlson, 2014).

Direct sampling of mantle rocks and minerals is necessary for ground-truthing of these remotely sensed properties, but our ability is limited to drilling, which reaches at best just a few kilometers into the crust; the deepest drill-depth of ~12km is on the Kola Peninsula of Russia. Fortunately, Earth has provided some exposures of upper mantle brought to the surface via tectonic processes (massifs) or explosive volcanic eruptions (xenoliths). These rocks provide insights into the mantle compositions and processes, especially for the lithospheric (non-convecting) mantle. Moreover, these rocks provide the ground truth for quantitative experimental-petrology research into the conditions of their formation (Green and Ringwood, 1967; Irving, 1974; Kelemen et al., 1990; Leuthold et al., 2015; Mitchell and

Grove, 2016).

The study of mantle-derived xenoliths and massifs suggest that the lithospheric mantle consists dominantly of peridotite with minor pyroxenite (<10%) (Downes, 2007). Therefore, representative peridotite xenoliths from the South China Craton and pyroxenite xenoliths from the Lachlan orogen of southeastern Australia have the major targets in this study to discuss mantle processes in different settings.

1.2 An overview of previous studies of mantle-derived peridotite xenoliths

1.2.1 Mantle peridotite xenoliths on- and off-craton

The subcontinental lithospheric mantle (SCLM) forms the lowermost part of the lithospheric plate complex that moves in a relatively rigid way over the hotter and rheologically weaker asthenosphere. The SCLM consists mainly of lherzolites, harzburgites and dunites. This compositional range is usually interpreted in terms of the progressive removal of basaltic components during partial melting events and is broadly related to the tectonothermal age of the overlying crust that was extracted by partial melting from the underlying lithospheric mantle (Hofmann, 1988; Griffin et al., 2009). Therefore, this secular evolution in SCLM composition implies quasi-contemporaneous formation (or modification) of the crust and its underlying mantle root, namely that there is long-term coupling between the crust and mantle in many cases (Boyd, 1989; Pearson, 1999; Griffin et al., 2003, 2009).

Generally, cratons are ancient continental regions that have been tectonically quiescent for billions of years. They are characterized by low surface heat-flow (Pollack and Chapman, 1977) and are underlain by highly depleted SCLM. Estimates of cratonic SCLM compositions can be mainly derived from xenoliths in kimberlite or lamproite, derived from a thick lithospheric mantle (180-220 km) beneath Archean cratons, because most peridotite massifs are found in young mobile belts. Most subcratonic peridotites are dominated by harzburgites and depleted lherzolites (Fig. 1-1), which have undergone a complex history of melt extraction that resulted in high degrees of depletion of the residual mantle (e.g., Nixon, 1987; Boyd et al., 1997; O'Reilly et al., 2001; Griffin et al., 2003). They have high Mg# in olivine, predominantly in the range of 92-94 (Boyd, 1989; O'Reilly et al., 2001; Pearson and Wittig, 2014) and also have low CaO (0.6-1%) and Al_2O_3 (1-1.5%) contents (Boyd, 1989; Griffin et al., 2009), which are useful measures of fertility (O'Reilly and Griffin, 2010). Simple mass-balance modeling shows that the required composition corresponds to that of the residue produced by 30 to 50% melting of fertile mantle peridotite (Walter, 1998, 1999; Lee, 2006). Such high degrees of melt depletion require unusually high temperatures, probably only achieved during the Archean and early Proterozoic when the mantle potential

temperature was high (Griffin et al., 2009; Herzberg and Rudnick, 2012). The depleted compositions have a low density (mean value of 3.31±0.016 g/cm^3 at standard temperature and pressure; O'Reilly et al., 2001). Most such xenoliths have equilibrated at temperatures below 1000-1100° C and pressure up to 4 Gpa (Griffin et al., 1999a), and thus stabilized on a relatively cool geotherm (average surface heat flow of 40 mW/m^2) (O'Reilly and Griffin, 1996).

In contrast, there are broad areas of continental crust bordering Archean cratons that are Proterozoic or younger and the mantle beneath these areas has been samples by a variety of xenoliths from basaltic volcanics or outcropping peridotite massifs, which are derived from relatively shallow SCLM (150-180 km beneath Proterozoic terrains and 60-130 km beneath Phanerozoic terrains) (Griffin et al., 2009). Unlike mantle xenoliths, peridotite massifs allow recognition of relationship between different rock types, but the mantle structures and mineralogical compositions may be obscured by deformation and metamorphic recrystallization during shallow upwelling, exhumation, and tectonic emplacement. Xenoliths from basaltic rocks provide samples from larger vertical sections of the SCLM, although relationships between rock types are seldom obvious. They show large compositional variation in different tectonic environment (Bodinier and Godard, 2014), but overall, in the Phanerozoic SCLM, they are mainly spinel lherzolites and minor garnet lherzolites below about 55-60 km depth (Fig. 1-1), with relatively low Mg# in olivine (88-90), and high bulk contents of CaO (3.1-3.2%) and Al_2O_3 (3.5-3.9%); they also plot close to the "oceanic trend" in terms of Mg# in olivine and the modal content of olivines (Boyd, 1989; Griffin et al., 2009). These xenoliths have a higher density (3.36±0.02 g/cm^3) than cratonic harzburgites. The geotherm in the Phanerozoic SCLM, before thermal relaxation to steady-state conditions, is typically high (mean 87 mW/m^2; Pollack et al., 1993) and strongly curved due to advective heat transfer from the passage of basaltic magmas, and the ponding of magmas around the crust–mantle boundary, as illustrated by the xenolith geotherm for southeastern Australia (Griffin et al., 1984; O'Reilly and Griffin, 1985, 1996; O'Reilly et al., 1997). A few spinel peridotite xenoliths from Phanerozoic setting are somewhat more depleted, but Re-Os analyses suggest that many of these xenoliths represent relict Proterozoic mantle preserved at shallow depths (Alard et al., 2002; Xu et al., 2008). Estimates for the mean composition of Proterozoic SCLM spread across the spectrum between the Archean and Phanerozoic SCLM with intermediate mean Mg# (90-92), CaO and Al_2O_3 contents (~2%) and density (~3.34±0.02 g/cm^3).

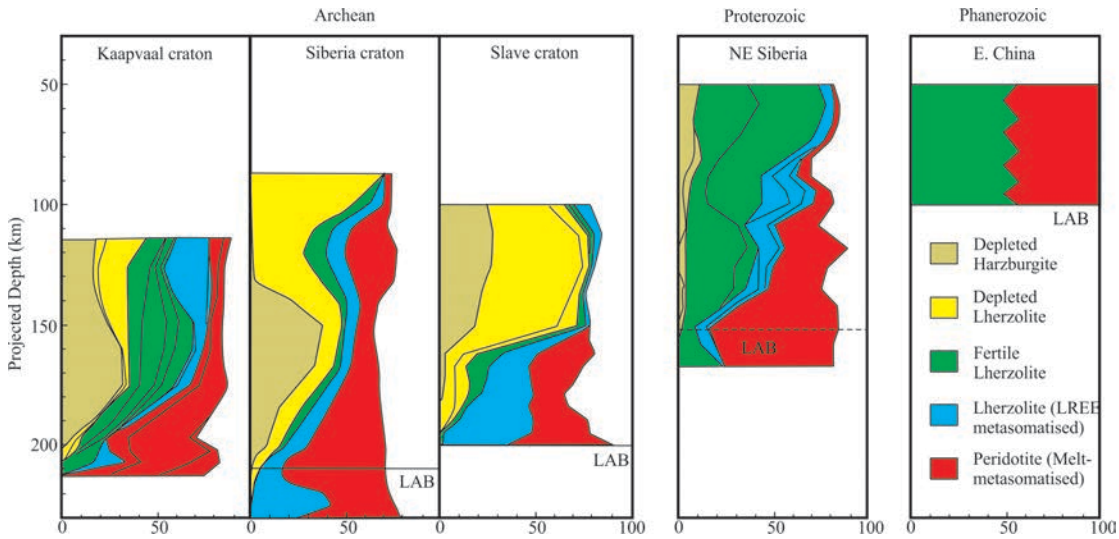

Fig. 1-1 Representative Archean, Proterozoic and Phanerozoic subcontinental lithospheric mantle sections, showing the abundance of different peridotite types (based on garnet compositions) with depth (after Griffin et al., 2003).

1.2.2 Peridotite xenoliths in Eastern China

The North China Craton (NCC) was one of the major Archean cratons in eastern Eurasia and contains rocks >3.6 Ga (Liu et al., 1992; Zheng et al., 2004a). Peridotite xenoliths collected from Paleozoic diamond-bearing kimberlites within the craton suggest an Archean (2.0-3.7 Ga) subcontinental lithospheric mantle (SCLM) existed underneath the eastern North China Craton during early Paleozoic time (Gao et al., 2002; Wu et al., 2006; Zhang et al., 2008), consistent with the Archean age of basement. However, most mantle xenoliths from Cenozoic basalts within the craton represent a fertile SCLM with Phanerozoic ages, e.g., peridotite xenoliths from Shanwang, which are mainly spinel lherzolites with fine-grained microstructures (Zheng et al., 1998). Only rare localities, such as some basaltic dikes in Hebi, contain harzburgites with coarse-grained microstructures and Archean Re-Os ages (2.5-3.0 Ga), representing shallow relics of the cratonic lithospheric mantle (Zheng et al., 2001, 2007; Liu et al., 2011). These observations suggest that the root of the Archean cratons has undergone significant Phanerozoic destruction and the SCLM was refertilized (e.g., O'Reilly et al., 2001; Foley, 2008; Xu et al., 2008; Griffin et al., 2009; Zheng et al., 2015), corresponding to the removal or strong modification of more than 100 km of cratonic lithosphere during late Mesozoic-Cenozoic time (Fan and Menzies, 1992; Griffin et al., 1992, 1998; Menzies et al., 1993; Xu, 2001; Gao et al., 2002; Zhang et al., 2003, 2005; Zheng et al., 2007). The refertilization-driven destabilization of subcontinental mantle within the craton has also occurred in the Wyoming Craton (Carlson et al., 2004; Kusky et al., 2014) and the North Atlantic Craton (Wittig et al., 2008, 2010), which are now characterized by the predominance of lherzolite with compositions similar to the primitive mantle.

Peridotite xenoliths from Paleozoic diamond-bearing kimberlites and Mesozoic-Cenozoic basalts were also found in the South China block (e.g., Qi et al., 1995; Xu et al., 1996, 2000, 2008; Zhang et al., 2001; Wang et al., 2003; Zheng et al., 2004b; Yu et al., 2006; Hao, 2010; Liu et al., 2012a, b; Lu et al., 2013). Moreover, recent research suggests that widespread Archean basement existed beneath the South China block (the Yangtze block and the Cathaysia block) and was reworked in the Proterozoic (Gao et al., 1999; Qiu et al., 2000; Zhang et al., 2006b, c; Zheng et al., 2006, 2011; Xu et al., 2007; Gao et al., 2011); this can be also considered as a modified Archean craton. Based on the idea of crust-mantle coupling, the SCLM should also have formed during Archean time. However, most xenoliths from Mesozoic–Cenozoic volcanics are fertile and Phanerozoic (Qi et al., 1995; Xu et al., 2000), with fewer relics of the relatively refractory SCLM (i.e., Anyuan, Qilin, Mingxi and Penghu; Xu et al., 1996, 2008; Wang et al., 2003). Has the South China Craton undergone destruction during Mesozoic, like the North China Craton? What are the similarities and differences between the North China Craton and the South China Craton? Why are these particular regions destabilized? What processes triggered the destabilization? When and how does mantle refertilization occur?

1.3 Overview previous work on mantle pyroxenite xenoliths

1.3.1 Mantle pyroxenite

Although pyroxenites probably make up only a minor (<10%) part of the upper mantle, the role of pyroxenites in the generation of mantle-derived magmas has received increasing attention during the last decades (Hirschmann and Stolper, 1996; Sobolev et al., 2005; Tuff et al., 2005). Preferential melting of pyroxenite or eclogite layers or veins may explain isotopic variations seen in oceanic basalts, and might also account for isotopic discrepancies between mid-ocean ridge basalts and residual abyssal peridotites (Salters and Dick, 2002). Experimental-petrology studies and isotopic considerations suggest that the presence of less than two percent of pyroxenite in basalt source regions may result in significant enhancements in magma production and may be responsible for a significant fraction of the melts that accumulate to form MORBs (Pertermann and Hirschmann, 2003b). Moreover, pyroxenite may be the missing link that can explain the imbalance between the compositions of the continental crust and primary arc magmas, commonly thought to represent the material that builds new continental crust (Lee et al., 2006). Therefore, pyroxenites may play a key role in global dynamic processes, although they represent only a small volume of the upper mantle. Understanding the nature and origin of the known pyroxenite occurrences worldwide is important for discussion of their distribution and the extent of geochemical heterogeneities

in the convective mantle.

The origin of mantle pyroxenites has been controversial. Early work (Dick and Sinton, 1979) suggested that they were the products of metamorphic segregation from the host peridotite, produced by dissolution and precipitation during plastic flow and pressure solution creep. *In situ* crystallization of partial melts of the peridotite, or solidification of percolating magmas have also been suggested (Chen et al., 2001; Lee et al., 2006; Aulbach et al., 2007). Although a few pyroxenites are still regarded as the residue after partial melting of earlier pyroxenites (Marchesi et al., 2013), most are interpreted as derived by high-pressure crystal segregation from mantle melts flowing through conduits in the mantle, creating a veined mantle (Frey, 1980; Irving, 1980; Medaris and Syada, 1999; Fabries et al., 2001; Xu, 2002; Upton et al., 2003; Ishikawa et al., 2004; Bizimis et al., 2005; Berger et al., 2007; Dantas et al., 2007; Medaris et al., 2013; Xiong et al., 2014; Martin et al., 2015).

However, there are increasing evidences of more complex petrogenesis for some pyroxenites, involving direct solid-state recycling of subducted lithosphere (Allègre and Turcotte, 1986; Kornprobst et al., 1990; Morishita et al., 2003) or metasomatic origins via melt-peridotite reaction (Garrido and Bodinier, 1999; Liu et al., 2005; Bodinier et al., 2008).

In some cases, more than one process may be recorded in a single pyroxenite sample. For instance, some pyroxenites are suggested to be remnants of subducted oceanic crust, streaked out into thin layers by mantle convection and incorporated into the lithosphere (Allègre and Turcotte, 1986). An alternative hypothesis suggests that they represent high-pressure crystal segregates from magmas derived from the melting of subducted ocean crust (Pearson et al., 1991, 1993; Ackerman et al., 2012). Pyroxenites could also be 'secondary' products of reaction between mantle peridotites or earlier pyroxenites and infiltrating melts that may be derived from recycled crustal components or from melting of peridotite (e.g., Garrido and Bodinier, 1999; Batanova, 2005; Liu et al., 2005; Sobolev et al., 2005; Aulbach et al., 2007; Garrido et al., 2007; Bodinier et al., 2008). They also could represent high-pressure cumulates from hybrid melts generated by the melting of metasomatic pyroxenites (e.g., Xu, 2002; Smit et al., 2014; Svojtka et al., 2016). These different models have been discussed by the earlier works of Irving (1980) who reviewed the origin of mantle pyroxenite xenoliths, Spray (1989) and Downes (2007) who discussed upper mantle segregation processes of pyroxenites in orogenic peridotites, and Bodinier and Godard (2014) who also discussed the compositional variations in pyroxenites from a wide range of tectonic settings.

By integrating the previous studies and experimental analyses, an idea of the origin of pyroxenites can be achieved from their major- and trace-elements, REE patterns and Sr-Nd isotopes (Figs. 1-2 – 1-6). If the pyroxenites represent recycled metamorphic oceanic crust,

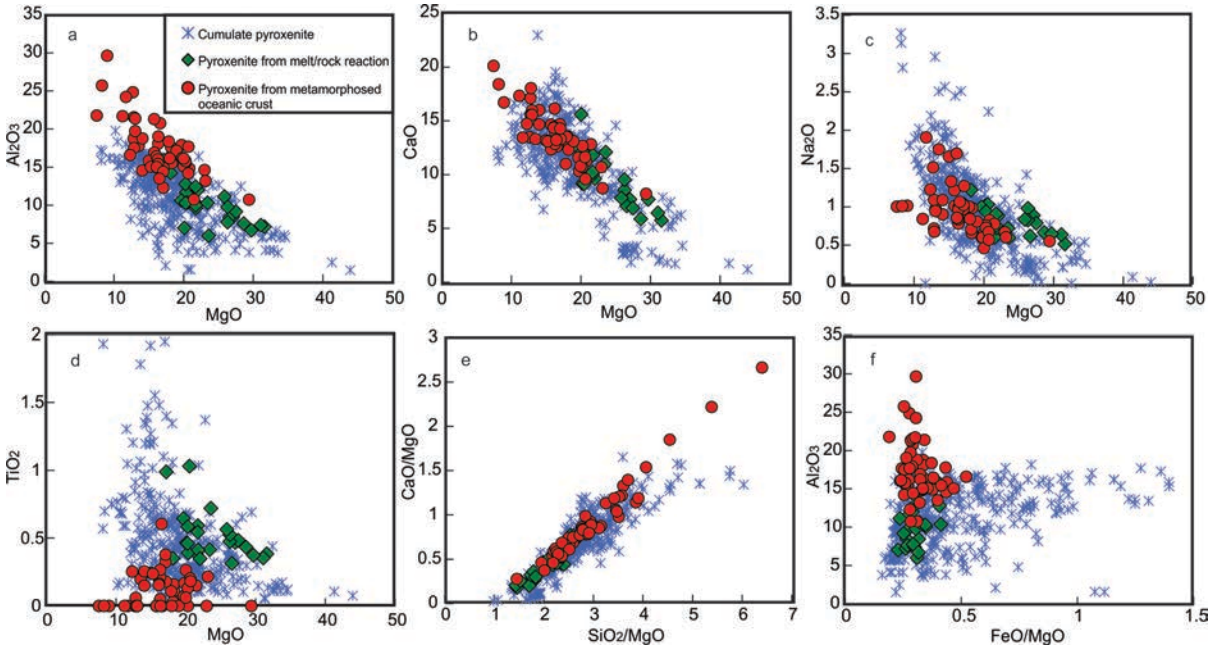

Fig. 1-2 Major element concentration of natural pyroxenite samples with different proposed origins. A database of pyroxenite cumulates, pyroxenites from metamorphic oceanic crust and from melt/rock reaction is from Xiong et al. (2014).

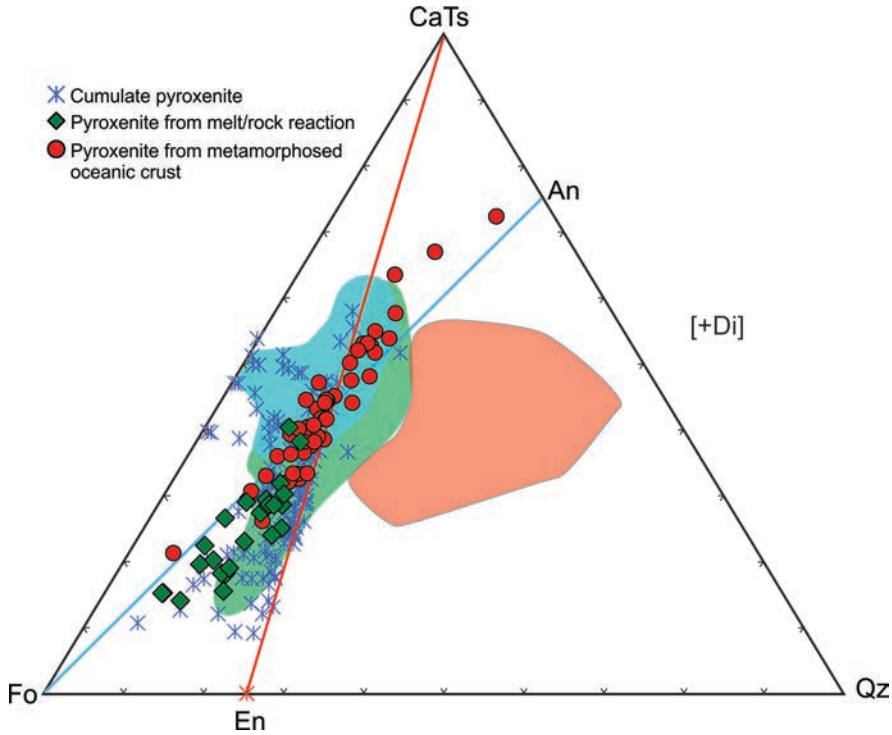

Fig. 1-3 Normative compositions of natural mantle pyroxenites with different origins in the pesudoternary system of Fo-CaTs-Qz projected from Di using the method of O'Hara (1968). Fo, forsterite; CaTs, Ca-Tschermak pyroxene; Qz, quartz; En, enstatite; An, anorthite; Di, diopside. Shaded areas represent experimental melts with different origin: Orange, silica-excess (SE) pyroxenite melt from partial melting of eclogite-like or MORB (Takahahshi et al., 1998; Pertermann and Hirschmann, 2003b; Spandler et al., 2008); Blue, silica-deficient (SD) pyroxenite melts from partial melting of previous pyroxenite (Hirschmann et al., 2003; Kogiso et al., 2003; Keshav et al., 2004; Lambart et al., 2009, 2013); Green, melts from partial melting of peridotites (Takahashi, 1986; Hirose and Kushiro, 1997; Walter, 1998; Falloon et al., 1998). Other symbols are as in Fig. 1-2.

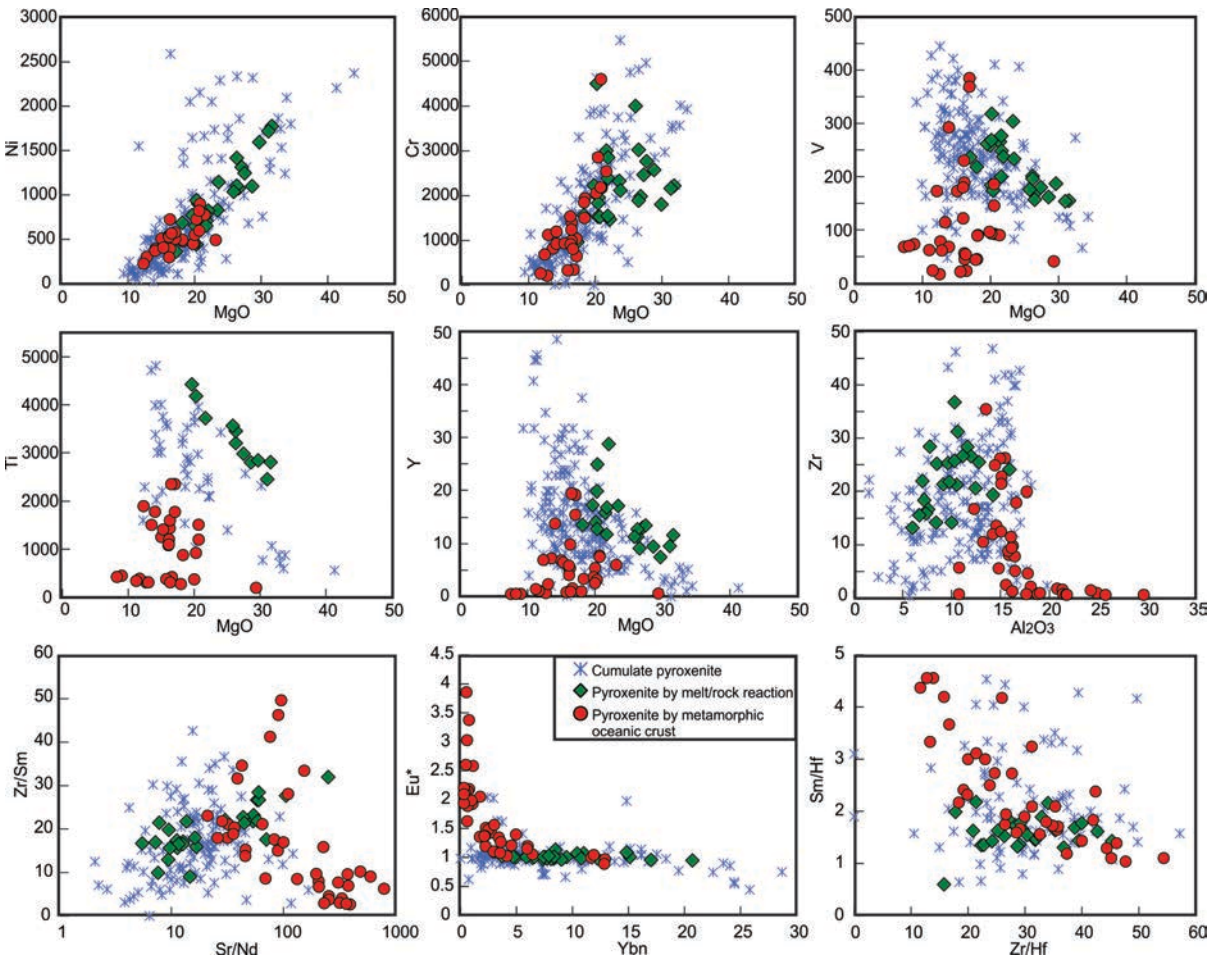

Fig. 1-4 Trace element concentrations and ratios plot in whole-rock mantle pyroxenite with different origins. Data source: pyroxenite from metamorphosed oceanic crust (red circle) is from (Takazawa et al., 1999; Morishita et al., 2003, 2004; Yu et al., 2010; Svojtka et al., 2016); pyroxenite from melt/rock reaction (green diamond) is from (Garrido and Bodinier, 1999; Liu et al., 2005; Bodinier et al., 2008); cumulate pyroxenite (blue star) is from (Frey, 1980; Xu, 2002; Liu et al., 2005; Bizimis et al., 2005; Lee et al., 2006; Zhang et al., 2009; Sen et al., 2011; Gysi et al., 2011; Ying et al., 2013; Svojtka et al., 2016).

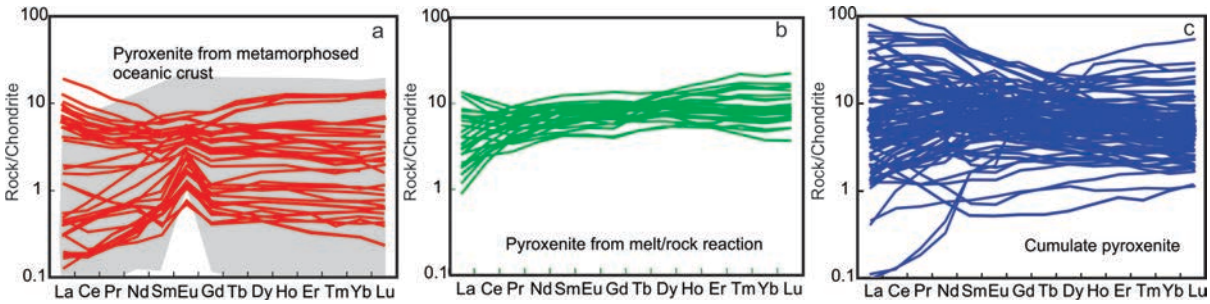

Fig. 1-5 Chondrite-normalised REE patterns for mantle pyroxenite with different origins. Shaded area is gabbros from Oman and SE Indian ridge (Benoit et al., 1996; Harte et al., 1999). Data source is the same as in Fig. 1-4.

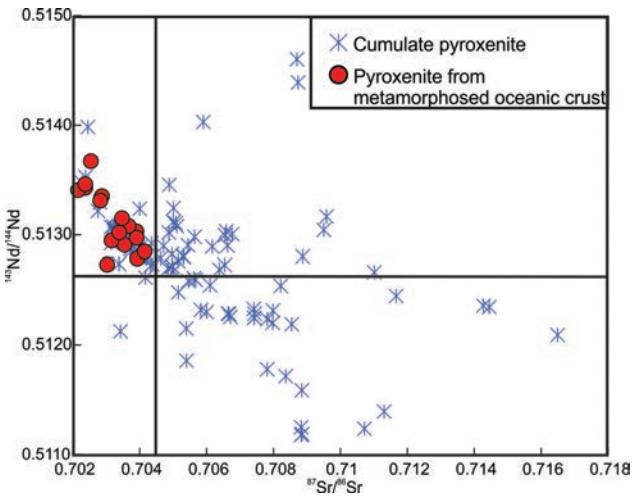

Fig. 1-6 Sr-Nd isotope variations in mantle pyroxenite with different origins. Data sources: cumulate pyroxenite is from (Pearson et al., 1993; Medaris et al., 1995, 2013; Xu, 2002; Bizimis et al., 2005; Ishikawa et al., 2007; Marchesi et al., 2012; Ying et al., 2013; Svojtka et al., 2016; Borghini et al., 2016); pyroxenite from metamorphosed oceanic crust is from (Kornprobst et al., 1990; Yu et al., 2010).

they should show relatively low Mg#, MgO, TiO_2 and high Al_2O_3, CaO and Na_2O (Fig. 1-2). They also would have lower Ni, Cr, V, Ti, Zr (Fig.1-4) and display obvious positive Eu anomalies in the whole rock (Fig. 1-5), clinopyroxene and garnet, and relatively depleted HREE in garnet. These pyroxenites would have show high $^{143}Nd/^{144}Nd$ and low $^{87}Sr/^{86}Sr$ (Fig. 1-6). All in all, they are similar in composition to oceanic gabbros and plot along Fo-An join in the Fo-CaTs-Qz [+Di] ternary (Fig. 1-3).

Pyroxenites interpreted as generated by melt-rock reaction generally display transitional contacts with the host peridotites and no deformation. They typically have higher contents of MgO, Ni, Cr and V, and lower Al_2O_3 and CaO than those derived from metamorphic oceanic crust, but are similar in compositions to cumulate pyroxenites, except for higher Ti contents.

Cumulate pyroxenites show variable compositions due to compositional variability of the melt sources, but they all plot within the field of partial melts from peridotite or in the area of overlap between peridotite melts and silica-deficient (SD) pyroxenite melts (Fig. 1-3). Moreover, cumulate pyroxenites plot along the CaTs-En join in the Fo-CaTs-Qz [+Di] ternary. These observations provide a basis for interpretation of the origin of pyroxenites, especially for xenolitic pyroxenites where spatial/geological context may not be clear.

This summary suggests that through the detailed petrological and geochemical studies of pyroxenites, we can understand their source and origins, constrain the history of mantle modification, and thus reveal deep-mantle geodynamic processes.

1.3.2 Pyroxenite xenoliths in the South China Craton and southeastern Australia

Pyroxenite xenoliths are only reported from the Mingxi and Qilin areas of the South

China Craton (Xu et al., 1996; Xu et al., 2002; Huang and Xu, 2010). Xu et al. (1996) used a group of well-equilibrated garnet pyroxenites from the Qilin locality to construct the first detailed, locality-specific paleogeotherm for the South China Craton and suggested that the crust-mantle boundary (CMB) lies at *ca* 27 km depth in this locality, which is shallower than the Moho (~31 Ma) defined by seismic refraction. The CMB forms a transiontional zone made up of interlayered garnet granulite, spinel lherzolite and pyroxenite from 27 to 31 km depth. Moreover, the strong curvature of this geotherm between 20 and 50 km depth indicates that advection, rather than conduction, was the dominant heat-transfer mechanism in the lower crust and upper mantle (Xu et al., 1996). These xenolith-defined geothermal gradient and lithospheric structure ares comparable to those for southeastern Australia (Xu et al., 1996, 1998). However, no studies have focused on the origin and evolution of these pyroxenites, their relationship with peridotite xenoliths and their contribution to the eruptive basalts. Due to the scarcity of the pyroxenite xenoliths, these studies did not further constrain the evolution of the lithospheric mantle.

Fortunately, ultramafic xenoliths (e.g., spinel peridotite, garnet- and spinel-pyroxenite, wehrlite, garnet granulite) derived from the lower crust and upper mantle are common in the dominantly Tertiary basaltic rocks from southeastern Australia (Wass and Irving, 1976), which provide a good chance to study the modification of the SCLM. Mantle-derived spinel lherzolites are the most abundant and ubiquitous xenolith type; garnet-bearing lherzolites have been reported from only three localities (Ferguson et al., 1977; Sutherland and Hollis, 1982). Al-augite type xenoliths, inferred to have crystallized from basaltic melts at high pressures, are also common (Lovering and White, 1969; Irving, 1974; Wilkinson and Kalocsai, 1974; Griffin et al., 1984; Stolz, 1984; Griffin et al., 1988; Roach, 2004; Sutherland et al., 2004). These xenoliths have been examined in studies with a variety of themes, including Sr-Nd isotopes (e.g., Griffin et al., 1988; Stolz and Davies, 1988), fluid inclusions (e.g., Andersen et al., 1984; O'Reilly et al., 1990; O'Reilly and Griffin, 2000), noble gases (e.g., Matsumoto et al., 2000), and mineralogy, geochemistry and metasomatism (e.g., Hollis, 1981; Griffin et al., 1984, 1988; O'Reilly and Griffin, 1988, 2000; Stolz and Davies, 1988; Adam et al., 1992; Powell et al., 2004).

Spinel lherzolite xenoliths from the Bullenmerri/Gnotuk maars in western Victoria differ from those described in other places; amphibole-bearing spinel lherzolite (~70%) is the most abundant, followed by anhydrous (~20%) and mica-bearing (~10%) lherzolite and rare apatite-bearing peridotite (Griffin et al., 1984). At least 3 types of metasomatism from different mantle events are recognised in the peridotite xenoliths: cryptic metasomatism recorded in the anhydrous samples with enriched LILE and LREE patterns compared to the

primary, unmetasomatized Cr-diopside lherzolite wall rock; amphibole ± mica metasomatism which is the most common type and is characterized by significant enrichments in Zr, Sr, LREE, Nb and Ta; apatite metasomatism which is independent of the amphibole ± mica addition and shows pronounced enrichment in Sr, P, LREE, Ta, Nb, Th, U and Ba (O'Reilly and Griffin, 1988; Stolz and Davies, 1988; Powell, 2005). Cryptic metasomatism and amphibole ± mica metasomatism are thought to have involved CO_2-rich silicate melts which may have been transported from depth dissolved in mafic melts and exsolved when these partially crystallized to form Al-augite pyroxenite xenoliths (Griffin et al., 1984, 1988; O'Reilly and Griffin, 1987, 1988). This is supported by data showing that the amphibole ± mica lherzolites are isotopically similar to pyroxenite xenoliths (Griffin et al., 1988). This metasomatism also caused Fe enrichment in the lherzolites, which show a large range in Mg#. Apatite metasomatism is inferred to represent a younger metasomatic event (<100 Ma ago) which overprinted the previous Sr and Nd isotopic signature and resulted in isotopic characteristics similar to those of the "Bulk Earth" ($^{87}Sr/^{86}Sr$ = 0.7043 – 0.7056, $^{143}Nd/^{144}Nd$ = 0.5124 – 0.5127; Griffin et al., 1988; Stolz and Davies, 1988), because apatite-bearing lherzolites always have higher Sr and Nd contents than other samples. This metasomatism also introduced Ca into the lherzolites (Yaxley et al., 1998). The apatite metasomatism also affected the wehrlites, which have similar geochemical characteristics to apatite-bearing lherzolites but lower Mg# (Powell, 2005). Most wehrlites are characterized by igneous or partially re-equilibrated igneous microstructures, in contrast to the cooling textures found in pyroxenite xenoliths. This suggests that the wehrlites represent a younger magmatic event. In addition, these wehrlites show lower Mg#, Al, higher Ti, Zr contents and smooth and upwardly convex REE patterns compared to the pyroxenites, and overlap the isotopic range ($^{87}Sr/^{86}Sr$ = 0.70366-0.70374, $^{143}Nd/^{144}Nd$=0.51276-0.51288) of the basalts in the Newer Volcanic Province (NVP) in Victoria ($^{87}Sr/^{86}Sr$=0.70356 - 0.70531, $^{143}Nd/^{144}Nd$=0.51271-0.51286), which suggests they crystallized from magmas similar to NVP lavas (Griffin et al., 1988).

Pyroxenite xenoliths from this area show abundant microstructural evidence for cooling, in the form of exsolution of spinel, orthopyroxene, garnet and rare plagioclase and ilmenite from complex clinopyroxenes (Hollis, 1981; Griffin et al., 1984, 1988; O'Reilly and Griffin, 1987, 2000; O'Reilly et al., 1989; Adam et al., 1992). They are considered to represent clinopyroxene (± spinel ± orthopyroxene) cumulates, followed by exsolution and recrystallization during cooling to the ambient geotherm (Griffin et al., 1984). Abundant garnet websterites allow for P-T estimates and were used to define the first empirical paleo-geotherm from 900 °C, 11kb to 1100°C, 16kb, which is consistent with the high regional heat

flow (>84 mW/m^2) (Griffin et al., 1984). Moreover, a reconstructed lithospheric mantle column is consistent with geophysical data, where the crust-mantle boundary is very shallow at ~25 km. The mantle from 25-55km consists of spinel lherzolite interleaved with spinel-and garnet-pyroxenites and basaltic cumulates; garnet lherzolite is stable at depths greater than 55 km (O'Reilly and Griffin, 1985). All available P-T data from other eastern Australian xenolith localities lie close to this geotherm, suggesting that a similar thermal regime (southeastern Australian geotherm) has characterized parts of this region at various times from the Permian to the present (O'Reilly and Griffin, 1985). The empirical paleo-geotherms constructed from the geothermobarometry of deep-seated xenoliths can be used to construct a realistic distribution of rock types with depth, thus providing constraints for the geologically meaningful interpretation of geophysical data and for placing geochemical and mantle process information in a spatial context, which is a key to 4-D lithosphere mapping (O'Reilly, 1989; O'Reilly and Griffin, 1996; Xu et al., 1996, 1998; O'Reilly et al., 1997).

However, these studies of the pyroxenites mainly focused on the construction of a paleo-geotherm (SEA geotherm), and used bulk-rock analysis techniques to study their geochemistry; there are few studies on the trace-element and isotopic compositions of minerals, which would allow us to infer the primary characteristics of the pyroxenites, the conditions and timing of their formation, the geochemical affinities of their parental melts, and their later petrological evolution.

1.4 Research targets and aims of this study

The research presented in this thesis is concerned with the details of the processes that modified the lithospheric mantle in two different settings (the South China Craton and the Lachlan Orogen), through studies on mantle peridotite xenoliths in southeastern China and garnet pyroxenite xenoliths in southeastern Australia, using detailed petrographic, petrochemical and multi-isotopic techniques. The aims are:

(1) to reveal the nature of the SCLM beneath the South China Craton and its modification;

(2) to distinguish multi-stage melt-rock reactions and to reveal the significance for decratonization of the South China Craton.

(3) to resolve the origin, timing, genesis and metasomatism of the garnet pyroxenite from SE Australia and to provide a P-T-t dynamic model for their generation and exhumation.

(4) to understand the contributions of subduction to the mantle dynamics in the subcontinental lithospheric mantle with off-craton characteristics beneath the South China Craton and the Lachlan orogen of southeastern Australia.

1.5 Thesis outline

This thesis is divided into 7 chapters. *Chapter 1* presents the significance and the main objectives of this research including peridotites and pyroxenites. *Chapter 2* presents the geological settings of the sampling positions in the South China Craton and the Lachlan Orogen of southeastern (SE) Australia. *Chapter 3* provides the details of analytical methods used in this study. *Chapter 4* discusses the nature and evolution of the lithospheric mantle beneath the South China Craton. *Chapter 5* discusses the microscale effects of multi-stage melt infiltration into the lithospheric mantle beneath the South China Craton. *Chapter 6* discusses the origin of the garnet pyroxenite xenoliths from SE Australia and its tectonic implications. *Chapter 7* summaries the conclusions reached in this study.

CHAPTER 2
GEOLOGICAL SETTINGS

The mantle carries a record of multiple large-scale tectonic events (O'Reilly et al., 2008), but it is difficult to see the deep interior of Earth. The deep-seated events are commonly mirrored in the crust (O'Reilly et al., 2008). Therefore understanding the geological evolution of the respective terranes helps us to better interpret the record of the studies of mantle samples in a lithosphere-scale tectonic context.

The formation and breakup of supercontinents has been an important feature of the Precambrian and Phanerozoic global tectonic framework and geological evolution. The South China block (Yangtze Craton and Cathaysia block) serves as the missing link between Australia and Laurentia, which assembled to form the core of the supercontinent Rodinia at ~1.0 Ga (Fig. 2-1; Li et al., 1995); this is demonstrated by the close biogeographic and paleomagnetic affinities of South China with Australia during early to mid-Paleozoic time (e.g., Burrett et al., 1990; Yang et al., 2004). During the breakup of Rodinia around ~0.7 Ga, South China separated from Australia, and they have experienced complex tectonic-thermal events in the Phanerozoic, but the geological evolution of southeastern China still has close analogies with southeastern Australia (e.g. Hsü et al., 1990; Finlayson et al., 1993; Crawford et al., 2003; Wang et al., 2013).

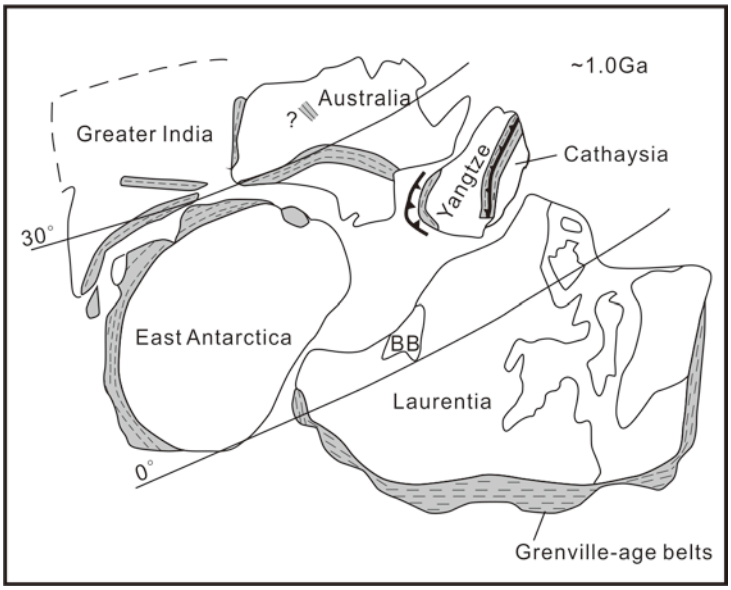

Fig. 2-1 Possible reconstruction of Rodinia supercontinent at ~ 1Ga (modified from Li et al., 1995).

2.1 Geological setting of southeastern Australia

The Australian continent consists of two broad tectonic units: the western two-thirds comprises Archean-Proterozoic cratonic terranes overlain in places by Palaeozoic strata, and the eastern one-third consists of the complex Paleozoic-Mesozoic Tasmanides, a collage of several orogenic belts and an internal Permian-Triassic foreland fold-thrust belt (Fig. 2-2a). These two regions are separated by the Tasman Line in the surface, approximating the locus of ~600Ma rifting – the second of two rifting events in the breakup of Rodinia in Australia (Veever, 1984). Following that breakup, a series of convergent-margin orogenic belts formed between cratonic Australia and the proto-Pacific plate boundary from ~540 to 100 Ma. In general, there was a southwest to northeast deposition of geological units in the southern Tasmanides represented now by the Delamerian, Lachlan, Thomson and New England orogens (Fig. 2-2a; Glen, 2005). The Delamerian orogen underlies eastern South Australia, western Victoria, western NSW and possibly part of Queensland. The western part of Tasmania has also been included in the Delamerian Orogen (Fig. 2-2a). The Lachlan Orogen underlies most of NSW, central and eastern Victoria and eastern Tasmania (VandenBerg et al., 2000). The boundary between the Lachlan and Delamerian fold belts is a major crustal feature-the Moyston Fault (VandenBerg et al., 2000; Cayley et al., 2011).

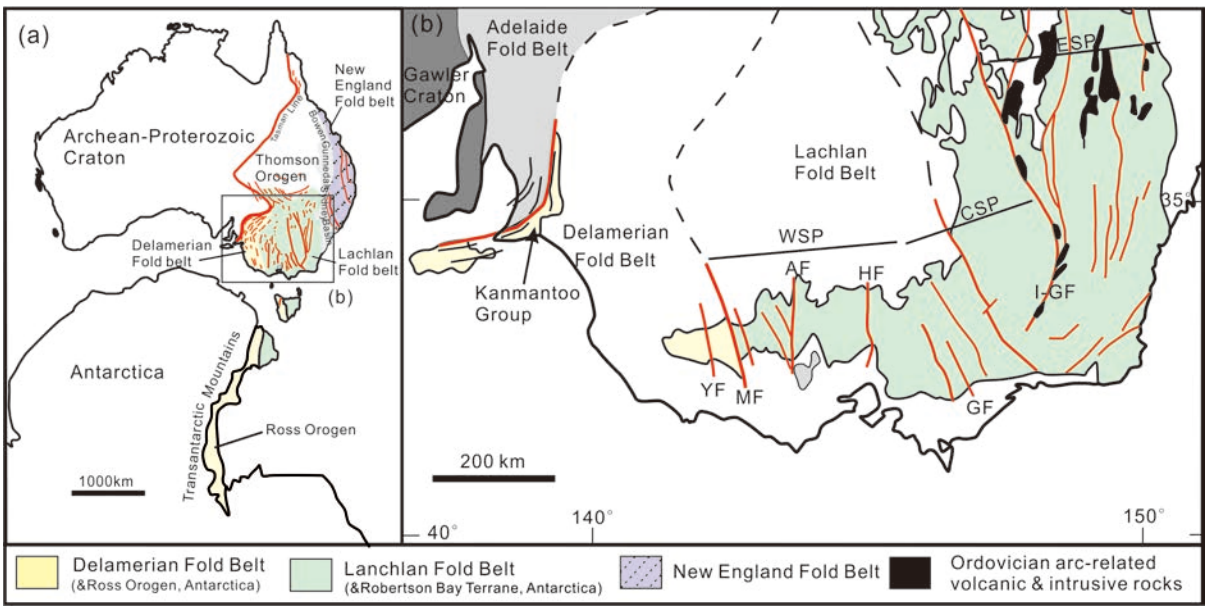

Fig. 2-2 (a) Major tectonic divisions of Australia and relationship to the Antarctica (locations of Antarctica and Australia reflect relative positions at about 110 Ma prior to the breakup of eastern Gondwana). (b) Map of the Delamerian and Lachlan orogen belts, SE Australia (modified from Miller et al., 2005). WSP, western subprovince; CSP, central subprovince; ESP, eastern subprovince. YF, Yarramyljup fault; MF, Moyston fault; AF, Avoca fault; HF, Heathcote fault; GF, Governor fault; I-GF, Indi-Glimore fault.

2.1.1 Paleozoic continental accretion

2.1.1.1 Delamerian orogenic belt

The Delamerian Orogen produced a west-vergent foreland-type fold and thrust belt that overprinted the Neoproterozoic Adelaidean successions during ca 514-490 Ma (Betts et al., 2002; Foden et al., 2006). The fold belt is 300km long and 600km wide and is represented by three main lithotectonic units: (1) generally shallow water and amagmatic rocks that were deposited in the Adelaide Rift from ~830- 600 Ma (Powell et al., 1994; Preiss, 2000), and stretched during rifting and then drifting, which reflects the breakup of the supercontinent Rodinia. (2) Rapidly deposited fill (Kanmantoo Group) (~526-514 Ma; (Foden et al., 2002) of a backarc rift basin (Kanmantoo Trough; Flöttmann et al., 1998). The Kanmantoo Group extends eastward, where it is known as the Glenelg zone in western victoria (Fig. 2-2b). The Glenelg zone contains lower Cambrian turbidites, carbonates, serpentinite, and probably volcanics ranging from intra-plate basalts and rift tholeiites to rocks transitional to MORBs (VandenBerg et al., 2000; Gray et al., 2002). Both were intruded by abundant (I-, S-, and A-type) granites (Foden et al., 2002). (3) At approximately the same age, or extending to ~500 Ma, a supra-subduction zone arc system extended from western Tasmania through poor outcrop in western Victoria and western NSW into western Queensland. In western Tasmania, there was an east to west obduction of forearc igneous crust above a continental fragment with metamorphic rocks. This was followed by post-collisional rifting and extrusion of the Mount Read Volcanics. These volcanics could extend to the mainland where they comprise the called 'Mount Stavely Volcanic Complex' in western Victoria (Fig. 2-3).

These Cambrian rocks are unconformably overlain by the late Silurian Grampians Group in western Victoria (Fig. 2-3). The Grampian Group is a sequence of sandstone, mudstone and minor conglomerate that were deformed by east-west compression to form a thrust and fold belt, followed by the intrusion and extrusion of felsic igneous rocks during early Devonian (~410Ma). The deformation does not occur in the underlying Cambrian rocks, suggesting the Grampian Group is a post-Delamerian Orogeny unit but shows an affinity with rocks in the adjacent Lachlan orogenic belt (VandenBerg et al., 2000).

2.1.1.2 Lachlan orogenic belt

The Lachlan fold belt consists mainly of Cambrian to Devonian sedimentary rocks that were deformed progressively over the period from ca 440 Ma to ca 340 Ma. It can be subdivided into western, central and eastern subprovinces with differences in rock type, metamorphic grade, structural history, and geological evolution on the Australia mainland

(Fig. 2-2b). The boundaries between the eastern and central, and between the central and western subprovinces are major oblique over-thrusts and are called the Indi-Glimore fault zone and the Governor fault zone, respectively.

The western parts of the western subprovince, the Stawell and Bendigo zones (Fig. 2-2b), consist mainly of thick accumulations of deep-marine turbiditic successions deposited during Cambrian-late Middle Ordovician (~500-460Ma) (Gray and Foster, 1997; Foster and Gray, 2000), and initially deformed between ~455Ma and 440Ma (Betts et al., 2002). The turbidites are metamorphosed to low-P greenschist facies, but locally reach amphibolite facies close to the Moyston Fault (The Moornambool Metamorphic complex). The basement of the Stawell and Bendigo zones consists of Cambrian (~500Ma) metavolcanics (tholeiitic basalts, boninites, andesites, and rare ultramafics), cherts, and volcaniclastics with MORB affinities (Foster and Gray, 2000). Both zones are intruded by numerous early- and late-Devonian granite plutons (dominant I-type). The eastern part of the western subprovinces is the Melbourne zone; it is bounded by the Heathcote and Governor fault zones. This zone is characterized by a thick, unbroken sedimentary sequence of lower Silurian to Middle Devonian rocks deposited in the Melbourne trough with 9-10km thick in the west but only 4 km thick in the east (Gray et al., 1997; Offler et al., 1998). Deformation in the sedimentary sequence is constrained to the Middle Devonian. The metamorphic grade in this zone is lower than in other parts of the Lachlan fold belt, ranging from unmetamorphosed in the west to low greenschist in the easternmost outcrops. This zone is also intruded by Middle and Late Devonian granites. The deformation and metamorphism had no effect on the underlying Ordovician sedimentary rocks (turbidites and black shale) and the basement (VandenBerg et al., 2000). Based on the results of a deep seismic reflection survey (Cayley et al., 2011), the basement in the zone is inferred to consist of Cambrian volcanics overlain by lower to middle Ordovician sedimentary rocks. The Cambrian rocks along the fault zone in the eastern part of the Melbourne zone (the old Mount Wellington Fault Zone) are thought to be bits of the basement of the underlying old microcontinent (Selwyn block), which appears to have formed a relatively rigid basement from the late Cambrian onwards (Cayley et al., 2002).

The central subprovince is dominated by an Ordovician quartz-rich turbidite succession, overlain locally by a Lower Silurian turbidite succession in the Tabberabbera and Wagga–Omeo Zones (Fig. 2-2b). Deformation was at ~440 and 435 Ma on either side of the lower Silurian turbidites, followed by major mid-Silurian – mid-Devonian extension associated with formation of rift basins (plus the inferred foreland basin of the Melbourne trough), and outpouring of felsic and lesser mafic volcanics and emplacement of granitoids.

The eastern subprovince consists of Ordovician turbidite basement overlain by extensive rift basins developed in the mid- Silurian to early Devonian (~430-400 Ma) and inverted in the middle Devonian by both east- and west-dipping reverse faults and folds. These basins are filled with Silurian-Devonian marine sediments which overlie Ordovician turbidites and less common calcalkaline volcanic rocks with arc affinity (VandenBerg et al., 2000). Deformation of the sediments occurred at ~400Ma in the west and at ~380Ma and 360Ma in the east (VandenBerg et al., 2000). Numerous late-Silurian to early-Devonian granites (I-, S- and A-types) have intruded these rocks. Before the deformation, most rocks experienced sub-greenschist-facies metamorphism.

These rocks are overlain by late Devonian (~370-360Ma) fluviatile molasse (Lambie facies) that was deposited widely across NSW and has been folded into a series of open, meridional folds in the west. Further east Carboniferous strain is higher and the Lambie facies is restricted to synclinal hinges and below thrust faults (~360-340Ma; Glen, 1992; Gray and Foster, 1998). The intensity of this early Carboniferous deformation increases dramatically eastwards.

2.1.1.3 Tectonic history

The Delamerian orogeny resulted from inversion of the Neoproterozoic and early Cambrian passive margin and rift sequence, presumably driven by subduction and collision of continental fragments (Glen et al., 1998). The major Delamerian element is the deformed Kanmantoo basin, which closed due to collision of a previously rifted continental fragment and an island arc (Stavely volcanic arc) at ~510-500Ma. Shortly after major crustal thickening, the Delamerian belt began to extend rapidly, accompanied by the emplacement of post-tectonic A-type granite plutons at ~490Ma. The post-orogenic extension may have been caused by subduction rollback after the Delamerian orogen, which could have also formed most of the oceanic (back arc) basement for the Lachlan turbidites deposited during the late Cambrian and Ordovician (Glen, 1992; Foster and Gray, 2000). Extension and rollback may have also rifted small continental fragments away from the Delamerian fold belt and distributed them within the back-arc basin (Gray and Foster, 1997). The deposition of abundant Ordovician turbidites probably reflects an interval of tectonic quiescence and formation of a marginal ocean basin.

From ~455 Ma to 440 Ma, shallow-angle subduction led to the development of a volcanic arc complex in the eastern subprovince and an associated accretionary complex (Narooma complex) as well as back-arc deformation in the western subprovince in the Lachlan orogen. The subduction could have closed a significant part of the marginal ocean

basin in the west and resulted in crustal shortening in most of the western subprovince. During the interval, sedimentation continued in the Melbourne zone (Melbourne Trough). Then, double convergence began along the western part of the central Lachlan, forming mélange zones (Wagga-Omeo metamorphic zone) and magmatism during the early to middle Silurian (440-420 Ma). By ~420 Ma, extensive granite emplacement and rift basin development in the central and eastern subprovince suggest a regional extension during this period. In the Middle Devonian (~390-380 Ma), the last undeformed part of the marginal basin in the west collided with the central subprovince, causing crustal thickening and deformation of the younger sediments in the Melbourne zone. The collision led to attainment of freeboard over most of the orogens in Victoria, followed by widespread post-orogenic extension, basin-and-range style faulting, explosive volcanism, and high-level plutonism. This period of post-orogenic extension was dominated by bimodal volcanism and continental-rift clastic sedimentation from the late Devonian through early Carboniferous (~370-360 Ma) time (Glen et al., 1998).

2.1.2 Mesozoic rifting

By the end of the Triassic period, Gondwana began to break up, with the separation of Australia from Antarctica, associated with basaltic volcanism (O'Reilly and Zhang, 1995; Edwards et al., 1996). The rifting process initiated systems of block faults parallel to the eventual line of separation. Subsequent rapid deposition of continental and fluvio-lacustriine sediments led to the formation of widespread Jurassic-Cretaceous shallow-water basins (Edwards et al., 1996). Localized erosion of the Palaeozoic rift margins provided sediments for the early rift-fill sequences in the Otway Basin, along the northern margins of these basins in western Victoria (Edwards et al., 1996). During the mid-Cretaceous, rifting between Australia and Antarctica developed into sea-floor spreading from ~95 Ma (Veevers, 1986). This spreading led to the opening of the Tasman Sea and presumably to uplift of the marginal subcontinental lithospheric mantle. Extensional tectonic activity continued into the Tertiary and thick deposits of sediments accumulated towards the end of the middle Eocene (Fig. 2-3).

2.1.3 Cenozoic volcanics and mantle xenoliths

Magmatism is commonly associated with lithospheric extension at evolving passive margins. Basaltic volcanism is exposed in a belt that extends for around 4400 km from North Queensland to Tasmania and the activity has continued from the earliest initial rifting at ~95

Ma to virtually the present day (O'Reilly and Zhang, 1995; Vasconcelos et al., 2008). On the basis of geomorphological characteristics and age, this basaltic volcanism is generally divided into two types: central-volcano provinces and lava-field. The central-volcano provinces show a regular age progression of younging southwards from central Queensland (~34-27 Ma) to Cosgrove in Victoria (~17-9 Ma) and are widely believed to mark the passage (~2000 km) of the northward-migrating Australian plate over one or more mantle plumes that now lie to the northwest of Tasmania (O'Reilly and Zhang, 1995; Davies et al., 2015). The magma compositions have a strong correlation with lithospheric thickness but the dominant type, where the lithosphere is <110 km thick, is a basaltic composition similar to typical OIB. When the lithospheric thickness exceeds 110 km, low-volume, leucitite-bearing volcanism erupted due to very low-degree partial melting (Davies et al., 2015). The extensive lava-field volcanism took place mainly during the last 70 Ma and erupted through a variety of terrains of different ages; most them contain xenoliths of mantle rock types (O'Reilly et al., 1989). This volcanism involved the addition of SCLM components along with an OIB component (O'Reilly and Zhang, 1995; Zhang and O'Reilly, 1997). This lava-field basaltic volcanism is also distributed across the state of Victoria over an area more than 700 km from east to west and around 300km north to south (McDonough et al., 1985; Vogel and Keays, 1997; McBride et al., 2001; Price et al., 2003, 2014; Demidjuk et al., 2007; Oostingh et al., 2016). Basaltic rocks with ages from 95 to 18 Ma, referred to as the "Older Volcanics", occur in small lava fields scattered across eastern and south-eastern Victoria and they have also been recovered from bore holes in the west of the state (Price et al., 2014). Their composition ranges from SiO_2-undersaturated nephelinites, basanites, basalts and hawaiites through transitional basalts to hypersthene- and quartz-normative tholeiites, but around two thirds of the basalts are nepheline normative (Price et al., 2014). More volumetrically extensive (~150,000km^2) and younger (mainly < 4.6 Ma) lava fields, comprising the "Newer Volcanics Province" (NVP) in western Victoria, began at 4.6 Ma, reached a peak at 2.6 Ma, and continued until about 4.6 Ka (Finlayson et al., 1993). The NVP can be subdivided into two series, the early Plains (dominant) and slightly later Cones, on the basis of geomorphology and composition (Wellman and McDougall, 1974). The former usually contain significant amounts of felsic components with dominantly tholeiitic to chemically transitional character, whereas the latter dominantly comprises silica-undersaturated alkali basalts, often erupted as scoria or cinder cones, maars and tuff rings. Major- and trace-element and Sr-Nd-Pb isotope analyses of these volcanics in Victoria suggest that the Older Volcanics were generated by low degrees of partial melting of an originally depleted mantle metasomatised by the addition of an enriched component similar to EM I type intraplate basalt (Group 1) or a calci-

carbonatite composition (Group 2), followed by fractional crystallization with or without limited assimilation of crust (Price et al., 2014; Oostingh et al., 2016). The lavas of the NVP Cones were generated by up to 15% partial melting of a spinel-garnet peridotite mantle with a mixture of depleted MORB-source asthenosphere and metasomatised subcontinental lithospheric mantle (SCLM), followed by up to 20% fractional crystallization. The lavas of the NVP Plains are the result of higher degrees of partial melting of mixtures of depleted SCLM with MORB-source asthenosphere and assimilation of ~5% continental crust with variable isotopic signatures (McBride et al., 2001; Demidjuk et al., 2007; Oostingh et al., 2016). This volcanism is not related to the mantle plume but was produced by asthenospheric upwelling triggered by 3D thickness variations in the lithosphere, which causes edge-driven convection (EDC) with shear below the irregular base of the lithosphere as the Australian Plate moved northward (Demidjuk et al., 2007; Price et al., 2014; Oostingh et al., 2016). A recent teleseismic tomography study, based on variations in P-wave velocity, has revealed the presence of a low-velocity anomaly in the upper mantle that spatially corresponds to the surface extent of the NVP and is elongated in the east-west direction (Davies and Rawlinson, 2014).

Mantle xenoliths used in this study are from Lakes Bullenmerri and Gnotuk (Bullenmerri/Gnotuk), Quaternary maars of the NVP Cones located adjacent to one another (<1km apart). The locality is located close to the Mortlake discontinuity, which represents a discontinuity in the deeper lithospheric mantle based on differing Sr and Pb isotopic compositions of NVP Plains ($^{87}Sr/^{86}Sr$ is low in the west to high in the east) (Price et al., 1997). The mantle xenolith age distribution also suggests a significant age change from Proterozoic in the west to dominantly Phanerozoic in the east of the Mortlake discontinuity (Handler et al., 1997; Handler and Bennett, 2001). The discontinuity appears coincident with the surface expression of the east-dipping Moyston Fault separating the Paleozoic Delamerian-Lachlan fold belts (Glen, 1992). The basanite tuffs have compositions within the range of the NVP Cones, with low MgO (~6.71 wt%), CaO (~6.89 wt%) and high alkali contents, and they also have limited ranges in Sr-Nd isotopes ($^{87}Sr/^{86}Sr$=0.7039-0.7041, $^{143}Nd/^{144}Nd$=~0.51283; Griffin et al., 1988; Stolz and Davies, 1988). The basalts are extraordinarily rich in xenoliths of spinel lherzolites, wehrlite, and metapyroxenite.

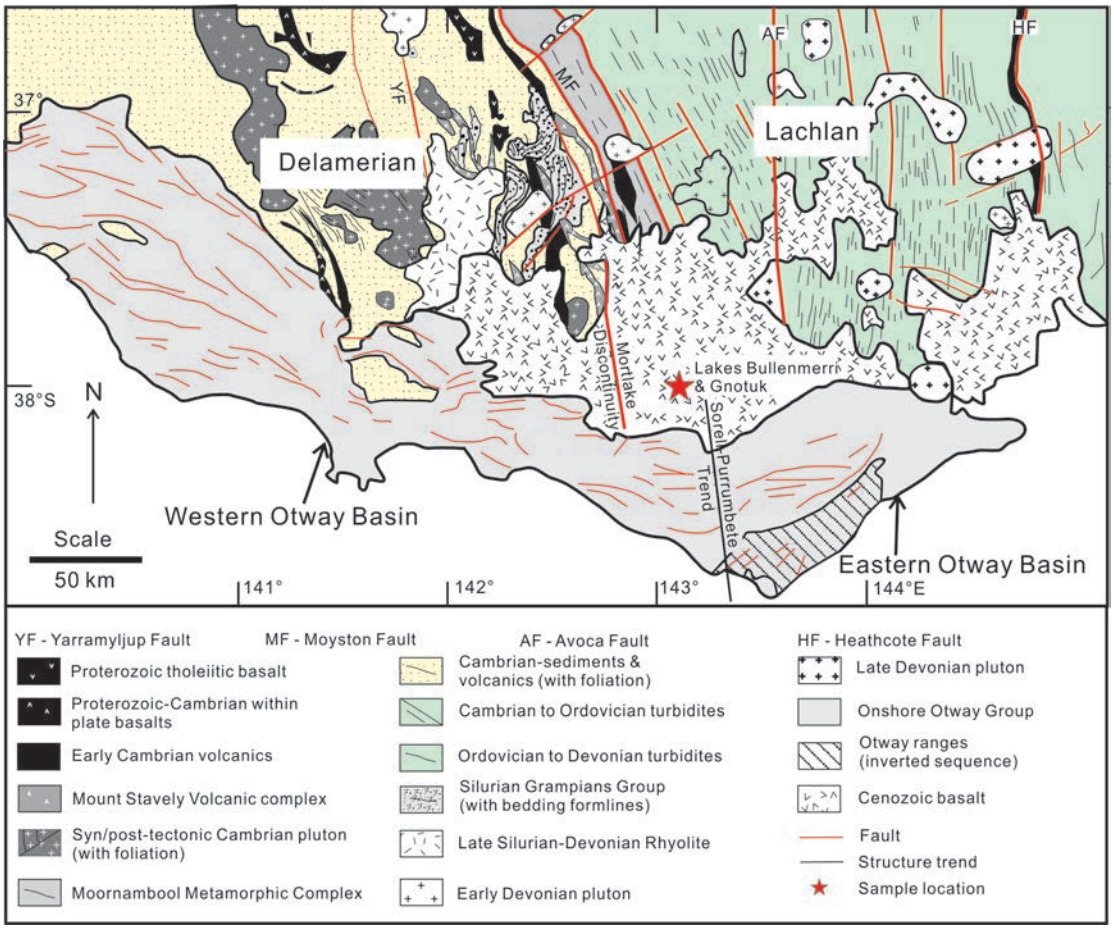

Fig. 2-3 Geological sketch map of western Victoria showing the Lachlan orogenic belt, Delamerian orogenic belt and Otway Basin (compiled from Miller et al., 2002, 2005).

2.2 Geological setting of the South China block

The South China block is composed of the Yangtze Craton in the northwest and the Cathaysia block in the southeast, which have been considered as two separate terranes of the Neoproterozoic Rodinia supercontinent (Li et al., 1995); they were amalgamated along the Shaoxing- Jiangshan-Pingxiang-Yushan fault zones (JS-PYFZ; Fig. 2-4a) during late Proterozoic (Li et al., 2009; Zhao and Cawood, 2012). Exposed basement in the Yangtze Craton is dominantly Proterozoic with scattered Archean outcrops (the Kongling Complex; Gao et al., 1999; Qiu et al., 2000; Zhang et al., 2006a, c). The latter include TTG gneisses and migmatites with ages of 2.9-2.95 (Qiu et al., 2000; Zhang et al., 2006c), metasedimentary rocks with zircons of 3.2-2.9 Ga (Qiu et al., 2000), and minor lenticular-like amphibolites and mafic granulites (Wu et al., 2009). Moreover, recent research on detrital zircons (Zhang et al., 2006b), inherited cores of zircons in igneous or metamorphic rocks (Huang et al., 2006) and zircon xenocrysts in volcanic rocks (Zheng et al., 2006) suggest that widespread Archean basement existed beneath the Yangtze Craton and was reworked in the Proterozoic. The Cathaysia block is composed mainly of Neoproterozoic crust with scattered exposures of

Paleoproterozoic basement rocks (Zhao and Cawood, 2012). However, U-Pb ages and Hf-isotope systematics of detrital zircons (Xu et al., 2007; Yao et al., 2011) and zircon xenocrysts in igneous rocks (Zheng et al., 2011) show Archean ages, suggesting that highly evolved Archean basement may underlie the Cathaysia block as well (Zheng et al., 2011). Therefore, the South China block should be regarded as an Archean craton. After the breakup of Rodinia at ca. 830 Ma, the South China block was subsequently overprinted by at least three tectonothermal events in the middle Paleozoic (~415-460 Ma), Triassic (Indosinian) and Jurassic-Cretaceous (Yanshanian) (e.g., Li et al., 1993; Li, 1998; Zhou and Li, 2000; Zhou et al., 2006; Wang et al., 2013).

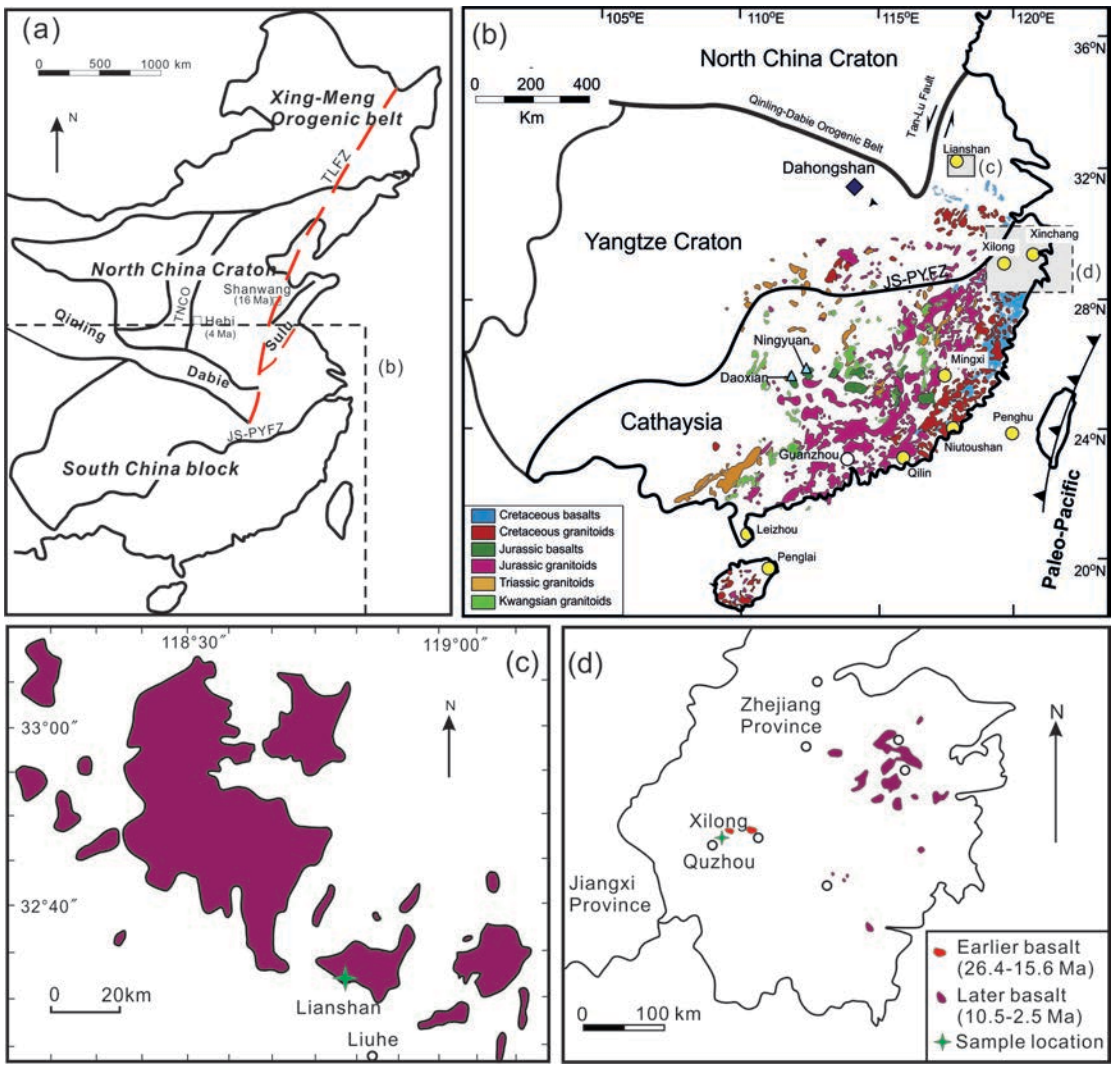

Fig. 2-4 (a) Map of major tectonic units in eastern China; (b) Map of Phanerozoic magmatic activity and representative peridotite xenolith localities in South China (modified from Wang et al., 2011; Liu et al., 2012a). Symbols are color-coded for age of basalt host: dark blue is Paleozoic, sky blue is Mesozoic, and yellow is Cenozoic. (c, d) Cenozoic basalts and sample locations in Subei basin and Zhejiang province, respectively. TNCO, Trans-North China orogen; TLFZ, Tanlu fault zone; JS-PYFZ, Jiangshan-Shanxing and Pingxiang-Yushan translithospheric fault zone.

2.2.1 Paleozoic Wuyi-Yunkai Orogen and associated magmatism

The middle Paleozoic event was originally named the Kwangsian movement by Ting (1929) due to the recognition of an angular uncomformity between post-Silurian cover and strongly deformed pre-Devonian strata (e.g., Huang et al., 1980; Ren, 1991). The tectonic belt associated with this event was named the Wuyi-Yunkai tectonic zone or the Wuyi-Yunkai orogen (Li et al., 2010), which is coeval with the classic Caledonian orogeny in Europe (e.g., Huang et al., 1980; Ren, 1991). The orogeny is an intraplate orogenic belt (i.e., Ren, 1991; Li, 1998; Wang et al., 2007), which closed the mid-Neoproterozoic-early Paleozoic Nanhua failed rift basin - the Nanhua Rift (Li, 1998). The Nanhua Rift was filled with dominantly Neoproterozoic volcanic and volcaniclastic rift successions and younger deposits as well as minor Paleoproterozoic rocks. During the orogeny (~415-460 Ma) (Li et al., 2010; Wang et al., 2011), the Proterozoic and early Paleozoic rift-related rocks underwent high-grade (upper greenschist to granulite-facies) metamorphism (e.g., Wan et al., 2007; Li et al., 2010), associated with strong folding and ductile shearing, extensive magmatic activity and the development of a regional angular unconformity. Granites intruded within the 440-415 Ma and (e.g., Wan et al., 2010; Yang et al., 2010; Wang et al., 2011); they are mainly S-type peraluminous granite that originated from Precambrian crustal materials (e.g., Chen and Jahn, 1998; Li et al., 2010; Wang et al., 2011). Geodynamically the Wuyi-Yunkai orogeny may have been a far-field response to the amalgamation of the Australian-Indian plate and the Cathaysia block along the northern margin of east Gondwana (Li et al., 1998; Wang et al., 2011).

2.2.2 Mesozoic Indosinian and Yanshanian orogeny and associated magmatism

By the late Triassic, the South China block appears to have amalgamated with the North China craton along a suture represented by the Dabie-Sulu UHP belt. Both the North China Craton and the South China Block are small relative to many other cratons, and have been disturbed by post-Archean magmatic events and lithosphere thinning. Abundant igneous rocks are exposed, occupying ~90% of a total outcrop area of nearly 220,000 km^2 in South China (Zhou et al., 2006; Li and Li, 2007), and they are associated with large-scale mineralization (Sun et al., 2012). Early Mesozoic (251–205 Ma) magmatic rocks occur only as small plutons in the interior of Cathaysia (mainly in Guangxi and Hunan area), with a total outcrop area of ~14,300 km^2. The plutons are mainly peraluminous S-type granites with minor calc-alkaline I-type granites (e.g., Zhou et al., 2006; Shu et al., 2008; Chen et al., 2011), which are related to the collision of some micro-continents (including North China, South China, Indochina, Siman and Sibumasu blocks) during Permian to Triassic time (e.g.,

(Metelkin et al., 2010). These collisional events have been referred to as the "Indosinian orogeny". During this orogeny, the South China block experienced north-south compression, forming a nearly east-west trending fold belt (Shu et al., 2008). No coeval volcanic rocks are associated with the intrusives.

In the Jurassic and Cretaceous, the block was intruded by vast granitic plutons with some mafic intrusive and volcanic rocks (Zhou et al., 2006), which referred to "Yanshanian event". The large-scale Yanshanian granitoid-volcanic rocks are distributed widely in South China, and become progressively younger northeastward from Jurassic (180–150 Ma) in the interior of the South China block to 140–67 Ma in the Lower Yangtze River Belt and the coastal region of northeast Zhejiang Province (Zhou et al., 2006). The early Yanshanian (180-142 Ma) granitoid-volcanic rocks are characteristic of rift-type intraplate magmatism, whereas the late Yanshanian (142-67 Ma) K1 granitoid-volcanic rocks are interpreted as representing active continental margin magmatism. The K2 tholeiitic basalts interlayered with redbeds are interpreted as genetically associated with the development of back-arc extensional basins in the South China block. The formation of the late Mesozoic granitic and volcanic rocks has most commonly been interpreted as the result of subduction of the paleo-Pacific oceanic plate (Zhou and Li, 2000; Zhou et al., 2006; Li and Li, 2007). The rollback of the paleo-Pacific plate left a broad wake of lithospheric extension in southeastern China, as exemplified by the opening of the South China Sea (~90 Ma) and other early Tertiary basins (i.e., Chung et al., 1994). The continental margin of the South China block was transformed from an Andean-type plate margin at 280-90 Ma, to the present-day Western Pacific-type plate margin soon after 90 Ma (Li et al., 2012).

2.2.3 Cenozoic basalt and mantle xenoliths

Due to the Mesozoic-Cenozoic paleo-Pacific subduction, abundant intraplate basaltic volcanism occurred in the South China block, especially Cenozoic basalts along the coastal area, i.e., in Zhejiang, Fujian, Guangdong and Hainan Provinces (Fig. 2-4b). Small but locally voluminous outcrops of Mesozoic volcanic rocks and mafic dikes also occurred in association with the Mesozoic granites in the interior of the South China block (i.e., Jiangxi and Hunan Provinces). The Sr-Nd and Pb isotopic compositions of middle Jurassic to late Cretaceous mafic rocks across the Chenzhou–Linwu Fault suggest the presence of multiple mantle reservoirs include FOZO-, DMM-, EM I- and EM II-like components beneath the South China Block (Zhao et al., 2007; Wang et al., 2008). West of the fault, the rocks originated from mixing between EM I and FOZO-like asthenospheric mantle; east of the fault,

the mafic rocks suggest a DMM-EM II reservoir in the uppermost asthenospheric mantle source (Zhao et al., 2007; Wang et al., 2008). These widespread Cenozoic basalts can be divided into two periods relative to the cessation of South China Sea seafloor spreading (~16 Ma; Chung et al., 1997). Volcanic rocks of the first period (≥ 16 Ma) consist of sparse basanite dykes and nephelinite pipes; volcanic rocks of the secondary period (≤16 Ma) are particularly abundant and are dominated by alkali olivine basalts and tholeiites. Detailed studies on the basalts (~35.5 Ma) from Qilin, Guangdong and their ambient basalts (~20-6.6 Ma) show that the Eocene basalts have overall characteristics of "Island Arc" basalts with high $(^{87}Sr/^{86}Sr)_i$, negative $\varepsilon_{Nd\ (t)}$ and relatively low $\varepsilon_{Hf\ (t)}$, reflecting contributions from relict ancient metasomatized mantle lithosphere; the Miocene basalts show OIB-like trace-element and isotopic characteristics and are mainly derived from depleted asthenospheric mantle. The widespread basalts erupted since the Miocene may reflect the effects of a mantle plume or hotspot (Zou and Fan, 2010; Wang et al., 2012). Seismic tomography defines a plume-like mantle low-velocity structure beneath the north Hainan Island-Leizhou Peninsula basalt province (i.e., Lei et al., 2009a), and basaltic lava from Hainan Island show high mantle potential temperature (mean 1541°C), high Mg# in olivine phenocryst ($Fo_{90.7}$) and recycled oceanic crust in the source, which support a young mantle plume associated with deep slab subduction beneath the Hainan area (Wang et al., 2012).

Mantle xenoliths were collected from the late Miocene (~10–12 Ma; Shao et al., 1989) Lianshan basalts, lying astride the Tan-Lu fault zone (TLFZ) where the mantle belongs to the Yangtze Craton (Fig. 2-4a), and from the Oligocene (Ar–Ar age: 26.4–23.7 Ma; Ho et al., 2003) nephelinites in the Xilong area, which belongs to the Cathaysia block (Fig. 2-4b).

CHAPTER 3
ANALYTICAL METHODS

The geochemical (including Sr-Nd-Hf isotopic) compositions of minerals and whole rocks were analyzed based on the detailed petrographic studies in the labs of China University of Geosciences, Wuhan (CUGW) and the Geochemical Analytical Unit (GAU) of the ARC Centre of Excellence for Core to Crust Fluid Systems (CCFS) and GEMOC, Macquarie University. The oxygen isotope ratios ($^{18}O/^{16}O$) of garnets from the garnet pyroxenites were determined in the Centre for Microscopy, Characterization and Analysis (CMCA), the University of Western Australia.

3.1 Sample preparation and mineral separates

All garnet pyroxenite xenoliths studied here were collected from maars at Lakes Bullenmerri and Gnotuk, SE Australia and peridotite xenoliths were collected from Cenozoic basalts in Lianshan and Xilong areas, South China. Two rock slabs were cut from each large sample using a saw. One was used to make the polished thick section (~ 0.2 mm thick); the other was used for mineral separation and whole-rock analysis.

Rock slabs were crushed in the State Key Laboratory of Geological Processes and Mineral Resources (GPMR), CUGW. Whole-rock fragments (~1 cm^3 in size) free of dust were ground into powder less than 200 mesh using an agate mill. The powdered samples were kept in plastic bottles and mixed well before further analysis.

Mineral separation was completed in the GAU of CCFS, Macquarie University. Rock slabs were put in thick plastic bags and crushed into pieces less than 2 cm in diameter with a hammer. Then the rock fragments were processed using the SelFrag equipment, which disaggregates the rocks and liberates intact minerals by propagating electrical pluses along phase boundaries and internal cracks. The size fractions 0.25-0.5 mm and 0.5-0.8 mm were then sieved, washed and dried. Transparent grains of clinopyroxene, garnet and rare amphibole, free of microscopically visible cracks or blemishes or inclusions, were then handpicked under a binocular microscope. About ten garnet grains from each sample and the standards (UWG-2 and MON GT) were picked to make a mount cylinder with a diameter of 25 mm and a height of ~4.5 mm to do *in situ* O analyses by SIMS. About 200 mg of clinopyroxene, amphibole and ~400 mg of garnet were kept in plastic bottles for solution

work. After weighting, they were leached using method 2 described by Huang et al. (2012a) in hot 6N HCl overnight followed by leaching in 6N HNO_3 for half an hour at 80 °C. The residues were then ultrasonically washed in MQ water for 20 minutes, three times, and then digested for isotopic analysis.

3.2 Optical and Scanning Electronic Microscopy (SEM) imaging

Petrographic observation is the necessary first step before any subsequent *in situ* mineral analysis. Thick (~0.2 mm) sections were examined and imaged using an Olympus Microscope and a Zeiss EVO MA15 scanning electron microscope (SEM) under an accelerating voltage of 15 kV and a beam current of 20 nA in the GAU of CCFS, Macquarie University. Backscattered electron (BSE) images and elemental X-ray maps were acquired using a BSE Detection System and an Energy Dispersive Spectroscopy (EDS) System on the Zeiss SEM, respectively. Crystallographic orientation measurements were obtained by the electron backscatter diffraction (EBSD) method. The EBSD patterns were acquired using a charge-coupled-device camera attached to the SEM. Diffraction patterns were acquired using an accelerating voltage of 20 kV, a beam current of 8.0 nA, and a working distance of 13–25.5 mm. The resulting image was then processed and indexed in terms of crystal orientation using the Aztec software distributed by Oxford Instruments.

3.3 Major- and trace-element analyses of whole-rock samples

Whole-rock major-element compositions of the Lianshan peridotite were determined by X-ray fluorescence technique using fused glass disks at Key Lab of Biogeology and Environmental Geology Ministry of Education, CUGW. The loss on ignition (LOI) was also measured on dried rock powder by heating in a pre-heated corundum crucible to 1000°C for 90 min. The operation condition is an accelerating voltage of 50 kV, a beam current of 50 mA on a constant temperature of 35 °C. The measurement procedure and data quality were monitored by repeated samples (one in ten samples), USGS BHVO-2 and Chinese National standards GBW07113 and GBW07102 (Table 3-1). The accurancy is better than 4% for elements with concentrations >0.1 wt%.

Whole-rock trace-element compositions of the Lianshan peridotite were analyzed by ICP-MS (Agilent 7500a with shielded torch) in the GPMR of CUGW. The method and instrument are described in detail by Liu et al. (2008). 50 mg powder of each sample and standards were weighted and digested using HF+HNO_3 in Teflon bombs, along with a blank sample. The results for the monitoring standards (USGS BHVO-2 and BCR-2) are given in

Table 2-2. Analyses of USGS glasses agree with recommended values within 5 % for most trace elements.

Whole-rock major- and trace-compositions for the garnet pyroxenites were reconstructed using mineral data and point-counted modes. The volume modal proportions were estimated by counting ~2000 points on each thick section, and then were converted to mass proportions by multiplying by the mineral densities.

3.4 Major- and trace-element analyses of minerals

3.4.1 Electron microprobe: Major-element analysis

Major-element compositions of minerals were determined by electron microprobe analysis (EMPA) using a CAMECA SX100 instrument fitted with 5 wavelength dispersive spectrometers in the GAU of CCFS, Macquarie University. An accelerating voltage of 15 kV and a beam current of 20 nA were the usual operating conditions. A beam size is approximately 1-2 µm for anhydrous silicates and ~5-10 µm for volatile-rich minerals. Measured elements were counted for 10 s for peaks and 5 s for backgrounds on either side of the peak. The peaks were calibrated using the method of Pouchou and Pichoir (1984) by measurements of standards (natural minerals and synthetic oxides) at the start of each analytical session. In order to assess both intra- and inter-grain chemical homogeneity, several grains of each phase per sample were analyzed across both core and rim areas of the minerals.

3.4.2 LA-ICPMS: Trace-Element analysis

Trace-element compositions of silicates on garnet pyroxenites were measured using laser-ablation inductively coupled plasma mass spectrometry (LA-ICPMS) in the GAU of CCFS, Macquarie University. The instrument was an Agilent 7700 ICPMS with a 193 nm ArF EXCIMER laser. The ablation was carried out in high-purity He gas, which was then mixed with Ar gas to introduce the samples into the ICPMS. The operational conditions were 5 Hz pulse frequency and energy intensity of ~4.93 J/cm^2. Each analysis includes a 60 s record of background at the beginning, and then 120 s collections of sample data. The analytical spots were 50 µm in diameter for garnet, clinopyroxene, amphibole and phologopite, ~85-110 µm for orthopyroxene and spinel and ~30-40 µm for apatite. In each run of analyses (≤14 unknown samples), SRM NIST 610 was measured as the element-concentration calibration, and standards USGS BCR-2 and MONGOL (an in-house garnet standard) were analyzed to monitor the instrument working conditions and the calibration (Norman et al., 1996). ^{44}Ca for high-Ca minerals (clinopyroxene, garnet, amphibole and

apatite), ^{29}Si for low-Ca minerals (olivine, orthopyroxene, phlogopite) and ^{27}Al for spinel, were used as the internal standard to calculate the trace-element compositions of unknown samples, relative to SRM NIST 610. We acquired the trace-element data on different minerals under the conditions that give precise and accurate results of the monitoring standards (Table 3-3). The raw data were processed using the online software program GLITTER 4.4 (Griffin et al., 2008), which allows for the selection of the most stable sections of the time-resolved data.

Trace-element analyses of melts and minerals on peridotite xenoliths from Lianshan and Xilong area were done at GPMR of CUGW using a 193 nm ArF-excimer laser attached to an Agilent 7500 ICPMS. Detailed analytical procedures and operating conditions are given by Liu et al. (2008). In this analysis, a 44 µm spot size was used on all primary minerals while the spot size on melts and secondary minerals in the reaction patches from peridotite xenoliths in Xilong area was 32 µm. Each spot analysis consists of approximately 20 s of background acquisition followed by 50 s of data acquisition for the sample. The NIST 610 glass and the USGS glasses BCR-2G, BHVO-2G and BIR-1G were used as external standards. No internal standard was applied for correction. The precision of the LA-ICPMS data can be evaluated from results obtained for USGS glasses BCR-2, BIR-1 and BHVO-2G (Table 3-3). The accurancy is better than 5%. This method could also be used to obtain major-element compositions of anhydrous silicate minerals (Liu et al., 2008). The major-element data obtained by LA-ICPMS are identical to those obtained by EMP analysis.

3.5 Radiogenic isotope analysis

3.5.1 Sr-Nd-Hf solution analysis

Sr and Nd isotopic compositions of whole rock from the Lianshan peridotite xenoliths were determined using a multicollector Finnigan MAT-261 TIMS operated in static multi-collector mode at GPMR of CUGW. After being powdered with an agate mill to 200 meshes, samples were digested in Teflon bombs with a mixture of concentrated HF and HNO_3 at 190°C for 48 h. The decomposed samples were then dried on a hot plate and converted into chlorides by adding 2 ml of concentrated HCl; the residue was redissolved in 100 µl $HClO_4$ and concentrated HCl and then evaporated to dryness. The dried salts were dissolved again in 1 ml of dilute HCl and loaded onto columns of AG50W-X8 resin for separation and purification of Sr and REE, with the REE cut finally loaded onto HDEHP columns for separation of Nd by HCl eluants. The measured $^{143}Nd/^{144}Nd$ and $^{87}Sr/^{86}Sr$ ratios were normalized to $^{143}Nd/^{144}Nd = 0.7219$ and $^{87}Sr/^{86}Sr = 0.1194$, respectively. Repeated analyses

yielded $^{143}Nd/^{144}Nd$ of 0.511847 ± 3 (2σ, n = 25) for the La Jolla standard, $^{143}Nd/^{144}Nd$ = 0.512637 ± 3 (2σ, n = 2) for BCR-2, and $^{87}Sr/^{86}Sr$ = 0.710254 ± 8 (2σ, n = 22) for SRM NBS-987. Analytical details and analysis of reference materials are reported in Rudnick et al. (2004).

About 200 mg of clinopyroxene, amphibole and ~400 mg of garnet separates from garnet pyroxenites were prepared for Sr-Nd-Hf isotopic analysis after being leached in the GAU/CCFS, Macquarie University. The samples and reference standard BHVO-2 were digested and processed using ion-exchange techniques described by (Blichert-Toft et al., 1997; Pin and Zalduegui, 1997; Huang et al., 2012b).

Sr and Nd isotopic ratios were analyzed using a Thermo Finnigan Triton thermal ionization mass spectrometer (TIMS). Sr was loaded on single Re filaments and Nd was loaded on double filaments. The standard SRM 978 and JMC321 were analyzed to tune the instrument and yielded 0.710244 ±0.000007 (2SD) and 0.511129 ±0.000002 (2SD), respectively, within uncertainty of the GeoReM recommended values (http://georem.mpch-mainz.gwdg.de/). The USGS BHVO-2 was also analyzed to check the chemical procedures and the measured ratios are 0.703468±0.000008 (2SD) for $^{87}Sr/^{86}Sr$ and 0.512985±0.000003 for $^{143}Nd/^{144}Nd$, identical with the GeoRem recommended values of 0.703469± 0.000034 for $^{87}Sr/^{86}Sr$ and 0.512980 ± 0.000012 for $^{143}Nd/^{144}Nd$. The measured $^{87}Sr/^{86}Sr$ and $^{143}Nd/^{144}Nd$ ratios were normalized to $^{87}Sr/^{86}Sr$ = 0.1194 and $^{143}Nd/^{144}Nd$ = 0.7219 to correct for mass fractionation.

Hf isotopic ratios were analysed using a Nu Plasma MC-ICPMS. The standard JMC475 gave an average $^{176}Hf/^{177}Hf$ ratio of 0.282156 ±0.000008, within error of the recommended values (0.282159 ±0.000026). The average $^{176}Hf/^{177}Hf$ ratio of BHVO-2 was 0.283108±0.000024 (2SD; the GeoReM value is 0.283109±0.000012).

All $^{147}Sm/^{144}Nd$ and $^{176}Lu/^{177}Hf$ ratios were calculated using LA-ICPMS data. The decay constants [$\lambda_{Sm} = 6.54\times10^{-12}$ a^{-1} (DePaolo, 1981) and $\lambda_{Lu} = 1.865\times10^{-11}$ a^{-1} (Scherer et al., 2001)] were chosen to calculate initial $^{143}Nd/^{144}Nd$ and $^{176}Hf/^{177}Hf$ ratios at reasonable ages for specific targets. The present-day CHUR values of the ^{147}Sm-^{143}Nd and ^{176}Lu-^{176}Hf systems are taken as $^{147}Sm/^{144}Nd$ = 0.1960, $^{143}Nd/^{144}Nd$ = 0.512630 and $^{176}Lu/^{177}Hf$ = 0.0336, $^{176}Hf/^{177}Hf$ = 0.282785 (Bouvier et al., 2008). Sm-Nd and Lu-Hf isochrons were processed using the isoplot program (Ludwig, 2003).

3.5.2 In situ *Sr isotopes of minerals*

In situ Sr isotopes of clinopyroxene, amphibole, apatite and plagioclase were analyzed using a Nu Plasma multi-collector ICPMS (MC-ICPMS) in combination with the

Mechantek/New Wave LUV213 laser system at the GAU/CCFS, Macquarie University. Typical operating conditions for the laser were a 5 Hz repetition rate and 89-100 % energy (density of 7.5-9.3 J/cm^2), which provided improved signal stability and analytical precision because of the low Sr (<200 ppm) contents of the clinopyroxene. The spot size was 155 µm for clinopyroxene, amphibole, 85-110 µm for plagioclase and 30-50 µm for apatite. Each analysis includes 60 s of background followed by 140 s of data collections. Before analysis, the instrument was calibrated to the optimal conditions by measurement of a SRM987 Sr solution. All analyses were done in the time-resolved analysis mode, in which the signals for each mass and ratio were monitored as a function of time by the Nu Plasma analysis software. It allows the most stable interval of the signal to be selected for each run. The procedure for interference correlations has been explained by Donnelly et al. (2012). A well-characterized Batbjerg Cr-diopside was used as a monitoring standard. In our sessions, analyses of the Batbjerg Cpx gave an average $^{87}Sr/^{86}Sr$ of 0.704454±46 (2SD, n=59), within the uncertainty of the LA-ICPMS results ($^{87}Sr/^{86}Sr$ = 0.704437±96; Neumann et al., 2004).

3.6 In situ O-isotopic analysis of garnet

In situ oxygen-isotope ratios of garnet separates were analyzed using a CAMECA IMS 1280 large-radius SIMS at the Centre for Microscopy, Characterisation and Analysis (CMCA), the University of Western Australia. The analyzed method is similar to that described by Raimondo et al. (2012). UWG-2 was used as the master reference standard and MON GT as a check standard. Raw $^{18}O/^{16}O$ ratios were calibrated for drift using bracketing analyses of UWG-2, followed by instrumental mass fractionation (IMF) correction using a laser-fluorination value of MON-GT ($\delta^{18}O$ = 5.38±0.10‰, 2SD; Raimondo et al., 2012). Due to the compositional similarity between the analyzed samples and UWG-2 (Xgrossular=0.13), matrix effect can be negligible. All $^{18}O/^{16}O$ ratios and uncertainties are reported in $\delta^{18}O$ notation, in per mil variations relative to the $^{18}O/^{16}O$ ratio (0.0020052) of Vienna Standard Mean Ocean Water (V-SMOW).

CHAPTER 4
NATURE AND EVOLUTION OF THE LITHOSPHERIC MANTLE BENEATH THE YANGTZE CRATON, SE CHINA

4.1 Introduction

Commonly, the age of the subcontinental lithospheric mantle (SCLM) is coupled with the age of the overlying crust (Boyd, 1989; Griffin et al., 1999a,b; Pearson, 1999). However, this coupling may be destroyed by asthenosphere-lithosphere and crust-mantle interactions (Griffin et al., 1998; O'Reilly et al., 2001; Zheng et al., 2001, 2007). It is generally accepted that a large thickness (more than 100 km) of old refractory lithospheric mantle beneath the eastern North China craton was removed or strongly modified during Mesozoic-Cenozoic time (Fan and Menzies, 1992; Griffin et al., 1992, 1998; Menzies et al., 1993; Zheng, 1999; Xu, 2001; Deng et al., 2004; Zhang, 2005), especially along the translithospheric Tanlu Fault Zone (TLFZ, i.e., Shanwang, Fig. 2-4a). Shallow relics of Archean lithospheric mantle have only been documented in areas away from the TLFZ (i.e., Hebi).

Xenolith-bearing basalts are widespread in the South China block which is divided by JiangShao-PingYu fault zone (JS-PYFZ) into the Yangtze block to the northwest and the Cathaysia block to the southeast (Fig. 2-4a). Both garnet and spinel-bearing peridotite xenoliths from the Cathaysia block are essentially fertile and yield Phanerozoic ages (Qi et al., 1995; Xu et al., 2000, 2003, 2008; Zheng et al., 2004b). The rare occurrences of refractory xenoliths from this block suggest that an older residual SCLM coexists with younger mantle beneath the block (Xu et al., 2000, 2003, 2008; Wang et al., 2003; Zheng et al., 2004b).

Relatively few studies have been carried out on the lithospheric mantle beneath the lower Yangtze block (Chen et al., 1994; Sun et al., 1998; Reisberg et al., 2005). The lack of detailed knowledge about the Mesozoic-Cenozoic SCLM of the block has constrained the overall understanding of the lithospheric evolution of eastern China. However, the eruption of xenolith-bearing basalts in the Subei basin located in the northeastern part of the lower Yangtze block makes up the drawback. Therefore, this paper presents an integrated analysis of petrography, geochemistry and Sr-Nd isotopes of a suite of peridotite xenoliths from the Lianshan region within the basin. Our aims are: 1) to illustrate the nature of the SCLM

beneath the lower Yangtze block; 2) to trace the evolution and dynamic environment of the SCLM in eastern China.

4.2 Petrography

Nearly all samples collected from the Cenozoic Lianshan basalts are fresh and large in size (typically 5-14 cm in diameter). They are spinel-facies xenoliths, ranging from abundant lherzolites to minor harzburgites, dunites and websterites. Modal compositions (Table 4-1), which were calculated using bulk chemistry and mineral compositions, show that the modal abundance of clinopyroxene in peridotites has a large range (1.8%-15.1%) and two types can be roughly distinguished: Type 1 with <6.5% clinopyroxene and Type 2 with 9-15% clinopyroxene.

The diverse microstructures of mantle-derived xenoliths play an important role in understanding mantle evolution. As deformation and recrystallization become stronger, coarse-grained microstructures gradually change toward porphyroclastic-, sheared-, and finally fine-grained microstructures (Harte, 1977). The peridotites from Lianshan area have dominantly porphyroclastic microstructures with minor course- (LS0906, LS0910) and fine-grained microstructures (LS0902). The coarse-grained samples are classified into Type 1 xenoliths. The grain size of olivine and orthopyroxene is generally from 2.5 to 5mm. An olivine-rich region shows triple junctions and curved grain boundaries (Fig. 4-1a). Clinopyroxenes in the Type 1 xenoliths contain abundant CO_2 fluid inclusions (Fig. 4-1b). However, one fine-grained lherzolite (LS0902) has less than 5 percent of olivine occurring as porphyroclast around a crack, and most mineral grains are < 2mm (Fig. 4-1c). This sample is also classified as Type 1 due to the similar proportions of minerals. All Type 1 xenoliths have minor green spinel grains enclosed in the clinopyroxene (Fig. 4-1b), but most spinels are brown and distribute either as dispersed interstitial phases at grain boundaries of silicates or as inclusions in other minerals. All porphyroclastic xenoliths belong to Type 2 and the grain size of at least 10% of the olivine is larger than 4 mm. Orthopyroxenes often have irregular curved grain boundaries and some of them show fine exsolution lamellae of clinopyroxene. A few sulfides are enclosed in the orthopyroxene in addition to in cracks. Spongy textures of clinopyroxene are extensively developed in Type 2 peridotites (Fig. 4-1d).

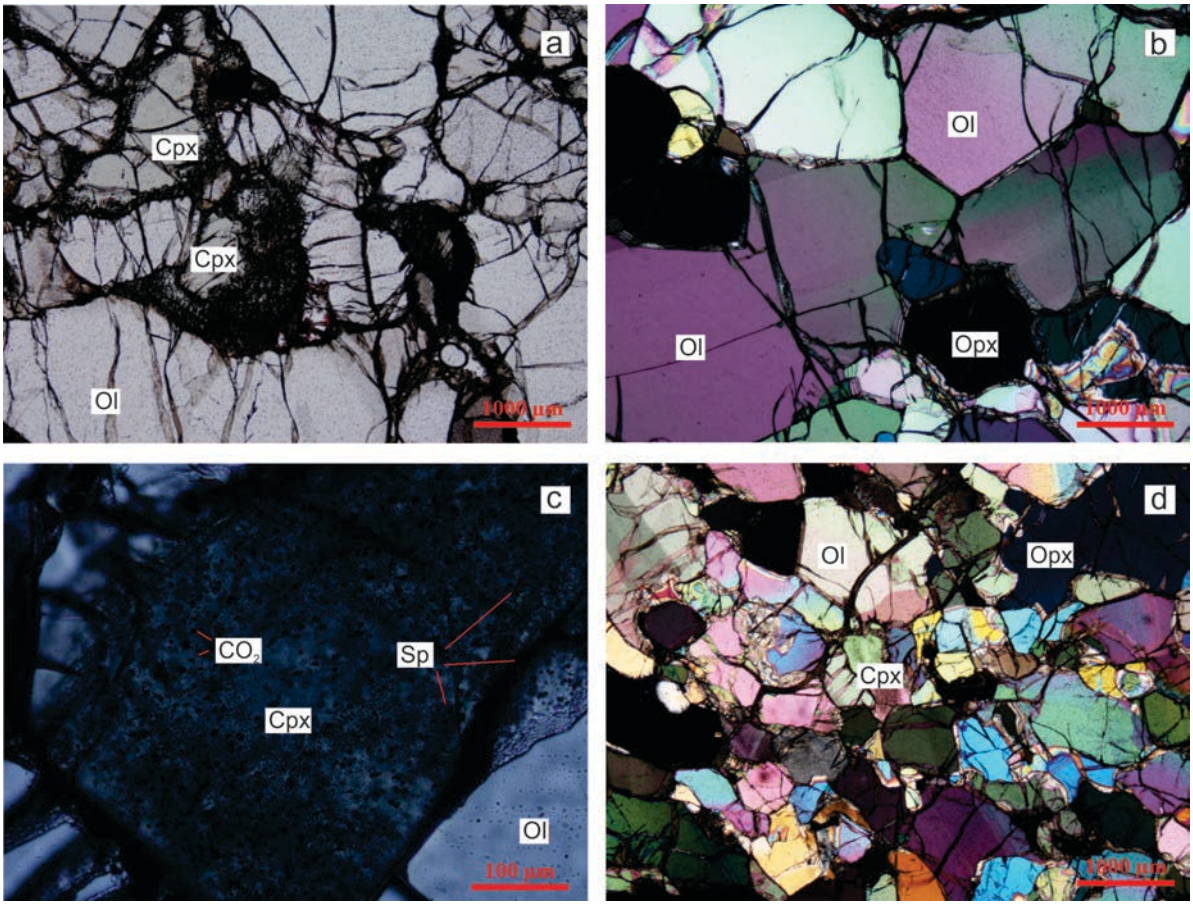

Fig. 4-1 Photomicrographs of Lianshan xenoliths illustrating some key petrographic features. (a) Spongy textures of clinopyroxenes (plane polarized light) in LS0926. (b) Coarse-grained microstructure of LS0910 showing triple junctions and curved grain boundaries (cross polarized light). (c) Abundant CO_2 fluid inclusions and green spinels in clinopyroxenes of LS0910 (plane polarized light). (d) Fine-grained microstructure of LS0902 (cross polarized light).

4.3 Results

4.3.1 Mineral chemistry

The Mg# of olivine in Lianshan xenoliths varies from 88.4-91.6 (Fig. 4-2a; Table 4-2), covering the composition range of the transitional refractory Type 1 xenoliths with higher Mg# (90.8-91.6) and the fertile lower-Mg# Type 2 xenoliths (88.4-89.7). The fertile and refractory types were originally defined from the Shanwang and Hebi localities in the North China craton (Fig. 4-2b). Such magnesium peridotites are similar to the xenoliths in the Cathaysia block (Fig. 4-2c). CaO contents of olivine (Table 4-2) show no obvious difference between Type 1 (0.02-0.03%) and Type 2 (0.02-0.05%) xenoliths, but MnO contents decrease with increasing Mg# of olivine.

Olivines in Type 1 and Type 2 xenoliths show similar Ni contents (3071-3187 ppm vs. 3024-3138 ppm) (Table 4-3), which are intermediate between those of the refractory Hebi (3450-4088 ppm, Zheng et al., 2001) and fertile Shanwang xenoliths (1997-2610 ppm, Zheng

et al., 1998). Ni/Co ratios increase with increasing Mg# in olivine and are 21.7 on average, close to the chondritic value (21.9, McDonough and Sun, 1995).

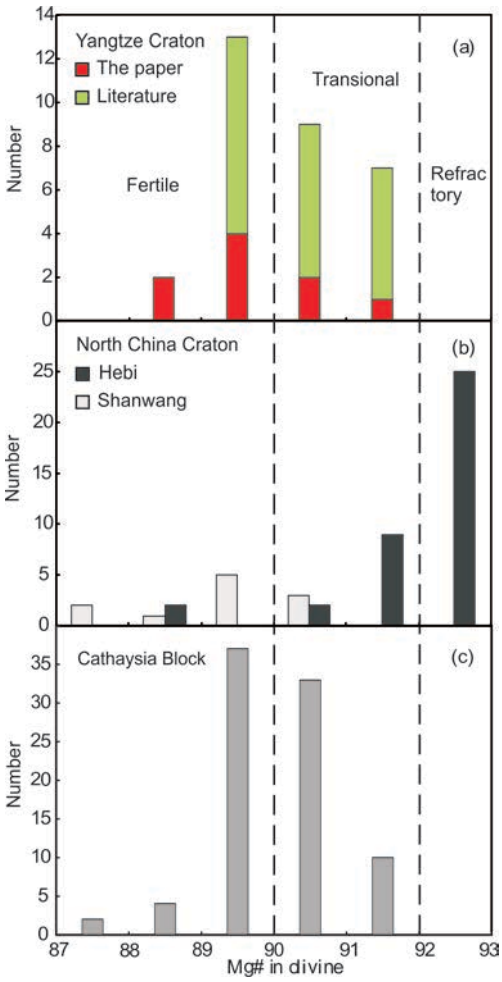

Fig. 4-2 Frequency distribution of Mg# in olivine from Lianshan peridotite xenoliths and other relevant samples from eastern China. Data sources: (a) Lianshan in the lower Yangtze block, this paper and (Lei et al., 2009b); (b) the Cathaysia block, Xu et al. (1996, 2000), Zheng et al. (2004a); (c) Hebi, Zheng et al. (2001), Shanwang, Zheng et al. (1998) in the North China Craton.

Orthopyroxenes are $En_{89.1-95.2}Fs_{3.6-9.3}Wo_{0.9-1.7}$. Orthopyroxenes in Type 1 xenoliths have higher Mg# (91.1-92.2 vs. 89.1-90.0), but lower TiO_2 (0.03-0.04% vs. 0.11-0.29%) and Al_2O_3 (2.16-3.13% vs. 4.09-5.41%) than Type 2 peridotites (Table 4-2), indicating they are partial melting residues. Ni and Co contents (Table 4-4) vary within limited ranges, 616-935 ppm and 51.8-65.3 ppm, respectively, and show no correlation with Mg#. Y and HREE decrease with increasing Mg#. All orthopyroxenes from Type 2 xenoliths have positive anomalies in Ti, while ones from Type 1 have low Ti contents (not shown).

All clinopyroxenes analyzed here are Cr-Diopside with 0.72-1.26 wt% of Cr_2O_3 (Table 4-2). Clinopyroxenes in Type 1 xenoliths have higher Mg# (93-93.6 vs. 89.5-91.2), Cr# (15.7-23.4 vs. 6.4-9.3), and lower Al_2O_3 (2.77-3.26% vs. 6.46-7.38%) than those in Type 2. The contents of Na_2O and CaO show limited ranges, 1.03-2.41% and 21.0-23.5%, respectively.

Clinopyroxenes from Type 1 xenoliths show LREE-enriched ((La/Yb)n=3.62-46.2), strongly HREE-depleted patterns (Fig. 4-3a), and obvious negative anomalies in Nb, Ta, Zr, Hf and Ti, positive anomalies in U (Fig. 4-3b). Sr shows no (LS0906) to positive anomalies. Clinopyroxenes from Type 2 peridotites have depleted LREE ((La/Yb)n=0.08-0.46), relatively flat HREE ((Gd/Yb)n=0.87~1.60) (Fig. 4-3c; Table 4-5), positive anomalies in U, and negative anomalies in Ba, Ti, Pb and Nb (Fig. 4-3d). LS0929, a websterite, has negative anomalies in U and no obvious anomalies in Nb. Cpx in LS0926 is heterogeneous with negative Nb anomalies in the cores and positive Nb anomalies in the rims although there are no obvious difference in other moderately incompatible elements (Nd-Lu), indicating that these clinopyroxenes have probably experienced metasomatism after partial melting. Sr shows negative (LS0926) to weak positive anomalies. Y and HREE concentrations decrease with increasing Mg# and decreasing TiO_2 and Al_2O_3, as might be expected from progressive partial melting. However, concentrations of highly incompatible elements such as LREE, Sr and Th in Type 1 xenoliths show divergent behavior relative to Mg#, suggesting that at least two events, primary depletion and secondary enrichment, have affected the lithospheric mantle beneath the Lianshan region.

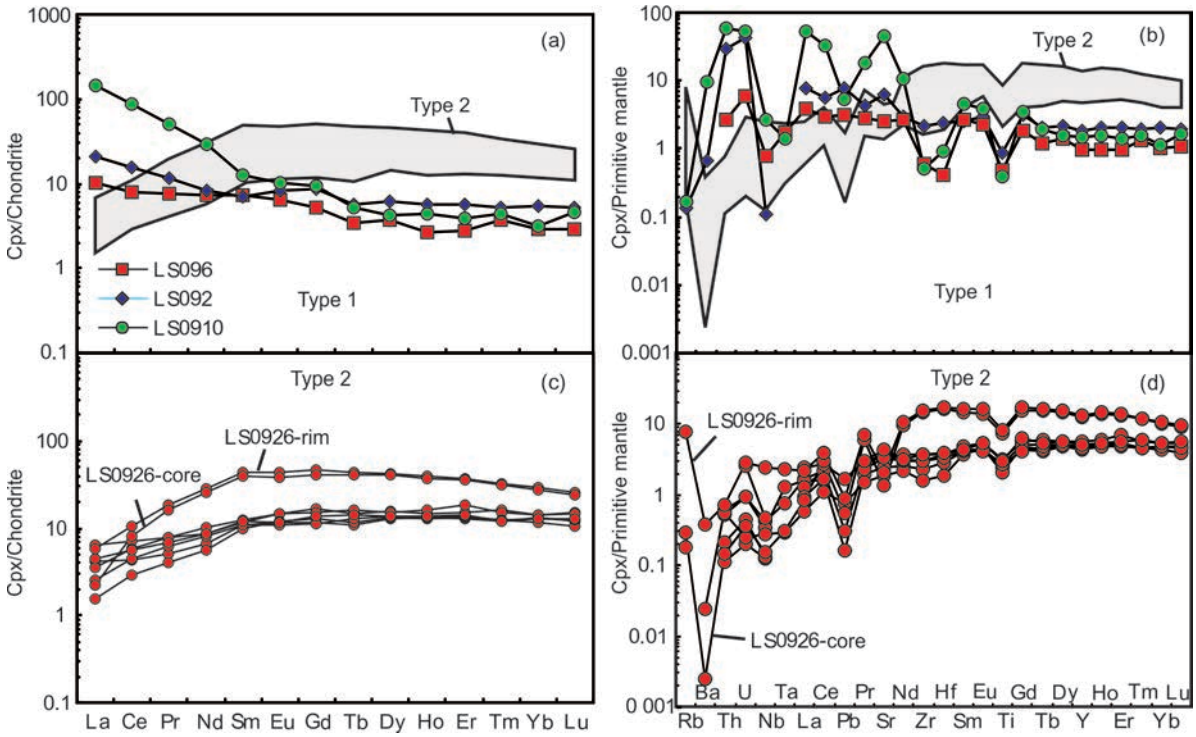

Fig. 4-3 Chondrite-normalized REE patterns and primitive mantle-normalized trace element spidergrams in clinopyroxene of the Lianshan peridotites. Chondrite and primitive mantle data are from McDonough and Sun, (1995). The shaded area shows the range of Type 2 Cpx patterns.

Compared to the coexisting orthopyroxenes, clinopyroxenes from Type 1 and Type 2 xenoliths have low Ni (240-413 ppm vs. 616-935 ppm), Co (14.4-22.3 vs. 54-65.3 ppm), high V (201-343 ppm vs. 56.4-106.6 ppm), Sc (55.7-98.7 ppm vs. 14.2-19.3 ppm) and Cr (4961-8649 ppm vs. 2148-3674 ppm) (Table 4-5).

Spinels in Type 1 peridotites have higher contents of Cr_2O_3 (21.3-36.3% vs. 8-13.9%; Table 4-2) and thus higher Cr# (21.3-36.3% vs. 8-13.9%) than those of Type 2. The Mg# of silicate phases and Cr# of spinels are powerful monitors of melting, and increase with increasing degree of melting (Preβ et al., 1986; Hellebrand et al., 2001). Type 1 xenoliths, with high Cr# in spinel and high Mg# in clinopyroxene, overlap the field of the refractory peridotites from Hebi which are considered as the relics of Archean mantle (2.5-3.0 Ga; Zheng et al., 2007) and have undergone higher degrees of partial melting (Fig. 4-4a). The low Cr# of spinels and low Mg# of coexisting clinopyroxenes in Type 2 peridotites, similar to the fertile xenoliths from Shanwang, indicate that most of samples beneath the studied region have been subjected to relatively low degrees of melt extraction. The wide variations between Cr# in spinel and Mg# in clinopyroxene from the Lianshan xenoliths are similar to the relationship seen in the Cathaysia peridotites (Fig. 4-4b). Spinels in Type 1 have lower Ni contents (Table 4-6) than those of Type 2 (1217-2065 ppm vs. 3044-4098 ppm). Ni and Ni/Co contents decrease with increasing Cr#, showing a control by partial melting.

4.3.2 Equilibration temperatures

Equilibration temperatures calculated from Ca-in-orthopyroxene thermometer, the distribution of Na between clinopyroxene and orthopyroxene (Brey and Kohler, 1990), and clinopyroxene-orthopyroxene-olivine-spinel thermometers (Sachtleben and Seck, 1981) are given in Table 4-7. They give similar temperature estimates. Estimates based on the Ca-in-orthopyroxene thermometer (Brey and Kohler, 1990) for Type 1 and Type 2 xenoliths studied here are 892-928 ^{o}C and 909-1014 ^{o}C, respectively. Estimated depths are 35-60 km. Seismic refraction data indicate that the Subei basin is underlain by about 30 km of continental crust (Zhang et al., 1988), suggesting these xenoliths are derived from a shallow lithospheric mantle.

4.3.3 Whole-rock major and trace element compositions

The Lianshan peridotites display wide ranges in MgO (38-44.9 wt%), Al_2O_3 (0.85-3.88 wt%) and CaO (0.85-3.33 wt%; Table 4-8). Type 1 samples have higher Mg# (Fig. 4-5a) but lower Al_2O_3 and CaO (Fig. 4-5b) than Type 2 peridotites. Type 1 xenoliths overlap the

compositional field of the refractory Archean peridotites in Hebi, similar to the worldwide Archean mantle; Type 2 fall into the compositional field of fertile peridotites from Shanwang and overlaps the ranges defined by other Phanerozoic samples, reflecting a low degree of depletion in basaltic components.

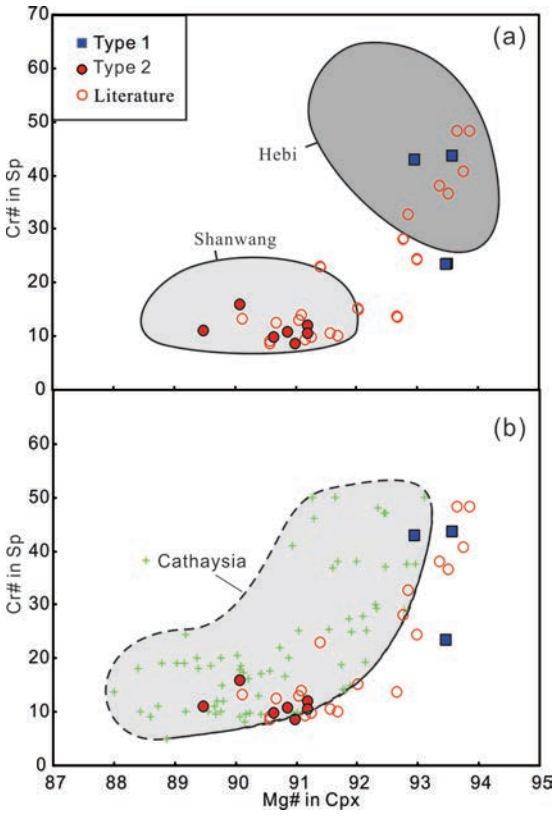

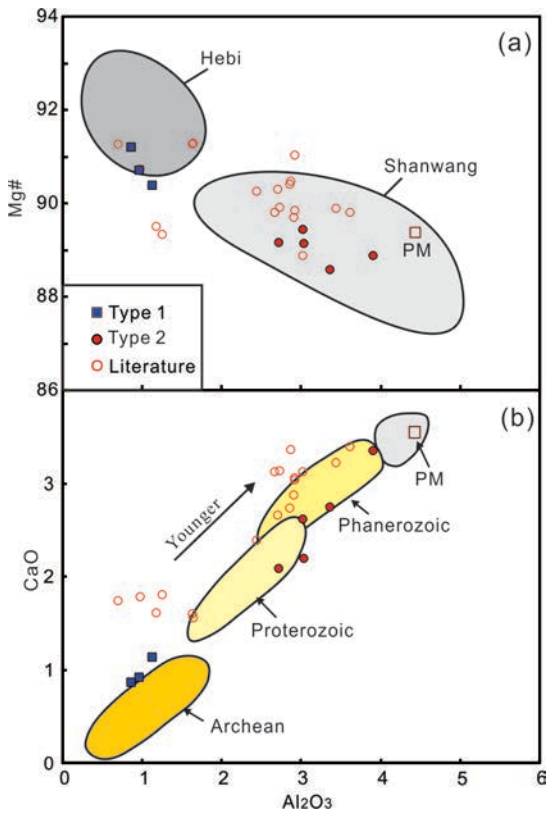

Fig. 4-4 (left) Mg# in clinopyroxene vs. Cr# in spinel in the Lianshan peridotite xenoliths. Data sources: Lianshan, this paper and Lei et al. (2009); Cathaysia, Xu et al. (1996, 2000) and Zheng et al.(2004a); Hebi, Zheng et al. (2001) and Shanwang, Zheng et al. (1998).

Fig. 4-5 (right) Mg# (a) and CaO (b) vs. Al_2O_3 contents of the whole-rock Lianshan peridotite xenoliths. Oxide compositions of Lianshan peridotites have been recalculated to 100% on an anhydrous basis. Archean, Proterozoic, Phanerozoic and Primitive mantle areas are from O'Reilly et al. (2001). Data sources: Lianshan, this paper and (Sun et al., 1998); Hebi, Zheng et al. (2001) and Shanwang, Zheng et al. (1998). The results of Shanwang and Hebi are calculated based on the mineral modals and their compositions.

Type 1 peridotites have lower HREE contents than Type 2 xenoliths (∑HREE= 0.17-0.28 vs. ∑HREE=1.19~2.27) and show LREE-enriched ((La/Yb)n=1.89-26.5), HREE-depleted patterns (Fig. 4-6a), and negative anomalies in Ba, Nb, Zr, Hf, as well as positive anomalies in Ti, Pb, Th and U (Fig. 4-6b). Sr shows no (LS0906) to obvious positive anomalies. LS0906 has lower contents of incompatible elements from Ba to Nd than other Type 1 xenoliths. Type 2 peridotites display LREE-depleted ((La/Yb)n=0.23-0.48), HREE-flat patterns ((Gd/Yb)n=0.69-0.93) (Fig. 4-6c; Table 4-8), and positive anomalies in Sr, U and Pb, negative anomalies in Ba and Nb, no obvious anomalies in Zr, Hf, Ti (Fig. 4-6b).

These trace-element patterns for the Lianshan peridotites are similar to those of the clinopyroxenes (Fig. 4-3), suggesting that clinopyroxene is the main repository of trace elements in these anhydrous spinel peridotites and can be therefore used in the petrogenetic interpretation of mantle processes (Salters and Shimizu, 1988; Meen et al., 1989; Yaxley et al., 1998). However, obvious positive Pb anomalies and no negative Ti anomalies in both Type 1 and Type 2 xenoliths (Fig. 4-6b, d) are completely different from those in clinopyroxenes from the same samples, indicating that these elements reside elsewhere, i.e., Ti in orthopyroxene (Table 4-4; Rampone et al., 1991; McDonough et al., 1992) or in the intergranular material in the case of Pb (Ionov et al., 1993).

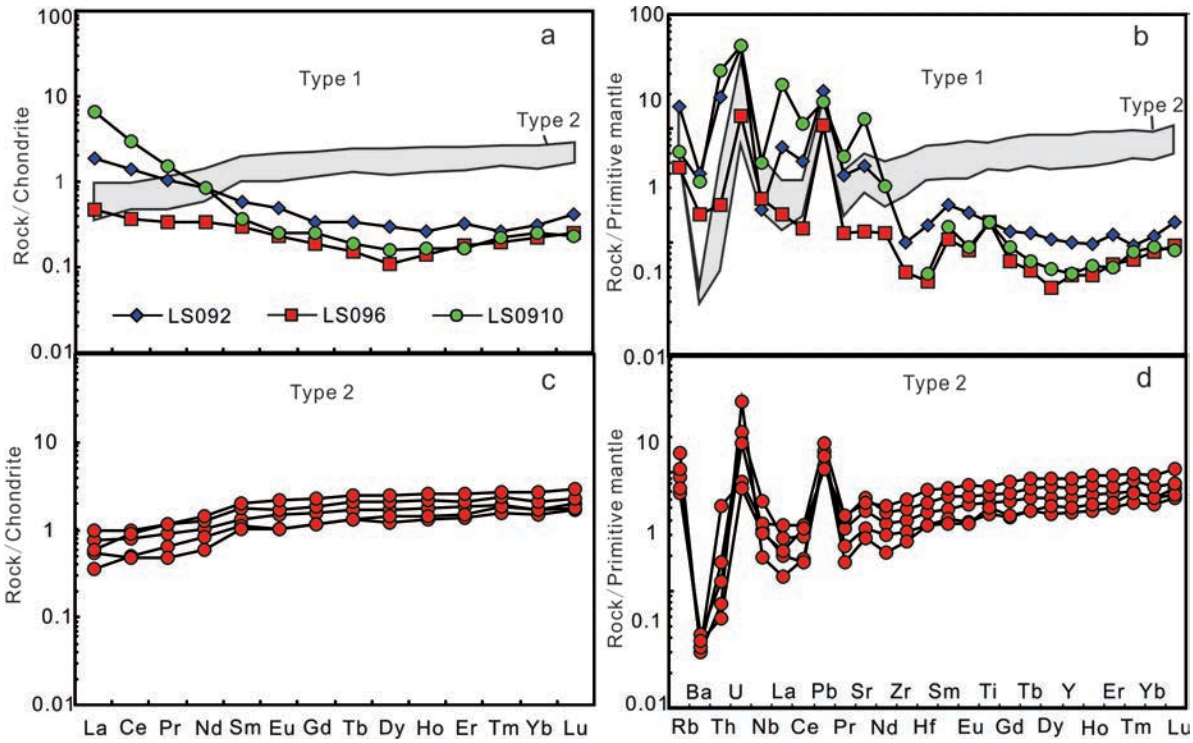

Fig. 4-6 Chondrite-normalized REE patterns and primitive mantle-normalized trace element spidergrams of the whole-rock samples from the Lianshan area. Chondrite and primitive mantle data are from McDonough and Sun, (1995). The shaded area shows the REE patterns of Type 2 peridotites.

Compatible (Ni) and moderately incompatible (i.e., V, Cu and Y) trace elements, and the highly incompatible trace elements (i.e., La, Ce, Nb and Sr) show positive, negative and no obvious correlation with Mg#, respectively, suggesting that at least two events (primary depletion and secondary enrichment) have affected the lithospheric mantle.

4.3.4 Sr-Nd isotopes

The Lianshan peridotite xenoliths have depleted Sr-Nd isotopic compositions (Fig. 4-7; Table 4-9), and are similar to the oceanic peridotites from the asthenosphere, indicating

that Sr-Nd isotopic system was probably affected by later geological processes. Type 1 peridotites display relatively higher $^{87}Sr/^{86}Sr$ (0.70328-0.70400), lower $^{144}Nd/^{143}Nd$ (0.51250-0.51296) and thus lower ε_{Nd} values (-2.7 to +6.4), and overlap with the OIB field, probably indicating the interaction between refractory peridotites and melts from asthenosphere (Zhang et al., 2009). Type 2 xenoliths have low $^{87}Sr/^{86}Sr$ (0.70228-0.70279), high $^{144}Nd/^{143}Nd$ (0.51322-0.51333), and thus high ε_{Nd} values (+11.3 to +13.4), and plot in or above the MORB field, indicating long-term depletion. One Type 2 sample, LS0920, has lower $^{144}Nd/^{143}Nd$ (0.51287) than other samples and falls close to the OIB domain, although the Sr isotopic ratio is constant.

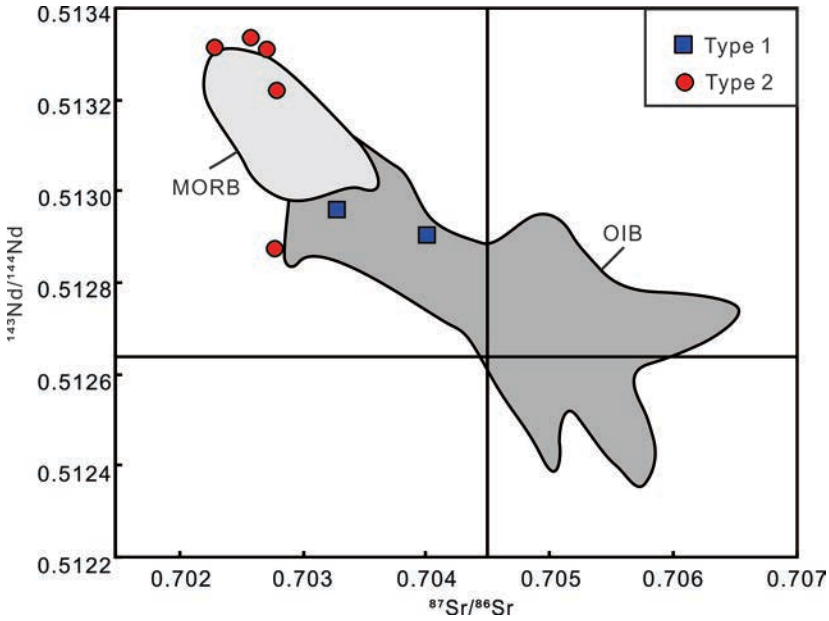

Fig. 4-7 $^{87}Sr/^{86}Sr$ vs. $^{143}Nd/^{144}Nd$ of the whole-rock compositions of Lianshan xenoliths. MORB and OIB components are from Zindler and Hart (1986).

4.4 Discussion

4.4.1 Melting history of Lianshan peridotites

Compatible elements may preserve primary information on the melting history of the mantle, while incompatible elements (especially the highly incompatible elements) may be easily influenced by metasomatism. Therefore, the integration of the compatible and incompatible elements can help distinguish primary partial melting and subsequent metasomatic processes within the SCLM.

The increase in the Cr# of spinel with increasing Mg# in clinopyroxene (Fig. 4-4), and the LREE-depleted patterns in both clinopyroxenes and whole rocks of Type 2 xenoliths (Figs. 4-3, 4-6), record the effects of mantle partial melting. Estimates of the degrees of partial melting using the Yb and Y concentrations of clinopyroxene (Norman, 1998) suggest

that Type 2 samples could have been produced by ~1% batch or fractional melting of a primitive source, while Type 1 xenoliths may have experienced 15-40% batch melting (Fig. 4-8a) or 9-14% fractional melting (Fig. 4-8b). Such high degrees of batch melting (~40%) have been regarded as unrealistic for the Phanerozoic mantle (Zimberlman and Gregg, 2000). The estimates of the fractional melting, 9-14 % for Type 1 samples and ~1% for Type 2 samples, are consistent with estimates (9.5-15.7% for Type 1, 1.4-5.5% for Type 2; Table 4-1) based on the spinel-Cr# values using the method of (Hellebrand et al., 2001).

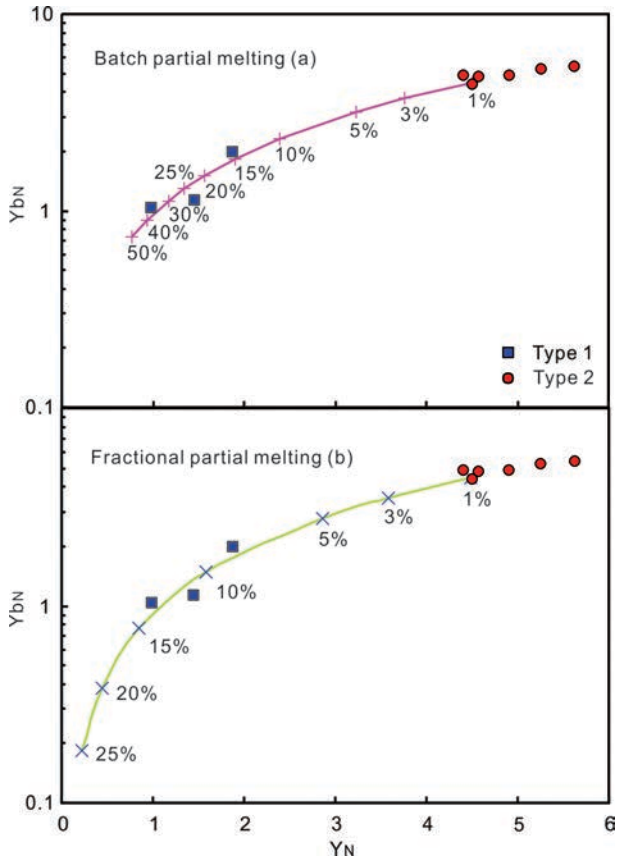

Fig. 4-8 Comparison of batch partial melting model (a) and fractional partial melting models (b). The melting trends are from (Norman, 1998). The subscript N indicates that Y and Yb contents have been normalized to the primitive mantle composition of McDonough and Sun (1995).

4.4.2 Mantle metasomatism

Incompatible trace elements, including LREE and LILE (i.e., Th, U, Sr), show obvious enrichments in clinopyroxenes and whole rocks of Type 1 (Figs. 4-3, 4-6) and scatter with Mg# (not shown). These relationships are not easily interpreted in terms of simple melt extraction, but reflect mantle metasomatism. Since no modal metasomatic minerals (i.e., mica, amphibole or apatite) are observed, a cryptic metasomatism is implied.

Potential metasomatic agents that could have affected anhydrous spinel peridotites in the SCLM include carbonatitic melts (Yaxley et al., 1991, 1998; Ionov et al., 1993), H_2O-

CO_2 fluids (Stalder et al., 1998) and alkaline-rich silicate melts (Zangana et al., 1999). Clinopyroxenes from LS0926 show no Nb anomalies in the rims of grains, but negative anomalies in the cores (Fig. 4-3b), indicating Nb was mobile in the metasomatic agents. The low solubility of Nb in H_2O-rich fluids suggests that the metasomatic agent was probably not H_2O-CO_2 fluids (Eggler, 1987). Relative to silicate melts, carbonatite melts have higher contents of LILE and $(La/Yb)_N$ and can fractionate REE and HFSE more effectively. In addition, HFSE depletion and low Ti/Eu ratios in clinopyroxenes have been widely interpreted as a key signature of carbonatite melts. Therefore, Coltorti et al. (1999) suggests the use of $(La/Yb)_N$ and Ti/Eu is to constrain the nature of metasomatic agents. Clinopyroxenes from Type 2 have low $(La/Yb)_N$, high Ti/Eu and overlap the range defined by fertile xenoliths in Shanwang (Fig. 4-9), suggesting that these xenoliths have undergone weak silicate-melt metasomatism; the depleted Sr-Nd isotopic composition indicate that Type 2 xenoliths was mainly derived from an upwelling asthenosphere (Fig. 4-7). Cpx in LS0910 (a Type 1 sample) has the highest $(La/Yb)_N$ and the lowest Ti/Eu, and is similar to the refractory peridotites from Hebi which underwent carbonatitic melt metasomatism (Fig. 4-9); other Type 1 peridotites with $(La/Yb)_N$ and Ti/Eu transitional between Type 2 peridotites and LS0910, may have experienced multiple episodes of metasomatism by both silicate and carbonatitic melts. The metasomatism is also evidenced by the ubiquitous CO_2-rich micro-inclusions in clinopyroxene of Type 1 (Fig. 4-1c; Wiechert et al., 1997).

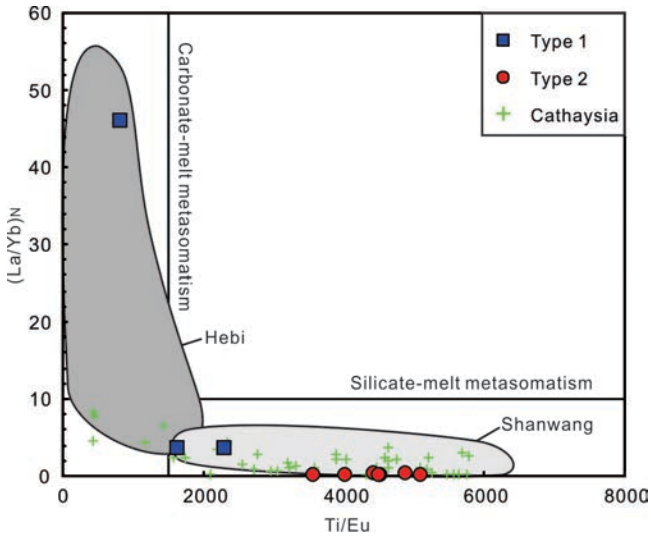

Fig. 4-9 $(La/Yb)_N$ vs. Ti/Eu of clinopyroxenes from the Lianshan peridotites. Signatures of silicate melts and carbonatite melts metasomatism modified from Coltorti et al. (1999). Fields for Hebi and Shanwang clinopyroxenes are from Zheng et al. (2001) and Zheng et al. (1998), respectively.

4.4.3 Nature and evolution of the SCLM beneath the lower Yangtze block

Studies of cratonic xenoliths suggest that the most refractory components are relics of Archean SCLM which was thick and cold (Boyd and Gurney, 1986; Menzies et al., 1993; Zheng and Lu, 1999; Xu et al., 2007). For example, in the Kaapvaal craton from South Africa, the petrology and geochemistry of mantle peridotites from diamondiferous kimberlites suggest that areas of Archean crust were underlain by refractory peridotites which originated from an Archean (>3.0 Ga) lithospheric keel at depths ranging down to 200 km (Boyd and Nixon, 1978; Boyd and Gurney, 1986). These mantle keels are often stable beneath cratons due to their inherent buoyancy and high viscosity (Griffin et al., 1999b). However, they also can be modified or even finally replaced by more fertile material through asthenosphere-lithosphere interaction (Zheng, 1999; O'Reilly et al., 2001). In eastern China, the refractory xenoliths from the Mengying and Fuxian diamondiferous kimberlites in the North China craton show a thick and cold Archean lithospheric mantle was preserved in early Paleozoic (Menzies et al., 1993; Griffin et al., 1998; Zheng and Lu, 1999; Gao et al., 2002). In contrast, most fertile spinel lherzolites from Cenozoic basalts are derived from a thin (60-80 km) lithosphere, suggesting that more than 100 km of cratonic lithosphere was removed during late Mesozoic-Cenozoic time (Griffin et al., 1992; Griffin et al., 1998; Zheng, 1999; Gao et al., 2002).

The Yangtze block mainly consists of Paleoproterozoic rocks (Chen and Jahn, 1998) with only minor occurrences of Archean outcrops (i.e., the Kongling complex; Gao et al., 1999; Qiu et al., 2000; Zhang et al., 2006 a, b, c). Recent studies on the xenocrystic zircons in lamproite diatremes (Zheng et al., 2006), zircon inherited cores from granitic gneisses (Chen et al., 2004) and detrital zircons from sandstones (Liu et al., 2006) in the craton have shown that the Archean basement may be more widespread. In the studied region, the lower Yangtze block, the oldest outcrop is Nanhuang TTG gneiss, which formed at 2.5 Ga (Tu et al., 2001). On the other hand, Archean components (i.e., detrital zircon) also are found in Mesozoic volcanic rocks ~50 km south of Nanjing city (Zhang et al., 2003). All these observations indicate that the Yangtze block is an Archean craton. Basing on the consideration of the crust-mantle coupling, the formation age of the SCLM beneath the lower Yangtze block should be Archean. On the other hand, the Paleozoic diamondiferous kimberlites and lamproites were found from Zhenyuan (Luo et al., 1989; Fang et al., 2002), Ningxiang (Li et al., 1993), Dahongshan (Ye et al., 1991; Liu et al., 1993) within the upper Yangtze block, suggesting that a thick (>150 km) lithospheric mantle may have been preserved during the Paleozoic time, consistent with geophysical investigations (Zhu et al.,

2005). In contrast, geophysical data also suggest that the lithosphere of the lower Yangtze block is 60-100 km. And spinel-facies peridotites studied here also indicate that they are derived from a shallow lithospheric mantle (35-60 km). These results indicate that large thickness has been thinned beneath the lower Yangtze block.

The covariation of modal olivine contents vs. Mg# can roughly distinguish different mantle type (Fig. 4-10). The Lianshan Type 1 xenoliths plot in the Proterozoic field or overlap the field between Proterozoic and Archean (LS0910). Type 2 samples have compositions similar to worldwide Phanerozoic lherzolites, near the "oceanic" trend. Re-Os data also indicate that clinopyroxene-poor peridotites (similar to Type 1) represent refractory relics of an older (~1.8 Ga) SCLM but most fertile peridotites (similar to Type 2) yield younger (Neoproterozoic-Phanerozoic) model ages beneath the Lianshan area (Reisberg et al., 2005). The coexistence of refractory (Type 1) and fertile (Type 2) xenoliths reflects the multi-stage evolution of the lithospheric mantle beneath the region. Neither type shows a correlation between equilibration temperatures and Mg# of olivine (Fig. 4-11), indicating that the refractory and fertile lithospheric mantles are not compositionally stratified but coexist over a range of depths. These compositional characteristics suggest that the SCLM beneath the Lianshan region has been thinned but still preserves rare ancient lithospheric relics.

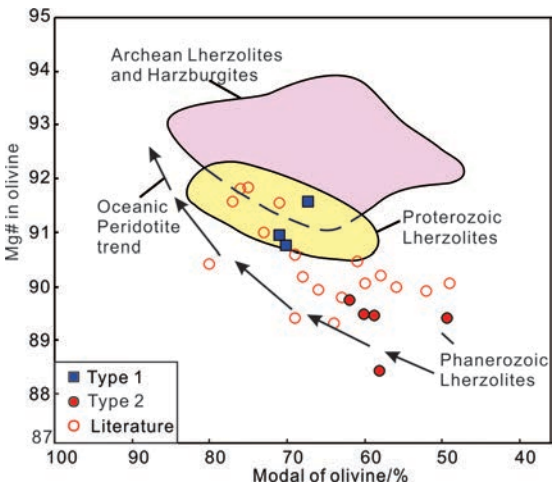

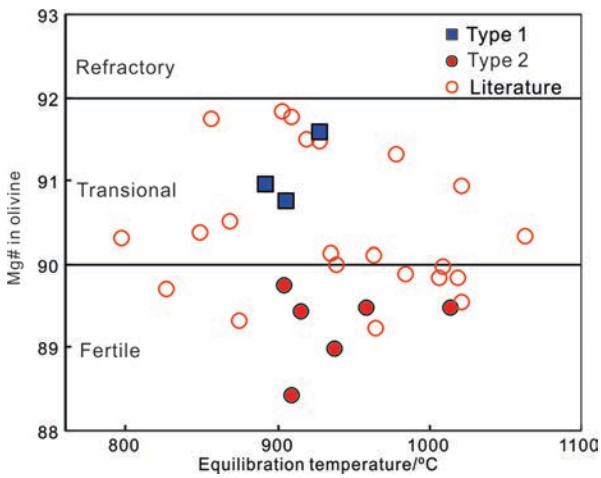

Fig. 4-10 (Left) Modal olivine contents vs. Mg# in olivine from Lianshan peridotite xenoliths. The oceanic trend is from Boyd (1989). Archean, Proterozoic, and Phanerozoic areas are from (Griffin et al., 1999b). Data source: Lianshan, this paper and Lei et al. (2009).

Fig. 4-11 (Right) Equilibration temperature vs. Mg# in olivine from the Lianshan peridotite xenoliths. Data sources as in Fig. 4-10.

A "mushroom cloud" model has been used to interpret thinning mechanism for the eastern North China craton (Yuan, 1996a, b; Lu et al., 2000; Yuan, 2007; Zheng et al.,

2007). Similar seismic tomography (a "mushroom cloud" image) has also been found in the lower Yangtze block (Yuan, 1996a). The pre-existing ancient lithospheric mantle has been pulled apart during extension, and hot asthenospheric material with depleted Sr-Nd isotopic signatures has risen along the weak zones (i.e., major faults or block boundaries) and eroded the overlying the old cold lithospheric mantle. The long-term processes caused melting and subsequent melt removal of the SCLM, and thus resulted in thinning and replacement by upwelling asthenospheric material. Due to mantle heterogeneity, a few relics of old lithospheric mantle may be preserved but have been strongly refertilized or modified and they have less depleted Sr-Nd isotopes (Fig. 4-7). Finally, cooling of the upwelling asthenosphere lowered the boundary between the lithosphere and the asthenosphere and created new lithospheric mantle (i.e., Type 2) with only minor compositional modification and asthenospheric Sr-Nd isotope signatures (Fig. 4-7). The collision and assembly of the Yangtze block with the North China craton in Triassic along the Qinling-Dabie-Sulu orogenic belt (Li et al., 1993) made them form a unified continent (i.e., eastern China) which belongs to a part of the eastern edge of Eurasia continent, and was affected by the westward subduction of the Pacific Plate during late Mesozoic-Cenozoic time. The subduction caused heat perturbation and upwelling of hot asthenospheric materials, thus resulted in the large scale of lithospheric thinning and subsequent replacement. The process suggests that the lower Yangtze block has undergone similar lithospheric evolution and shares a common dynamic environment with the North China craton during late Mesozoic-Cenozoic time.

4.5 Conclusions

Petrologic, geochemical and Sr-Nd isotopic data on mantle-derived xenoliths from the Lianshan locality indicate that the SCLM beneath the region is mainly fertile clinopyroxene-rich (9-15 %) lherzolites which have undergone ~1% fractional partial melting and weak silicate-melt metasomatism; these features are interpreted as mantle formed in the Phanerozoic by asthenospheric upwelling. Minor refractory xenoliths (olivine-Mg# > 90) have convex-down REE patterns, high contents of highly compatible elements (Th, U, Sr and LREE) and negative anomalies in HFSE, recording higher degrees of partial melting (9-14%) and silicate- to carbonatitic-melt metasomatism. The refractory xenoliths are similar to shallow relics of the Archean-Proterozoic SCLM beneath the North China craton, suggesting that ancient mantle residues may have been preserved beneath this region.

The coexistence between fertile and refractory peridotites over a range of depths is due to upwelling of the asthenosphere and associated modification and replacement of the older lithosphere. Upwelling asthenospheric material strongly penetrated the preexisting refractory lithosphere mantle (i.e., Type 1; a “mushroom cloud” model) and subsequent cooling resulted in the irregular mantle replacement to form fertile lithosphere mantle (i.e., Type 2 xenoliths) beneath the lower Yangtze block.

Chapter 5 and 6 of this thesis have been removed due to copyright reasons

CHAPTER 7
SUMMARY OF CONCLUSIONS

Detailed petrographic, geochemical (including multi-isotopic) studies of peridotite xenoliths from the South China Craton and garnet pyroxenite xenoliths from the Lachlan orogen (southeastern Australia) presented here have led to the following conclusions.

(1) Peridotite xenoliths in the South China Craton can be divided into two compositional groups. *Group* 1 has olivine Mg# ~90-92, (and is thus relatively refractory) and shows the trace-element geochemical signature of "old" carbonatitic metasomatism, similar to the Hebi peridotite xenoliths, which represent the relic Archean lithospheric mantle beneath the North China Craton during Cenozoic time. *Group 2* is more fertile with olivine Mg# generally ~89–90, and represents fragments of recently accreted fertile lithospheric mantle, which is similar to the contemporary "oceanic-like" lithospheric mantle which is widespread in the North China Craton. The coexistence suggests that the residual refractory lithospheric mantle (represented by *Group 1* peridotites) may be irregularly eroded by upwelling asthenosphere materials along weak zones and eventually replaced to create a new and fertile lithosphere mantle (represented by *Group 2* xenoliths) as the asthenosphere cooled. The lithospheric mantle replacement beneath the Archean crust may have been triggered by paleo-Pacific subduction and roll-back during the late Mesozoic-Cenozoic, which resulted in extension of the lithosphere and the upwelling of the asthenosphere.

(2) Peridotite xenoliths in the South China Craton record sequential infiltration by two compositionally distinct silicate melts (Na-rich and K-rich) after early-stage melting and metasomatic events. The Na-rich melts are enclosed in spongy clinopyroxene and spinel rims and are inferred to have triggered the reactions that formed the spongy rims, which have lower Al_2O_3, Na_2O and Mg#, but higher FeO, TiO_2 and Cr# than the primary phases. The undersaturated Na-rich mafic melts were probably formed in the asthenosphere by low-degree melting. The infiltration of K-rich melts occurred after the percolation of Na-rich melts, and the melts occur mainly in reaction zones around orthopyroxene and in reaction patches. The melts have high contents of SiO_2, K_2O (mean 14.3 wt%), Rb, Ba, and LREE but

very low Na_2O/K_2O (0.01–0.29), positive anomalies in Eu and Sr, and variable HFSE anomalies. These compositional characteristics are consistent with an origin as low-degree partial melts of pre-existing phlogopite-bearing rocks.

(3) The preservation of modification of the large reservoir of lherzolite by the relatively small volumes of melts in the mantle would be rare, whereas melts represented by individual pyroxenite veins should be more sensitive to the mantle processes. Garnet pyroxenite xenoliths from Lakes Bullenmerri and Gnotuk in the Lachlan Orogen of southeastern Australia record partial melting and metasomatism of the convective mantle wedge. The Paleozoic subduction of the Proto-Pacific oceanic slab beneath southeastern Australia triggered melting of the convective mantle wedge at the initial stage due to slab dehydration and generated hydrous tholeiitic melts that crystallized high-MgO garnet pyroxenites at ~1420-1460 °C and 23-30 kb (~75-100 km). These rocks are characterized by high contents of Mg and Cr in whole rock and minerals, relatively flat LREE patterns and OIB-like Sr-Nd-Hf isotopic compositions ($^{87}Sr/^{86}Sr$= 0.70386-0.70657; $^{143}Nd/^{144}Nd$= 0.51260-0.51283; $^{176}Hf/^{177}Hf$= 0.28281-0.28305). Subsequently, fluid-fluxed melting of the mantle wedge by a mixture of recycled oceanic crust and its cover sediment generated the melts that precipated low-MgO garnet pyroxenites at 1280-1400°C and 16-20 kb (~53-66 km). These rocks have relatively low contents of Mg and Cr, variable REE patterns and heterogeneous Sr-Nd-Hf isotopic compositions ($^{87}Sr/^{86}Sr$= 0.70374-0.71548; $^{143}Nd/^{144}Nd$= 0.51221-0.51355; $^{176}Hf/^{177}Hf$= 0.28274-0.28396) in clinopyroxene but a narrow range of upper-mantle $\delta^{18}O_{V\text{-}SMOW}$ (4.9-5.2 ‰) in garnet. The results imply that the protoliths of these pyroxenites probably formed at a range of depths from ~50-100 km at ~300 Ma ago (whole-rock Sr-Nd mixing model).

(4) Microstructural evidence for the exsolution of garnet (± orthopyroxene ± spinel ± plagioclase ± ilmenite) from complex clinopyroxene megacrysts suggest that the garnet pyroxenite xenoliths finally equilibrated at ~950-1100°C and 12-18 kb (40-60 km). Thus, all garnet pyroxenites were uplifted by at least 10~20 km in Paleogene time (~40 Ma; determined by Cpx-Gt Sm-Nd isochrons); this was accompanied by rifting associated with crustal inflation and thinning in southeastern Australia due to the Mesozoic-Cenozoic paleo-Pacific subduction. Our findings indicate the protoliths of garnet pyroxenites formed along a decompressional cooling path and underwent a long-term evolution within the sub-arc lithospheric mantle, which led to a significant compositional and isotopic diversity.

(5) Peridotite xenoliths in the South China Craton and garnet pyroxenite xenoliths in southeastern Australia provides evidence of a scenario where subduction plays a critical role in the formation and evolution of the subcontinental lithospheric mantle, a major factor in Earth's dynamics.

REFERENCES

Ackerman, L., Špaček, P., Medaris Jr, G. et al., 2012. Geochemistry and petrology of pyroxenite xenoliths from Cenozoic alkaline basalts, Bohemian Massif. Journal of Geosciences, 57: 199-219.

Ackerman, L., Bizimis, M., Haluzová, E. et al., 2016. Re–Os and Lu–Hf isotopic constraints on the formation and age of mantle pyroxenites from the Bohemian Massif. Lithos, 256-257: 197-210.

Adam, J., Green, T.H., Day, R.A., 1992. An experimental study of two garnet pyroxenite xenoliths from the Bullenmerri and Gnotuk Maars of western Victoria, Australia. Contributions to Mineralogy and Petrology, 111(4): 505-514.

Alard, O., Griffin, W.L., Pearson, N.J. et al., 2002. New insights into the Re–Os systematics of sub-continental lithospheric mantle from in situ analysis of sulphides. Earth and Planetary Science Letters, 203(2): 651-663.

Aliani, P., Ntaflos, T., Bjerg, E., 2009. Origin of melt pockets in mantle xenoliths from southern Patagonia, Argentina. Journal of South American Earth Sciences, 28(4): 419-428.

Allègre, C.J., Turcotte, D.L., 1986. Implications of a two-component marble-cake mantle. Nature, 323(6084): 123-127.

Andersen, T., O'Reilly, S.Y., Griffin, W.L., 1984. The trapped fluid phase in upper mantle xenoliths from Victoria, Australia: implications for mantle metasomatism. Contributions to Mineralogy and Petrology, 88(1-2): 72-85.

Aoki, K.I., Fujimaki, H., Kitamura, M., 1980. Exsolved garnet-bearing pyroxene megacrysts from some South African kimberlites. Lithos, 13(3): 269-279.

Arculus, R.J., Ishizuka, O., Bogus, K.A. et al., 2015. A record of spontaneous subduction initiation in the Izu–Bonin–Mariana arc. Nature Geoscience, 8(9): 728-733.

Aulbach, S., Pearson, N.J., O'Reilly, S.Y. et al., 2007. Origins of xenolithic eclogites and pyroxenites from the Central Slave Craton, Canada. Journal of Petrology, 48(10): 1843-1873.

Aulbach, S., Jacob, D.E., 2016. Major- and trace-elements in cratonic mantle eclogites and pyroxenites reveal heterogeneous sources and metamorphic processing of low-pressure protoliths. Lithos, 262: 586-605.

Baker, M.B., Grove, T.L., Price, R., 1994. Primitive basalts and andesites from the Mt. Shasta region, N. California: products of varying melt fraction and water content. Contributions to Mineralogy and Petrology, 118(2): 111-129.

Barnes, S.J., 1986. The effect of trapped liquid crystallisation on cumulus mineral compositions in layered intrusions. Contributions to Mineralogy and Petrology, 93(4): 524-531.

Batanova, V.G., Pertsev, A.N., Kamenetsky, V.S. et al., 2005. Crustal evolution of island-arc ultramafic magma: Galmoenan pyroxenite-dunite plutonic complex, Koryak Highland (Far East Russia). Journal of Petrology, 46(7): 1345-1366.

Beccaluva, L., Bonadiman, C., Coltorti, M. et al., 2001. Depletion events, nature of metasomatizing agent and timing of enrichment processes in lithospheric mantle xenoliths from the Veneto Volcanic Province. Journal of Petrology, 42(1): 173-187.

Becker, H., 1996. Crustal trace element and isotopic signatures in garnet pyroxenites from garnet peridotite massifs from Lower Austria. Journal of Petrology, 37(4): 785-810.

Bell, D.R., Grégoire, M., Grove, T.L. et al., 2005. Silica and volatile-element metasomatism of Archean mantle: a xenolith-scale example from the Kaapvaal Craton. Contributions to Mineralogy and Petrology, 150(3): 251-267.

Benoit, M., Polvé, M., Ceuleneer, G., 1996. Trace element and isotopic characterization of mafic cumulates in a fossil mantle diapir (Oman ophiolite). Chemical Geology, 134(1): 199-214.

Berger, J., Féménias, O., Coussaert, N. et al., 2007. Cumulating processes at the crust-mantle transition zone inferred from Permian mafic-ultramafic xenoliths (Puy Beaunit, France). Contributions to Mineralogy and Petrology, 153(5): 557-575.

Betts, P.G., Giles, D., Lister, G.S. et al., 2002. Evolution of the Australian lithosphere. Australian Journal of Earth Sciences, 49(4): 661-695.

Bizimis, M., Sen, G., Salters, V.J.M. et al., 2005. Hf-Nd-Sr isotope systematics of garnet pyroxenites from Salt Lake Crater, Oahu, Hawaii: Evidence for a depleted component in Hawaiian volcanism. Geochimica et Cosmochimica Acta, 69(10): 2629-2646.

Blichert-Toft, J., Chauvel, C., Albarède, F., 1997. Separation of Hf and Lu for high-precision isotope analysis of rock samples by magnetic sector-multiple collector ICP-MS. Contributions to Mineralogy and Petrology, 127(3): 248-260.

Blichert-Toft, J., 1999. Lu-Hf isotope systematics of garnet pyroxenites from Beni Bousera, Morocco: implications for basalt origin. Science, 283(5406): 1303-1306.

Bodinier, J.L., Guiraud, M., Fabriés, J. et al., 1987. Petrogenesis of layered pyroxenites from the Lherz, Freychinéde and Prades ultramafic bodies (Ariége, French Pyrénées). Geochimica et Cosmochimica Acta, 51(2): 279-290.

Bodinier, J.L., Vasseur, G., Vernieres, J. et al., 1990. Mechanisms of mantle metasomatism: geochemical evidence from the Lherz Orogenic Peridotite. Journal of Petrology, 31(3): 597-628.

Bodinier, J.L., Garrido, C.J., Chanefo, I. et al., 2008. Origin of pyroxenite-peridotite veined mantle by refertilization reactions: evidence from the Ronda Peridotite (Southern Spain). Journal of Petrology, 49(5): 999-1025.

Bodinier, J.L., Godard, M., 2014. Orogenic, Ophiolitic, and Abyssal Peridotites. In: Holland, H.D., Turekian, K.K. (Eds.), Treatise on Geochemistry (Second Edition), Volume 3, Elsevier, Pergamon, Oxford, pp 103-167.

Bonadiman, C., Coltorti, M., Milani, L. et al., 2001. Metasomatism in the lithospheric mantle and its relationships to magmatism in the Veneto Volcanic Province, Italy. Periodico di Mineralogia, 70: 333-357.

Bonadiman, C., Beccaluva, L., Coltorti, M. et al., 2005. Kimberlite-like metasomatism and 'garnet signature' in spinel-peridotite xenoliths from Sal, Cape Verde Archipelago: Relics of a subcontinental mantle domain within the Atlantic oceanic lithosphere? Journal of Petrology, 46(12): 2465-2493.

Bonadiman, C., Coltorti, M., Duggen, S. et al., 2008. Palaeozoic subduction-related and kimberlite or carbonatite metasomatism in the Scottish lithospheric mantle. Geological Society, London, Special Publications, 293(1): 303-333.

Bonadiman, C., Coltorti, M., Beccaluva, L. et al., 2011. Metasomatism versus host magma infiltration: A case study of Sal mantle xenoliths, Cape Verde Archipelago. Geological Society of America Special papers, 478: 283-305.

Borghini, G., Rampone, E., Zanetti, A. et al., 2016. Pyroxenite layers in the Northern Apennines' upper mantle (Italy) - Generation by pyroxenite melting and melt infiltration. Journal of Petrology, 57(4): 625-653.

Bouvier, A., Vervoort, J.D., Patchett, P.J., 2008. The Lu–Hf and Sm–Nd isotopic composition of CHUR: Constraints from unequilibrated chondrites and implications for the bulk composition of terrestrial planets. Earth and Planetary Science Letters, 273(1-2): 48-57.

Boyd, F.R., Nixon, P.H., 1978. Ultramafic nodules from the Kimberley pipes, South Africa. Geochimica et Cosmochimica Acta, 42(9): 1367-1382.

Boyd, F.R., Gurney, J.J., 1986. Diamonds and the african lithosphere. Science, 232(4749): 472-7.

Boyd, F.R., 1989. Compositional distinction between oceanic and cratonic lithosphere. Earth and Planetary Science Letters, 96(1-2): 15-26.

Boyd, F.R., Pokhilenko, N.P., Pearson, D.G. et al., 1997. Composition of the Siberian cratonic mantle: evidence from Udachnaya peridotite xenoliths. Contributions to Mineralogy and Petrology, 128(2-3): 228-246.

Brey, G.P., Kohler, T., 1990. Geothermobarometry in four-phase lherzolites II. New thermobarometers, and practical assessment of existing thermobarometers. Journal of Petrology, 31(6): 1353-1378.

Burgess, S.R., Harte, B., 2004. Tracing Lithosphere Evolution through the Analysis of Heterogeneous G9-G10 Garnets in Peridotite Xenoliths, II: REE Chemistry. Journal of Petrology, 45(3): 609-633.

Burrett, C., Long, J., Stait, B., 1990. Early-Middle Palaeozoic biogeography of Asian terranes derived from Gondwana. Geological Society, London, Memoirs, 12(1): 163-174.

Carlson, R.W., Irving, A.J., Schulze, D.J. et al., 2004. Timing of Precambrian melt depletion and Phanerozoic refertilization events in the lithospheric mantle of the Wyoming Craton and adjacent Central Plains Orogen. Lithos, 77(1-4): 453-472.

Carlson, R.W., 2005. Physical, chemical, and chronological characteristics of continental mantle. Reviews of Geophysics, 43(1).

Carlson, R.W., 2014. Volume Editor's Introduction. In: Holland, H.D., Turekian, K.K. (Eds.), Treatise on Geochemistry (Second Edition), Pergamon, Oxford, pp. xxiii-xxvi.

Carlson, W.D., 2012. Rates and mechanism of Y, REE, and Cr diffusion in garnet. American Mineralogist, 97(10): 1598-1618.

Carpenter, R.L., Edgar, A.D., Thibault, Y., 2002. Origin of spongy textures in clinopyroxene and spinel from mantle xenoliths, Hessian Depression, Germany. Mineralogy and Petrology, 74(2-4): 149-162.

Cawood, P.A., 2005. Terra Australis Orogen: Rodinia breakup and development of the Pacific and Iapetus margins of Gondwana during the Neoproterozoic and Paleozoic. Earth-Science Reviews, 69(3–4): 249-279.

Cawood, P.A., Johnson, M.R.W., Nemchin, A.A., 2007. Early Palaeozoic orogenesis along the Indian margin of Gondwana: Tectonic response to Gondwana assembly. Earth and Planetary Science Letters, 255(1–2): 70-84.

Cayley, R.A., Taylor, D.H., 2001. Geological Survey report for the Ararat 1:100000 map sheet. Geological Survey report of Victoria Report, 115.

Cayley, R.A., Taylor, D.H., VandenBerg, A.H.M. et al., 2002. Proterozoic – Early Palaeozoic rocks and the Tyennan Orogeny in central Victoria: the Selwyn Block and its tectonic implications. Australian Journal of Earth Sciences, 49(2): 225-254.

Cayley, R.A., Korsch, R.J., Moore, D.H. et al., 2011. Crustal architecture of central Victoria: results from the 2006 deep crustal reflection seismic survey. Australian Journal of Earth Sciences, 58(2): 113-156.

Chen, C.-H., Hsieh, P.-S., Lee, C.-Y. et al., 2011. Two episodes of the Indosinian thermal event on the South China Block: Constraints from LA-ICPMS U–Pb zircon and electron microprobe monazite ages of the Darongshan S-type granitic suite. Gondwana Research, 19(4): 1008-1023.

Chen, D.G., Li, B.X., Zhi, X.C. et al., 1994. Mineral chemistry and REE compositions of peridotite xenoliths from Liuhe, Jiangsu and its implications. Acta Petrologica Sinica, 10(1): 68-80.

Chen, J., Xu, Z.Q., 2005. Pargasite and ilmenite exsolution texture in clinopyroxenes from Hujialing garnet-pyroxenite, Su-Lu UHP terrane, Central China: a geodynamic implication. European Journal of Mineralogy, 17(6): 895-903.

Chen, J.F., Jahn, B.M., 1998. Crustal evolution of southeastern China: Nd and Sr isotopic evidence. Tectonophysics, 284(1-2): 101-133.

Chen, S., O'Reilly, S.Y., Zhou, X. et al., 2001. Thermal and petrological structure of the lithosphere beneath Hannuoba, Sino-Korean Craton, China: evidence from xenoliths. Lithos, 56(4): 267-301.

Cheng, H., King, R.L., Nakamura, E. et al., 2008. Coupled Lu-Hf and Sm-Nd geochronology constrains garnet growth in ultra-high-pressure eclogites from the Dabie orogen. Journal of Metamorphic Geology, 26(7): 741-758.

Chung, S.L., Sun, S.S., Tu, K. et al., 1994. Late Cenozoic basaltic volcanism around the Taiwan Strait, SE China: Product of lithosphere-asthenosphere interaction during continental extension. Chemical Geology, 112(1-2): 1-20.

Chung, S.L., Cheng, H., Jahn, B.M. et al., 1997. Major and trace element, and Sr-Nd isotope constraints on the origin of Paleogene volcanism in South China prior to the South China Sea opening. Lithos, 40(2-4): 203-220.

Clarke, D.B., Pe-Piper, G.G., 1983. Multiply exsolved clinopyroxene megacrysts from the Frank Smith Mine, Cape Province, South Africa. Lithos, 16(1): 75-84.

Coltorti, M., Bonadiman, C., Hinton, R.W. et al., 1999. Carbonatite metasomatism of the oceanic upper mantle: Evidence from clinopyroxenes and glasses in ultramafic xenoliths of Grande Comore, Indian Ocean. Journal of Petrology, 40(1): 133-165.

Crawford, A.J., Meffer, S., Symonds, P.A., 2003. 120 to 0 Ma tectonic evolution of the southwest Pacific and analogous geological evolution of the 600 to 220 Ma Tasman Fold Belt System. Geological Society of America Special papers, 372: 383-403.

Dantas, C., Ceuleneer, G., Gregoire, M. et al., 2007. Pyroxenites from the southwest Indian Ridge, 9-16 °E: Cumulates from incremental melt fractions produced at the top of a cold melting regime. Journal of Petrology, 48(4): 647-660.

Davies, D.R., Rawlinson, N., 2014. On the origin of recent intraplate volcanism in Australia. Geology, 42(12): 1031-1034.

Davies, D.R., Rawlinson, N., Iaffaldano, G. et al., 2015. Lithospheric controls on magma composition along Earth's longest continental hotspot track. Nature, 525: 511-514.

Demarchi, G., Antonini, P., Piccirillo, E. et al., 2001. Significance of orthopyroxene and major element constraints on the petrogenesis of Ferrar tholeiites from southern Prince Albert Mountains, Victoria Land, Antarctica. Contributions to Mineralogy and Petrology, 142(2): 127-146.

Demidjuk, Z., Turner, S., Sandiford, M. et al., 2007. U-series isotope and geodynamic constraints on mantle melting processes beneath the Newer Volcanic Province in South Australia. Earth and Planetary Science Letters, 261(3-4): 517-533.

Deng, J.F., Mo, X.X., Zhao, H.L. et al., 2004. A new model for the dynamic evolution of Chinese lithosphere: ‘continental roots–plume tectonics’. Earth-Science Reviews, 65(3-4): 223-275.

DePaolo, D.J., 1981. Neodymium isotopes in the Colorado Front Range and crust–mantle evolution in the Proterozoic. Nature, 291(5812): 193-196.

Dick, H.J.B., Sinton, J.M., 1979. Compositional layering in Alpine Peridotites: Evidence for pressure solution creep in the mantle. The Journal of Geology, 87(4): 403-416.

Dobosis, G., Kurat, G., Wall, F. et al., 2007. Trace element fractionation exsolution of garnet from clinopyroxene, Goldschmidt conference.

Donnelly, C.L., Griffin, W.L., Yang, J.H. et al., 2012. In situ U-Pb dating and Sr-Nd isotopic analysis of perovskite: Constraints on the age and petrogenesis of the Kuruman Kimberlite Province, Kaapvaal Craton, South Africa. Journal of Petrology, 53(12): 2497-2522.

Downes, H., 2007. Origin and significance of spinel and garnet pyroxenites in the shallow lithospheric mantle: Ultramafic massifs in orogenic belts in Western Europe and NW Africa. Lithos, 99(1-2): 1-24.

Duchene, S., Blichert-Toft, J., Luais, B. et al., 1997. The Lu-Hf dating of garnets and the ages of the Alpine high-pressure metamorphism. Nature, 387(6633): 586-589.

Dziewonski, A.M., Romanowicz, B.A., 2015. Deep Earth Seismology: An Introduction and Overview. 1-28.

Edwards, J., Leonard, J.G., Pettifer, G.R. et al., 1996. Colac-1:250000 map geological report.

Eggler, D.H., 1987. Solubility of major and trace elements in mantle metasomatic fluids: experimental constraints. In: Menzies, M.A., Hawkesworth, C.J. (Eds.), Mantle metasomatism. Academic Press Geology Series, London, pp. 21-41.

El Atrassi, F., Brunet, F., Chazot, G. et al., 2013. Metamorphic and magmatic overprint of garnet pyroxenites from the Beni Bousera massif (northern Morocco): Petrography, mineral chemistry and thermobarometry. Lithos, 179: 231-248.

Ellis, D.J., Green, D.H., 1979. An experimental study of the effect of Ca upon garnet-clinopyroxene Fe-Mg exchange equilibria. Contributions to Mineralogy and Petrology, 71(1): 13-22.

Erlank, A.J., Waters, F.G., Hawkesworth, C.J. et al., 1987. Evidence for mantle metasomatism in peridotite nodules from the Kimberley Pipes, South Africa. In:

Hawkesworth, C.J., Menzies, M. (Eds.), Mantle metasomatism. Academic Press, pp. 221-331.

Fabries, J., Lorand, J.P., Guiraud, M., 2001. Petrogenesis of the amphibole-rich veins from the Lherz orogenic lherzolite massif (Eastern Pyrenees, France): a case study for the origin of orthopyroxene-bearing amphibole pyroxenites in the lithospheric mantle. Contributions to Mineralogy and Petrology, 140(4): 383-403.

Falloon, T.J., Green, D.H., Hatton, C.J., Harris, K.L., 1988. Anhydrous Partial Melting of a Fertile and Depleted Peridotite from 2 to 30 kb and Application to Basalt Petrogenesis. Journal of Petrology, 29(6): 1257-1282.

Fan, W.-M., Menzies, M.A., 1992. Destruction of aged lower lithosphere and accretion of asthenosphere mantle beneath eastern China. Geotectonica et Metallogenia, 16: 171-180.

Faryad, S.W., Dolejs, D., Machek, M., 2009. Garnet exsolution in pyroxene from clinopyroxenites in the Moldanubian zone: constraining the early pre-convergence history of ultramafic rocks in the Variscan orogen. Journal of Metamorphic Geology, 27(9): 655-671.

Ferguson, J., Ellis, D.J., England, R.N., 1977. Unique spinel-garnet lherzolite inclusion in kimberlite from Australia. Geology, 5: 278-280.

Finlayson, D.M., Owen, A., Johnstone, D. et al., 1993. Moho and petrologic crust-mantle boundary coincide under southeastern Australia. Geology, 21(8): 707-710.

Flöttmann, T., Haines, P., Jago, J. et al., 1998. Formation and reactivation of the Cambrian Kanmantoo Trough, SE Australia: implications for early Palaeozoic tectonics at eastern Gondwana's plate margin. Journal of the Geological Society, 155(3): 525-539.

Foden, J.D., Elburg, M.A., Turner, S.P. et al., 2002. Granite production in the Delamerian Orogen, South Australia. Journal of the Geological Society, 159(5): 557-575.

Foden, J.D., Elburg, M.A., Dougherty-Page, J. et al., 2006. The timing and duration of the Delamerian Orogeny: correlation with the Ross Orogen and implications for Gondwana assembly. The Journal of Geology, 114: 189-210.

Foley, S.F., 2008. Rejuvenation and erosion of the cratonic lithosphere. Nature Geoscience, 1(8): 503-510.

Foster, D.A., Gray, D.R., 2000. Evolution and structure of the Lachlan Fold Belt (Orogen) of Eastern Australia. Annual Review of Earth and Planetary Sciences, 28(1): 47-80.

Frey, F.A., 1980. The origin of pyroxenites and garnet pyroxenites from Salt Lake Crater, Oahu, Hawaii: trace element evidence. American Journal of Science, 280-A: 427-449.

Gao, S., Ling, W., Qiu, Y. et al., 1999. Contrasting geochemical and Sm-Nd isotopic compositions of Archean metasediments from the Kongling high-grade terrain of the Yangtze craton: evidence for cratonic evolution and redistribution of REE during crustal anatexis. Geochimica et Cosmochimica Acta, 63(13-14): 2071-2088.

Gao, S., Rudnick, R.L., Carlson, R.W. et al., 2002. Re–Os evidence for replacement of ancient mantle lithosphere beneath the North China craton. Earth and Planetary Science Letters, 198(3-4): 307-322.

Gao, S., Yang, J., Zhou, L. et al., 2011. Age and growth of the Archean Kongling terrain, South China, with emphasis on 3.3 ga granitoid gneisses. American Journal of Science, 311(2): 153-182.

Garrido, C.J., Bodinier, J.L., 1999. Diversity of mafic rocks in the Ronda Peridotite: Evidence for pervasive melt-rock reaction during heating of subcontinental lithosphere by upwelling asthenosphere. Journal of Petrology, 40(5): 729-754.

Garrido, C.J., Bodinier, J.L., Dhuime, B. et al., 2007. Origin of the island arc Moho transition zone via melt-rock reaction and its implications for intracrustal differentiation of island arcs: Evidence from the Jijal complex (Kohistan complex, northern Pakistan). Geology, 35(8): 683-686.

Garrison, J.R., Taylor, L.A., 1981. Petrogenesis of pyroxene-oxide intergrowths from kimberlite and cumulate rocks; co-precipitation or exsolution? American Mineralogist, 66(7-8): 723-740.

Gasparik, T., 2014. Phase diagrams for Geoscientists.

Gingele, F.X., De Deckker, P., 2005. Clay mineral, geochemical and Sr–Nd isotopic fingerprinting of sediments in the Murray–Darling fluvial system, southeast Australia. Australian Journal of Earth Sciences, 52(6): 965-974.

Glen, R.A., 1992. Thrust, extensional and strike-slip tectonics in an evolving Palaeozoic orogen-a structural synthesis of the Lachlan Orogen of southeastern Australia. Tectonophysics, 214(1-4): 341-380.

Glen, R.A., Walshe, J.L., Barron, L.M. et al., 1998. Ordovician convergent-margin volcanism and tectonism in the Lachlan sector of east Gondwana. Geology, 26(8): 751-754.

Glen, R.A., 2005. The Tasmanides of eastern Australia. Geological Society, London, Special Publications, 246(1): 23-96.

Gonzaga, R.G., 2007. Garnet-clinopyroxene assemblages in the Earth's mantle, Royal Holloway, University of London, pp1-471.

Gonzaga, R.G., Menzies, M.A., Thirlwall, M.F. et al., 2010. Eclogites and garnet pyroxenites: Problems resolving provenance using Lu-Hf, Sm-Nd and Rb-Sr isotope systems. Journal of Petrology, 51(1-2): 513-535.

Gray, C.M., 1990. A strontium isotopic traverse across the granitic rocks of southeastern Australia: Petrogenetic and tectonic implications. Australian Journal of Earth Sciences, 37(3): 331-349.

Gray, C.M., Kemp, A.I.S., Anderson, J.A.C. et al., 2002. Delamerian Glenelg tectonic zone, western Victoria: Geology and metamorphism of stratiform rocks. Australian Journal of Earth Sciences, 49(2): 187-200.

Gray, D.R., Foster, D.A., 1997. Orogenic concepts - application and definition: Lachlan fold belt, eastern Australia. American Journal of Science, 297(9): 859-891.

Gray, D.R., Foster, D.A., Bucher, M., 1997. Recognition and definition of orogenic events in the Lachlan Fold Belt. Australian Journal of Earth Sciences, 44(4): 489-501.

Gray, D.R., Foster, D.A., 1998. Character and kinematics of faults within the turbidite-dominated Lachlan Orogen: implications for tectonic evolution of eastern Australia. Journal of Structural Geology, 20(12): 1691-1720.

Green, D.H., Ringwood, A.E., 1967. An experimental investigation of the gabbro to eclogite transformation and its petrological applications. Geochimica et Cosmochimica Acta, 31(5): 767-833.

Green, T.H., Blundy, J.D., Adam, J. et al., 2000. SIMS determination of trace element partition coefficients between garnet, clinopyroxene and hydrous basaltic liquids at 2-7.5 GPa and 1080–1200°C. Lithos, 53(3-4): 165-187.

Griffin, W.L., Wass, S.Y., Hollis, J.D., 1984. Ultramafic xenoliths from Bullenmerri and Gnotuk Maars, Victoria, Australia: petrology of a sub-continental crust-mantle transition. Journal of Petrology, 25(1): 53-87.

Griffin, W.L., O'Reilly, S.Y., 1987. The composition of the lower crust and the nature of the continental Moho-xenolith evidence. In: Nixon, P.H. (Ed.), Mantle xenoliths. Wiley, London, pp. 413-430.

Griffin, W.L., O'Reilly, S.Y., Stabel, A., 1988. Mantle metasomatism beneath western Victoria, Australia: II. Isotopic geochemistry of Cr-diopside lherzolites and Al-augite pyroxenites. Geochimica et Cosmochimica Acta, 52(2): 449-459.

Griffin, W.L., O'Reilly, S.Y., Ryan, C.G., 1992. Composition and thermal structure of the lithosphere beneath South Africa, Siberia and China: proton microprobe studies., International Symposium on Cenozoic Volcanic Rocks and Deep-seated Xenoliths of China and its Environs, Beijing, pp. 20.

Griffin, W.L., Zhang, A.D., O'Reilly, S.Y. et al., 1998. Phanerozoic Evolution of the Lithosphere Beneath the Sino-Korean Craton. In: Flower, M.F.J. et al. (Eds.), Mantle Dynamics and Plate Interactions in East Asia. American Geophysical Union, Washington, D.C., pp. 107-126.

Griffin, W.L., Fisher, N.I., Friedman, J. et al., 1999a. Cr-Pyrope garnets in the lithospheric mantle. I. Compositional systematics and relations to tectonic setting. Journal of Petrology, 40(5): 679-704.

Griffin, W.L., O'Reilly, S.Y., Ryan, C.G., 1999b. The composition and origin of subcontinental lithospheric mantle. In: Fei, Y.W. et al. (Eds.), Mantle Petrology: Field Observations and High-Pressure Experimentation, The Geochemical Society, Stony Brook, N.Y., pp. 13-45.

Griffin, W.L., O’Reilly, S.Y., Abe, N. et al., 2003. The origin and evolution of Archean lithospheric mantle. Precambrian Research, 127(1-3): 19-41.

Griffin, W.L., Powell, W.J., Pearson, N.J. et al., 2008. GLITTER: data reduction software for laser ablation ICP-MS. In: Sylvester, P. (Ed.), Laser Ablation-ICP-MS in the Earth Sciences. Mineralogical Association of Canada Short Course Series, pp. 204-207.

Griffin, W.L., O'Reilly, S.Y., Afonso, J.C. et al., 2009. The composition and evolution of lithospheric mantle: a re-evaluation and its tectonic implications. Journal of Petrology, 50(7): 1185-1204.

Gysi, A.P., Jagoutz, O., Schmidt, M.W. et al., 2011. Petrogenesis of pyroxenites and melt infiltrations in the ultramafic complex of Beni Bousera, Northern Morocco. Journal of Petrology, 52(9): 1679-1735.

Hanson, G.N., Langmuir, C.H., 1978. Modelling of major elements in mantle-melt systems using trace element approaches. Geochimica et Cosmochimica Acta, 42(6): 725-741.

Hao, Y., 2010. Petrological features of Subei Basin (Eastern China) lithospheric mantle and their relationships with H2O contents in NAMs, Universita degli Studi di Ferrara.

Hart, S.R., Blusztajn, J., Dick, H.J.B. et al., 1999. The fingerprint of seawater circulation in a 500-meter section of ocean crust gabbros. Geochimica et Cosmochimica Acta, 63(23): 4059-4080.

Harte, B., 1977. Rock Nomenclature with Particular Relation to Deformation and Recrystallisation Textures in Olivine-Bearing Xenoliths. The Journal of Geology, 85(3): 279-288.

Harte, B., Kirkley, M.B., 1997. Partitioning of trace elements between clinopyroxene and garnet: data from mantle eclogites. Chemical Geology, 136(1-2): 1-24.

Handler, M.R., Bennett, V.C., Esat, T.M., 1997. The persistence of off-cratonic lithospheric mantle: Os isotopic systematics of variably metasomatised southeast Australian xenoliths. Earth and Planetary Science Letters, 151(1-2): 61-75.

Handler, M.R., Bennett, V.C., 2001. Constraining continental structure by integrating Os isotopic ages of lithospheric mantle with geophysical and crustal data: An example from southeastern Australia. Tectonics, 20(2): 177-188.

Hasterok, D., Chapman, D.S., 2011. Heat production and geotherms for the continental lithosphere. Earth and Planetary Science Letters, 307(1-2): 59-70.

Hauri, E.H., Shimizu, N., Dieu, J.J. et al., 1993. Evidence for hotspot-related carbonatite metasomatism in the oceanic upper mantle. Nature, 365(6443): 221-227.

Hawkesworth, C.J., Kemp, A.I., 2006. Evolution of the continental crust. Nature, 443(7113): 811-7.

Hellebrand, E., Snow, J.E., Dick, H.J. et al., 2001. Coupled major and trace elements as indicators of the extent of melting in mid-ocean-ridge peridotites. Nature, 410(6829): 677-81.

Hermann, J., 2001. Differentiation of Mafic Magma in a Continental Crust-to-Mantle Transition Zone. Journal of Petrology, 42(1): 189-206.

Herzberg, C., Rudnick, R., 2012. Formation of cratonic lithosphere: An integrated thermal and petrological model. Lithos, 149: 4-15.

Herzberg, C.T., 1978. Pyroxene geothermometry and geobarometry: experimental and thermodynamic evaluation of some subsolidus phase relations involving pyroxenes in the system CaO-MgO-Al2O3-SiO2. Geochimica et Cosmochimica Acta, 42(7): 945-957.

Hirschmann, M.M., Stolper, E.M., 1996. A possible role for garnet pyroxenite in the origin of the "garnet signature" in MORB. Contributions to Mineralogy and Petrology, 124(2): 185-208.

Hirose, K., Kushiro, I., 1993. Partial melting of dry peridotites at high pressures: Determination of compositions of melts segregated from peridotite using aggregates of diamond. Earth and Planetary Science Letters, 114(4): 477-489.

Ho, K.S., Chen, J.C., Lo, C.H. et al., 2003. ^{40}Ar-^{39}Ar dating and geochemical characteristics of late Cenozoic basaltic rocks from the Zhejiang-Fujian region, SE China: eruption ages, magma evolution and petrogenesis. Chemical Geology, 197(1-4): 287-318.

Ho, K.S., 1999. Sr-Nd isotope and geochemical evidence for the origin of clinopyroxene, amphibole, and mica megacrysts in alkali basaltic rocks from southeastern China and Penghu island.

Hofmann, A.W., 1988. Chemical differentiation of the Earth: the relationship between mantle, continental crust, and oceanic crust. Earth and Planetary Science Letters, 90(3): 297-314.

Hofmann, A.W., 1997. Mantle geochemistry: the message from oceanic volcanism. Nature, 385(6613): 219-229.

Hollis, J.D., 1981. Ultramafic and gabbroic nodules from the Bullenmerri and Gnotuk maars, Camperdown, Victoria. Proceeding of the Royal Society of Victoria: 155-166.

Hsü, K.J., Li, J., Chen, H. et al., 1990. Tectonics of South China: Key to understanding West Pacific geology. Tectonophysics, 183(1-4): 9-39.

Huang, J., Ren, J.S., Jiang, C. et al., 1980. The Geotectonic Evolution of China. Science Press, Beijing.

Huang, J., Zheng, Y.-F., Zhao, Z.-F. et al., 2006. Melting of subducted continent: Element and isotopic evidence for a genetic relationship between Neoproterozoic and Mesozoic granitoids in the Sulu orogen. Chemical Geology, 229(4): 227-256.

Huang, J.-X., Griffin, W.L., Gréau, Y. et al., 2012a. Seeking the primary compositions of mantle xenoliths: Isotopic and elemental consequences of sequential leaching treatments on an eclogite suite. Chemical Geology, 328: 137-148.

Huang, J.X., Gréau, Y., Griffin, W.L. et al., 2012b. Multi-stage origin of Roberts Victor eclogites: Progressive metasomatism and its isotopic effects. Lithos, 142-143: 161-181.

Huang, X., Xu, Y., 2010. Thermal state and structure of the lithosphere beneath eastern China: A synthesis on basalt-borne xenoliths. Journal of Earth Science, 21(5): 711-730.

Huang, X.-L., Niu, Y.L., Xu, Y.-G. et al., 2012. Geochronology and geochemistry of Cenozoic basalts from eastern Guangdong, SE China: constraints on the lithosphere evolution beneath the northern margin of the South China Sea. Contributions to Mineralogy and Petrology, 165(3): 437-455.

Huang, X.L., Xu, Y.G., Lo, C.H. et al., 2007. Exsolution lamellae in a clinopyroxene megacryst aggregate from Cenozoic basalt, Leizhou Peninsula, South China: petrography and chemical evolution. Contributions to Mineralogy and Petrology, 154(6): 691-705.

Ionov, D.A., Dupuy, C., O'Reilly, S.Y. et al., 1993. Carbonated peridotite xenoliths from Spitsbergen: implications for trace element signature of mantle carbonate metasomatism. Earth and Planetary Science Letters, 119(3): 283-297.

Ionov, D.A., Prikhod'ko, V.S., O'Reilly, S.Y., 1995. Peridotite xenoliths in alkali basalts from the Sikhote-Alin, southeastern Siberia, Russia: trace-element signatures of mantle beneath a convergent continental margin. Chemical Geology, 120(3-4): 275-294.

Ionov, D.A., Chanefo, I., Bodinier, J.L., 2005. Origin of Fe-rich lherzolites and wehrlites from Tok, SE Siberia by reactive melt percolation in refractory mantle peridotites. Contributions to Mineralogy and Petrology, 150(3): 335-353.

Irving, A.J., 1974. Geochemical and high pressure experimental studies of garnet pyroxenite and pyroxene granulite xenoliths from the Delegate basaltic pipes, Australia. Journal of Petrology, 15(1): 1-40.

Irving, A.J., 1980. Petrology and geochemistry of composite ultramafic xenoliths in alkalic basalts and implications for magmatic processes within the mantle. American Journal of Science, 280-A: 389-426.

Ishikawa, A., Maruyama, S., Komiya, T., 2004. Layered lithospheric mantle beneath the Ontong Java Plateau: Implications from xenoliths in Alnoite, Malaita, Solomon Islands. Journal of Petrology, 45(10): 2011-2044.

Ishikawa, A., Kuritani, T., Makishima, A. et al., 2007. Ancient recycled crust beneath the Ontong Java Plateau: Isotopic evidence from the garnet clinopyroxenite xenoliths, Malaita, Solomon Islands. Earth and Planetary Science Letters, 259(1-2): 134-148.

Jacob, D.E., Bizimis, M., Salters, V.J.M., 2004. Lu-Hf and geochemical systematics of recycled ancient oceanic crust: evidence from Roberts Victor eclogites. Contributions to Mineralogy and Petrology, 148(6): 707-720.

Kelemen, P.B., Joyce, D.B., Webster, J.D. et al., 1990. Reaction Between Ultramafic Rock and Fractionating Basaltic Magma II. Experimental Investigation of Reaction Between

Olivine Tholeiite and Harzburgite at 1150-1050 C and 5 kb. Journal of Petrology, 31(1): 99-134.

Kelemen, P.B., 1995. Genesis of high Mg# andesites and the continental crust. Contributions to Mineralogy and Petrology, 120(1): 1-19.

Keshav, S., Gudfinnsson, G.H., Sen, G., et al., 2004, High-pressure melting experiments on garnet clinopyroxenite and the alkalic to tholeiitic transition in ocean-island basalts: Earth and Planetary Science Letters, 223 (3-4): 365-379.

Keshav, S., Sen, G., Presnall, D.C., 2007. Garnet-bearing xenoliths from Salt Lake Crater, Oahu, Hawaii: high-pressure fractional crystallization in the oceanic mantle. Journal of Petrology, 48(9): 1681-1724.

Kogiso, T., Hirschmann, M.M., Frost, D.J., 2003. High-pressure partial melting of garnet pyroxenite: possible mafic lithologies in the source of ocean island basalts. Earth and Planetary Science Letters, 216(4): 603-617.

Kohler, T.P., Brey, G.P., 1990. Calcium exchange between olivine and clinopyroxene calibrated as a geothermobarometer for natural peridotites from 2 to 60 kb with applications. Geochimica et Cosmochimica Acta, 54(9): 2375-2388.

Konrad-Schmolke, M., Zack, T., O'Brien, P.J. et al., 2008. Combined thermodynamic and rare earth element modelling of garnet growth during subduction: Examples from ultrahigh-pressure eclogite of the Western Gneiss Region, Norway. Earth and Planetary Science Letters, 272(1-2): 488-498.

Kornprobst, J., Piboule, M., Roden, M. et al., 1990. Corundum-bearing Garnet Clinopyroxenites at Beni Bousera (Morocco): Original Plagioclase-rich Gabbros Recrystallized at Depth within the Mantle? Journal of Petrology, 31(3): 717-745.

Kusky, T.M., Windley, B.F., Wang, L. et al., 2014. Flat slab subduction, trench suction, and craton destruction: Comparison of the North China, Wyoming, and Brazilian cratons. Tectonophysics, 630: 208-221.

Lambart, S., Laporte, D., Schiano, P., 2009. An experimental study of pyroxenite partial melts at 1 and 1.5GPa: Implications for the major-element composition of Mid-Ocean Ridge Basalts. Earth and Planetary Science Letters, 288(1-2): 335-347.

Lambart, S., Laporte, D., Provost, A. et al., 2012. Fate of pyroxenite-derived melts in the peridotitic mantle: Thermodynamic and experimental constraints. Journal of Petrology, 53(3): 451-476.

Lambart, S., Laporte, D., Schiano, P., 2013. Markers of the pyroxenite contribution in the major-element compositions of oceanic basalts: Review of the experimental constraints. Lithos, 160-161: 14-36.

Le Roux, V., Nielsen, S.G., Sun, C. et al., 2016. Dating layered websterite formation in the lithospheric mantle. Earth and Planetary Science Letters, 454: 103-112.

Lee, C.-T.A., 2006. Geochemical/petrologic constraints on the origin of cratonic mantle. 164: 89-114.

Lee, C.-T.A., Cheng, X., Horodyskyj, U., 2006. The development and refinement of continental arcs by primary basaltic magmatism, garnet pyroxenite accumulation, basaltic recharge and delamination: insights from the Sierra Nevada, California. Contributions to Mineralogy and Petrology, 151(2): 222-242.

Lee, C.-T.A., Morton, D.M., Kistler, R.W. et al., 2007. Petrology and tectonics of Phanerozoic continent formation: From island arcs to accretion and continental arc magmatism. Earth and Planetary Science Letters, 263(3-4): 370-387.

Lee, C.-T.A., Anderson, D.L., 2015. Continental crust formation at arcs, the arclogite "delamination" cycle, and one origin for fertile melting anomalies in the mantle. Science Bulletin, 60(13): 1141-1156.

Lei, J., Zhao, D., Steinberger, B. et al., 2009a. New seismic constraints on the upper mantle structure of the Hainan plume. Physics of the Earth and Planetary Interiors, 173(1-2): 33-50.

Lei, N.Z., Xia, Q.K., Hao, Y.T. et al., 2009b. Water contents in peridotite xenoliths from Subei Basin, Eastern China. Earth Science-Journal of China University of Geosciences, 34: 75-88.

Leuthold, J., Blundy, J.D., Brooker, R.A., 2015. Experimental petrology constraints on the recycling of mafic cumulate: a focus on Cr-spinel from the Rum Eastern Layered Intrusion, Scotland. Contributions to Mineralogy and Petrology, 170:12.

Li, S., Xiao, Y., Liou, D. et al., 1993. Collision of the North China and Yangtse Blocks and formation of coesite-bearing eclogites: Timing and processes. Chemical Geology, 109(1): 89-111.

Li, X.-H., Li, W.-X., Li, Z.-X. et al., 2009. Amalgamation between the Yangtze and Cathaysia Blocks in South China: Constraints from SHRIMP U–Pb zircon ages, geochemistry and Nd–Hf isotopes of the Shuangxiwu volcanic rocks. Precambrian Research, 174(1-2): 117-128.

Li, X.Y., Zheng, J.P., Ma, Q. et al., 2014. From enriched to depleted mantle: Evidence from Cretaceous lamprophyres and Paleogene basaltic rocks in eastern and central Guangxi Province, western Cathaysia block of South China. Lithos, 184-187: 300-313.

Li, Z.-X., Zhang, L.-H., Powell, C.M., 1995. South China in Rodinia: Part of the missing link between Australia–East Antarctica and Laurentia? Geology, 23(5): 407-410.

Li, Z.-X., Li, X.-H., 2007. Formation of the 1300-km-wide intracontinental orogen and postorogenic magmatic province in Mesozoic South China: A flat-slab subduction model. Geology, 35(2): 179-182.

Li, Z.-X., Li, X.-H., Wartho, J.-A. et al., 2010. Magmatic and metamorphic events during the early Paleozoic Wuyi-Yunkai orogeny, southeastern South China: New age constraints and pressure-temperature conditions. Geological Society of America Bulletin, 122: 772-793.

Li, Z.-X., Li, X.-H., Chung, S.-L. et al., 2012. Magmatic switch-on and switch-off along the South China continental margin since the Permian: Transition from an Andean-type to a Western Pacific-type plate boundary. Tectonophysics, 532-535: 271-290.

Li, Z.X., 1998. Tectonic history of the major east Asian lithospheric blocks since the mid-Proterozoic— A Synthesis, Mantle Dynamics and Plate Interactions in East Asia. American Geophysical Union, pp. 221-243.

Liang, Y., Elthon, D., 1990. Geochemistry and petrology of spinel lherzolite xenoliths from Xalapasco de La Joya, San Luis Potosi, Mexico: Partial melting and mantle metasomatism. Journal of Geophysical Research, 95(B10): 15859-15877.

Liang, Y., 2014. Time scales of diffusive re-equilibration in bi-mineralic systems with and without a fluid or melt phase. Geochimica et Cosmochimica Acta, 132: 274-287.

Liu, C.-Z., Liu, Z.-C., Wu, F.-Y. et al., 2012a. Mesozoic accretion of juvenile sub-continental lithospheric mantle beneath South China and its implications: Geochemical and Re–Os isotopic results from Ningyuan mantle xenoliths. Chemical Geology, 291: 186-198.

Liu, C.-Z., Wu, F.-Y., Sun, J. et al., 2012b. The Xinchang peridotite xenoliths reveal mantle replacement and accretion in southeastern China. Lithos, 150: 171-187.

Liu, D.Y., Nutman, A.P., Compston, W. et al., 1992. Remnants of ≥3800 Ma crust in the Chinese part of the Sino-Korean craton. Geology, 20(4): 339-342.

Liu, J., Rudnick, R.L., Walker, R.J. et al., 2011. Mapping lithospheric boundaries using Os isotopes of mantle xenoliths: An example from the North China Craton. Geochimica et Cosmochimica Acta, 75(13): 3881-3902.

Liu, X.M., Gao, S., Ling, W.L. et al., 2006. Identification of 3.5 Ga detrital zircons from Yangtze Craton in south China and the implication for Archean crust evolution. Progress in Natural Science, 16(6): 663-666.

Liu, Y., Gao, S., Lee, C. et al., 2005. Melt–peridotite interactions: Links between garnet pyroxenite and high-Mg# signature of continental crust. Earth and Planetary Science Letters, 234(1-2): 39-57.

Liu, Y., Hu, Z., Gao, S. et al., 2008. In situ analysis of major and trace elements of anhydrous minerals by LA-ICP-MS without applying an internal standard. Chemical Geology, 257(1-2): 34-43.

Lovering, J.F., White, A.J.R., 1969. Granulitic and eclogitic inclusions from basic pipes at Delegate, Australia. Contributions to Mineralogy and Petrology, 21(1): 9-52.

Lu, F.X., Zheng, J.P., Li, W.P. et al., 2000. The main evolution pattern of Phanerozoic mantle in the Eastern China: the "Mushroom Cloud" model. Earth Science Frontiers, 7(1): 97-107.

Lu, J., Zheng, J., Griffin, W.L. et al., 2013. Petrology and geochemistry of peridotite xenoliths from the Lianshan region: Nature and evolution of lithospheric mantle beneath the lower Yangtze block. Gondwana Research, 23(1): 161-175.

Ludwig, K.R., 2003. User’s Manual for Isoplot 3.0: A Geochronological Toolkit for Microsoft Excel, Berkeley Geochronology Center, Special Publication, Berkeley.

Mallik, A., Dasgupta, R., 2012. Reaction between MORB-eclogite derived melts and fertile peridotite and generation of ocean island basalts. Earth and Planetary Science Letters, 329-330: 97-108.

Marchesi, C., Garrido, C. J., Bosch, D., et al., 2012. A late Oligocene suprasubduction setting in the Westernmost Mediterranean revealed by intrusive pyroxenite dikes in the Ronda Peridotite (Southern Spain). The Journal of Geology, 120 (2): 237-247.

Marchesi, C., Garrido, C.J., Bosch, D. et al., 2013. Mantle refertilization by melts of crustal-derived garnet pyroxenite: Evidence from the Ronda peridotite massif, southern Spain. Earth and Planetary Science Letters, 362: 66-75.

Martin, A.P., Price, R.C., Cooper, A.F. et al., 2015. Petrogenesis of the rifted Southern Victoria Land Lithospheric Mantle, Antarctica, inferred from petrography, geochemistry, thermobarometry and oxybarometry of peridotite and pyroxenite xenoliths from the Mount Morning Eruptive Centre. Journal of Petrology, 56(1): 193-226.

Matsumoto, T., Honda, M., McDougall, I. et al., 2000. Noble gases in pyroxenites and metasomatised peridotites from the Newer Volcanics, southeastern Australia: implications for mantle metasomatism. Chemical Geology, 168(1-2): 49-73.

APPENDICES

Table 3-1 Major-element compositions of Chinese standards GBW07102 and GBW07113 measured in this thesis and reference values by XRF

Sample ID	GBW07102			GBW07113		
	Measured	Reference	RE%	Measured	Reference	RE%
SiO_2	38.72	37.75	2.6	72.58	72.78	0.3
TiO_2	0.01	0.00		0.29	0.3	3.3
Al_2O_3	0.19	0.21	7.6	12.99	12.96	0.2
Fe_2O_3	7.12	7.04	1.1	3.19	3.21	0.6
MnO	0.11	0.10	15.5	0.14	0.14	0.0
MgO	38.66	38.34	0.8	0.15	0.16	6.3
CaO	1.95	1.98	1.6	0.58	0.59	1.7
Na_2O	0.03	0.03	10.7	2.58	2.57	0.4
K_2O	0.01	0.00		5.46	5.43	0.6
P_2O_5	0.01	0.00		0.04	0.05	20.0
LOI	14.02	14.02	0.0	1.55	1.71	
Total	100.82	99.48	1.4	100.82	99.477	1.4

RE: relative error between measured and reference values.

Table 3-2 Trace element analysis of USGS basalt (BHVO-2 and BCR-2) and Chinese national standards (GSR-1)

	BHVO-2 (n=7)			BCR-2 (n=5)			GSR-1 (n=3)		
	Measured	Reference	RE(%)	Measured	Reference	RE(%)	Measured	Reference	RE(%)
Li	4.34	4.50	3.56	9.05	9.13	0.82	138	131	4.97
Be	0.91	1.08	15.43	1.85	2.17	14.93	13.1	12.4	5.84
Sc	30.6	31.8	3.86	32.7	33.5	2.41	6.50	6.10	6.53
V	321	318	0.88	425	418	1.86	23.3	24.0	2.84
Cr	286	287	0.42	16.1	15.9	1.78	2.63	1.45	81.33
Co	44.6	44.9	0.65	37.8	37.3	1.27	2.80	3.40	17.76
Ni	122	120	1.84	12.4	12.6	1.07	1.48	0.98	51.22
Cu	131	129	1.31	19.0	19.7	3.22	2.52	2.87	12.12
Zn	99.5	104	4.23	129	130	0.16	25.6	25.0	2.34
Ga	20.9	21.4	2.20	22.0	22.1	0.47	19.5	19.0	2.43
Rb	8.90	9.26	3.90	46.9	46.0	1.87	464	466	0.51
Sr	400	394	1.50	345	337	2.39	112	106	5.53
Y	26.1	25.9	0.73	36.7	36.1	1.84	69.5	67.6	2.78
Zr	165	171	3.62	180	187	3.50	177	167	6.28
Nb	18.2	18.1	0.55	12.3	12.4	0.75	43.2	43.5	0.59
Ba	132	131	0.84	686	684	0.36	333	343	2.85
La	15.4	15.2	1.32	25.6	25.1	2.19	53.5	54.0	1.00
Ce	37.4	37.5	0.35	53.9	53.1	1.42	107	108	0.77
Pr	5.32	5.34	0.36	6.85	6.83	0.35	12.3	12.7	2.99
Nd	24.2	24.3	0.29	28.7	28.3	1.62	44.0	47.0	6.31
Sm	6.15	6.02	2.11	6.73	6.55	2.82	9.75	9.70	0.52
Eu	2.05	2.04	0.34	2.02	1.99	1.81	0.86	0.85	1.10
Gd	6.21	6.21	0.05	6.89	6.81	1.17	9.17	9.30	1.37
Tb	0.93	0.94	0.98	1.06	1.08	1.56	1.59	1.65	3.44
Dy	5.17	5.28	2.08	6.27	6.42	2.44	10.1	10.2	1.41
Ho	0.95	0.99	3.91	1.29	1.31	2.00	2.09	2.05	1.81
Er	2.44	2.51	2.83	3.64	3.67	0.75	6.69	6.50	2.92
Tm	0.33	0.33	1.46	0.54	0.53	1.06	1.12	1.06	5.28
Yb	1.90	1.99	4.71	3.27	3.39	3.69	7.75	7.40	4.72
Lu	0.27	0.28	1.96	0.50	0.50	0.64	1.18	1.15	2.93
Hf	4.32	4.47	3.36	4.84	4.97	2.64	6.16	5.86	5.14
Ta	1.14	1.15	1.21	0.75	0.79	4.69	7.32	7.20	1.64
Pb	1.76	1.65	6.47	11.0	10.6	4.21	33.5	31.0	8.21
Th	1.18	1.22	3.59	5.90	5.83	1.18	56.3	54.0	4.28
U	0.41	0.41	0.49	1.72	1.68	2.15	21.3	19.0	12.14

Recommended values are from http://georem.mpch-mainz.gwdg.de/sample_query_pref.asp.

Table 3-3 Trace-element compositions of USGS BCR-2G, BHVO-2, BIR-1G and natural Mongol garnet measured in this thesis and their recommended values.

	USGS basalt BCR-2G						USGS BHVO-2				USGS BIR-1G				Mongol garnet			
Element	Reference	1 σ	Average (GAU)	1 σ	Average (GPRM)	1 σ	Reference	1 σ	Average (GPRM)	1 σ	Reference	1 σ	Average (GPRM)	1 σ	Reference	1 σ	Average (GAU)	1 σ
ppm			n=47		n=30				n=29				n=31				n=36	
Li	9	1	9.94	0.24	9.09	0.26	4.5	0.085	4.36	0.23	3	0.7	3.18	0.20			0.43	0.10
Be	2.3	0.4	2.21	0.18	2.58	0.53	1.076	0.046	1.28	0.24	0.1		0.13	0.12			0.06	0.01
B	6	1	7.95	2.47	6.07	0.29	2.95	0.26	3.98	0.80	n.d.		2.00	1.19			2.87	2.91
Sc	33	2	33.78	1.54	33.71	1.24	31.83	0.34	32.16	0.81	43	3	43.99	1.35	43	3	46.42	1.55
Ti	14100	1000	14076	370	13958	212	16386	108	16522	217	5400	200	5713	99			3939	127
V	425	18	430	4.7	425	4.4	318.2	2.3	318.70	3.50	326	32	322.94	4.35	164	5	168.28	5.14
Cr	17	2	15.02	0.57	15.58	2.11	287.2	3.1	292.61	8.25	392	24	399.18	11.02			81.72	4.96
Co	38	2	37.44	0.53	36.76	0.87	44.89	0.32	45.01	0.88	52	5	53.31	1.35	74	4	78.89	1.72
Ni	13	2	11.65	0.34	11.57	1.10	119.8	1.2	121.15	3.56	178	18	176.65	4.76	28	4	30.02	0.87
Cu	21	5	17.77	0.85	17.04	0.70	129.3	1.4	129.52	2.82	119	12	122.75	4.23			0.19	0.12
Zn	125	5	144	5.6	134.50	4.41	103.9	1	104.05	3.40	78	17	72.35	3.23			48.88	1.88
Ga	23	1	22.86	0.60	32.66	14.73	21.37	0.2	21.34	1.25	15	2	13.81	2.81	10	1	10.46	0.32
Rb	47	0.5	50.78	0.95	47.44	0.84	9.261	0.096	9.35	0.38	0.197	0.007	0.21	0.08			0.06	0.04
Sr	342	4	346.31	4.54	344.23	5.37	394.1	1.7	402.10	6.63	109	2	109.65	2.07	0.5	0.2	0.46	0.04
Y	35	3	34.09	0.84	35.09	1.45	25.91	0.28	25.70	1.08	14.3	1.4	15.35	0.73	67	3	63.22	1.79
Zr	184	15	191.09	3.59	187.00	6.94	171.2	1.3	171.49	7.14	14	1.2	14.35	0.96	71	4	69.81	3.99
Nb	12.5	1	13.29	0.20	12.78	0.46	18.1	0.2	18.44	0.50	0.52	0.04	0.53	0.08			0.09	0.23
Ba	683	7	681	8.7	690	11.6	130.9	1	132.45	3.18	6.5	0.07	6.49	0.73			0.05	0.11
La	24.7	0.3	24.57	0.42	25.11	0.58	15.2	0.08	15.26	0.55	0.609	0.02	0.63	0.08			0.02	0.02
Ce	53.3	0.5	51.91	0.84	54.06	0.95	37.53	0.19	37.88	0.88	1.89	0.04	1.93	0.12	0.3	0.1	0.29	0.03
Pr	6.7	0.4	6.89	0.15	6.93	0.21	5.339	0.028	5.28	0.17	0.37	0.02	0.38	0.05			0.14	0.04
Nd	28.9	0.3	29.50	0.63	29.24	1.26	24.27	0.25	24.82	1.22	2.37	0.03	2.51	0.37	1.6	0.3	1.67	0.14
Sm	6.59	0.07	6.61	0.25	6.68	0.41	6.023	0.057	6.26	0.46	1.09	0.02	1.10	0.17	1.9	0.6	1.85	0.16
Eu	1.97	0.02	1.96	0.08	1.98	0.13	2.043	0.012	2.11	0.15	0.517	0.005	0.54	0.06	1.1	0.2	1.13	0.07
Gd	6.44	0.06	6.42	0.26	6.76	0.42	6.207	0.038	6.33	0.47	1.85	0.02	1.91	0.26	5.2	0.7	5.25	0.31
Tb	1.02	0.08	0.96	0.04	1.05	0.09	0.9392	0.006	0.92	0.07	0.35	0.04	0.36	0.04			1.22	0.08
Dy	6.44	0.06	6.30	0.24	6.49	0.36	5.28	0.028	5.38	0.36	2.55	0.02	2.62	0.24	10.3	0.5	10.42	0.51
Ho	1.27	0.08	1.29	0.05	1.29	0.11	0.9887	0.0053	0.99	0.07	0.56	0.03	0.58	0.06	2.4	0.1	2.42	0.14
Er	3.7	0.04	3.53	0.14	3.75	0.27	2.511	0.014	2.58	0.19	1.7	0.02	1.77	0.17	6.8	0.7	6.93	0.38
Tm	0.51	0.04	0.50	0.03	0.54	0.06	0.3349	0.0031	0.33	0.04	0.24	0.03	0.26	0.04			0.91	0.06
Yb	3.39	0.03	3.39	0.14	3.47	0.36	1.994	0.027	2.04	0.22	1.64	0.03	1.68	0.20	5.6	0.5	5.67	0.35
Lu	0.503	0.005	0.50	0.03	0.51	0.08	0.2754	0.0024	0.28	0.05	0.248	0.009	0.26	0.03	0.69	0.08	0.72	0.04
Hf	4.84	0.28	5.01	0.19	4.91	0.42	4.47	0.025	4.45	0.31	0.57	0.03	0.59	0.12	1.2	0.2	1.25	0.13
Ta	0.78	0.06	0.78	0.04	0.80	0.07	1.154	0.019	1.19	0.11	0.036	0.006	0.04	0.02			0.01	0.01
Pb	11	1	10.49	0.56	10.96	0.51	1.653	0.038	1.92	0.14	3.7	0.3	3.72	0.25			0.05	0.04
Th	5.9	0.3	6.06	0.20	6.01	0.15	1.224	0.016	1.22	0.12	0.03	0.002	0.03	0.01			0.02	0.03
U	1.69	0.12	1.82	0.10	1.72	0.08	0.412	0.035	0.42	0.04	0.023	0.006	0.02	0.02			0.01	0.01

Recommended values for USGS basalts are from http://georem.mpch-mainz.gwdg.de/sample_query_pref.asp ; Recommended values for Mongol garnet are from Norman et al. (1996).

Table 4-1 Microstructure and modal of the Lianshan xenoliths from the Yangtze craton

Type	Sample	Rock	microstructure	Mg# in Ol	Cr# in Sp	F(%)	Modal(%)			
							Ol	Opx	Cpx	Sp
	LS0907	Spinel lherzolite	porphyroclastic	89.5	10.6	1.6	60.3	28.3	9.9	1.7
	LS0909	Spinel lherzolite	porphyroclastic	89.7	11.9	2.7	62.2	26.2	10.3	1.6
	LS0920	Spinel lherzolite	porphyroclastic	89.5	10.4	1.4	59.0	30.4	9.0	2.0
Type 2	LS0922	Spinel lherzolite	porphyroclastic	88.4	9.8		58.3	29.0	10.6	2.5
	LS0927	Spinel lherzolite	porphyroclastic	89.4	8.6		49.6	33.3	15.1	2.4
	LS0926	Spinel lherzolite	porphyroclastic	89.0	15.8	5.5				
	LS0929	Websterite	coarse		11.0	1.9				
	LS0902	Spinel lherzolite	fine-grained	91.0	23.5	9.5	71.2	22.6	6.2	0.3
Type 1	LS0906	Spinel harzburgite	coarse	90.8	43.6	15.7	70.5	27.1	1.8	1.0
	LS0910	Spinel harzburgite	coarse	91.6	43.0	15.6	67.4	29.0	3.4	0.4

$Mg^{\#}$=molar 100*Mg/(Mg+Fe); $Cr^{\#}$= molar 100*Cr/(Cr+Al); F(%), calcultated after the method of Hellebrand et al. (2001). Ol=olivine; Opx=orthopyroxene; Cpx=clinopyroxene; Sp=spinel.

Table 4-2 LA-ICPMS analyses (wt%) of minerals from the Lianshan peridotite xenoliths

Type	Type 2																			
Sample	LS0907				LS0909				LS0920				LS0922				LS0927			
Mineral	Ol	Opx	Cpx	Sp	Ol	Opx	Cpx	Sp	Ol	Opx	Cpx	Sp	Ol	Opx	Cpx	Sp	Ol	Opx	Cpx	Sp
SiO_2	39.3	53.8	50.2	0.25	39.6	54.4	50.3	0.22	39.6	54.6	50.8	0.23	39.7	54.5	50.4	0.23	39.2	54.6	50.3	0.16
TiO_2	0.00	0.13	0.54	0.12	0.00	0.11	0.54	0.08	0.00	0.12	0.50	0.06	0.00	0.11	0.62	0.07	0.00	0.13	0.63	0.06
Al_2O_3	0.01	4.84	6.88	55.5	0.00	4.18	6.97	54.2	0.01	4.42	6.50	54.21	0.01	4.14	7.05	55.81	0.00	4.44	7.13	56.95
Cr_2O_3	0.01	0.39	0.00	9.83	0.00	0.36	0.98	10.9	0.00	0.39	0.00	9.39	0.00	0.31	0.00	9.04	0.00	0.32	0.00	8.00
FeO	10.5	6.62	2.83	11.9	10.2	6.69	2.59	12.8	10.5	6.75	2.63	13.1	11.4	7.25	2.73	13.1	10.6	6.94	2.61	12.4
MnO	0.15	0.15	0.09	0.11	0.15	0.16	0.09	0.11	0.15	0.16	0.09	0.11	0.16	0.17	0.09	0.11	0.15	0.16	0.09	0.11
MgO	49.5	33.2	15.6	21.6	49.6	33.4	14.9	21.0	49.3	32.5	15.1	22.2	48.3	32.8	14.7	20.9	49.6	32.7	14.6	21.5
CaO	0.05	0.67	21.0	b.d.	0.03	0.52	21.3	b.d.	0.02	0.85	21.5	b.d.	0.04	0.53	21.4	b.d.	0.01	0.55	21.7	b.d.
Na_2O	0.01	0.11	1.88	b.d.	0.00	0.07	2.16	b.d.	0.00	0.10	2.01	b.d.	0.00	0.08	2.15	b.d.	0.00	0.08	2.08	b.d.
NiO	0.39	0.09	0.04	0.41	0.40	0.08	0.03	0.41	0.38	0.08	0.04	0.45	0.39	0.08	0.03	0.45	0.39	0.08	0.04	0.45
Total	99.9	100.0	99.1	99.8	100.0	100.0	99.9	99.3	100.0	100.0	99.1	99.7	100.0	100.0	99.1	99.7	100.0	100.0	99.2	99.7
[O]	4	6	6	4	4	6	6	4	4	6	6	4	4	6	6	4	4	6	6	4
Si	0.972	1.868	1.832	0.007	0.977	1.886	1.835	0.006	0.978	1.895	1.852	0.006	0.983	1.893	1.839	0.006	0.970	1.894	1.835	0.004
Ti	0.000	0.003	0.015	0.002	0.000	0.003	0.015	0.002	0.000	0.003	0.014	0.001	0.000	0.003	0.017	0.001	0.000	0.003	0.017	0.001
Al	0.000	0.198	0.296	1.710	0.000	0.171	0.300	1.684	0.000	0.181	0.280	1.682	0.000	0.170	0.303	1.726	0.000	0.181	0.307	1.749
Cr	0.000	0.011	0.024	0.203	0.000	0.010	0.028	0.226	0.000	0.011	0.022	0.195	0.000	0.009	0.022	0.187	0.000	0.009	0.021	0.165
Fe	0.217	0.192	0.086	0.261	0.210	0.194	0.079	0.282	0.216	0.196	0.080	0.287	0.236	0.211	0.083	0.288	0.218	0.201	0.080	0.271
Mn	0.003	0.004	0.003	0.002	0.003	0.005	0.003	0.003	0.003	0.005	0.003	0.003	0.003	0.005	0.003	0.002	0.003	0.005	0.003	0.002
Mg	1.825	1.716	0.850	0.840	1.822	1.728	0.813	0.826	1.816	1.678	0.822	0.871	1.784	1.700	0.800	0.816	1.829	1.688	0.796	0.837
Ca	0.001	0.025	0.819	0.000	0.001	0.019	0.835	0.000	0.001	0.032	0.839	0.000	0.001	0.020	0.836	0.000	0.000	0.020	0.849	0.000
Na	0.000	0.007	0.133	0.000	0.000	0.005	0.153	0.000	0.000	0.007	0.142	0.000	0.000	0.005	0.152	0.000	0.000	0.005	0.147	0.000
Ni	0.008	0.003	0.001	0.009	0.008	0.002	0.001	0.009	0.008	0.002	0.001	0.009	0.008	0.002	0.001	0.010	0.008	0.002	0.001	0.009
Sum	3.03	4.03	4.06	3.03	3.02	4.02	4.06	3.04	3.02	4.01	4.05	3.05	3.02	4.02	4.06	3.04	3.03	4.01	4.06	3.04
$Mg^{\#}$	89.5	90.0	90.9	76.5	89.7	90.0	91.2	74.7	89.5	89.6	91.2	75.4	88.4	89.1	90.6	74.1	89.4	89.4	91.0	75.7
$Cr^{\#}$			7.5	10.6			8.6	11.9			7.4	10.4			6.8	9.8			6.4	8.6

Continued

Type	Type 2							Type 1											
Sample	LS0926				LS0929			LS0902				LS0906				LS0910			
Mineral	Ol	Opx	Cpx	Sp	Opx	Cpx	Sp	Ol	Opx	Cpx	Sp	Ol	Opx	Cpx	Sp	Ol	Opx	Cpx	Sp
SiO_2	39.0	53.8	48.4	0.1	53.5	49.5	0.27	39.4	55.2	51.8	0.06	39.9	56.4	52.3	0.19	39.7	55.7	52.3	0.17
TiO_2	0.01	0.29	1.58	0.44	0.08	0.42	0.08	0.00	0.04	0.17	0.02	0.00	0.04	0.10	0.12	0.00	0.03	0.08	0.11
Al_2O_3	0.01	4.09	6.46	49.97	5.41	7.38	55.39	0.00	3.13	4.45	46.5	0.00	2.19	2.77	31.5	0.01	2.16	3.26	31.6
Cr_2O_3	0.01	0.40	0.00	13.95	0.48	0.00	10.16	0.00	0.50	0.00	21.3	0.01	0.54	0.00	36.3	0.01	0.51	0.00	35.5
FeO	11.00	7.23	3.15	14.76	6.92	3.16	12.7	9.11	6.05	1.98	11.7	9.22	5.92	2.08	15.4	8.47	5.40	2.34	14.8
MnO	0.17	0.18	0.10	0.14	0.16	0.10	0.12	0.13	0.14	0.06	0.10	0.13	0.14	0.08	0.16	0.12	0.13	0.07	0.15
MgO	49.3	33.2	15.9	19.9	32.6	14.9	20.5	50.9	34.3	15.8	19.6	50.3	34.1	16.8	15.7	51.2	35.3	17.2	17.1
CaO	0.05	0.61	21.64	b.d.	0.54	21.4	b.d.	b.d.	0.49	22.4	b.d.	0.02	0.53	23.5	b.d.	0.03	0.59	21.5	b.d.
Na_2O	0.00	0.09	1.41	b.d.	0.09	1.84	b.d.	0.00	0.09	2.01	b.d.	0.00	0.04	1.03	b.d.	0.01	0.10	1.82	b.d.
NiO	0.39	0.09	0.04	0.39	0.12	0.05	0.52	0.40	0.08	0.03	0.26	0.39	0.09	0.04	0.15	0.41	0.10	0.04	0.17
Total	99.57	99.86	98.9	99.6	100.0	98.9	99.8	100.0	100.0	98.7	99.6	100.0	100.0	98.7	99.6	100.0	100.0	98.5	99.7
[O]	4	6	6	4	6	6	4	4	6	6	4	4	6	6	4	4	6	6	4
Si	0.967	1.874	1.783	0.004	1.860	1.814	0.007	0.968	1.908	1.890	0.002	0.979	1.946	1.911	0.006	0.973	1.922	1.907	0.005
Ti	0.000	0.008	0.044	0.009	0.002	0.012	0.002	0.000	0.001	0.005	0.000	0.000	0.001	0.003	0.003	0.000	0.001	0.002	0.002
Al	0.000	0.168	0.280	1.590	0.222	0.319	1.714	0.000	0.127	0.192	1.492	0.000	0.089	0.119	1.093	0.000	0.088	0.140	1.090
Cr	0.000	0.011	0.029	0.298	0.013	0.031	0.211	0.000	0.014	0.036	0.459	0.000	0.015	0.037	0.845	0.000	0.014	0.036	0.822
Fe	0.228	0.211	0.097	0.333	0.201	0.097	0.280	0.187	0.175	0.060	0.266	0.189	0.171	0.063	0.379	0.173	0.156	0.072	0.362
Mn	0.004	0.005	0.003	0.003	0.005	0.003	0.003	0.003	0.004	0.002	0.002	0.003	0.004	0.002	0.004	0.003	0.004	0.002	0.004
Mg	1.824	1.725	0.874	0.799	1.690	0.816	0.802	1.866	1.767	0.858	0.796	1.841	1.753	0.916	0.690	1.868	1.816	0.935	0.748
Ca	0.001	0.023	0.853	0.000	0.020	0.841	0.000	0.000	0.018	0.877	0.000	0.001	0.019	0.919	0.000	0.001	0.022	0.840	0.000
Na	0.000	0.006	0.101	0.000	0.006	0.131	0.000	0.000	0.006	0.142	0.000	0.000	0.003	0.073	0.000	0.000	0.007	0.128	0.000
Ni	0.008	0.003	0.001	0.008	0.003	0.002	0.011	0.008	0.002	0.001	0.006	0.008	0.002	0.001	0.004	0.008	0.003	0.001	0.004
Sum	3.03	4.03	4.07	3.04	4.02	4.06	3.03	3.03	4.02	4.06	3.02	3.02	4.00	4.04	3.02	3.03	4.03	4.06	3.04
$Mg^{\#}$	89.0	89.2	90.1	70.8	89.5	89.5	74.3	91.0	91.1	93.5	75.1	90.8	91.2	93.6	64.8	91.6	92.2	93.0	67.6
$Cr^{\#}$			9.3	15.8		8.7	11.0			15.7	23.5			23.4	43.6			20.4	43.0

b.d.= below detection limit.

Table 4-3 Trace element compositions of olivines in the Lianshan xenoliths (ppm)

Type	Type 2					Type 1			
Sample	LS0907	LS0909	LS0920	LS0922	LS0927	LS0926	LS0902	LS0906	LS0910
Li	1.54	1.80	1.57	1.98	1.82	4.36	1.69	1.46	2.28
Sc	2.34	1.66	1.49	1.36	1.50	2.37	1.53	2.08	2.53
V	3.38	1.25	1.21	1.23	2.10	2.39	0.98	1.28	1.88
Cr	60.6	18.2	14.1	19.0	13.5	48.7	18.1	39.5	93.0
Co	148	149	144	149	148	150	143	144	139
Ni	3080	3138	3024	3081	3056	3068	3137	3071	3187
Zn	51.2	37.2	36.2	40.6	33.4	65.5	0.8	40.7	44.5

Table 4-4 Trace element compositions of orthopyroxenes in the Lianshan xenoliths (ppm)

Type	Type 2							Type 1		
Sample	LS0907	LS0909	LS0920	LS0922	LS0927	LS0926	LS0929	LS0902	LS0906	LS0910
Li	2.21	4.64	2.92	4.34	5.12	21.19	13.94	4.70	7.05	6.01
Sc	17.2	15.6	15.6	13.9	14.6	17.6	14.2	17.0	19.3	15.2
V	100.0	86.8	99.4	87.4	93.5	106.6	78.2	88.2	64.5	56.4
Cr	2696	2485	2678	2148	2214	2740	3306	3438	3674	3461
Co	57.5	54.7	54.0	55.3	56.2	59.2	65.3	51.8	54.9	56.3
Ni	742	656	659	655	667	723	935	616	679	762
Cu	0.75	0.64	0.41	b.d.	23.4	13.4	11.3	25.9	0.69	1.78
Zn	30.4	23.7	24.0	25.4	3.1	41.0	23.3	2.1	27.9	28.8
Ga	3.54	2.75	3.16	3.21	0.19	4.77	5.50	0.91	1.61	1.33
Sr	0.14	0.08	b.d.	0.38	b.d.	b.d.	0.24	b.d.	0.08	1.12
Zr	1.56	0.93	1.31	b.d.	1.59	5.30	1.41	1.22	b.d.	b.d.
Y	1.19	0.73	1.13	0.81	0.96	2.07	0.93	0.29	0.20	0.27
Ho	b.d.	0.04	0.04	0.07	0.06	0.07	0.05	b.d.	0.02	0.03
Er	0.16	b.d.	0.20	0.18	0.14	0.35	0.19	b.d.	b.d.	0.10
Yb	0.27	0.20	0.25	0.44	0.31	0.51	0.36	b.d.	b.d.	0.22
Lu	0.04	0.05	0.03	0.04	0.05	0.09	0.04	b.d.	b.d.	0.03

Table 4-5 Trace element compositions of clinopyroxenes in the Lianshan xenoliths (ppm)

Type	Type 2							Type 1			
Sample	LS0907	LS0909	LS0920	LS0922	LS0927	LS0926-core	LS0926-rim	LS0929	LS0902	LS0906	LS0910
Li	3.43	5.35	2.72	3.93	5.25	22.1	6.14	5.55	5.43	6.64	4.03
Sc	72.6	80.2	70.5	75.3	74.4	82.7	89.8	55.7	86.3	91.2	98.7
V	271	277	270	276	279	331	355	205	266	201	213
Cr	5700	6702	5322	5247	4961	6739	6771	7210	8473	8649	8522
Co	20.1	17.1	16.9	16.2	17.1	20.0	19.8	22.3	14.4	18.4	18.7
Ni	330	271	278	265	278	317	286	413	240	309	338
Cu	1.18	0.96	0.81	0.93	0.75	6.80	2.64	12.8	1.30	1.77	4.30
Zn	7.82	5.31	5.00	5.90	3.88	9.17	10.7	5.13	4.47	5.84	7.84
Ga	3.95	4.02	3.57	3.83	3.92	6.38	8.28	6.25	2.25	1.67	3.54
Rb	b.d.	b.d.	b.d.	b.d.	b.d.	0.18	4.76	0.11	0.08	b.d.	0.10
Ba	0.16	b.d.	b.d.	b.d.	b.d.	0.02	2.57	b.d.	4.40	b.d.	63.0
Th	0.05	0.02	0.04	0.00	0.01	0.01	0.06	0.04	2.30	0.21	4.68
U	0.02	0.01	0.02	0.05	0.00	0.01	0.06	0.01	0.87	0.12	1.09
Nb	0.29	0.09	0.23	0.31	0.08	0.10	1.58	0.18	0.07	0.52	1.76
Ta	0.03	b.d.	0.05	b.d.	b.d.	0.01	0.08	0.01	b.d.	0.07	0.05
La	1.08	0.62	1.02	1.58	0.85	0.54	1.41	0.38	4.96	2.45	34.0
Ce	3.60	2.84	2.70	4.54	3.62	5.10	6.75	1.85	9.60	4.89	54.1
Pb	0.05	b.d.	0.03	0.25	b.d.	0.08	0.14	0.11	1.18	0.48	0.80
Pr	0.66	0.60	0.49	0.75	0.75	1.55	1.76	0.39	1.07	0.71	4.66
Sr	74.3	67.5	48.7	87.8	73.6	27.4	42.2	37.9	126	49.8	889
Nd	4.01	3.83	3.14	4.03	4.78	12.2	13.3	2.69	3.81	3.31	13.6
Zr	31.5	31.8	24.0	39.0	38.7	158	166	16.5	23.1	6.34	5.43
Hf	1.04	0.95	0.83	1.11	1.07	4.65	4.82	0.54	0.68	0.12	0.26
Sm	1.82	1.65	1.67	1.75	1.93	5.97	6.57	1.52	1.03	1.08	1.87
Eu	0.67	0.63	0.67	0.84	0.84	2.20	2.52	0.71	0.46	0.36	0.59
Gd	2.83	2.30	2.37	3.42	3.14	8.41	9.50	2.65	1.71	1.02	1.87
Tb	0.52	0.48	0.41	0.55	0.60	1.51	1.61	0.44	0.21	0.12	0.19
Dy	3.47	3.43	3.29	3.94	3.86	10.2	10.7	3.37	1.49	0.93	1.05
Y	21.1	19.7	18.9	22.6	24.2	53.1	57.3	19.3	8.05	4.22	6.24
Ho	0.77	0.74	0.74	0.81	0.91	2.06	2.21	0.72	0.31	0.14	0.24
Er	2.35	2.23	2.14	2.47	3.01	5.84	6.03	2.20	0.91	0.44	0.61
Tm	0.31	0.32	0.31	0.41	0.39	0.80	0.83	0.32	0.13	0.09	0.11
Yb	2.16	2.13	2.17	2.32	2.39	4.48	4.79	1.94	0.89	0.46	0.50
Lu	0.33	0.32	0.30	0.38	0.37	0.61	0.66	0.27	0.13	0.07	0.11

Table 4-6 Trace element compositions of spinels in the Lianshan xenoliths (ppm)

Type	Type 2							Type 1		
Sample	LS0907	LS0909	LS0920	LS0922	LS0927	LS0926	LS0929	LS0902	LS0906	LS0910
Sc	0.43	b.d.	0.33	0.76	0.23	0.52	0.64	0.94	1.78	1.33
V	400	409	374	369	364	621	314	587	922	785
Cr	67264	74330	64266	61827	54744	95423	69544	145879	248505	243202
Co	253	318	323	322	319	277	292	338	311	272
Ni	3208	3240	3513	3566	3517	3044	4098	2065	1217	1339
Cu	2.24	2.01	1.86	2.18	2.05	50.07	35.95	b.d.	4.68	7.24
Zn	885	1409	1288	1349	1249	1498	1308	1991	1308	1028
Ga	80.8	84.2	84.3	90.8	82.4	127.7	39.5	57.1	39.5	36.1

Table 4-7 Major element compositions of the whole rocks from the Lianshan peridotite xenoliths (wt%)

Type	Type 2					Type 1		
Sample	LS0907	LS0909	LS0920	LS0922	LS0927	LS0902	LS0906	LS0910
SiO_2	43.6	43.8	44.3	44.0	45.0	43.0	44.1	44.2
TiO_2	0.11	0.09	0.10	0.13	0.15	0.03	0.03	0.03
Al_2O_3	2.99	2.70	3.02	3.34	3.88	1.11	0.95	0.85
Fe_2O_3	8.67	9.00	8.89	9.16	8.54	8.48	8.27	7.78
MnO	0.12	0.12	0.12	0.13	0.12	0.11	0.11	0.11
MgO	40.8	41.2	40.6	39.5	38.0	44.3	44.9	44.9
CaO	2.59	2.07	2.18	2.72	3.33	1.12	0.91	0.85
Na_2O	0.27	0.25	0.24	0.31	0.34	0.12	0.11	0.14
K_2O	0.02	0.03	0.01	0.02	0.01	0.05	0.01	0.01
P_2O_5	0.01	0.01	0.01	0.01	0.01	0.01	0.00	0.02
LOI	0.37	0.48	0.68	0.31	0.36	1.20	0.22	0.68
Total	99.6	99.7	100.1	99.6	99.7	99.5	99.6	99.5
$Mg^{\#}$	90.3	90.1	90.0	89.5	89.8	91.2	91.5	92.0

Table 4-8 Trace element compositions of the whole rocks from the Lianshan peridotite xenoliths (ppm)

Type	Type 2					Type 1		
Sample	LS0907	LS0909	LS0920	LS0922	LS0927	LS0902	LS0906	LS0910
Li	3.11	2.76	3.10	3.37	2.91	3.36	1.89	2.62
Sc	13.0	12.0	11.9	13.9	15.9	6.83	8.98	7.25
V	64.8	59.9	61.5	71.6	83.4	32.9	33.5	27.7
Cr	2398	2553	2193	2348	2474	1994	3408	2648
Co	117	121	124	134	132	122	119	127
Ni	1972	2006	1870	1840	1747	2208	2097	2182
Cu	22.0	16.8	16.2	24.4	28.9	5.28	2.12	4.88
Zn	51.5	52.8	49.1	53.8	50.2	46.7	44.7	42.5
Ga	4.23	6.34	3.22	4.12	4.04	1.79	1.60	3.68
Rb	0.56	0.88	0.40	0.64	0.44	0.92	0.27	0.38
Ba	0.22	0.20	0.28	0.22	0.24	2.60	1.16	2.23
Th	0.01	0.01	0.01	0.04	0.00	0.15	0.02	0.25
U	0.05	0.08	0.04	0.02	0.01	0.11	0.03	0.11
Nb	0.38	0.13	0.21	0.25	0.20	0.13	0.16	0.33
Ta	0.09	0.06	0.10	0.10	0.12	0.05	0.06	0.10
La	0.18	0.086	0.13	0.24	0.14	0.44	0.11	1.56
Ce	0.48	0.31	0.29	0.61	0.56	0.87	0.22	1.82
Pb	0.17	0.23	0.21	0.27	0.16	0.32	0.16	0.26
Pr	0.08	0.06	0.04	0.11	0.11	0.10	0.03	0.14
Sr	9.55	6.78	5.56	12.0	11.0	9.24	2.49	24.0
Nd	0.47	0.37	0.27	0.57	0.66	0.39	0.15	0.39
Zr	4.13	3.28	2.72	5.18	6.25	1.04	0.57	
Hf	0.13	0.10	0.10	0.16	0.20	0.04	0.01	0.01
Sm	0.20	0.17	0.15	0.26	0.30	0.09	0.04	0.05
Eu	0.08	0.06	0.06	0.10	0.12	0.03	0.01	0.01
Gd	0.31	0.23	0.23	0.37	0.46	0.07	0.04	0.05
Tb	0.06	0.05	0.05	0.07	0.09	0.01	0.01	0.01
Dy	0.41	0.30	0.35	0.52	0.61	0.07	0.03	0.04
Y	2.63	2.01	2.21	3.14	3.82	0.43	0.22	0.23
Ho	0.10	0.07	0.08	0.12	0.14	0.01	0.01	0.01
Er	0.30	0.22	0.24	0.33	0.41	0.05	0.03	0.03
Tm	0.05	0.04	0.05	0.06	0.07	0.01	0.00	0.01
Yb	0.27	0.24	0.27	0.34	0.42	0.05	0.04	0.04
Lu	0.05	0.04	0.04	0.05	0.07	0.01	0.01	0.01

Table 4-9 Sr and Nd isotopic data for the Lianshan peridotite xenoliths

Type	Sample	$^{87}Rb/^{86}Sr$	$^{87}Sr/^{86}Sr\pm2\sigma$	$^{147}Sm/^{144}Nd$	$^{143}Nd/^{144}Nd\pm2\sigma$	$^{87}Rb/^{86}Sr$	$\varepsilon_{Nd}(t)$	$(^{87}Sr/^{86}Sr)_i$	$(^{143}Nd/^{144}Nd)_i$
	LS0907	0.1695747	0.702789±20	0.257294479	0.513219±5	0.1695747	11.3	0.702765	0.513202
	LS0909	0.3753408	0.702701±5	0.277814261	0.513307±4	0.3753408	12.9	0.702648	0.513289
Type 2	LS0920	0.2080468	0.702775±5	0.33588492	0.512874±3	0.2080468	4.43	0.702745	0.512852
	LS0922	0.1542291	0.702578±4	0.275808907	0.513331±3	0.1542291	13.4	0.702556	0.513313
	LS0927	0.1156684	0.702279±8	0.274843244	0.513311±6	0.1156684	13.0	0.702263	0.513293
	LS0902	0.2879677	0.703997±6	0.133321356	0.512902±6	0.2879677	5.23	0.703956	0.512893
Type 1	LS0906			0.17733156	0.512499±12		-2.69	b.d.	0.512487
	LS0910	0.0457899	0.703275±5	0.085264743	0.512956±6	0.0457899	6.35	0.703268	0.512950

$^{87}Rb/^{86}Sr$ and $^{147}Sm/^{144}Nd$ ratios are calculated using Rb, Sr, Sm and Nd contents by ICP-MS and measured $^{87}Sr/^{86}Sr$ and $^{143}Nd/^{144}Nd$ ratios by TIMS; the $^{147}Sm/^{144}Nd$ and $^{143}Nd/^{144}Nd$ ratios are 0.1967 and 0.512637 for Chondrite Uniform Reservoir (CHUR), and 0.2137 and 0.51315 for depleted mantle, respectively; the $^{87}Rb/^{86}Sr$ and $^{87}Sr/^{86}Sr$ are 0.0827 and 0.7045 for CHUR; Initial isotopic ratios are calculated using 10 Ma for the basalts.

Table 4-10 Equilibration temperature estimation for the Lianshan peridotite xenoliths (°C)

Type	Sample P=1.5GPa	T(BK) Ca in Opx	T(BK) Na in Opx-Cpx	T(SS,a) Opx-Cpx	T(SS, b) Sp-Opx	T(SS, c) Sp-Opx
Type 2	LS0907	959	1001	1043	1068	789
	LS0909	905	854	992	1014	747
	LS0920	1014	972	1009	1027	924
	LS0922	909	885	979	996	805
	LS0927	915	890	1003	1016	908
	LS0926	938	1018	1016	1051	553
	LS0929	913	959			
Type 1	LS0902	892	927	912	932	533
	LS0906	906	983	936	947	832
	LS0910	928	892	912	946	

Note: T(BK), Ca in Opx thermometers, Na in Opx-Cpx thermometers, Brey and Kohler (1990).
T(SS, a), T(SS, b), T(SS, c): two-pyroxene thermometers, Sp-Opx thermometers (Fe as Fe_{Total}) and Sp-Opx thermometers (Fe as Fe^{3+}), respectively, Sachtleben and Seck (1981).

Table 5-1 Summary of petrological and geochemical data for Xilong xenoliths in this study

Type	Sample	Rock type	Microstructure	Mg#	Cr#	P(Kbar)	Te(°C)	Estimated modal abundances (wt%)			
				Ol	Sp			Ol	Opx	Cpx	Sp
Group 1	XL-01[a]	Dunite	protogranular	91.1		19.5[b]	1120[b]	98		2	
	XL-04	Harzburgite	porphyroclastic	91.5		19.5	1120	55	40	3	
	XL-37	Wehrlite	protogranular	91.3		15.0[b]	1000[b]	60		40	
	XL-61[a]	Wehrlite	sheared texture	90.9		18.7	1100	85		15	
	XL-77	Lherzolite	porphyroclastic	91.4		19.2	1115	40	45	15	
Group 2	XL-22	Sp-lherzolite	protogranular	89.8	12.7	14.6	980	75	10	13	2
	XL-25[a]	Sp-lherzolite	porphyroclastic	89.7	11.3	12.5	900	75	10	10	3
	XL-32	Sp-lherzolite	sheared texture	90.3	18.5	17.5	1070	75	15	7	3
	XL-33[a]	Sp-lherzolite	porphyroclastic	89.7	10.9	16.4	1040	65	13	20	1
	XL-40	Sp-lherzolite	porphyroclastic	90.5	17.2	13.5	940	55	10	15	15
	XL-55[a]	Sp-lherzolite	porphyroclastic	88.7	8.83	15.0	995	63	25	10	2
	XL-63[a]	Sp-lherzolite	porphyroclastic	89.4	9.48	14.8	990	50	35	10	5
	XL-78[a]	Sp-lherzolite		89.9	17.2	13.7	950				

Mg#=molar 100*Mg/(Mg+Fe); Cr#=molar 100*Cr/(Cr+Al); Ol, Olivine; Opx, orthpyroxene; Cpx, clinopyroxene; Sp, spinel.
[a] major element compositions analyzed by LA-ICPMS; the data of other samples are from EMP.
[b] T is estimated using Ol-Cpx thermometers from Köhler and Brey (1990) at different P; T from other samples is estimated by Ca-in-Opx thermometers from Brey and Köhler (1990).

Table 5-2 Representative major element analyses (wt%) of primary minerals in Xilong peridotites

Type	Group 1																			Group 2			
Sample	XL-37		XL-37[a]		XL-04			XL-04[a]			XL-77			XL-77[a]			XL-61[a]			XL-22			
Mineral	Ol 1	Cpx1	Ol 1	Cpx1	Ol 1	Opx	Cpx1	Ol 1	Opx	Cpx1	Ol 1	Opx	Cpx1	Ol 1	Opx	Cpx1	Ol 1	Opx	Cpx1	Ol 1	Opx	Cpx1	Sp1
SiO_2	40.9	52.9	39.4	51.2	41.0	55.8	53.0	39.1	54.9	50.0	41.3	56.2	53.1	39.2	54.2	51.4	39.2	54.6	52.0	41.0	54.8	51.5	0.08
TiO_2		0.09	0.00	0.10		0.03	0.06	0.00	0.03	0.05				0.00	0.01	0.02	0.00	0.03	0.06		0.12	0.52	0.18
Al_2O_3		4.10	0.02	4.25	0.04	2.48	2.59	0.02	2.61	2.68		3.45	3.38	0.02	3.72	3.54	0.02	2.82	2.77		4.75	6.68	54.7
Cr_2O_3		1.47	0.03	1.38	0.06	0.82	1.21	0.05	0.81	1.20	0.05	0.83	1.10	0.05	0.84	1.10	0.03	0.76	1.06		0.47	0.95	12.9
FeO	8.62	2.40	8.92	2.58	8.45	5.28	2.57	8.57	5.53	2.82	8.59	5.28	2.49	8.72	5.52	2.66	9.20	5.83	2.82	10.1	6.13	2.66	10.5
MnO	0.13	0.09	0.13	0.09	0.12	0.15	0.10	0.13	0.13	0.09	0.12	0.16	0.12	0.13	0.13	0.10	0.14	0.14	0.10	0.18	0.17	0.11	0.13
MgO	50.1	16.9	51.0	17.8	50.8	34.4	18.5	51.6	34.6	21.3	50.6	33.8	18.4	51.4	34.2	18.9	50.9	34.5	18.5	49.3	33.0	15.4	20.4
CaO	0.09	20.7	0.09	21.2	0.10	1.22	21.4	0.11	1.19	21.3	0.10	1.17	21.4	0.11	1.19	21.7	0.09	1.14	22.1	0.05	0.76	19.9	
Na_2O	0.05	1.15	0.01	1.23		0.05	0.52	0.01	0.05	0.43		0.06	0.37	0.01	0.03	0.39	0.01	0.03	0.43		0.11	1.81	
K_2O			0.00	0.00						0.02			0.03			0.02			0.01				
NiO	0.39	0.07	0.37	0.05	0.39	0.12	0.09	0.39	0.11	0.06	0.40	0.12	0.07	0.38	0.11	0.06	0.39	0.11	0.06	0.37	0.10	0.07	0.36
Total	100	100	100	100	100	100	100	100	100	100	101	101	100	100	100	100	100	100	100	101	100	100	99.2
Mg#	91.3	92.7	91.1	92.5	91.5	92.1	92.8	91.5	91.8	93.1	91.4	92.0	93.0	91.4	91.8	92.8	90.9	91.4	92.2	89.8	90.7	91.3	77.8
Cr#		19.4		17.9			23.9			23.0			18.0			17.3			20.4			8.74	13.7

Continued

Type	Group 2																						
Sample	XL-22[a]				XL-25[a]				XL-32				XL-32[a]				XL-33[a]				XL-40		
Mineral	Ol 1	Opx	Cpx1	Sp1	Ol 1	Opx	Cpx 1	Sp1	Ol 1	Opx	Cpx1	Sp1	Ol 1	Opx	Cpx1	Sp1	Ol 1	Opx	Cpx1	Sp1	Ol 1	Opx	Cpx1
SiO_2	38.3	52.8	49.7	0.26	39.3	55.5	51.0	0.16	41.0	54.7	51.9	0.1	39.3	55.0	50.2	0.30	38.5	53.7	49.9	0.24	41.1	55.1	52.4
TiO_2	0.00	0.13	0.49	0.16	0.00	0.10	0.44	0.06		0.24	0.75	0.50	0.01	0.22	0.71	0.48	0.01	0.14	0.55	0.18		0.03	0.09
Al_2O_3	0.02	4.98	7.14	54.1	0.00	4.02	5.85	56.0	0.04	4.91	6.55	49.3	0.03	4.77	6.61	47.7	0.03	5.17	7.30	54.4		4.13	4.47
Cr_2O_3	0.01	0.44	0.93	11.8	0.00	0.37	0.71	10.6	0.04	0.63	1.16	17.3	0.03	0.66	0.86	16.2	0.01	0.42	0.82	9.94		0.49	0.86
FeO	10.1	6.44	2.90	11.8	10.3	6.70	2.61	11.6	9.68	6.08	3.25	13.0	10.38	6.60	3.45	14.1	10.38	6.51	3.24	12.3	9.44	6.12	2.48
MnO	0.15	0.15	0.10	0.12	0.16	0.16	0.09	0.12	0.15	0.16	0.09	0.12	0.16	0.15	0.11	0.12	0.15	0.15	0.11	0.11	0.13	0.15	0.09
MgO	50.9	34.0	16.1	21.4	49.9	32.4	15.7	20.7	49.8	32.8	16.1	19.6	49.5	31.3	16.1	20.4	50.4	32.7	15.8	22.3	49.9	33.8	16.8
CaO	0.06	0.78	20.5		0.01	0.54	21.7	0.07	0.09	1.02	18.8		0.08	0.94	19.7	0.09	0.07	0.91	19.9		0.05	0.78	22.3
Na_2O	0.01	0.14	1.98		0.00	0.05	1.54			0.18	1.83		0.01	0.19	1.80		0.01	0.17	2.13			0.06	0.77
K_2O		0.04	0.00			0.01	0.00							0.01	0.01				0.00				
NiO	0.36	0.09	0.04	0.36	0.36	0.08	0.05	0.33	0.39	0.12		0.40	0.40	0.12	0.05	0.37	0.34	0.09	0.04	0.40	0.40	0.11	0.06
Total	100	100	100	100	100	100	100	100	101	101	100	100	100	100	100	100	100	100	100	100	101	101	100
Mg#	90.0	90.5	90.9	76.5	89.7	89.7	91.5	76.3	90.3	90.7	89.9	73.1	89.6	89.5	89.3	72.3	89.7	90.0	89.8	76.6	90.5	90.9	92.4
Cr#			8.03	12.7			7.57	11.3			10.6	19.0			8.04	18.51			6.99	10.9			11.4

Continued

Type	Group 2																						
Sample	XL-40	XL-40[a]				XL-55[a]				XL-63[a]				XL-78[a]				Host related minerals					
Mineral	Sp1	Ol 1	Opx	Cpx1	Sp1	Ol 1	Opx	Cpx1	Sp1	Ol 1	Opx	Cpx1	Sp1	Ol 1	Opx	Cpx1	Sp1	Sph	Sph	Olh	Olh	Olh	Cpxh
SiO_2	0.05	39.1	55.4	50.3	0.24	39.3	54.3	50.5	0.28	39.1	53.5	50.2	0.23	39.4	55.1	49.5	0.24			39.91	38.4	38.1	48.8
TiO_2	0.05	0.00	0.03	0.10	0.05	0.00	0.15	0.55	0.17	0.01	0.14	0.56	0.16	0.00	0.04	0.14	0.05	14.2	10.3		0.03	0.06	2.58
Al_2O_3	51.9	0.01	3.85	4.63	49.1	0.03	5.52	7.28	56.2	0.01	5.32	7.37	56.6	0.01	4.04	5.66	50.1	6.72	12.0				3.12
Cr_2O_3	17.2	0.01	0.46	0.86	15.2	0.01	0.37	1.18	8.12	0.01	0.34	0.73	8.83	0.01	0.53	1.18	15.5	9.30	11.7	0.04			
FeO	10.3	10.4	6.62	2.81	14.5	11.2	6.98	3.35	12.4	10.6	6.62	3.06	11.3	10.1	6.22	2.48	12.5	58.2	55.0	15.0	21.0	21.7	6.80
MnO	0.12	0.15	0.15	0.10	0.17	0.17	0.16	0.11	0.11	0.17	0.16	0.10	0.12	0.15	0.15	0.09	0.12	0.65	0.54	0.34	0.63	0.61	0.17
MgO	19.9	49.8	32.6	17.4	19.9	48.8	31.4	15.6	22.0	49.6	32.9	15.8	22.3	49.9	33.0	16.4	21.1	6.24	7.12	44.1	39.2	39.5	13.6
CaO		0.04	0.63	22.8	0.11	0.06	0.78	19.9	0.10	0.06	0.77	20.1		0.03	0.66	23.2	0.08	0.02	0.02	0.24	0.43	0.57	24.2
Na_2O		0.00	0.05	0.86		0.01	0.16	1.88		0.01	0.14	2.01		0.00	0.06	1.27							0.78
K_2O			0.00	0.00			0.01	0.00				0.00			0.01	0.00							0.04
NiO	0.29	0.39	0.10	0.05	0.35	0.37	0.10	0.04	0.41	0.36	0.10	0.05	0.42	0.40	0.09	0.04	0.36	0.14	0.14	0.23	0.11	0.11	
Total	100	100	100	100	100	100	100	100	100	100	100	100	100	100	100	100	100	95.5	96.8	100	100	101	100
Mg#	77.6	89.6	89.9	91.8	71.3	88.7	89.0	89.3	76.2	89.4	89.9	90.3	78.0	89.9	90.5	92.2	75.3	16.2	18.9	84.1	77.1	76.6	78.3
Cr#	18.2			11.09	17.2			9.84	8.83			6.26	9.48			12.3	17.2	48.2	39.6				

[a] major element compositions analyzed by LA-ICPMS; the data of other samples are from EMP.

Table 5-3 Major element analyses (wt%) of melts in spongy-textured minerals from Xilong peridotites by EDS.

Host minerals	Cpx1	Cpx1	Cpx1	Cpx1	Cpx1	Sp1	Sp1	Sp1	Sp1	Sp1	Sp1	Sp1
SiO_2	61.8	62.5	60.3	61.1	62.3	60.8	47.1	57.5	49.8	62.34	55.1	56.7
Al_2O_3	26.3	26.8	24.6	25.1	21.8	26.2	30.9	26.8	31.4	26.43	30.4	31.6
Cr_2O_3						0.69	2.81	2.02	3.69	0.43		
FeO		0.33		0.91		0.30	1.59	1.08	1.89	0.46		0.46
MgO			0.72	0.56	3.62		2.90	5.52	1.37	0.00	0.28	
CaO			0.52	0.54	4.82	0.92	0.81	0.16	0.59	0.00		
Na_2O	11.9	10.3	13.9	11.6	7.62	11.1	13.3	6.93	11.0	10.34	14.3	11.2
K_2O				0.16			0.35		0.25	0.00		
Total	100	100	100	100	100	101	100	100	100	100	100	100

Table 5-4 Major element compositions analyses (wt%) of secondary clinopyroxene (Cpx2-A, Cpx2-B, Cpx2-C) by EMP in Xilong peridotites

Sample	XL-37									XL-04					XL-77										
Mineral	Cpx2-B	Cpx2-B	Cpx2-B	Cpx2-B	Cpx2-B	Cpx2-B	Cpx2-B	Cpx2-B	Cpx2-B	Cpx2-B	Cpx2-B	Cpx2-B	Cpx2-B	Cpx2-B	Cpx2-B	Cpx2-B	Cpx2-B	Cpx2-B	Cpx2-B	Cpx2-B	Cpx2-B	Cpx2-C	Cpx2-C	Cpx2-C	Cpx2-C
SiO_2	54.0	55.0	54.6	54.8	54.7	54.5	54.9	54.3	54.4	54.9	55.1	54.5	54.1	54.4	55.1	55.2	55.0	54.6	54.9	55.4	55.6	55.0	55.3	54.8	54.2
TiO_2	0.12	0.08	0.19	0.08	0.11	0.11	0.11	0.12	0.14	0.11	0.11	0.16	0.03		0.08	0.03	0.15	0.26	0.09	0.08	0.08	0.21	0.18	0.17	0.32
Al_2O_3	0.20	0.16	0.2	0.19	0.17	0.21	0.19	0.23	0.23	0.2	0.29	0.17	0.15	0.13	0.2	0.2	0.23	0.25	0.19	0.21	0.17	0.34	0.3	0.32	0.38
Cr_2O_3	3.43	2.49	3.17	3.55	3.61	3.86	2.75	2.26	2.62	3.1	2.44	3.09	3.59	3.69	4.89	3.54	2.99	4.42	3.56	3.82	2.94	1.41	1.34	1.7	1.43
FeO	2.54	2.83	3.03	2.47	2.93	2.46	2.69	2.61	2.69	3.53	3.00	3.12	2.73	2.86	2.46	2.81	2.48	2.47	2.6	2.51	2.54	2.42	2.54	2.47	2.47
MnO	0.15	0.13	0.12	0.14	0.18	0.13	0.16	0.13	0.1	0.17	0.2	0.12	0.12	0.16	0.13	0.14	0.13	0.11	0.1	0.09	0.15	0.08	0.09	0.09	0.08
MgO	17.7	18.7	18.0	17.7	18.1	17.0	17.5	17.3	17.1	17.5	18.9	18.6	17.8	18.7	17.2	18.8	17.4	18.0	18.4	17.2	17.9	17.9	17.8	17.7	17.7
CaO	19.7	19.4	19.1	19.1	18.1	19.8	20.5	21.2	21.3	19.0	19.2	18.4	19.4	17.9	17.9	17.6	20.7	17.7	18.7	19.1	19.8	22.5	22.5	22.1	22.3
Na_2O	1.72	1.40	1.53	1.72	1.77	1.86	1.46	1.36	1.49	1.64	1.39	1.52	1.85	1.78	2.36	1.81	1.63	2.27	1.79	1.98	1.46	0.93	1.03	0.99	0.97
K_2O							0.05	0.04			0.16														
NiO				0.06																					
Total	99.6	100.1	99.8	99.8	99.7	99.9	100.3	99.6	100.0	100.1	100.8	99.7	99.7	99.7	100.3	100.0	100.6	100.1	100.3	100.3	100.7	100.8	101.2	100.4	99.8
Mg#	92.6	92.2	91.4	92.8	91.7	92.6	92.1	92.3	92.0	89.9	91.9	91.5	92.2	92.2	92.7	92.3	92.6	92.9	92.7	92.5	92.7	93.0	92.7	92.8	92.8
Cr#	92.0	91.3	91.4	92.6	93.4	92.5	90.7	86.8	88.4	91.2	85.0	92.4	94.1	95.0	94.3	92.2	89.7	92.2	92.6	92.4	92.1	73.6	75.0	78.1	71.6

Continued

Sample	XL-22								XL-40					XL-32							
Mineral	Cpx2-A	Cpx2-A	Cpx2-A	Cpx2-A	Cpx2-B	Cpx2-B	Cpx2-B	Cpx2-C	Cpx2-B	Cpx2-B	Cpx2-B	Cpx2-B	Cpx2-B	Cpx2-A	Cpx2-A	Cpx2-B	Cpx2-B	Cpx2-B	Cpx2-B	Cpx2-C	Cpx2-C
SiO_2	51.9	52.1	51.5	52.1	54.2	54.3	54.9	54.2	54.1	54.5	54.2	54.7	54.3	49.7	50.3	54.6	53.9	54.9	54.8	55.0	54.8
TiO_2	0.67	0.68	0.73	0.54	0.10	0.19	0.22	0.26	0.04	0.07	0.05	0.07	0.08	1.86	1.67	0.35	0.53	0.22	0.21	0.27	0.38
Al_2O_3	3.98	4.06	4.27	5.63	0.23	1.17	0.31	0.41	0.24	0.25	0.22	0.21	0.22	5.52	5.81	0.33	0.35	0.23	0.25	0.33	0.63
Cr_2O_3	1.08	1.18	1.11	1.00	2.91	2.95	2.92	2.46	5.34	3.55	3.19	2.36	2.71	1.36	1.18	2.9	3.9	4.27	2.8	3.09	2.53
FeO	2.90	2.98	3.52	2.91	2.52	2.28	2.72	2.14	2.56	2.62	2.74	2.92	2.55	3.46	3.62	2.12	2.33	2.51	2.62	2.05	2.13
MnO	0.09	0.13	0.13	0.10	0.13	0.10	0.16	0.08	0.15	0.14	0.14	0.16	0.10		0.14	0.11	0.15	0.14	0.08	0.08	0.13
MgO	16.2	16.1	16.1	15.9	18.0	16.9	18.1	17.4	17.3	17.7	18.1	18.3	18.1	15.3	15.5	17.4	17.4	17.5	17.4	16.9	17.4
CaO	22.0	21.9	20.9	20.4	19.7	19.9	19.2	21.4	17.5	19.3	19.0	20.1	20.8	21.4	20.4	20.8	19.6	18.5	20.5	21.2	21.0
Na_2O	1.00	0.97	1.32	1.58	1.43	1.52	1.41	1.17	2.44	1.62	1.71	1.38	1.52	1.02	1.29	1.69	1.96	1.98	1.38	1.64	1.54
K_2O					0.03	0.20		0.13								0.06	0.03	0.03		0.06	0.07
NiO	0.07		0.07	0.07				0.06												0.06	
Total	99.8	100.1	99.6	100.2	99.2	99.5	99.8	99.6	99.7	99.8	99.4	100.3	100.4	99.8	100.0	100.4	100.0	100.2	100.0	100.6	100.6
Mg#	90.9	90.7	89.2	90.8	92.8	93.0	92.3	93.6	92.4	92.4	92.2	91.9	92.7	88.8	88.5	93.7	93.1	92.6	92.3	93.7	93.6
Cr#	15.4	16.3	14.9	10.6	89.5	62.9	86.3	80.1	93.7	90.5	90.7	88.3	89.2	14.2	12.0	85.5	88.2	92.6	88.3	86.3	72.9

Table 5-5 Major element compositions analyses (wt%) of secondary spinel (Sp2-A, Sp2-B, Sp2-C) by EDS in Xilong peridotites

Sample	XL-63	XL-32	XL-22	XL-40									
Mineral	Sp2-C	Sp2-B	Sp2-B	Sp2-A	Sp2-A	Sp2-A	Sp2-A	Sp2-A	Sp2-C	Sp2-C	Sp2-C	Sp2-B	Sp2-B
SiO_2	5.44	0.43	0.00	0.54	0.43	2.14	0.00	0.00	3.13	1.28	1.48	0.20	0.00
TiO_2	0.41	0.58	0.60	0.54	0.77	3.15	1.15	0.39	0.58	0.48	0.00	0.33	0.28
Al_2O_3	2.72	1.11	0.85	38.3	39.3	26.9	35.6	44.0	2.32	2.06	1.79	1.30	1.13
Cr_2O_3	62.1	69.3	70.5	29.0	27.6	27.8	24.1	24.9	62.5	64.2	65.7	68.1	69.9
FeO	19.3	20.7	18.1	14.3	15.0	24.9	23.8	11.7	23.6	24.2	20.4	19.8	18.8
MgO	8.91	7.85	9.93	17.3	17.0	13.7	15.0	19.0	7.32	7.38	9.93	10.14	9.76
Na_2O	0.00	0.00	0.00	0.00	0.00	1.16	0.00	0.00	0.00	0.00	0.00	0.00	0.00
K_2O	1.13	0.00	0.00	0.00	0.00	0.28	0.00	0.00	0.64	0.37	0.39	0.13	0.15
Total	100.0	100.0	100.0	100.0	100.1	100.0	100.0	100.0	100.0	100.0	100.3	100.0	100.0
Mg#	45.4	40.6	49.7	68.6	67.1	49.8	53.1	74.6	35.9	35.4	46.7	47.9	48.3
Cr#	94.0	97.7	98.3	34.1	32.4	41.4	31.6	27.9	94.8	95.5	96.2	97.3	97.7

Table 5-6 Major element compositions analyses (wt%) of K-melt by EMP in Xilong peridotites

Sample	XL-04					XL-37						XL-77							XL-22				
SiO_2	56.8	60.1	59.5	62.0	61.1	60.0	58.0	63.5	59.6	57.3	58.4	57.5	63.2	59.4	62.2	61.4	60.5	60.4	60.3	61.3	60.3	61.8	63.0
TiO_2	0.88	0.66	0.69	0.16	0.41	0.32	0.2	0.14	0.44	0.21	0.30	0.22	0.17	0.24	0.31	0.06	0.43	0.34	0.47	0.37	0.96	0.18	0.22
Al_2O_3	9.9	12.1	13.5	17.1	14.8	13.7	14.7	18.0	17.2	14.1	14.9	13.9	15.6	12.9	12.9	16.2	14.4	14.3	15.3	12.9	13.2	14.5	15.7
FeO	4.62	3.68	2.66	1.38	2.1	3.15	3.03	1.39	2.72	2.91	2.7	2.21	1.35	2.08	2.07	2.01	2.89	2.90	2.38	1.74	3.68	1.54	1.84
MnO	0.11					0.1	0.07			0.09					0.06		0.06				0.07		
MgO	11.81	7.49	6.54	3.39	4.25	5.49	7.2	0.5	2.51	6.16	8.4	6.77	2.73	6.55	3.95	3.12	4.04	6.12	3.10	2.22	3.61	2.55	2.52
CaO	0.57	0.36	0.3	0.15	0.17	0.13	0.14	0.07	0.08	0.12	0.21	0.47	0.02	0.06	0.05	0.06	0.12	0.08	0.12	0.23	0.15	0.12	0.09
Na_2O	3.11	2.41	2.27	0.66	1.58	1.12	0.62	0.39	0.43	0.81	0.70	0.71	0.62	1.11	1.28	0.23	0.81	0.92	0.45	2.16	1.25	1.12	0.55
K_2O	10.7	12.1	13.0	15.3	14.4	13.8	13.9	16.6	16.1	13.4	13.1	13.7	15.7	14.4	14.9	15.6	15.5	14.1	14.9	14.4	13.8	14.6	13.2
Total	98.5	98.9	98.5	100.2	98.8	97.8	97.9	100.5	99.0	95.0	98.6	95.7	99.3	96.8	97.6	98.6	98.8	99.1	97.0	95.3	97.0	96.4	97.2

Continued

Sample	XL-40						XL-32						
SiO_2	59.2	61.7	59.6	62.5	61.8	58.4	60.8	59.4	60.0	60.6	61.2	60.1	62.2
TiO_2	0.20	0.15	0.10	0.17	0.16	0.16	0.50	0.54	0.52	0.44	0.60	0.52	0.12
Al_2O_3	16.8	15.8	16.9	15.6	11.9	16.5	14.1	13.9	14.6	13.8	14.1	13.7	16.4
Cr_2O_3			0.05			0.08							
FeO	2.69	2.1	1.9	1.97	3.74	2.62	2.33	2.67	2.2	2.33	2.95	3.26	0.92
MnO	0.1	0.06		0.06		0.08	0.08		0.08	0.08	0.09		
MgO	3.66	2.07	3.81	2.1	6.12	5.84	3.21	5.45	4.79	4.67	2.25	2.17	1.52
CaO	0.14	0.16	0.09	0.11	0.27	0.15	0.11	0.05	0.06	0.04	0.09	0.2	0.02
Na_2O	0.31	0.58	0.34	0.78	0.74	0.3	0.73	0.71	0.76	0.92	1.36	1.64	0.43
K_2O	15.3	15.7	15.4	16.0	14.1	13.8	14.3	13.7	14.2	13.8	13.9	13.8	15.6
Total	98.5	98.3	98.1	99.3	98.8	97.9	96.2	96.3	97.2	96.7	97.1	95.4	96.5

Table 5-7 Major element compositions analyses (wt%) of secondary olivine (Ol2) by EMP in Xilong peridotites

Sample	XL-22							XL-40				XL-32								
SiO_2	41.4	41.7	41.0	40.3	40.7	40.3	40.5	40.4	41.2	41.1	40.7	41.4	41.2	41.1	40.7	41.1	40.9	40.5	41.3	41.0
Cr_2O_3	0.07	0.09	0.04		0.06	0.05	0.06	0.12	0.06	0.05		0.09	0.11	0.1	0.06	0.06	0.06	0.06	0.06	0.05
FeO	8.55	8.49	9.08	8.54	10.0	11.1	10.9	9.11	9.72	10.1	10.8	8.76	8.51	8.6	9.79	9.69	9.45	9.11	8.74	8.64
MnO	0.17	0.20	0.22	0.23	0.24	0.25	0.29	0.18	0.22	0.22	0.26	0.16	0.2	0.19	0.16	0.18	0.17	0.18	0.15	0.23
MgO	50.2	50.2	49.7	50.1	49.2	48.0	47.9	50.2	49.3	49.7	48.7	50.5	50.8	50.6	49.8	49.8	50.2	50.5	50.6	51.3
CaO	0.13	0.10	0.14	0.13	0.13	0.12	0.10	0.09	0.11	0.09	0.11	0.08	0.09	0.08	0.11	0.11	0.09	0.11	0.13	0.11
Na_2O									0.06										0.05	
K_2O							0.03									0.04	0.04			
NiO	0.18	0.19	0.19	0.16	0.13	0.16	0.17	0.26	0.17	0.21	0.17	0.27	0.27	0.25	0.21	0.24	0.23	0.26	0.25	0.21
Total	100.7	100.9	100.4	99.4	100.5	100.1	99.9	100.2	100.7	101.2	100.4	101.2	101.1	100.9	100.8	101.1	101.1	100.7	101.3	101.6
Mg#	91.4	91.4	90.8	91.3	89.8	88.6	88.8	90.8	90.1	89.9	89.1	91.2	91.5	91.4	90.1	90.2	90.5	90.9	91.2	91.4

Sample	XL-37						XL-04			XL-77										
SiO_2	40.6	40.7	41.3	40.4	40.2	40.9	40.4	41.2	40.7	41.9	41.7	41.1	41.7	41.8	40.6	40.6	41.0	40.5	40.4	40.1
Cr_2O_3	0.09	0.05	0.09		0.08	0.07	0.21	0.07	0.07	0.08	0.1	0.08	0.07	0.07	0.05	0.06	0.06	0.04	0.07	
FeO	8.33	8.63	8.09	9.77	9.88	9.63	8.65	8.33	9.02	7.28	7.53	7.29	7.94	8.22	9.08	9.39	9.83	10.8	10.9	10.4
MnO	0.21	0.21	0.17	0.25	0.24	0.29	0.19	0.19	0.19	0.16	0.22	0.18	0.16	0.23	0.23	0.21	0.25	0.25	0.27	0.25
MgO	50.7	50.4	50.8	49.3	48.8	49.3	50.9	50.7	50.6	51.4	51.6	51.5	51.1	50.7	50.6	50.4	49.3	49.0	48.9	49.2
CaO	0.1	0.09	0.1	0.12	0.17	0.12	0.1	0.09	0.1	0.08	0.09	0.08	0.1	0.1	0.13	0.11	0.12	0.16	0.18	0.18
Na_2O		0.05												0.05			0.06			
NiO	0.16	0.18	0.21	0.21	0.2	0.17	0.25	0.25	0.23	0.19	0.19	0.21	0.29	0.22	0.27	0.16	0.2	0.21	0.19	0.21
Total	100.1	100.4	100.8	100.1	99.7	100.4	100.4	100.6	100.7	101.2	101.4	100.4	101.4	101.4	101.0	101.0	101.0	101.0	100.9	100.2
Mg#	91.6	91.3	91.9	90.1	89.9	90.2	91.4	91.6	91.0	92.7	92.5	92.7	92.0	91.7	90.9	90.6	90.0	89.1	89.0	89.5

Table 5-8 Major element composition variation of clinopyroxene in a profile AB from sample LS-22.

Mineral	Cpx2-B			Cpx2-C	Cpx1			Cpx2-A		
Distance/μm	120	273	307	465	486	513	549	625	651	687
SiO_2	54.2	54.3	54.9	54.2	51.8	51.1	51.6	51.9	52.1	51.5
TiO_2	0.10	0.19	0.22	0.26	0.51	0.51	0.53	0.67	0.68	0.73
Al_2O_3	0.23	1.17	0.31	0.41	6.71	6.64	6.69	3.98	4.06	4.27
Cr_2O_3	2.91	2.95	2.92	2.46	1.03	0.94	0.89	1.08	1.18	1.11
FeO	2.52	2.28	2.72	2.14	2.74	2.63	2.60	2.90	2.98	3.52
MnO	0.13	0.10	0.16	0.08	0.09	0.12	0.11	0.09	0.13	0.13
MgO	18.0	16.9	18.1	17.4	15.5	15.3	15.4	16.2	16.1	16.1
CaO	19.7	19.9	19.2	21.4	19.8	20.0	19.9	22.0	21.9	20.9
Na_2O	1.43	1.52	1.41	1.17	1.92	1.78	1.72	1.00	0.97	1.32
K_2O	0.03	0.20		0.13						
NiO				0.06			0.07	0.07		0.07
Total	99.2	99.5	99.8	99.6	100.1	99.0	99.4	99.8	100.1	99.6
Mg#	92.8	93.0	92.3	93.6	91.1	91.3	91.4	90.9	90.7	89.2

Table 5-9 Representative trace element analyses (ppm) of clinopyroxene in Xilong peridotites by LA-ICPMS

Type	Group 1							Group 2								
Sample	XL-77		XL-04		XL-61	XL-37	XL-01	XL-22	XL-63	XL-33	XL-25	XL-32	XL-55	XL-40		XL-78
Mineral	Cpx1	Cpx2-A	Cpx1	Cpx2-A	Cpx1	Cpx1	Cpx1	Cpx1	Cpx1	Cpx1	Cpx1	Cpx1	Cpx1	Cpx1	Cpx2-A	Cpx1
Li	31.1	15.2	40.2	8.36	27.8	36.8	24.2	35.0	29.5	32.9	18.0	55.9	41.9	31.1	5.83	2.90
Sc	39.6	138	43.8	54.4	47.4	66.8	70.3	68.7	64.6	62.3	71.7	49.3	60.8	64.6	114	67.6
V	169	531	167	241	179	252	270	259	258	248	258	244	258	227	519	232
Cr	7532	29905	8186	17692	7248	9426	12708	6354	5019	5593	5711	8145	4886	5895	18365	8094
Co	26.0	15.7	26.8	29.3	25.8	24.3	24.1	21.6	22.5	22.5	20.2	26.2	23.2	22.5	14.7	19.7
Ni	474	175	464	395	472	395	395	349	370	340	257	430	368	384	153	330
Cu	0.85	0.18	0.76	0.33	2.15	0.75	2.32	1.90	1.41	1.28	0.27	2.56	3.53	0.69		0.98
Zn	11.4	16.2	10.5	30.1	11.1	10.6	12.7	8.0	9.2	11.4	6.3	12.1	10.3	8.7	16.8	6.7
Ga	1.65	3.63	1.77	0.83	1.40	2.04	3.98	3.55	3.69	4.37	2.08	3.47	2.61	1.47	1.18	1.73
Ge	0.80	0.84	1.62	1.19	1.22	1.30	1.66	1.58	1.05	1.61	0.83	0.83	0.93	0.73	1.42	0.92
Rb		4.70		0.01							0.22	0.00	0.01	0.00	0.72	0.04
Ba	0.61	0.00	0.75	0.00	0.27	0.18	0.06	0.16			1.64	0.13		0.51	4.56	
Th	0.08	0.19	0.94	0.00	1.10	2.88	0.58	0.02	0.11	0.64	0.05	0.13	0.65	0.01		
U	0.02	0.03	0.15		0.24	0.67	0.14	0.01	0.03	0.14	0.02	0.03	0.26	0.00	0.00	0.00
Nb	1.17	10.9	1.38		2.41	2.80	0.97	0.23	1.02	1.75	0.54	1.33	5.99	0.02	0.24	0.10
Ta	0.01	0.15	0.09		0.24	0.55	0.17	0.01	0.01	0.30	0.02	0.11	0.65			0.02
La	0.54	5.32	10.1	8.27	12.5	20.4	6.23	0.78	1.22	7.65	0.73	2.35	7.26	0.06	6.45	0.33
Ce	0.97	13.73	16.3	22.0	28.7	38.7	13.3	3.42	3.67	20.6	2.52	6.80	11.7	0.08	15.9	1.08
Pb	0.07	0.47	0.14	0.13	0.24	0.29	0.07	0.05	0.15	0.11	2.96	0.06	0.19	0.01	0.28	0.06
Pr	0.15	2.06	1.57	2.97	3.58	4.14	1.90	0.66	0.61	2.49	0.53	1.28	0.87	0.01	2.50	0.21
Sr	8.70	830	143	899	410	366	169	80.3	84.9	210	47.7	86.8	138	0.79	951	15.3
Nd	0.49	9.06	7.92	12.92	13.71	15.64	9.76	4.65	4.16	8.10	2.99	5.98	4.93	0.04	10.96	1.42
Zr	1.25	10.0	12.6	2.44	6.29	8.32	49.7	37.1	34.9	44.1	20.5	34.0	34.1	0.15	1.52	4.31
Hf	0.05	0.37	0.26	0.02	0.19	0.24	1.54	1.01	1.15	1.04	0.77	1.37	0.99	0.05		0.19
Sm	0.12	1.78	1.32	2.32	2.23	2.05	2.33	1.58	1.80	1.83	1.40	1.92	1.83	0.20	2.67	0.56
Eu	0.05	1.24	0.52	1.80	0.70	0.57	0.86	0.79	0.78	0.85	0.58	0.72	0.70	0.10	2.08	0.23
Ti	120	648	324	547	349	602	2014	2938	3337	3292	2615	4253	3272	575	358	841
Gd	0.12	1.47	1.28	2.22	1.51	1.69	3.07	2.53	2.94	2.65	2.15	2.78	2.91	0.50	2.07	0.88
Tb	0.02	0.26	0.18	0.33	0.18	0.20	0.41	0.50	0.51	0.54	0.46	0.50	0.51	0.14	0.38	0.22
Dy	0.10	1.20	0.51	1.35	0.96	1.30	2.36	3.30	3.38	3.18	2.96	3.00	3.44	1.13	1.90	1.72
Y	1.18	5.24	2.84	5.96	4.66	6.47	10.6	21.4	21.9	19.8	18.0	14.2	19.9	8.45	6.82	11.1
Ho	0.05	0.23	0.12	0.21	0.18	0.24	0.43	0.85	0.83	0.77	0.66	0.58	0.74	0.31	0.38	0.46
Er	0.19	0.60	0.23	0.62	0.59	0.73	1.25	2.55	2.64	2.25	2.15	1.51	2.35	0.90	0.65	1.43
Tm	0.04	0.09	0.04	0.07	0.05	0.08	0.16	0.35	0.36	0.32	0.31	0.28	0.33	0.21	0.09	0.17
Yb	0.21	0.36	0.26	0.32	0.29	0.86	0.87	2.32	2.16	2.23	1.98	1.24	2.01	1.05	0.52	1.47
Lu	0.03	0.04	0.06	0.05	0.06	0.14	0.11	0.27	0.38	0.28	0.27	0.15	0.30	0.17	0.12	0.20

Table 5-10 Representative trace element analyses (ppm) of K-melt in Xilong peridotites by LA-ICPMS

Sample	XL-37			XL-04		XL-77		XL-40			XL-22		XL-32
Li	64.9	82.5	138.9	9.2	10.7	358	145	39.8	61.6	70.3	17.5	23.5	42.5
Sc	5.44	5.20	4.48	7.44	6.44	9.96	11.4	9.02	4.44	5.01	7.41	3.98	15.2
V	51.3	54.6	80.8	76.9	60.9	39.0	55.6	31.3	32.9	46.3	36.7	27.3	46.1
Co	7.73	9.18	13.22	14.33	12.82	9.32	7.93	6.92	8.96	9.81	10.32	13.57	8.73
Ni	1.84	1.58	6.45	9.59	10.5	68.1	60.7	12.7	18.1	101.5	8.44	27.9	2.35
Zn	32.6	38.8	59.4	35.9	43.5	35.8	19.3	40.0	60.8	42.8	22.2	29.0	16.4
Ga	17.0	17.5	26.9	15.3	17.6	18.1	16.0	15.2	20.7	40.1	14.9	19.3	17.6
Rb	225	228	318	165	169	238	194	140	222	240	227	300	221
Ba	2798	2391	2336	776	719	1275	1068	1286	4511	1329	1346	1442	1329
Th	2.72	2.82	3.04	5.93	7.42	3.32	2.41	0.59	2.78	1.41	0.29	0.18	1.39
U	1.08	0.93	1.06	1.28	1.77	0.75	0.32	0.20	0.56	0.39	0.07	0.10	0.32
Nb	23.8	30.9	23.9	91.0	104	31.8	25.0	9.9	18.7	13.2	3.4	4.5	5.6
Ta	0.93	1.16	1.18	4.34	5.39	1.82	0.86	0.15	1.13	0.39	0.10	0.20	0.66
La	11.8	11.9	10.6	7.24	7.32	12.5	3.44	7.79	10.7	4.47	1.81	2.54	5.54
Ce	17.7	19.3	16.8	13.0	13.4	22.3	6.2	12.4	19.8	7.7	3.9	3.8	11.2
Pb	2.28	1.72	2.86	1.89	1.24	4.04	1.78	1.68	4.62	4.75	2.79	1.39	2.12
Pr	1.42	1.67	1.38	1.14	1.50	1.76	0.45	1.29	1.82	0.69	0.35	0.41	1.22
Sr	414	329	299	218	218	139	54.2	192	195	147	141	96.6	369
Nd	4.82	4.52	4.30	4.72	5.37	5.63	2.29	4.30	5.06	2.75	0.83	1.43	4.79
Zr	19.3	20.3	23.9	152.6	178.9	72.9	53.0	5.58	38.8	27.7	7.53	6.57	40.1
Hf	0.28	0.35	0.46	3.12	4.16	1.31	1.47	0.05	0.81	0.46	0.19	0.16	1.04
Sm	0.66	0.73	0.77	1.23	0.90	0.87	0.39	1.11	1.64	0.38		0.31	0.76
Eu	0.42	0.37	0.53	0.55	0.39	0.50	0.28	0.52	0.52	0.34	0.09	0.23	0.30
Ti	1544	1950	1448	4695	4597	1784	1510	1240	1433	1567	794	651	1486
Gd	0.37	0.44	0.39	0.94	1.59	0.86	0.39	0.67	0.97	0.61	0.17	0.31	0.79
Tb	0.11	0.10	0.05	0.20	0.34	0.17	0.11	0.05	0.19	0.08	0.03	0.03	0.18
Dy	0.34	0.67	0.47	1.75	1.96	0.54	0.48	0.48	1.08	0.80	0.55	0.40	0.81
Y	3.15	3.51	2.74	6.53	8.17	3.69	2.46	3.19	4.92	2.72	1.84	2.34	5.04
Ho	0.16	0.12	0.07	0.27	0.34	0.07	0.08	0.12	0.25	0.05	0.10	0.03	0.13
Er	0.38	0.33	0.29	0.76	0.70	0.44		0.28	0.50	0.36	0.34	0.25	0.56
Tm	0.03	0.01	0.06	0.07	0.08	0.06	0.04	0.02	0.10	0.04	0.02	0.02	0.08
Yb		0.26	0.17	0.65	0.65	0.21		0.24	0.50	0.38	0.44	0.29	0.46
Lu	0.09	0.07	0.03	0.07	0.07	0.07	0.01	0.05	0.09	0.04	0.04	0.08	0.05

Table 6-1 Point counted and calculated modal compositions (wt%) of garnet pyroxenites from Lakes Bullenmerri and Gnotuk

Sample ID	Cpx	Opx	Gt	Amp	Sp	Ilm	Phl	Pl	Ol
Type I garnet websterite									
BM99-2	52	13	30	4	1				
BM99-6	61		38	<0.5	1				
BM99-4	57	20	18	5					
BME-1	55	11	33	<0.5					
BM99-2	55	13	31						
BM96-3	23	15	60	<0.5			2		
BM99-5	64	28	5	3		<0.5			
DR9748*	40(41)	44(45)	11(13)	5(0)					
DR10165*	49(46)	25(28)	17(17)	3(0)	6(8)				
GN35*	54(50)	27(37)	8(0.28)	4(0)	7(12)				
Type II a garnet clinopyroxenite									
BM99X2	64		36						
GN85-1	43		57						
BM99-9	66		32					2	
BM99X1	80		19	<0.5				1	
BM99-8	63		36					1	
GN51*	50(38)		49(62)		1(0)				
GN18*	51(64)		49(35)						
GN41*	55(45)		45(53)						
DR10162*	46(51)	0(0.27)	53(47)	0(0.24)	1(0)				
Type II b spinel-bearing garnet clinopyroxenite									
BMC-1	75	2	11	6	4				2
BM90-3	69	5	24	1	<0.5				1
BM99-7	70		11	19	1				
DR11022*	78(75)	4(6)	4(12)	2(0)	12(7)				
DR11017c*	66(77)	5(10)	14(8)	8(0.01)	7(5)				

Mineral modes were estimated from point-counted modes and converted to wt% from mineral densities using d cpx=3.2, d opx=3.2, d gt=3.71, d amp=3.12, d sp=3.6, d ilm=4.72, d phl=2.8, d pl=2.67, d ol=3.34. Least-squares fitted modes (results in parentheses) were calculated from whole-rock and mineral major element compositions.
* samples are from Griffin et al., 1984, 1988; O'Reilly and Griffin, 1985.

Table 6-2 Major-element compositional profile of BM99X2 (Line A-B shown in Fig. 6-2e)

A-B	Lamellar zone									Recrystallized zone																		
SiO_2	52.2	51.4	51.2	50.9	40.2	40.1	40.3	40.1	51.5	51.3	51.5	52.0	40.6	40.7	50.8	50.9	50.7	51.2	51.3	51.0	40.3	40.7	50.7	50.8	40.5	40.8	40.5	51.1
TiO_2	0.54	0.52	0.48	0.44	0.07	0.06	0.08	0.07	0.54	0.53	0.50	0.51	0.09	0.12	0.52	0.54	0.55	0.57	0.57	0.53	0.10	0.10	0.62	0.59	0.08	0.07	0.08	0.65
Al_2O_3	6.80	6.69	7.04	6.98	22.91	22.82	23.18	23.15	6.93	7.09	7.43	6.89	23.01	23.01	7.68	7.24	7.63	7.03	7.12	7.24	23.03	23.01	7.76	7.48	23.00	23.01	23.00	7.69
Cr_2O_3	0.10	0.08	0.06	0.07	0.06	0.06	0.06	0.06	0.06	0.08	0.11	0.09	0.07	0.07	0.09	0.08	0.11	0.12	0.11	0.08	0.08	0.10	0.10	0.10	0.10	0.11	0.08	0.10
FeO	6.04	6.04	6.22	6.28	16.58	16.57	16.50	16.39	6.19	6.05	5.91	5.90	15.58	15.76	5.68	5.73	5.63	5.59	5.60	5.73	15.37	15.40	5.53	5.58	15.59	15.59	15.42	5.73
MnO	0.11	0.08	0.10	0.11	0.48	0.46	0.45	0.47	0.10	0.11	0.08	0.09	0.44	0.43	0.09	0.07	0.08	0.06	0.05	0.08	0.44	0.41	0.06	0.08	0.44	0.44	0.41	0.08
MgO	13.4	13.5	13.5	13.6	14.4	14.4	14.5	14.4	13.6	13.4	13.3	13.5	14.3	14.2	12.9	13.0	13.0	13.1	13.1	13.1	14.4	14.4	12.8	12.9	14.3	14.3	14.3	13.0
CaO	20.7	20.6	20.2	20.3	6.6	6.5	6.7	6.7	20.6	20.5	20.4	20.6	6.7	6.7	20.3	20.4	20.3	20.6	20.6	20.6	6.9	7.0	20.6	20.6	6.8	6.9	7.0	21.1
Na_2O	1.67	1.55	1.61	1.67	b.d.	b.d.	b.d.	b.d.	1.51	1.66	1.74	1.70	0.02	0.04	1.79	1.73	1.75	1.75	1.63	1.73	0.02	0.02	1.74	1.70	0.02	0.02	0.02	1.54
NiO	b.d.	b.d.	b.d.	b.d.	b.d.	b.d.	b.d.	b.d.	b.d.	b.d.	0.06	b.d.	b.d.	b.d.	b.d.	0.06	0.07	0.07	b.d.	b.d.	b.d.	b.d.	0.08	b.d.	b.d.	b.d.	b.d.	b.d.
Total	101.6	100.5	100.4	100.3	101.3	101.0	101.7	101.3	101.0	100.7	101.0	101.2	100.8	101.1	99.9	99.8	99.8	100.1	100.0	100.1	100.6	101.0	100.0	99.9	100.8	101.2	100.8	100.9
Mg#	80.0	80.1	79.7	79.5	61.0	61.0	61.2	61.2	79.8	79.9	80.2	80.4	62.3	61.9	80.4	80.4	80.6	80.9	80.8	80.5	62.7	62.6	80.7	80.7	62.2	62.3	62.5	80.4

Continued

A-B	Coarse zone																											
SiO_2	51.4	51.4	39.9	40.1	40.6	40.5	50.2	49.6	50.8	50.5	50.8	50.3	50.7	40.1	40.3	40.8	40.8	40.2	40.4	40.1	40.7	40.9	50.3	50.3	50.4	50.5	50.9	50.0
TiO_2	0.63	0.56	0.07	0.07	0.07	0.09	0.65	0.60	0.63	0.59	0.56	0.58	0.59	0.06	0.06	0.09	0.08	0.08	0.10	0.09	0.09	0.10	0.74	0.70	0.81	0.70	0.64	0.68
Al_2O_3	7.62	7.34	22.88	22.97	22.98	22.85	7.76	8.18	7.61	7.88	7.79	8.04	8.43	22.97	23.02	22.95	23.13	22.90	23.35	22.82	22.68	22.89	8.41	9.06	8.25	8.10	8.76	8.62
Cr_2O_3	0.11	0.10	0.10	0.11	0.10	0.12	0.10	0.11	0.11	0.11	0.11	0.12	0.13	0.09	0.08	0.12	0.09	0.11	0.08	0.11	0.11	0.09	0.13	0.12	0.09	0.12	0.09	0.13
FeO	5.70	5.86	16.33	16.33	15.51	15.58	5.43	5.47	5.48	5.48	5.43	5.53	5.43	16.25	16.31	15.90	15.58	15.58	15.93	15.38	15.56	15.59	5.83	5.82	5.83	5.41	5.57	5.21
MnO	0.09	0.09	0.42	0.44	0.41	0.40	0.08	0.09	0.06	0.10	0.06	0.08	0.08	0.47	0.45	0.39	0.42	0.42	0.41	0.41	0.40	0.42	0.10	0.08	0.07	0.06	0.08	0.08
MgO	13.1	13.3	14.3	14.3	14.3	14.2	13.0	12.8	13.0	12.9	12.9	12.8	12.6	14.2	14.2	14.0	14.3	14.1	14.3	13.9	13.7	14.0	12.7	12.3	12.7	12.6	12.3	12.3
CaO	20.9	20.7	6.9	7.1	7.0	7.1	20.7	20.5	20.7	20.5	20.4	20.4	20.5	7.1	7.2	7.3	7.1	7.0	7.4	7.2	7.3	7.3	21.0	21.2	21.2	21.1	20.8	21.2
Na_2O	1.51	1.63	b.d.	b.d.	0.02	0.01	1.67	1.80	1.72	1.71	1.70	1.76	1.72	b.d.	0.02	0.02	0.01	0.02	0.02	0.02	0.01	0.01	1.72	1.71	1.63	1.73	1.75	1.67
NiO	b.d.	0.06	b.d.	b.d.	b.d.	b.d.	0.06	b.d.	b.d.	b.d.	b.d.	b.d.	b.d.	b.d.	b.d.	b.d.	b.d.	b.d.	b.d.	b.d.	b.d.	b.d.	0.07	b.d.	0.07	b.d.	b.d.	0.08
Total	101.1	101.0	101.0	101.4	100.9	100.9	99.6	99.2	100.0	99.7	99.8	99.6	100.3	101.2	101.6	101.7	101.5	100.4	102.1	100.0	100.5	101.3	101.0	101.3	101.0	100.2	100.8	100.0
Mg#	80.6	80.3	61.3	61.2	62.4	62.2	81.1	80.9	81.0	80.9	81.0	80.7	80.7	61.1	61.0	61.3	62.2	61.9	61.8	61.8	61.3	61.7	79.7	79.2	79.6	80.7	79.9	81.0

b.d. = below detection limit.

Table 6-3 Major-element compositions of clinopyroxene in the garnet pyroxenites from Lakes Bullenmerri and Gnotuk

Rock type	Type I															Type II a		
Sample No.	BM99-2	BM99-6	BM99-4		BME-1		BM99-2		BM96-3	BM99-5	DR9748	GN35		DR10165		GN85-1	BM99-9	
Type	M	M	H	M	H	M	H	M	M	H	M	H	M	H	M1	M	H	M
SiO_2	51.17	51.33	51.03	51.42	51.47	51.84	50.91	51.25	51.37	51.30	50.88	51.10	51.44	51.08	51.43	50.98	50.75	51.27
TiO_2	0.37	0.36	0.73	0.79	0.43	0.42	0.40	0.40	1.02	0.80	0.88	0.68	0.62	0.53	0.51	0.57	0.22	0.21
Al_2O_3	6.62	6.75	7.14	7.51	6.33	6.42	6.43	6.34	6.20	4.87	5.98	7.29	7.11	6.5	6.02	7.51	9.28	8.77
Cr_2O_3	0.28	0.17	0.30	0.30	0.24	0.26	0.19	0.22	0.11	0.32	0.44	0.37	0.2	0.2	0.17	0.11	0.14	0.13
FeO	5.12	3.25	3.32	3.29	3.58	3.60	4.56	4.43	5.00	6.67	5.86	3.47	3.77	3.61	3.77	5.99	4.55	4.52
MnO	0.09	0.07	0.07	0.09	0.06	0.06	0.08	0.08	0.09	0.13	0.13	0.13	0.12	b.d.	0.10	0.08	0.09	b.d.
MgO	14.47	15.40	14.66	14.28	14.88	14.63	14.96	14.93	14.75	14.24	14.47	14.27	14.53	14.84	15.22	13.17	12.03	12.23
CaO	20.34	21.56	20.85	20.92	21.70	22.05	20.96	21.01	21.06	20.29	21.13	20.87	20.47	22.15	21.49	20.84	21.44	21.36
Na_2O	1.55	1.28	1.51	1.58	1.17	1.19	1.41	1.43	1.16	1.26	1.03	1.49	1.5	1.03	1.00	1.63	1.62	1.57
NiO	0.08	0.08	b.d.	b.d.	0.07	0.07	b.d.	b.d.	0.09	0.08	n.d.	n.d.	n.d.	n.d.	n.d.	0.08	0.07	b.d.
Total	100.1	100.2	99.6	100.2	99.9	100.5	99.9	100.1	100.8	99.9	100.80	99.67	99.76	99.94	99.71	100.9	100.1	100.1
Mg#	83.6	89.5	88.8	88.7	88.2	88.0	85.5	85.8	84.1	79.3	81.5	88.1	87.4	88.1	87.9	79.8	82.6	83.0

Continued

Rock type												Type II a					
Sample No.	BM99X2			BM99X1		BM99-8		GN51	GN18	GN41	DR10162	BM90-3		BMC-1	BM99-7	DR11017c	DR11022
Type	H	M1	M2	H	M	H	M	M	M	M	M	H	M	M	M	M	M
SiO_2	51.42	51.13	50.40	51.85	51.73	51.16	51.76	49.00	50.85	50.12	51.29	51.99	51.73	52.08	51.56	52.12	51.23
TiO_2	0.50	0.56	0.65	0.61	0.59	0.16	0.15	0.61	0.24	0.79	0.31	0.48	0.49	0.45	0.45	0.42	0.41
Al_2O_3	6.89	7.37	8.22	7.96	7.75	6.41	6.58	9.81	8.23	8.5	7.51	5.33	5.41	5.02	5.03	5.26	5.34
Cr_2O_3	0.07	0.10	0.11	0.09	0.08	0.11	0.11	b.d.	0.11	0.08	0.21	0.09	0.09	0.07	0.08	0.05	b.d.
FeO	6.15	5.73	5.53	4.76	4.83	4.37	3.91	5.08	4.44	5.54	4.4	4.71	4.69	5.14	4.90	4.98	4.8
MnO	0.10	0.08	0.08	0.08	0.08	0.07	0.07	b.d.	b.d.	0.06	b.d.	0.10	0.10	0.10	0.11	0.09	0.1
MgO	13.52	13.12	12.68	13.35	13.43	14.68	14.38	12.3	13.78	12.75	14.09	15.00	14.78	14.62	15.29	15.09	15.05
CaO	20.49	20.58	20.77	20.66	20.70	21.50	21.90	20.9	20.75	20.37	21.36	21.72	22.00	21.82	22.12	22.00	22.11
Na_2O	1.60	1.69	1.71	1.85	1.83	1.27	1.31	1.96	1.73	1.95	1.39	0.84	0.85	0.86	0.76	0.75	0.7
NiO	b.d.	0.07	0.07	b.d.	b.d.	b.d.	b.d.	n.d.	n.d.	n.d.	n.d.	b.d.	b.d.	b.d.	b.d.	0.04	n.d.
Total	100.8	100.4	100.2	101.2	101.0	99.7	100.2	99.7	100.1	100.2	100.6	100.3	100.0	100.1	100.2	100.8	99.74
Mg#	79.8	80.47	80.49	83.5	83.4	85.8	86.9	81.3	84.8	80.6	85.2	85.1	85.0	83.7	84.9	84.39	84.9

Note: H, host clinopyroxene in the lamellar zone; M, clinopyroxene in the recrystallized granular zone.
b.d. = below detection limit.

Table 6-4 Major-element compositions of orthopyroxene in the garnet pyroxenites from Lakes Bullenmerri and Gnotuk

Sample No.	BM99-2	BME-1	BM99-4				BM99-2		BM96-3	BM99-5	DR9748	GN35	DR10165			BM90-3		BM99-7	BMC-1	DR11022	DR11017c
Type	M	E	M	E	M	H	E	M	M	E	M	E1	M	E1	M	E	M	M	M	M	M
SiO_2	53.30	55.23	54.44	54.55	54.77	55.02	53.49	53.35	54.92	53.32	53.64	54.23	54.28	54.17	54.44	54.44	53.80	53.90	53.98	53.87	54.29
TiO_2	0.08	0.07	0.08	0.11	0.10	0.12	0.06	0.05	0.22	0.25	0.15	0.12	0.10	b.d.	0.10	0.11	0.09	0.11	0.10	b.d.	0.12
Al_2O_3	4.63	4.61	4.60	4.61	4.72	4.79	4.70	4.60	4.12	3.69	4.07	4.99	4.92	4.84	4.77	4.05	4.01	4.10	4.11	4.06	4.15
Cr_2O_3	0.14	0.12	0.12	0.14	0.14	0.15	0.10	0.11	0.06	0.16	0.21	0.19	0.09	0.1	0.08	0.07	0.06	b.d.	0.06	b.d.	0.02
FeO	11.60	9.41	9.43	8.44	9.18	8.57	10.51	10.57	11.69	15.38	13.14	8.47	8.71	9.3	9.45	11.64	11.59	12.05	11.86	11.87	11.40
MnO	0.16	0.12	0.09	0.17	0.19	0.19	0.15	0.16	0.15	0.25	0.22	0.21	0.22	0.12	0.16	0.21	0.17	0.21	0.16	0.16	0.18
MgO	29.7	31.1	30.5	31.2	31.4	31.7	30.6	30.9	29.2	26.6	28.6	31.1	31.0	30.7	30.9	28.6	29.2	29.4	28.7	29.6	29.8
CaO	0.75	0.55	0.60	0.61	0.52	0.51	0.67	0.68	0.77	0.86	0.71	0.69	0.63	0.48	0.56	0.72	0.69	0.67	0.68	0.64	0.64
Na_2O	0.09	0.05	b.d.	0.08	0.10	0.07	0.09	0.08	0.08	0.11	0.08	b.d.	0.08	b.d.	0.06	b.d.	b.d.	0.05	0.05	b.d.	0.02
NiO	0.12	0.12	0.13	b.d.	b.d.	b.d.	0.11	0.11	0.14	0.10	n.d.	n.d.	n.d.	n.d.	n.d.	b.d.	b.d.	0.07	0.08	n.d.	0.06
Total	100.6	101.4	100.0	100.0	101.1	101.1	100.5	100.5	101.4	100.7	100.79	99.97	100.02	99.74	100.49	99.8	99.6	100.5	99.7	100.23	100.64
Mg#	82.0	85.5	85.2	86.8	85.9	86.8	83.8	83.9	81.7	75.5	79.5	86.7	86.4	85.5	85.3	81.4	81.8	81.3	81.2	81.7	82.3
En	0.84	0.84	0.84	0.86	0.86	0.86	0.86	0.87	0.80	0.75	0.80	0.85	0.85	0.85	0.85	0.80	0.81	0.82	0.80	0.82	0.82
Fs	0.15	0.14	0.15	0.13	0.13	0.13	0.13	0.12	0.18	0.23	0.19	0.13	0.13	0.14	0.14	0.18	0.18	0.17	0.19	0.17	0.17
Wo	0.02	0.01	0.01	0.01	0.01	0.01	0.01	0.01	0.02	0.02	0.01	0.01	0.01	0.01	0.01	0.01	0.01	0.01	0.01	0.01	0.01

Note: E, exsolved orthopyroxene in the lamellar zone; M, orthopyroxene in the recrystallized zone; H, host orthopyroxene.
b.d. = below detection limit.

Table 6-5 Major-element compositions of garnet in the garnet pyroxenites from Lakes Bullenmerri and Gnotuk

Rock type	Type I																Type II a			
Sample No.	BM99-2	BM99-6	BM99-4			BME-1		BM99-2			BM96-3	BM99-5	DR9748	GN35		DR10165	BM99X2			GN85-1
Type	C	C	E1	E2	M	E1	C	E1	M	C	C	E1	M	E1	C	M	E1	M	C	C
SiO_2	41.17	41.80	40.87	40.86	41.04	41.85	41.59	41.42	41.46	41.34	41.70	40.57	41.09	41.85	41.83	41.81	40.16	40.02	40.39	39.93
TiO_2	0.08	0.04	0.07	0.08	0.07	0.04	0.04	0.04	0.07	0.04	0.14	0.17	0.10	b.d.	b.d.	b.d.	0.07	0.07	0.07	0.07
Al_2O_3	23.22	24.24	23.50	23.50	23.52	23.31	23.60	23.76	23.54	23.91	22.97	22.64	22.88	23.69	23.37	23.99	23.02	22.93	22.98	22.74
Cr_2O_3	0.45	0.18	0.24	0.25	0.25	0.27	0.24	0.21	0.23	0.26	0.12	0.44	0.64	0.32	0.52	0.17	0.06	0.11	0.10	0.11
FeO	13.29	9.34	10.73	10.52	10.82	10.87	11.70	12.25	12.55	11.88	13.67	16.56	15.03	10.13	10.58	11.64	16.51	16.33	16.15	16.43
MnO	0.41	0.31	0.50	0.51	0.52	0.25	0.30	0.42	0.42	0.42	0.42	0.57	0.56	0.54	0.56	0.44	0.47	0.43	0.44	0.49
MgO	17.40	19.63	19.07	19.25	18.99	17.84	18.63	17.76	18.29	17.74	15.86	14.64	15.45	18.64	18.35	17.73	14.42	14.32	14.12	13.78
CaO	5.30	5.47	4.28	4.20	4.24	5.80	5.42	5.46	5.39	5.46	5.61	5.79	5.81	5.23	5.16	5.53	6.62	6.99	7.21	7.23
Na_2O	b.d.	b.d.	b.d.	b.d.	b.d.	0.24	b.d.	b.d.	b.d.	b.d.	b.d.	0.02	b.d.	b.d.	b.d.	b.d.	b.d.	b.d.	0.02	b.d.
Total	101.3	101.0	99.3	99.2	99.5	100.4	101.5	101.3	102.0	101.0	100.5	101.4	101.6	100.4	100.4	101.3	101.3	101.2	101.5	100.8
Mg#	70.2	79.1	76.2	76.7	76.0	74.7	74.1	72.3	72.4	72.9	67.6	61.4	64.7	76.6	75.6	73.1	61.1	61.2	61.1	60.2
Pyrope	0.64	0.71	0.71	0.71	0.70	0.66	0.68	0.65	0.67	0.65	0.59	0.55	0.58	0.67	0.67	0.64	0.54	0.54	0.53	0.52
Almandine	0.23	0.16	0.19	0.18	0.19	0.20	0.19	0.22	0.20	0.21	0.29	0.30	0.29	0.19	0.21	0.22	0.28	0.27	0.28	0.29
Grossular	0.10	0.14	0.10	0.10	0.10	0.14	0.11	0.13	0.11	0.14	0.13	0.11	0.12	0.13	0.12	0.14	0.15	0.15	0.16	0.16

Continued

Rock type	Type II b																	
Sample No.	BM99-9		BM99X1		BM99-8		GN51	GN18	GN41	DR10162	BM90-3		C-1			BM99-7	DR11022	DR11017c
Type	E1	M	E1	M	E1	M	C	C	C	C	E1	M	E1	M1	M2	M	M	M
SiO_2	41.29	41.37	40.76	40.52	40.99	41.15	40.30	41.15	41.49	42.45	40.75	41.34	40.86	40.85	40.97	40.66	41.27	41.80
TiO_2	0.03	0.03	0.06	0.05	b.d.	b.d.	b.d.	b.d.	b.d.	b.d.	0.08	0.09	0.05	0.06	0.07	0.05	b.d.	0.06
Al_2O_3	22.19	22.30	23.12	23.26	23.90	22.44	23.10	23.40	23.47	23.95	23.30	22.73	23.09	23.27	23.17	23.24	23.34	23.50
Cr_2O_3	0.09	0.10	0.09	0.08	0.10	0.09	b.d.	0.11	0.1	0.14	0.17	0.13	0.10	0.10	0.18	0.08	0.17	0.11
FeO	14.73	14.72	15.06	15.47	12.89	12.50	14.50	12.82	14.88	12.44	13.90	13.88	14.05	14.73	14.48	13.95	13.83	13.74
MnO	0.47	0.47	0.49	0.50	0.42	0.40	0.34	0.32	0.35	0.26	0.56	0.56	0.54	0.54	0.44	0.60	0.61	0.57
MgO	13.09	12.91	15.15	15.19	16.58	15.83	14.40	16.68	15.41	17.36	15.90	16.37	16.04	16.00	15.74	16.68	15.97	16.24
CaO	8.13	8.14	6.32	6.10	6.09	6.43	7.81	5.71	5.97	6.07	5.01	5.23	5.92	5.88	5.97	5.85	5.48	5.66
Na_2O	b.d.	b.d.	0.25	0.03	b.d.	0.28	b.d.	b.d.	b.d.	b.d.	0.39	0.35	0.02	b.d.	b.d.	b.d.	b.d.	b.d.
Total	100.0	100.0	101.3	101.2	100.9	99.1	100.5	100.2	101.7	102.7	100.1	100.7	100.7	101.4	101.0	101.1	100.7	101.68
Mg#	61.5	61.2	64.4	63.9	69.8	69.5	63.90	69.87	64.86	71.33	67.10	67.77	67.06	65.95	65.96	68.07	67.30	67.82
Pyrope	0.47	0.49	0.56	0.57	0.61	0.60	0.54	0.61	0.56	0.62	0.59	0.61	0.60	0.60	0.59	0.62	0.58	0.59
Almandine	0.31	0.31	0.25	0.27	0.23	0.23	0.26	0.24	0.29	0.23	0.24	0.24	0.25	0.26	0.27	0.22	0.27	0.27
Grossular	0.20	0.19	0.16	0.14	0.16	0.16	0.19	0.14	0.15	0.14	0.13	0.13	0.13	0.13	0.14	0.12	0.13	0.13

Note: E, garnet in the lamellar zone; M, garnet in the recrystallized granular zone; C, garnet in the coarse equant zone.
b.d. = below detection limit.

Table 6-6 Major-element compositions of spinel in the garnet pyroxenites from Lakes Bullenmerri and Gnotuk

Sample	BM99-2			BM99-6	BME-1	DR10165		GN35	GN18	DR10162	BMC-1		BM99-7					BM90-3		DR11022	DR11017c
Type	Type I	I	AS	I	Type I	Type II	I	I	I	I	Type II	I	AS	Type I	Type I	Type II	I	E	I	Type II	I
SiO_2	0.07	0.06	0.07	0.09	0.04	b.d.	b.d.	b.d.	b.d.	b.d.	0.06	0.06	0.04	0.06	b.d.	0.10	0.08	0.04	0.05		0.037
TiO_2	0.34	0.10	0.08	0.05	0.05	b.d.	b.d.	0.12	0.10	b.d.	0.14	0.10	0.12	0.21	0.12	0.13	0.11	0.12	0.10	0.13	0.12
Al_2O_3	47.2	59.7	57.7	64.6	61.3	64.2	64.4	64.6	64.4	64.4	62.1	62.6	62.5	59.0	62.5	61.9	62.7	61.9	61.0	62.9	63.9
Cr_2O_3	14.24	3.74	5.55	1.94	4.23	2.84	2.31	3.49	0.41	1.89	1.42	1.62	1.11	3.45	2.37	1.45	1.50	2.27	3.59	1.20	1.21
FeO	22.0	17.8	18.3	11.3	13.8	13.7	13.7	13.0	16.6	15.8	18.1	17.8	17.0	19.4	17.7	17.6	17.3	17.4	17.2	17.6	17.2
MnO	0.11	0.08	0.10	0.07	0.06	b.d.	0.05	0.14	0.12	b.d.	0.10	0.08	0.10	0.13	0.12	0.09	0.10	0.10	0.11		0.10
MgO	14.7	17.3	16.7	20.5	19.1	19.5	19.6	19.6	18.6	18.4	17.2	16.8	18.0	17.2	18.2	17.8	18.0	17.2	16.8	17.8	18.1
CaO	0.02	b.d.	b.d.	0.05	b.d.	b.d.	b.d.	b.d.	0.16	b.d.	b.d.	b.d.	b.d.	b.d.	b.d.	b.d.	b.d.	0.04	0.06		
ZnO	0.18	0.23	0.24	0.13	0.36						0.19	0.17	0.12	0.15	0.19	0.19	0.18	0.17	0.25		
V_2O_3	0.09	0.06	b.d.	0.05	0.06						0.14	0.13	0.11	0.13	0.11	0.11	0.10	0.10	0.15		
NiO	0.42	0.59	0.51	0.65	0.65	0.27	0.24	0.33			0.37	0.39	0.31	0.33	0.34	0.37	0.30	0.27	0.32	0.28	0.41
Total	99.5	99.6	99.3	99.3	99.6	100.5	100.3	101.2	100.4	100.5	99.7	99.8	99.3	100.0	101.6	99.7	100.3	99.6	99.6	99.8	
Mg#	54.4	63.3	62.0	76.3	71.2	71.7	71.9	72.9	66.6	67.5	62.9	62.8	65.3	61.3	64.6	64.4	65.0	63.7	63.4	64.2	65.3
Cr#	16.83	4.04	6.06	1.97	4.42	2.88	2.35	3.50	0.43	1.93	1.51	1.71	1.18	3.77	2.48	1.55	1.58	2.40	3.80	1.27	1.26

Note: Type I, garnet-rimmed spinel without other phases;Type II, garnet-rimmed spinel with olivine and orthopyroxene; AS, amphibole-rimmed spinel; E, exsolved spinel; I, interstitial.
b.d.= below detection limit.

Table 6-7 Major-element compositions of amphibole in the garnet pyroxenites from Lakes Bullenmerri and Gnotuk

Sample ID	BM99-2		BM99-6	BM99-4		BME-1	BM96-3	BM99-5	DR 9748		GN 35	DR 10165	BM 99X1		GN 41	DR 10162	BMC-1		BM90-3	BM99-7	DR 11022	DR 11017
Type	Amp2	Amp3	Amp2	Amp2	Amp3	Amp1	Amp2	Amp1	Amp2	Amp3	Amp2	Amp2	Amp1	Amp2	Amp2	Amp2	Amp1	Amp2	Amp1	Amp2	Amp2	Amp2
SiO_2	42.19	41.78	42.08	41.91	42.66	41.96	41.94	40.90	42.03	42.13	42.89	42.53	41.61	42.20	41.90	42.60	42.77	42.64	41.63	41.95	42.74	42.77
TiO_2	1.57	0.92	1.47	2.56	0.84	1.63	3.97	2.24	3.47	1.62	2.60	2.09	2.55	2.40	2.80	1.30	1.91	1.76	1.70	1.68	1.80	1.55
Al_2O_3	15.49	15.94	16.21	15.55	15.77	15.69	13.36	14.19	14.80	15.64	15.98	15.85	16.04	15.00	15.96	17.22	14.37	14.44	15.40	15.65	15.82	15.84
Cr_2O_3	0.29	0.26	0.24	0.43	0.35	0.35	0.13	0.42	0.54	0.40	0.34	0.29	0.12	0.12	0.13	0.31	0.13	0.12	0.17	0.11		0.11
FeO	6.86	7.14	4.65	5.03	5.34	5.33	6.97	9.72	8.54	8.46	5.92	5.38	7.62	7.65	8.16	6.56	7.18	7.12	6.75	6.82	6.72	7.57
MnO	0.06	0.06	0.04	0.07	0.10	0.05	0.05	0.10		0.09	0.10		0.07	0.08	0.04		0.09	0.08	0.08	0.08	0.10	0.08
MgO	15.98	15.90	17.08	16.71	16.88	16.70	14.48	14.05	14.93	14.68	16.78	16.78	14.98	14.15	14.63	15.89	15.62	15.59	16.21	16.50	16.48	16.51
CaO	10.58	10.53	11.03	11.00	10.98	11.04	11.41	10.42	10.65	10.56	10.51	11.10	10.77	10.90	10.57	11.31	11.22	11.05	11.23	11.34	11.24	10.96
Na_2O	3.28	3.01	3.36	3.93	3.44	3.58	2.50	3.21	3.35	2.80	3.69	3.60	3.53	3.39	3.85	2.91	3.45	3.48	3.46	3.28	3.23	3.58
K_2O	0.97	1.56	0.57	0.07	0.90	0.10	1.81	1.03	0.30	1.72	0.36	0.14	0.50	0.61	0.10	1.10	0.20	0.16	0.14	0.42	0.38	0.15
NiO	0.12	0.14	0.14	b.d.	b.d.	0.14	0.16	b.d.	0.14	0.11	0.11		0.11	b.d.			b.d.	0.10	0.12	0.11		0.08
Cl	0.07	0.09	0.07	0.04	0.04		0.18	0.04					0.15	0.20			b.d.	b.d.	0.03	0.06		
F	b.d.		b.d.	b.d.	b.d.	0.13	b.d.	0.07					0.06	0.09			0.31	0.29	0.22	0.18		
Total	97.43	97.26	96.91	97.29	97.26	96.59	96.96	96.35	98.75	98.21	99.26	97.76	98.02	96.78	98.14	99.20	97.21	96.68	97.02	98.07	98.51	99.19
Mg#	80.60	79.87	86.75	85.55	84.94	84.81	78.75	72.04	75.71	75.57	83.49	84.76	77.80	76.72	76.17	81.20	79.51	79.59	81.08	81.19	81.38	79.55
Structure Formula																						
Si	6.06	6.01	6.02	5.99	6.08	6.03	6.21	6.04	6.02	6.07	6.01	6.04	5.98	6.19	6.01	6.00	6.19	6.19	6.00	5.98	6.04	6.01
Ti	0.17	0.10	0.16	0.28	0.09	0.18	0.44	0.25	0.37	0.18	0.27	0.22	0.28	0.26	0.30	0.14	0.21	0.19	0.18	0.18	0.19	0.16
Al	2.62	2.70	2.73	2.62	2.65	2.66	2.33	2.47	2.50	2.65	2.64	2.65	2.72	2.59	2.70	2.86	2.45	2.47	2.62	2.63	2.63	2.62
Cr	0.03	0.03	0.03	0.05	0.04	0.04	0.02	0.05	0.06	0.05	0.04	0.03	0.01	0.01	0.01	0.03	0.01	0.01	0.02	0.01	0.00	0.01
Fe^{3+}	0.29	0.45	0.18	0.15	0.31	0.20	0.00	0.28	0.04	0.21	0.17	0.13	0.12	0.00	0.07	0.16	0.02	0.05	0.29	0.35	0.27	0.37
Fe^{2+}	0.53	0.41	0.38	0.46	0.33	0.44	0.86	0.92	0.98	0.81	0.52	0.50	0.79	0.94	0.90	0.62	0.85	0.82	0.52	0.46	0.52	0.52
Mn	0.01	0.01	0.01	0.01	0.01	0.01	0.01	0.01	0.00	0.01	0.01	0.00	0.01	0.01	0.00	0.00	0.01	0.01	0.01	0.01	0.01	0.01
Mg	3.42	3.41	3.64	3.56	3.59	3.58	3.20	3.09	3.19	3.15	3.51	3.55	3.21	3.09	3.13	3.34	3.37	3.38	3.48	3.51	3.47	3.46
Ca	1.63	1.62	1.69	1.68	1.68	1.70	1.81	1.65	1.64	1.63	1.58	1.69	1.66	1.71	1.62	1.71	1.74	1.72	1.73	1.73	1.70	1.65
Na	0.91	0.84	0.93	1.09	0.95	1.00	0.72	0.92	0.93	0.78	1.00	0.99	0.98	0.96	1.07	0.79	0.97	0.98	0.97	0.91	0.88	0.98
K	0.18	0.29	0.10	0.01	0.16	0.02	0.34	0.19	0.05	0.32	0.06	0.03	0.09	0.11	0.02	0.20	0.04	0.03	0.03	0.08	0.07	0.03
F	0.03	0.04	0.03	0.02	0.02	0.00	0.09	0.02	0.00	0.00	0.00	0.00	0.07	0.09	0.00	0.00	0.00	0.00	0.01	0.03	0.00	0.00
Cl	0.00	0.00	0.00	0.00	0.00	0.03	0.00	0.02	0.00	0.00	0.00	0.00	0.01	0.02	0.00	0.00	0.07	0.07	0.05	0.04	0.00	0.00
$Mg/Mg+Fe^{2+}$	0.87	0.89	0.91	0.89	0.92	0.89	0.79	0.77	0.77	0.80	0.87	0.88	0.80	0.77	0.78	0.84	0.80	0.80	0.87	0.88	0.87	0.87

Note: Amp1, amphibole in lamellar zone; Amp2, amphibole in recrystallized granular zone; Amp3, amphibole vein.

Table 6-8 Major-element compositions of olivine, ilmenite, phlogopite, apatite and plagioclase in the garnet pyroxenites from Lakes Bullenmerri and Gnotuk

Mineral	Ol				Ilm	Phl			Ap				Pl				
Sample No.	BM99-2	BMC-1	BM90-3	BM99-7	BM99-5	BM96-3			BME-1	BM99X1	BM99-7	BMC-1	BM99X1		BM99-8	BM99-9	
Type	M	M	M	M	E	Core	Rim 1	Rim 2	M	M	M	M	E	M	M	Inc	E
SiO_2	39.5	39.7	39.8	39.2	0.0	36.3	35.3	33.5					59.4	59.1	56.5	57.4	56.4
TiO_2					47.12	6.50	10.24	11.54									
Al_2O_3	0.03		0.04	0.03	0.35	15.49	15.62	15.66					26.06	26.09	27.03	27.56	26.37
Cr_2O_3				0.04	0.51	0.14	0.20										
FeO	18.0	20.5	19.5	20.1	39.4	7.90	9.01	10.75					0.15	0.13	0.11	0.22	0.17
MnO	0.15	0.21	0.21	0.20	0.35	0.04	0.06	0.08									
MgO	41.6	39.2	41.9	41.3	6.99	16.61	14.03	11.52									
CaO	0.07	0.07	0.05	0.06	0.08	0.05	0.05	0.08	52.5	52.43	53.18	53.5	7.46	7.58	8.94	10.38	9.98
Na_2O						0.51	0.42	0.30					7.40	7.40	6.15	5.65	6.06
K_2O						8.45	8.20	7.64					0.20	0.21	0.40	0.06	0.05
P_2O_5									40.79	39.46	41.01	41.02					
NiO	0.48	0.27	0.22	0.27	0.15	0.30	0.22										
Cl						0.27	0.10	0.08	0.29	2.2	0.89	0.2					
F						0.07	0.12	0.12	0.98	0.63	1.11	1.51					
Total	99.9	100.0	101.7	101.2	95.3	92.5	93.5	91.3	94.6	94.7	96.2	96.2	100.7	100.5	99.1	101.3	99.0
Mg#	80.4	77.3	79.3	78.5	24.0	78.9	73.5	65.6									

Note: E, minerals in the lamellar zone; M, minerals in the recrystallized granular zone; Inc, inclusion.

Table 6-9 Trace-element compositional profile of BM99X2 by LA-ICPMS (line A-B shown in Fig. 6-2e)

Texture	Lamellar zone										Recrystallized zone										Coarse Zone	
Sr	13.17	12.98	13.75	13.86	0.06	0.48	0.30	0.07	13.08	0.03	0.01	13.68	13.24	13.12	0.02	0.05	0.03	13.57	14.06	13.88	13.78	14.77
Y	1.09	1.10	1.21	1.26	17.53	17.85	16.79	17.58	1.13	17.30	18.60	1.68	1.40	1.39	20.29	19.95	23.30	1.82	1.83	2.29	2.39	3.05
Zr	2.27	2.36	2.14	2.01	1.74	1.66	1.37	1.65	2.53	1.61	1.56	2.62	2.81	2.96	1.46	1.42	2.23	3.50	3.46	3.64	3.86	4.21
Nb	0.11	0.11	0.13	0.13	b.d.	0.02	0.01	0.00	0.11	0.01	0.01	0.17	0.12	0.11	0.01	0.01	0.02	0.17	0.21	0.15	0.14	0.22
Ba	0.01	b.d.	0.10	0.02	b.d.	0.70	0.47	0.08	0.01	b.d.	b.d.	b.d.	0.01	0.01	b.d.	0.07	b.d.	0.01	0.01	0.02	0.02	0.60
La	0.50	0.51	0.56	0.58	0.00	0.02	0.01	0.01	0.51	b.d.	b.d.	0.60	0.55	0.52	b.d.	b.d.	b.d.	0.55	0.60	0.58	0.55	0.70
Ce	0.66	0.68	0.82	0.76	0.01	0.04	0.02	0.01	0.66	0.01	0.01	0.84	0.71	0.71	0.01	0.03	0.02	0.84	0.82	0.78	0.85	0.95
Pr	0.06	0.06	0.08	0.08	b.d.	0.01	0.01	b.d.	0.07	b.d.	b.d.	0.06	0.07	0.07	0.01	0.00	b.d.	0.09	0.08	0.10	0.09	0.12
Nd	0.54	0.47	0.59	0.50	0.05	0.12	0.06	0.07	0.54	0.07	0.09	0.62	0.56	0.58	0.09	0.09	0.08	0.60	0.63	0.60	0.67	0.63
Sm	0.55	0.57	0.58	0.56	0.36	0.38	0.37	0.37	0.61	0.36	0.24	0.58	0.59	0.69	0.29	0.34	0.35	0.67	0.66	0.54	0.66	0.69
Eu	0.25	0.23	0.25	0.24	0.29	0.32	0.30	0.29	0.27	0.30	0.29	0.30	0.28	0.30	0.28	0.30	0.37	0.28	0.31	0.29	0.28	0.30
Gd	0.75	0.76	0.80	0.81	1.64	1.74	1.61	1.60	0.79	1.83	2.08	0.87	0.92	0.89	1.84	1.89	1.90	1.04	1.00	1.06	1.08	1.14
Tb	0.09	0.10	0.09	0.09	0.43	0.43	0.41	0.41	0.10	0.45	0.45	0.13	0.13	0.12	0.46	0.46	0.56	0.13	0.13	0.15	0.13	0.15
Dy	0.41	0.43	0.43	0.46	3.39	3.50	3.26	3.27	0.47	3.51	3.64	0.58	0.55	0.57	3.98	3.91	4.30	0.63	0.66	0.75	0.81	0.87
Ho	0.06	0.06	0.05	0.06	0.68	0.73	0.65	0.71	0.04	0.69	0.74	0.07	0.07	0.07	0.80	0.78	0.90	0.08	0.09	0.10	0.11	0.14
Er	0.07	0.09	0.08	0.10	1.87	1.81	1.74	1.86	0.08	1.71	1.95	0.11	0.08	0.09	2.05	1.92	2.40	0.13	0.11	0.18	0.17	0.21
Tm	b.d.	0.01	0.01	0.01	0.22	0.24	0.23	0.23	b.d.	0.21	0.23	0.01	0.01	0.01	0.25	0.26	0.29	0.01	0.01	0.02	0.01	0.03
Yb	0.03	0.05	0.03	0.04	1.41	1.21	1.29	1.38	0.03	1.30	1.52	0.07	0.02	0.03	1.49	1.48	1.82	0.05	0.04	0.06	0.08	0.12
Lu	b.d.	b.d.	0.01	0.01	0.16	0.17	0.16	0.17	0.01	0.16	0.19	b.d.	0.00	0.00	0.20	0.19	0.22	0.00	0.00	0.02	0.01	0.02
Hf	0.26	0.24	0.22	0.27	0.06	0.06	0.04	0.07	0.23	0.04	0.05	0.26	0.24	0.26	0.03	0.03	0.04	0.32	0.29	0.37	0.39	0.40
Ta	0.00	b.d.	b.d.	0.00	0.00	b.d.	0.00	b.d.	b.d.	b.d.	b.d.	0.01	b.d.	b.d.	b.d.	0.00	b.d.	0.01	b.d.	b.d.	b.d.	0.01
Pb	0.07	0.09	0.08	0.12	0.02	0.50	b.d.	0.03	0.11	b.d.	b.d.	0.10	0.07	0.06	b.d.	0.03	b.d.	0.12	0.36	0.06	0.08	0.09
Th	0.08	0.08	0.10	0.12	b.d.	b.d.	b.d.	b.d.	0.09	b.d.	b.d.	0.16	0.09	0.09	0.01	b.d.	b.d.	0.11	0.13	0.13	0.08	0.14
U	0.02	0.02	0.03	0.03	b.d.	b.d.	0.01	0.01	0.02	b.d.	b.d.	0.02	0.01	0.01	b.d.	b.d.	0.01	0.02	0.03	0.02	0.02	0.03

Continued

Texture	Coarse Zone										Single Gt compositional profile												
Sr	14.47	14.68	14.37	14.40	14.51	14.66	15.08	0.02	0.02	0.03	*0.03*	*0.02*	*0.04*	*0.02*	*0.02*	*0.21*	*0.04*	*0.07*	14.59	14.89	14.69	14.61	14.09
Y	3.11	2.92	2.83	2.74	2.97	2.98	2.44	34.94	35.45	35.25	*34.68*	*35.74*	*35.53*	*35.25*	*35.27*	*37.89*	*40.11*	*42.95*	3.05	2.94	3.12	2.93	3.01
Zr	3.83	3.69	3.85	3.82	3.67	3.63	3.62	2.21	2.10	1.93	*2.03*	*1.95*	*1.89*	*1.96*	*1.88*	*2.70*	*2.01*	*2.15*	5.11	4.48	4.87	4.20	4.02
Nb	0.21	0.18	0.18	0.15	0.17	0.20	0.26	0.01	0.02	0.02	*b.d.*	*b.d.*	*b.d.*	*0.01*	*b.d.*	*0.07*	*b.d.*	*b.d.*	0.18	0.16	0.17	0.24	0.18
Ba	0.02	0.02	0.01	0.02	0.04	0.03	0.15	b.d.	0.01	b.d.	*b.d.*	*b.d.*	*b.d.*	*b.d.*	*b.d.*	*0.25*	*b.d.*	*0.01*	0.04	0.05	0.08	0.03	0.01
La	0.65	0.64	0.61	0.56	0.61	0.66	0.64	b.d.	0.00	b.d.	*0.00*	*b.d.*	*b.d.*	*b.d.*	*0.01*	*0.09*	*b.d.*	*b.d.*	0.61	0.67	0.67	0.59	0.55
Ce	0.84	0.84	0.84	0.75	0.87	0.91	0.81	0.02	0.02	0.02	*0.02*	*0.03*	*0.02*	*0.02*	*b.d.*	*0.24*	*0.03*	*0.03*	0.72	0.82	0.76	0.84	0.78
Pr	0.07	0.10	0.09	0.08	0.08	0.08	0.09	0.01	0.01	0.00	*b.d.*	*b.d.*	*0.02*	*b.d.*	*b.d.*	*0.05*	*0.02*	*b.d.*	0.08	0.08	0.07	0.09	0.09
Nd	0.66	0.68	0.36	0.58	0.56	0.68	0.54	0.04	0.11	0.09	*b.d.*	*0.15*	*b.d.*	*0.07*	*0.10*	*0.22*	*0.06*	*b.d.*	0.70	0.53	0.63	0.67	0.74
Sm	0.60	0.50	0.64	0.61	0.64	0.63	0.65	0.35	0.29	0.31	*0.38*	*0.41*	*0.35*	*0.32*	*0.36*	*0.45*	*0.32*	*0.38*	0.62	0.57	0.61	0.74	0.73
Eu	0.26	0.30	0.30	0.31	0.26	0.30	0.25	0.28	0.27	0.27	*0.28*	*0.28*	*0.31*	*0.29*	*0.30*	*0.29*	*0.31*	*0.36*	0.27	0.30	0.30	0.34	0.32
Gd	1.14	1.05	1.05	1.07	1.04	1.01	0.98	2.16	2.03	2.02	*2.02*	*2.05*	*2.00*	*1.97*	*2.00*	*1.99*	*2.15*	*1.96*	1.16	1.24	1.07	1.05	1.13
Tb	0.16	0.14	0.15	0.15	0.14	0.17	0.14	0.58	0.60	0.58	*0.58*	*0.58*	*0.58*	*0.59*	*0.61*	*0.56*	*0.63*	*0.60*	0.16	0.15	0.16	0.16	0.18
Dy	0.86	0.90	0.83	0.76	0.83	0.88	0.79	5.44	5.36	5.45	*5.49*	*5.48*	*5.60*	*5.58*	*5.58*	*5.85*	*5.78*	*6.65*	0.84	0.85	0.86	0.95	0.92
Ho	0.17	0.12	0.13	0.13	0.14	0.15	0.10	1.35	1.40	1.39	*1.36*	*1.39*	*1.39*	*1.42*	*1.38*	*1.56*	*1.59*	*1.63*	0.15	0.13	0.15	0.13	0.13
Er	0.28	0.21	0.27	0.22	0.24	0.29	0.22	4.21	4.57	4.56	*4.06*	*4.28*	*4.33*	*4.41*	*3.93*	*4.96*	*5.28*	*5.81*	0.24	0.28	0.32	0.20	0.28
Tm	0.02	0.03	0.02	0.02	0.02	0.02	0.02	0.59	0.69	0.68	*0.60*	*0.65*	*0.65*	*0.64*	*0.61*	*0.75*	*0.83*	*0.87*	0.02	0.04	0.03	0.03	0.03
Yb	0.13	0.15	0.10	0.12	0.11	0.13	0.11	3.80	5.02	5.22	*4.17*	*4.63*	*4.86*	*4.78*	*4.83*	*5.17*	*6.34*	*6.18*	0.15	0.16	0.14	0.13	0.11
Lu	0.02	0.02	0.01	0.02	0.01	0.01	b.d.	0.51	0.78	0.76	*0.60*	*0.70*	*0.73*	*0.72*	*0.57*	*0.78*	*0.93*	*1.02*	0.02	0.02	0.01	0.01	0.01
Hf	0.32	0.34	0.35	0.39	0.31	0.29	0.31	0.08	0.75	0.05	*0.05*	*0.06*	*0.05*	*0.07*	*0.12*	*0.08*	*b.d.*	*0.12*	0.42	0.43	0.35	0.35	0.33
Ta	b.d.	b.d.	b.d.	b.d.	0.01	0.01	0.01	0.00	b.d.	0.01	*b.d.*	*b.d.*	*b.d.*	*b.d.*	*b.d.*	*0.02*	*b.d.*	*b.d.*	b.d.	b.d.	b.d.	0.01	b.d.
Pb	0.09	0.10	0.10	0.13	0.09	0.13	0.09	b.d.	b.d.	b.d.	*b.d.*	*b.d.*	*0.03*	*b.d.*	*b.d.*	*b.d.*	*b.d.*	*b.d.*	0.12	0.19	0.07	0.12	0.11
Th	0.13	0.17	0.15	0.12	0.13	0.14	0.18	b.d.	b.d.	b.d.	*b.d.*	*0.02*	*b.d.*	*b.d.*	*0.01*	*b.d.*	*0.01*	*b.d.*	0.15	0.20	0.16	0.16	0.13
U	0.03	0.03	0.03	0.03	0.03	0.03	0.05	0.01	0.04	0.01	*0.01*	*b.d.*	*b.d.*	*b.d.*	*b.d.*	*0.02*	*b.d.*	*0.02*	0.03	0.03	0.04	0.03	0.02

Table 6-10 Trace-element compositional profile of garnet around spinel in DR11017c by LA-ICPMS

Element	Gt1	Gt2	Gt3	Gt4	Gt4	Gt6	Gt7	Gt8	Gt9	Gt10
						rim-core-rim				
Sc	130	129	137	132	131	132	129	128	128	129
Ti	430	414	372	472	546	550	561	545	533	492
V	95	101	83	96	107	104	108	104	101	100
Cr	1147	1090	568	937	1004	967	915	846	933	827
Co	54.1	53.9	54.7	53.2	55.3	53.5	53.4	53.4	53.2	52.4
Ni	23.6	23.9	23.5	21.9	21.3	19.3	19.6	20.2	20.4	21.2
Zn	9.23	9.05	8.77	8.43	8.25	7.94	8.08	8.07	7.82	8.64
Ga	4.17	4.19	2.57	4.14	5.20	5.55	5.31	5.13	5.19	4.73
Sr	0.08	0.08	0.08	0.11	0.10	0.10	0.11	0.12	0.09	0.08
Y	65.1	62.5	67.9	60.2	48.3	45.6	44.5	47.1	50.2	61.4
Zr	15.8	14.5	15.8	17.1	16.6	17.3	17.4	17.1	16.6	16.4
Nb	0.01	0.01	0.01	<0.006	0.01	0.01	<0.006	<0.006	<0.006	0.01
La	0.02	0.01	0.01	0.01	0.02	<0.0105	0.02	0.02	0.02	0.02
Ce	0.25	0.31	0.26	0.30	0.29	0.30	0.32	0.33	0.24	0.27
Pr	0.16	0.15	0.13	0.15	0.16	0.19	0.19	0.18	0.15	0.16
Nd	2.19	2.05	2.04	2.34	2.63	2.79	2.70	2.45	2.24	2.18
Sm	2.34	2.39	2.34	2.56	2.68	2.46	2.70	2.52	2.47	2.50
Eu	1.17	1.10	1.14	1.21	1.18	1.21	1.20	1.14	1.16	1.19
Gd	5.80	5.43	5.70	5.58	5.32	5.52	5.18	5.36	5.38	5.87
Dy	9.68	9.42	10.46	9.36	7.84	7.72	7.59	7.93	8.13	9.12
Er	7.44	6.91	8.08	6.53	4.89	4.83	4.81	4.79	5.31	6.82
Yb	7.80	7.61	8.92	7.04	4.94	4.77	4.53	4.58	4.94	7.22
Lu	1.14	1.10	1.31	1.00	0.71	0.64	0.62	0.66	0.71	1.08
Hf	0.26	0.27	0.26	0.23	0.30	0.27	0.31	0.27	0.27	0.33

Table 6-11 Trace-element composition of clinopyroxene, garnet and amphibole from different textures in DR10165 by LA-ICPMS

Clinopyroxene	Lamellae zone A						Recrystallized zone B							Recrystallized zone C				
Sc	27.85	30.11	30.98	30.42	33.65	36.33	33.78	32.29	31.47	31.17	29.29	43.31	46.70	38.62	40.77	38.97	38.15	39.33
Ti	2949.66	3198.19	3295.48	3062.68	3227.19	2967.85	3269.39	3125.65	2994.62	2884.39	3110.00	3332.07	3543.81	2964.71	3493.50	3218.58	3251.32	3270.25
V	194.60	192.94	205.83	199.61	204.94	196.09	198.38	200.16	200.67	200.55	198.79	198.13	196.76	184.93	190.99	190.77	193.33	195.23
Cr	1421.49	1278.98	1340.61	1294.19	1273.64	1150.25	1212.98	1224.79	1202.96	1204.04	1284.11	1214.07	1234.11	1234.13	1224.61	1212.94	1232.77	1258.88
Co	23.94	23.44	25.69	25.33	23.95	22.76	23.54	23.75	23.42	23.83	22.76	22.18	23.83	24.03	23.36	22.80	22.62	23.33
Ni	295.18	289.72	294.68	297.52	290.14	275.40	290.86	290.72	286.44	289.65	276.50	251.06	259.79	261.03	260.42	256.09	254.33	260.90
Cu	0.98	1.04	1.04	1.13	1.24	1.02	1.09	1.01	0.98	0.99	1.05	1.12	1.19	1.09	1.06	0.94	0.97	0.99
Zn	5.59	5.96	6.40	6.49	6.45	7.19	6.19	6.51	6.26	6.46	6.07	20.81	6.25	6.77	6.34	6.40	6.01	6.24
Ga	4.28	4.44	4.47	4.14	3.60	2.82	3.57	3.78	3.69	3.70	4.07	2.49	2.66	2.83	3.02	2.95	2.95	2.94
Sr	130.06	128.55	127.27	126.76	144.89	142.06	136.54	137.85	138.39	137.65	139.31	143.99	141.29	135.37	136.05	140.19	140.11	137.41
Y	2.96	2.76	2.78	2.79	3.65	4.02	3.89	3.84	3.83	3.65	3.73	7.25	6.66	7.08	6.25	6.90	6.89	6.40
Zr	20.80	22.25	22.44	21.89	23.16	23.85	24.25	23.00	22.50	21.84	22.30	29.02	30.92	26.55	29.41	27.26	27.43	27.87
Nb	0.09	0.09	0.06	0.06	0.09	0.10	0.13	0.14	0.11	0.12	0.12	0.15	0.12	0.16	0.14	0.14	0.14	0.16
Ba	0.11	0.12	0.10	0.11	0.16	0.14	0.13	0.12	0.12	0.12	0.12	0.14	0.15	0.50	0.13	0.14	0.13	0.16
La	8.03	8.04	8.13	8.07	8.61	8.40	8.57	8.36	8.28	8.35	8.81	9.12	9.23	8.52	8.78	8.82	8.76	8.91
Ce	24.99	24.39	25.02	24.49	27.07	25.97	27.31	28.04	27.25	26.98	26.81	27.29	27.93	26.29	26.93	27.00	27.19	27.26
Pr	3.66	3.70	3.57	3.55	4.19	3.82	4.09	4.05	3.95	3.91	3.99	4.11	4.31	3.98	4.08	4.05	4.10	4.10
Nd	15.64	15.68	15.16	14.64	17.51	17.82	17.10	16.98	16.59	16.44	16.90	17.48	18.02	17.00	16.94	17.49	17.55	17.48
Sm	2.67	2.52	2.36	2.39	2.94	2.52	2.90	2.73	2.87	2.62	2.79	2.64	3.21	2.86	3.08	3.09	3.06	2.86
Eu	0.73	0.77	0.70	0.76	0.78	0.88	0.86	0.84	0.85	0.82	0.78	0.98	0.92	0.88	0.91	0.88	0.94	0.92
Gd	1.74	1.74	1.64	1.51	1.85	1.80	1.96	1.96	1.93	1.86	1.81	2.49	2.52	2.21	2.38	2.43	2.50	2.30
Dy	0.91	0.91	0.82	0.88	1.03	1.14	1.13	1.14	1.12	1.11	1.03	1.53	1.86	1.73	1.71	1.62	1.74	1.75
Er	0.19	0.26	0.20	0.22	0.35	0.27	0.33	0.33	0.27	0.29	0.30	0.53	0.64	0.71	0.54	0.58	0.63	0.57
Yb	0.09	0.09	0.10	0.10		0.09	0.10	0.10	0.15	0.09	0.17	0.40	0.23	0.48	0.31	0.34	0.31	0.31
Lu	0.01	0.01	0.01	0.01	0.03	0.02	0.01	0.01	0.01	0.01	0.01	0.03		0.06	0.03	0.04	0.04	0.03
Hf	0.61	0.58	0.63	0.63	0.61	0.63	0.61	0.61	0.76	0.57	0.61	0.65	0.83	0.61	0.70	0.68	0.68	0.69
Ta	0.03	0.02	0.02	0.01	0.03		0.02	0.02	0.02	0.02	0.03	0.03	0.02	0.02	0.03	0.03	0.02	0.02
Pb	0.54	0.52	0.55	0.57	0.56	0.51	0.58	0.54	0.54	0.52	0.55	0.56	0.56	0.56	0.56	0.56	0.52	0.51
Th	0.44	0.46	0.48	0.45	0.46	0.55	0.45	0.43	0.41	0.43	0.44	0.44	0.47	0.44	0.50	0.46	0.42	0.50
U	0.10	0.09	0.11	0.10	*0.08*	*0.08*	0.11	0.09	0.08	0.09	0.08	*0.08*		0.10	0.10	0.09	0.09	0.09

Continue

Garnet	Lamellae zone A				Recrystallized zone B									Recrystallized zone C			
Sc	80.59	75.61	89.04	89.62	98.64	100.49	99.50	104.66	97.38	96.70	92.48	96.35	88.84	113.54	113.96	101.48	98.68
Ti	332.06	379.46	492.47	474.07	397.84	380.65	343.73	399.16	389.21	401.09	380.57	405.92	350.84	343.62	375.29	331.34	333.76
V	56.45	60.48	56.23	55.75	46.45	43.80	46.27	43.01	43.81	41.40	46.52	46.36	46.00	57.49	52.95	53.19	55.04
Cr	1593.37	1483.27	1434.71	1420.65	1398.02	1485.61	1494.82	1358.83	1296.83	1216.39	1419.18	1226.54	999.18	1571.22	1422.34	1476.01	1561.79
Co	51.38	50.63	53.56	53.94	52.37	51.98	52.65	51.11	51.51	50.86	50.81	51.23	49.74	48.09	45.69	46.19	47.17
Ni	29.45	31.28	30.40	30.47	30.57	30.55	30.59	29.09	28.80	28.10	29.93	28.96	29.40	28.30	28.98	25.45	25.94
Cu	0.20	0.62		0.06	0.17	0.06			0.19	0.13	0.10			0.14	0.28		
Zn	6.28	5.99	6.79	6.67	117.61	6.78	7.70	7.43	6.53	6.72	6.87	6.75	6.76	8.69	5.90	6.19	7.79
Ga	2.97	2.73	2.59	2.41	1.41	1.58	1.66	1.50	1.47	1.50	1.72	1.58	1.66	1.93	1.61	2.40	2.33
Sr	0.06	0.67	0.07	0.07	0.09	0.09	0.09	0.09	0.08	0.18	0.13	0.08	0.08	0.23	2.20	0.21	0.09
Y	24.26	23.90	23.29	23.59	32.54	38.14	37.06	37.31	33.60	34.52	31.69	31.76	34.78	60.84	58.58	61.24	57.90
Zr	11.67	12.00	14.62	14.36	11.52	11.98	12.24	12.55	12.33	12.19	11.30	12.23	14.19	13.57	13.17	14.28	13.26
Nb		0.03			0.01	0.01	0.01	0.01			0.01	0.01		0.02	0.08	0.01	0.01
Ba		0.73			0.06		0.01			0.19	0.07			0.07	0.65	0.09	0.05
La		0.07		0.01		0.02	0.02	0.01		0.02	0.03	0.01	0.03	0.02	0.11	0.13	0.01
Ce	0.10	0.28	0.11	0.13	0.21	0.21	0.22	0.18	0.20	0.20	0.20	0.20	0.19	0.23	0.65	0.30	0.15
Pr	0.05	0.07	0.05	0.06	0.07	0.10	0.09	0.09	0.08	0.10	0.09	0.09	0.08	0.10	0.12	0.08	0.05
Nd	0.70	0.69	0.73	0.81	0.80	0.92	0.97	0.88	0.95	1.08	0.82	0.99	0.94	0.66	0.74	0.78	0.61
Sm	0.63	0.59	0.83	0.71	1.16	0.75	0.68	0.88	0.84	0.75	0.75	0.84	0.84	0.58	1.05	0.71	0.67
Eu	0.38	0.39	0.47	0.48	0.49	0.47	0.41	0.44	0.48	0.49	0.50	0.50	0.46	0.38	0.52	0.46	0.44
Gd	1.56	1.46	1.78	1.88	1.78	2.09	1.90	2.30	2.21	2.26	2.00	2.14	2.08	2.14	1.86	2.28	2.13
Dy	3.48	3.47	3.56	3.61	5.00	5.20	5.14	5.24	4.50	4.97	4.41	4.73	5.20	6.49	7.13	6.99	6.76
Er	3.01	2.80	2.46	2.51	4.23	4.34	4.24	4.20	3.98	3.95	3.83	3.64	4.63	7.58	7.49	7.89	7.36
Yb	3.17	2.87	2.63	2.43	4.32	4.49	4.17	4.36	4.54	5.04	4.18	4.43	4.82	10.24	10.13	11.03	10.69
Lu	0.52	0.44	0.34	0.39	0.66	0.59	0.58	0.61	0.66	0.74	0.65	0.63	0.79	1.95	1.56	1.83	1.69
Hf	0.09	0.11	0.16	0.13		0.09	0.11	0.11	0.09	0.04	0.12	0.09	0.17	0.15	0.23	0.17	0.13

Continued

Amphibole	Recrystallized zone B											Recrystallized zone C			
Li	1.36	1.46	1.40	1.73	1.71	1.64	1.69	1.45	1.39	1.66	1.45	1.55	1.49	1.83	1.82
Be	0.30	0.38	0.33	0.31	0.30	0.29	0.27	0.33	0.27	0.27	0.27	0.30	0.28	0.27	0.23
B	9.48	10.13	3.60	3.09	2.98	3.34	3.03	2.67	2.51	2.52	2.76	2.72	2.68	3.10	3.01
Sc	26.18	27.80	27.58	26.80	26.94	28.34	27.64	29.35	28.30	31.22	32.94	36.50	37.07	45.08	40.19
Ti	12817	13056	13215	13239	13112	12037	12699	13650	13239	13505	12854	12600	12789	13282	12871
V	300	287	295	307	310	281	293	291	288	283	273	270	276	267	257
Cr	1967	1769	1961	2043	2093	1834	2028	1827	1762	2002	1658	1561	1652	1351	1329
Co	45.57	42.71	46.40	47.57	48.20	47.81	46.86	45.17	45.96	44.76	44.48	46.99	48.68	47.80	47.85
Ni	691	658	715	734	754	753	736	702	710	682	667	693	714	712	732
Cu	2.90	2.38	1.00	1.31	1.04	0.38	0.62	0.63	0.71	0.79	0.48	0.89	0.75	0.77	0.88
Zn	10.31	10.24	8.98	9.21	9.37	9.22	8.67	8.72	10.02	8.75	8.90	9.47	9.57	9.31	9.23
Ga	32.70	39.29	18.70	18.49	19.32	17.44	17.68	20.54	19.76	20.81	20.55	20.96	19.62	21.55	21.63
Rb	2.16	2.01	2.19	2.18	2.29	1.71	1.87	2.22	2.16	2.51	2.82	3.06	3.14	2.95	3.12
Sr	491	548	517	532	529	480	506	560	550	570	554	563	536	565	562
Y	4.56	5.98	4.80	4.70	4.55	4.74	4.87	6.47	6.08	7.14	9.12	10.68	10.61	12.83	11.80
Zr	20.17	21.79	21.24	20.22	19.97	20.84	20.49	23.07	22.72	24.41	24.43	25.66	25.70	25.58	24.86
Nb	8.11	10.09	7.92	8.22	8.23	5.18	6.57	9.93	10.10	11.66	11.44	11.84	11.29	12.77	12.39
Ba	114	146	120	119	127	104	109	153	148	162	168	174	152	173	173
La	10.62	12.27	11.08	11.63	11.82	10.87	10.89	12.79	12.08	13.48	12.20	12.78	11.96	12.41	12.84
Ce	32.56	36.90	33.33	35.52	36.22	32.43	32.97	37.42	37.34	40.01	37.20	39.10	36.61	37.20	38.23
Pr	4.90	5.67	5.16	5.37	5.30	4.85	5.06	5.80	5.77	6.09	5.68	5.99	5.56	5.68	5.91
Nd	21.14	24.38	23.02	23.64	22.43	21.02	22.42	25.18	24.40	26.66	25.49	25.94	24.34	25.20	25.94
Sm	4.19	4.27	4.09	4.07	4.03	3.75	3.94	4.43	4.03	4.56	4.68	4.59	4.23	4.20	4.58
Eu	0.98	1.28	1.23	1.19	1.25	1.15	1.12	1.28	1.31	1.35	1.36	1.45	1.34	1.42	1.50
Gd	2.37	3.06	2.78	2.80	2.90	2.78	2.54	3.17	3.32	3.43	3.67	3.73	3.69	3.79	3.70
Tb	0.26	0.42	0.32	0.32	0.32	0.29	0.29	0.40	0.35	0.41	0.42	0.49	0.47	0.50	0.52
Dy	1.41	1.77	1.49	1.42	1.48	1.40	1.42	1.77	1.74	1.94	2.36	2.86	2.54	2.94	2.79
Ho	0.14	0.20	0.19	0.20	0.19	0.21	0.18	0.25	0.24	0.28	0.36	0.41	0.41	0.54	0.48
Er	0.47	0.54	0.33	0.32	0.35	0.40	0.38	0.40	0.51	0.55	0.68	0.81	0.86	1.09	1.05
Tm	0.05	0.05	0.03	0.02	0.03	0.03	0.06	0.05	0.04	0.05	0.07	0.07	0.08	0.12	0.09
Yb		0.18	0.14	0.14	0.17	0.17	0.16	0.23	0.21	0.25	0.36	0.45	0.43	0.58	0.54
Lu	0.02	0.04	0.02	0.01	0.02	0.02	0.02	0.02	0.03	0.02	0.06	0.05	0.06	0.05	0.05
Hf	0.63	0.46	0.59	0.58	0.57	0.61	0.60	0.55	0.53	0.59	0.57	0.59	0.55	0.57	0.59
Ta	0.34	0.33	0.35	0.34	0.34	0.30	0.35	0.36	0.36	0.35	0.39	0.42	0.39	0.42	0.39
Pb	2.53	2.84	2.98	2.94	2.99	2.86	3.00	2.96	2.92	2.76	2.84	2.94	2.82	2.91	2.80
Th	0.56	0.55	0.52	0.55	0.54	0.55	0.52	0.57	0.56	0.60	0.55	0.57	0.58	0.67	0.62
U	0.11	0.09	0.10	0.10	0.10	0.10	0.10	0.10	0.12	0.11	0.09	0.11	0.11	0.11	0.10

Table 6-12 Trace-element composition of clinopyroxene and garnet from different textures in BMC-1 by LA-ICPMS

Texture	Recrystallized zone A												Spinel-garnet reaction zone B							
Mineral	Gt			Cpx									Gt							
Li	0.52	0.66	0.36	4.30	4.01	4.86	3.82	3.85	3.69	3.93	3.71	3.59	0.36	0.36	0.41	0.32	0.38	0.56	0.42	0.53
Be	<0.087	<0.10	<0.094	0.07	0.14	0.08	<0.085	0.09	0.12	0.09	0.11	<0.063	<0.085	<0.086	<0.059	<0.133	<0.132	<0.148	<0.139	<0.171
B	1.07	1.68	1.09	1.23	1.11	1.28	1.27	1.42	2.08	1.89	1.87	1.38	2.00	1.85	1.56	7.01	1.98	1.06	0.94	1.08
Sc	120	114	120	36	48	48	37	37	41	39	42	39	122	114	121	123	135	133	125	124
Ti	430	445	434	2481	2893	2958	3146	3065	2979	2695	3068	2959	345	508	386	399	352	323	425	358
V	104	107	108	350	307	312	322	325	321	316	319	323	90	104	89	78	82	86	96	92
Cr	628	644	656	539	413	425	446	461	443	442	445	467	484	521	653	430	434	531	575	555
Co	47.84	49.41	48.99	29.31	29.24	31.23	25.98	26.79	28.56	28.24	29	27.7	53.03	54.7	51.64	53.54	58.34	54.26	55.27	55.16
Ni	21.52	20.99	23.45	257.08	253.9	248.55	232.1	240.72	233.35	236.65	246.69	232.11	23.6	23.36	22.69	23.27	25.17	23.73	25.67	23.85
Cu	<0.168	<0.125	<0.193	0.40	0.27	0.35	0.43	0.41	0.29	0.34	0.26	0.26	<0.086	<0.085	<0.102	0.06	0.12	<0.160	<0.147	0.17
Zn	8.67	8.25	7.75	10.54	10.17	10.35	7.98	8.98	8.71	9.02	7.80	8.22	9.72	9.87	8.95	10.01	11.41	9.73	9.31	9.47
Ga	3.81	3.84	4.08	6.24	5.43	5.96	6.21	6.49	6.21	5.79	6.03	5.55	3.21	3.29	3.80	3.04	3.09	3.70	4.17	4.12
Rb	<0.113	<0.104	<0.098	<0.069	<0.068	<0.083	<0.0137	<0.0182	<0.0147	<0.0133	<0.024	<0.0141	<0.035	<0.030	0.03	0.04	<0.028	<0.100	<0.104	<0.100
Sr	0.09	0.09	0.08	134.95	134.30	133.49	148.20	145.80	144.61	141.41	143.68	140.75	0.08	0.12	0.08	0.10	0.61	0.07	0.13	0.09
Y	62.70	59.80	63.13	4.73	5.68	5.68	8.23	7.98	5.91	6.03	5.93	5.74	56.55	49.41	64.65	90.01	74.87	69.88	72.31	66.36
Zr	17.98	16.37	16.78	20.78	24.67	25.64	24.43	23.67	26.48	24.24	25.80	24.67	14.05	19.36	17.35	17.03	19.31	12.67	16.42	15.01
Nb	<0.0174	<0.0236	<0.0231	0.03	0.04	0.03	0.02	0.04	0.03	0.03	0.05	0.01	<0.0104	0.01	<0.0133	<0.0070	<0.0119	<0.0133	<0.034	<0.0182
Ba	<0.034	<0.0122	<0.0195	0.25	0.24	0.21	0.25	0.23	0.22	0.21	0.26	0.18	<0.0229	<0.0193	<0.0139	0.12	0.69	0.02	0.01	0.12
La	0.04	<0.0163	0.03	14.04	13.55	13.14	14.79	14.31	14.47	14.01	13.72	13.36	0.04	0.03	0.02	0.04	0.03	0.03	0.01	<0.0102
Ce	0.26	0.27	0.32	47.70	46.27	45.59	48.24	48.76	47.99	48.67	46.82	47.91	0.38	0.30	0.28	0.37	0.36	0.32	0.28	0.25
Pr	0.16	0.14	0.16	8.53	8.15	8.02	8.38	8.50	8.51	8.28	8.26	8.34	0.19	0.17	0.14	0.16	0.19	0.13	0.13	0.12
Nd	2.37	2.24	2.50	41.26	39.47	40.51	41.50	40.77	41.71	40.86	41.40	40.19	2.55	2.59	2.12	2.37	2.10	2.20	2.42	1.99
Sm	2.75	2.47	2.41	8.09	7.42	7.39	7.93	7.59	7.78	7.58	8.02	7.63	2.29	3.06	2.40	2.69	2.74	2.32	3.00	2.67
Eu	1.24	1.15	1.09	1.55	1.61	1.71	1.82	1.80	1.81	1.70	1.81	1.83	1.09	1.20	1.09	1.23	1.17	1.00	1.11	1.10
Gd	6.50	5.94	6.55	4.25	4.21	4.08	4.93	4.91	4.98	4.86	4.77	4.97	6.20	5.86	6.43	6.47	6.66	5.74	5.97	5.26
Tb	1.17	1.07	1.28	0.41	0.48	0.44	0.50	0.51	0.47	0.48	0.44	0.43	1.28	1.16	1.19	1.45	1.24	1.06	1.24	1.21
Dy	10.12	9.19	9.44	1.68	1.83	1.85	2.33	2.32	2.03	1.91	1.89	1.88	9.75	8.73	10.39	12.95	11.56	9.97	10.21	9.93
Ho	2.33	2.14	2.33	0.22	0.26	0.24	0.35	0.31	0.26	0.25	0.27	0.26	2.12	1.71	2.28	3.29	2.90	2.66	2.29	2.39
Er	6.73	6.43	6.55	0.31	0.49	0.44	0.68	0.62	0.35	0.46	0.48	0.45	5.66	4.82	6.77	10.76	9.09	8.35	7.29	7.14
Tm	1.03	0.93	0.92	0.03	0.04	0.03	0.09	0.06	0.04	0.04	0.04	0.05	0.75	0.69	1.03	1.63	1.35	1.21	1.03	1.11
Yb	6.53	6.57	6.91	0.07	0.15	0.21	0.30	0.24	0.17	0.19	0.15	0.17	4.43	4.55	5.99	11.41	9.10	8.91	8.26	7.69
Lu	1.04	0.97	1.01	0.02	0.01	<0.0135	0.03	0.02	0.01	0.02	0.02	0.02	0.58	0.59	0.91	1.62	1.48	1.44	1.07	1.11
Hf	0.30	0.31	0.28	1.05	1.05	1.08	1.23	1.20	1.16	1.08	1.16	1.22	0.21	0.37	0.34	0.23	0.27	0.25	0.27	0.23
Ta	<0.0083	<0.0178	0.00	<0.0073	0.01	0.01	0.01	<0.0072	0.01	0.01	0.01	0.01	<0.0105	<0.0117	<0.0154	<0.0054	0.01	<0.0154	0.01	<0.0122
Pb	<0.055	<0.050	0.08	0.90	0.98	0.96	1.10	1.00	1.12	1.06	1.06	0.99	0.02	<0.031	<0.0192	<0.025	<0.029	0.20	<0.064	<0.059
Th	<0.0170	0.01	0.02	0.48	0.46	0.51	0.51	0.52	0.51	0.48	0.48	0.46	<0.0144	<0.0182	<0.0152	0.01	<0.0194	<0.0211	<0.025	<0.0102
U	<0.0086	0.01	0.02	0.07	0.05	0.06	0.06	0.07	0.06	0.07	0.08	0.08	<0.0148	<0.0142	<0.0108	<0.0079	<0.0183	<0.0131	<0.0218	0.01

Continued

Texture					Spinel-garnet reaction zone C															
Mineral	Clinopyroxene				Garnet															
Li	4.46	4.79	5.13	5.07	<0.23	<0.26	<0.254	0.59	0.37	0.49	0.36	0.33	<0.27	<0.26	0.39	0.99	0.46	0.38	0.78	0.29
Be	0.02	<0.095	0.07	0.06	<0.00	<0.103	<0.058	<0.00	<0.087	0.06	<0.064	0.07	<0.113	<0.059	0.03	<0.062	<0.085	0.16	<0.129	<0.110
B	1.26	1.20	1.04	0.51	1.87	1.80	1.40	2.04	1.62	1.24	1.14	1.10	1.03	1.45	1.49	2.39	1.62	17.33	2.02	1.92
Sc	43	49	27	27	30	44	42	37	48	39	56	38	18	27	23	61	32	39	33	27
Ti	2622	2705	2221	2095	459	396	410	415	405	424	403	411	470	425	403	434	413	451	434	400
V	307	294	314	308	144	95	100	101	95	102	101	97	132	124	123	94	101	110	105	112
Cr	342	407	425	406	1402	777	806	832	735	767	733	708	875	1156	1227	700	709	798	1042	997
Co	31.34	31.64	31.09	32.39	51.76	54.36	54.44	54.43	54.87	53.19	55.41	54.77	54.12	52.82	53.86	54.03	52.44	56.29	54.27	57.01
Ni	262.86	271.89	264.59	268.37	23.35	25.14	25.91	24.3	25.08	24	24.3	25.49	25.92	22.74	22.79	26.19	23.94	27.04	21.21	26.43
Cu	0.52	0.42	0.39	0.43	<0.137	<0.153	0.19	<0.145	<0.127	<0.153	<0.158	<0.130	<0.150	0.16	<0.139	0.49	<0.142	0.41	0.34	<0.088
Zn	11.73	9.95	10.74	10.13	10.44	11.25	9.81	10.11	10.83	9.64	10.70	11.85	10.41	10.43	10.86	10.43	10.10	14.13	11.86	11.49
Ga	5.96	5.52	6.13	6.53	3.99	3.18	3.42	3.36	3.37	3.40	3.57	3.09	3.62	4.03	3.58	3.21	3.30	3.56	3.29	3.72
Rb	<0.061	<0.082	<0.077	<0.068	<0.108	<0.121	<0.115	<0.095	<0.130	<0.114	<0.118	0.16	<0.129	<0.109	<0.105	<0.122	<0.113	<0.098	<0.029	<0.030
Sr	136.85	139.08	136.31	136.14	0.10	0.10	0.07	0.08	0.12	0.12	0.10	0.06	0.11	0.07	0.07	2.56	0.13	2.1	0.097	0.109
Y	3.69	5.06	1.53	1.32	3.46	7.18	6.77	5.32	9.48	7.75	10.21	7.06	1.38	3.23	1.95	10.25	4.49	4.19	5.35	2.77
Zr	21.78	23.29	17.11	16.52	10.06	13.19	13.37	12.67	13.91	13.99	14.34	12.89	16.61	10.61	9.85	13.88	11.55	13.47	13.83	12.91
Nb	0.04	0.03	<0.0192	0.04	0.01	<0.0185	<0.0180	0.01	0.01	0.01	<0.0140	<0.00	<0.0282	<0.00	0.01	0.06	<0.0182	<0.0128	0.0128	<0.0145
Ba	0.21	0.21	0.20	0.21	<0.0122	0.01	<0.02	0.01	0.01	0.01	<0.0252	0.01	<0.036	0.02	<0.0181	1.86	0.05	2.52	0.15	0.0243
La	14.03	13.23	13.25	13.30	0.05	0.03	0.02	0.02	0.03	0.03	0.03	0.03	<0.030	0.02	0.04	0.16	0.05	0.133	0.099	0.0283
Ce	46.05	44.28	45.41	45.95	0.65	0.39	0.42	0.50	0.49	0.50	0.48	0.38	0.50	0.53	0.53	0.77	0.53	0.68	0.743	0.551
Pr	8.10	8.06	8.07	8.09	0.31	0.27	0.28	0.23	0.25	0.23	0.25	0.29	0.27	0.26	0.27	0.29	0.24	0.298	0.318	0.279
Nd	39.00	37.81	37.20	37.12	3.88	3.16	3.22	3.10	2.92	3.26	3.34	3.41	3.13	3.33	3.34	3.07	3.55	3.63	4.31	3.14
Sm	6.24	6.90	6.68	6.63	1.99	2.91	2.50	2.64	2.78	2.71	2.47	2.72	2.39	2.54	2.18	2.63	2.66	2.87	3.08	2.49
Eu	1.45	1.63	1.41	1.46	0.85	1.08	1.05	1.05	1.11	1.03	1.08	1.09	0.93	0.71	0.62	1.21	1.09	1.009	0.944	0.969
Gd	3.85	3.91	3.09	2.76	2.03	4.07	3.16	3.28	3.78	3.96	3.49	3.58	2.00	2.13	1.45	3.63	3.10	2.45	3.85	2.46
Tb	0.33	0.42	0.24	0.21	0.22	0.46	0.49	0.36	0.50	0.47	0.55	0.46	0.14	0.22	0.14	0.58	0.34	0.332	0.451	0.217
Dy	1.37	1.63	0.71	0.62	1.11	2.18	2.00	1.72	2.80	2.34	2.79	2.00	0.64	0.94	0.58	2.15	1.62	1.35	1.79	1.091
Ho	0.15	0.21	0.08	0.07	0.12	0.29	0.27	0.20	0.40	0.29	0.39	0.29	0.06	0.13	0.08	0.36	0.19	0.15	0.226	0.0933
Er	0.27	0.37	0.12	0.10	0.23	0.43	0.42	0.34	0.67	0.48	0.74	0.51	0.06	0.22	0.14	0.69	0.30	0.187	0.32	0.142
Tm	0.03	0.02	0.01	<0.0081	0.03	0.05	0.05	0.03	0.06	0.05	0.07	0.04	<0.0184	0.02	<0.0125	0.07	0.02	0.0165	0.0177	0.012
Yb	0.08	0.08	<0.042	<0.038	0.10	0.12	0.19	0.08	0.32	0.20	0.23	0.12	<0.054	0.10	0.04	0.41	0.13	<0.060	0.101	0.067
Lu	0.01	0.01	<0.0082	<0.0085	<0.0146	0.02	0.03	0.02	0.02	0.02	0.05	0.03	0.01	0.01	<0.0107	0.03	0.02	<0.0156	<0.0110	<0.0105
Hf	1.15	1.23	1.09	0.86	0.28	0.28	0.17	0.24	0.28	0.19	0.28	0.22	0.30	0.22	0.24	0.24	0.14	0.242	0.181	0.29
Ta	<0.0131	0.01	<0.0072	0.00	<0.0111	<0.00	<0.0120	0.00	0.00	0.01	<0.0133	<0.0122	0.01	0.00	<0.01	<0.0125	<0.0120	0.006	<0.0127	<0.0129
Pb	0.90	1.02	0.91	1.09	<0.040	<0.044	<0.063	<0.059	<0.057	<0.046	<0.060	<0.058	<0.087	<0.054	<0.067	0.12	<0.069	0.16	0.025	<0.028
Th	0.47	0.42	0.46	0.41	<0.0162	<0.0148	<0.0176	<0.0260	0.01	<0.0188	<0.0250	0.01	0.03	<0.0267	0.02	<0.0182	<0.0176	<0.0100	0.04	0.0241
U	0.04	0.06	0.08	0.07	<0.023	0.01	<0.0201	<0.0133	<0.0190	<0.0166	0.01	<0.0184	<0.0171	0.02	0.01	<0.0208	0.02	<0.0153	0.038	<0.0168

A-42

Table 6-13 Trace-element compositions (ppm) of clinopyroxene in the garnet pyroxenites from Lakes Bullenmerri and Gnotuk

Sample	BM99-2	BM99-6	BM99-4		BME-1		BM99-2		BM96-3	BM99-5	DR9748	GN35		DR10165			BM99X2			GN85-1	BM99-9	
Type	M	M	H	M	H	M	H	M	M	H	M	H	M	H	M1	M2	H	M1	M2	M	H	M
Li	3.24	1.57	4.62	4.04	2.15	2.58	2.13	2.12	3.09	4.07	3.84	2.21	2.04		2.76	2.81	6.22	5.88	5.19	3.32	2.70	2.90
Be	0.17	0.13	0.25	0.28	0.29	0.29	0.11	0.09	0.23	0.48	0.32								0.05	0.14	0.07	0.04
B	1.87	2.10	10.06	8.31	2.46	1.53	1.73	2.42	1.74	1.74	0.76	9.80	8.60		10.09	10.51	6.37	6.14	1.33	1.86	2.15	2.84
Sc	28.4	17.2	37.0	39.6	22.0	30.7	26.9	34.0	34.3	54.6	49.1	43.0	50.5	29.8	31.6	39.2	23.7	24.7	37.1	40.0	30.5	31.6
Ti	2285	2450	4066	4259	2478	2632	2302	2337	6059	4539	5280	4212	3597	3127	3077	3240	2907	3484	3725	3304	1266	1307
V	177	187	351	346	230	241	244	254	487	392	358	277	263	198	200	191	535	569	648	653	289	277
Cr	1816	1173	1794	1924	1407	1601	1245	1455	597	2047	2450	2397	1479	1334	1226	1233	471	542	608	659	756	814
Co	41.0	27.7	25.6	23.9	34.6	36.1	37.6	37.0	43.8	45.8	46.6	23.9	25.6	24.6	23.5	23.2	48.5	45.6	45.9	48.5	49.1	46.2
Ni	472	439	227	227	428	444	410	387	507	385	511	304	314	294	287	259	372	379	362	412	266	258
Cu	1.00	1.82	1.44	1.26	0.75	0.75	1.49	1.41	1.82	1.49	3.47	1.98	1.98	1.05	1.03	1.01	1.37	1.35	0.70	2.83	1.57	1.26
Zn	21.1	6.4	14.5	11.8	18.7	18.6	24.3	23.8	33.7	52.3	47.2	6.6	6.4	6.1	6.3	6.4	45.6	44.9	43.5	43.8	37.4	34.5
Ga	8.74	9.78	11.08	10.59	9.73	10.44	12.45	12.43	16.80	11.47	12.11	5.26	4.09	4.33	3.76	2.94	15.45	17.01	17.07	17.82	15.60	15.81
Rb			0.04				0.03									0.04				0.03		0.02
Sr	146	137	149	147	126	125	114	115	104	109	135	95	97	128	138	138	13	13	14	59	7	8
Y	1.56	0.72	5.07	5.62	1.68	1.99	1.21	1.36	3.06	6.54	6.23	6.28	7.68	2.82	3.79	6.70	1.24	1.61	2.85	3.50	1.13	1.05
Zr	6.64	14.27	25.35	26.01	16.44	19.90	5.49	6.23	47.95	30.48	32.16	18.51	18.07	21.85	22.78	27.70	2.32	3.18	4.03	10.93	0.99	1.11
Nb	0.14	0.55	0.20	0.17	0.08	0.06	0.18	0.22	0.86	0.07	0.45	0.20	0.22	0.08	0.12	0.15	0.13	0.15	0.19	1.26	0.01	0.01
Ba	0.05	0.12	0.09	0.05	0.09	0.07	0.04	0.05	0.12	0.06	0.07	0.09	0.11	0.11	0.12	0.21	0.03	0.01	0.08	0.31	0.03	0.01
La	2.64	2.24	4.98	4.66	4.03	3.72	1.71	1.74	4.45	2.61	3.77	4.80	4.80	8.07	8.47	8.76	0.54	0.55	0.62	4.39	0.02	0.03
Ce	3.64	4.43	11.73	10.50	16.17	15.82	3.53	3.51	10.54	6.38	10.95	9.49	9.66	24.72	27.28	26.93	0.73	0.77	0.82	7.27	0.35	0.37
Pr	0.46	0.60	1.72	1.50	3.09	3.03	0.48	0.48	1.47	1.13	1.87	1.17	1.16	3.62	4.00	4.06	0.07	0.07	0.09	0.75	0.11	0.12
Nd	2.34	3.03	8.29	7.33	14.89	15.23	2.42	2.41	6.82	6.69	9.59	5.46	5.32	15.28	16.80	17.29	0.54	0.59	0.62	2.77	0.73	0.81
Sm	0.71	0.81	2.32	2.12	2.68	2.97	0.72	0.72	2.15	2.23	2.60	1.69	1.66	2.49	2.78	2.99	0.57	0.65	0.63	0.82	0.22	0.23
Eu	0.31	0.33	0.91	0.89	0.71	0.69	0.26	0.30	0.73	0.79	0.89	0.70	0.71	0.74	0.83	0.90	0.26	0.29	0.29	0.32	0.12	0.13
Gd	0.74	0.64	2.31	2.20	1.49	1.35	0.64	0.68	2.17	2.43	2.44	1.91	1.99	1.66	1.90	2.36	0.80	0.96	1.08	1.22	0.42	0.36
Tb	0.09	0.07	0.30	0.31	0.13	0.15	0.08	0.08	0.25	0.33	0.31	0.23	0.40		0.25	0.32	0.10	0.13	0.15	0.18	0.06	0.05
Dy	0.47	0.30	1.78	1.67	0.57	0.61	0.40	0.43	1.06	1.73	1.72	1.58	1.94	0.88	1.10	1.71	0.46	0.60	0.85	0.93	0.33	0.32
Ho	0.07	0.03	0.25	0.26	0.06	0.09	0.05	0.07	0.14	0.28	0.26	0.33	0.32		0.16	0.27	0.06	0.08	0.13	0.15	0.04	0.05
Er	0.13	0.05	0.50	0.52	0.12	0.15	0.10	0.11	0.22	0.56	0.52	0.54	0.69	0.22	0.30	0.61	0.09	0.10	0.24	0.28	0.09	0.08
Tm	0.01		0.05	0.05	0.01	0.01	0.01	0.01	0.02	0.07	0.06	0.09	0.07		0.03	0.07	0.01	0.01	0.02	0.03	0.01	0.01
Yb	0.07		0.24	0.27	0.05	0.07	0.04	0.07	0.09	0.35	0.34	0.32	0.38	0.10	0.12	0.35	0.04	0.04	0.12	0.15	0.06	0.05
Lu	0.01	0.01	0.03	0.03		0.01	0.01	0.01	0.01	0.04	0.04	0.04	0.04	0.01	0.01	0.04	0.01	0.00	0.01	0.02	0.01	
Hf	0.35	0.58	1.18	1.08	0.49	0.59	0.29	0.36	2.50	1.38	1.41	0.67	0.68	0.61	0.63	0.67	0.25	0.28	0.36	0.45	0.11	0.11
Ta	0.02	0.14	0.02	0.02	0.03	0.02	0.03	0.03	0.05	0.02	0.04	0.01	0.01	0.02	0.02	0.02	0.00		0.01	0.10	0.01	
Pb	0.42	0.20	0.75	0.69	0.50	0.52	0.22	0.20	0.34	0.29	0.47	0.43	0.42	0.54	0.55	0.54	0.10	0.15	0.10	0.48	0.11	0.04
Th	0.55	0.29	0.71	0.72	0.22	0.22	0.31	0.28	0.56	0.63	0.76	0.61	0.60	0.46	0.43	0.46	0.11	0.11	0.15	0.61	0.01	0.01
U	0.13	0.06	0.17	0.19	0.06	0.04	0.07	0.07	0.13	0.15	0.15	0.14	0.14	0.10	0.09	0.09	0.02	0.02	0.03	0.13	0.01	0.01

Continued

Sample	BM99X1		BM99-8		GN51	GN18	GN41	DR10162	BM90-3		BMC-1	BM99-7	DR11017c	DR11017c	DR11022	DR11022
Type	H	M	H	M	M	M	M	M	H	M	M	M	E	M	E	M
Li	4.22	4.32	4.22	4.40	3.33	3.52	3.82	2.22	1.85	1.87	4.37	3.57	2.49	2.46	1.76	1.68
Be	0.08	0.09	0.12	0.11	0.19	0.39	0.30	0.06	0.22	0.10	0.09	0.14		0.17	0.08	0.07
B	1.55	2.63	6.46	6.74	0.88	1.10	1.35	2.21	1.42	1.59	1.37	6.04	9.26	8.78	2.73	2.62
Sc	42.4	43.4	36.2	35.2	24.8	22.0	33.3	18.3	55.8	53.4	36.0	45.0	43.2	46.7	48.2	47.2
Ti	3611	3322	962	992	3423	1799	5559	1919	2881	2747	2654	2593	2883	2881	2832	2812
V	455	437	224	229	663	198	424	152	306	304	324	295	329	314	320	323
Cr	559	547	781	776	401	785	877	1175	581	566	456	408	473	453	451	447
Co	36.0	35.3	48.0	51.0	42.4	39.6	46.6	50.2	30.7	30.7	29.9	26.9	29.1	28.4	25.6	25.8
Ni	165	171	327	334	334	410	476	607	199	200	256	208	245	237	206	214
Cu	1.48	1.55	1.28	1.33	2.83	1.00	1.08	1.93	0.53	0.62	0.37	0.58	0.71	0.72	0.46	0.47
Zn	30.4	31.7	26.4	27.0	37.5	24.9	43.1	29.5	11.7	13.8	10.1	8.6	8.3	9.5	6.4	6.2
Ga	15.99	15.50	9.37	9.70	18.01	12.94	17.95	10.99	6.51	6.40	6.09	5.07	7.48	5.15	5.08	5.33
Rb	0.12	0.11	0.01		0.06				0.17	0.11						0.19
Sr	114	129	135	132	154	143	62	158	128	125	138	172	141	146	144	150
Y	5.05	5.24	0.78	0.77	1.75	1.25	2.89	0.62	8.88	7.94	4.39	7.73	5.70	7.22	7.40	7.92
Zr	16.12	15.28	7.33	6.90	16.57	12.91	10.52	4.72	31.39	30.69	21.85	25.57	24.16	24.13	23.91	23.48
Nb	0.22	0.24	1.20	0.92	0.35	0.71	0.23	0.34	0.04	0.04	0.03	0.11	0.05	0.05	0.03	0.03
Ba	0.24	0.46	0.10	0.32	0.34	0.12	0.03	0.06	0.88	0.30	0.24	0.27	0.22	0.23	0.21	0.61
La	9.65	9.87	4.34	4.02	21.57	7.24	3.09	2.58	11.94	11.86	13.82	17.76	14.09	14.98	14.36	14.85
Ce	18.40	19.25	12.35	11.12	56.93	20.23	4.61	4.84	45.68	45.44	47.19	58.78	49.34	51.72	49.59	51.73
Pr	2.11	2.14	1.82	1.63	5.85	2.75	0.43	0.64	8.32	8.29	8.34	9.92	8.47	8.78	8.61	8.86
Nd	8.21	8.85	7.48	6.58	17.90	11.07	2.12	2.75	40.81	40.89	39.97	48.15	41.12	42.72	40.93	41.62
Sm	1.95	1.94	1.32	1.11	2.03	1.98	1.06	0.67	7.38	7.44	7.14	8.77	7.66	7.98	7.81	7.70
Eu	0.65	0.66	0.40	0.33	0.60	0.60	0.47	0.26	1.72	1.70	1.60	1.99	1.74	1.84	1.74	1.79
Gd	2.02	2.01	0.80	0.68	1.29	1.19	1.41	0.52	4.74	4.65	3.98	5.22	4.52	4.78	4.66	4.72
Tb	0.27	0.27	0.07	0.06	0.14	0.12	0.19	0.06	0.51	0.49	0.37	0.52	0.42	0.40	0.48	0.50
Dy	1.44	1.42	0.27	0.27	0.58	0.45	0.96	0.22	2.34	2.29	1.49	2.39	1.81	2.23	2.21	2.21
Ho	0.22	0.24	0.03	0.03	0.08	0.05	0.13	0.03	0.37	0.35	0.19	0.33	0.24	0.27	0.31	0.32
Er	0.45	0.43	0.06	0.06	0.15	0.09	0.22	0.04	0.73	0.68	0.33	0.61	0.45	0.58	0.56	0.65
Tm	0.04	0.04	0.01	0.01	0.02	0.01	0.02	0.01	0.09	0.07	0.03	0.06	0.03	0.05	0.06	0.07
Yb	0.22	0.21	0.04	0.03	0.07	0.04	0.11	0.03	0.46	0.31	0.14	0.27	0.21	0.29	0.27	0.37
Lu	0.03	0.03	0.01	0.00	0.01		0.01	0.00	0.05	0.04	0.01	0.03	0.02	0.03	0.03	0.04
Hf	1.05	1.11	0.14	0.16	0.65	0.29	0.69	0.23	1.37	1.44	1.10	1.16	1.16	1.09	1.08	1.11
Ta	0.01	0.01	0.11	0.09	0.02	0.15		0.03	0.01	0.01	0.01	0.01	0.01	0.01	0.01	0.01
Pb	1.25	1.32	0.38	0.40	0.76	0.43	0.51	0.30	0.79	0.80	0.99	1.21	0.86	0.87	0.84	0.90
Th	0.90	0.84	0.51	0.53	0.91	0.90	0.85	0.36	0.85	0.77	0.47	0.90	0.53	0.54	0.53	0.55
U	0.18	0.16	0.13	0.14	0.18	0.20	0.18	0.06	0.13	0.12	0.06	0.16	0.07	0.09	0.06	0.06

Note: H, host clinopyroxene in the lamellar zone; M, clinopyroxene in the recrystallized granular zone.

Table 6-14 Trace-element compositions (ppm) of orthopyroxene in the garnet pyroxenites from Lakes Bullenmerri and Gnotuk

Sample	BM99-2	BME-1		BM99-4		BM99-2		BM96-3	BM99-5	DR9748	GN35		DR10165	BM90-3		BM99-7		BMC-1	
Type	M1	E	M1	E	H	E	M1	M1	E	M1	E1	M1	M1	E	M1	M1	M2	M1	M2
Li	3.20	1.93	2.56	3.60	4.16	2.23	2.05	2.96	4.93	3.52	1.96	1.80	2.46	2.01	2.15	3.56	3.92	4.62	5.84
Be	0.04	0.06	0.06	0.06	0.04	0.04	0.03	0.04	0.11		0.04	0.02	0.03	0.04	0.02	0.04	0.03		0.04
B	1.44	1.00	0.93	1.19	1.59	1.01	1.19	0.95	1.50		2.16	2.15	2.11	0.99	0.95	1.42	1.40	0.61	1.34
Sc	9.12	6.51	6.63	9.64	9.74	7.13	8.65	8.76	18.00	16.29	13.48	15.52	14.15	11.76	11.37	15.16	11.98	9.79	6.26
Ti	343	359	349	578	627	375	354	1087	782	1252	727	678	541	515	485	494	558	486	491
V	61.3	84.9	95.4	115.7	131.5	87.1	90.9	172.9	104.4	144.3	77.6	78.0	65.7	132.7	128.9	120.4	138.3	122.4	143.0
Cr	1071	811	852	890	930	658	757	321	855	1623	982	703	499	435	262	168	253	198	219
Co	105	96	97	68	71	101	98	104	102	119	57	62	65	78	83	69	76	80	81
Ni	878	863	904	473	504	854	843	1002	628	1068	578	590	569	382	418	418	474	535	543
Cu	0.61	0.44	0.58	0.47	0.66	1.10	1.04	1.06	0.96	1.91	0.97	0.94	0.47	0.49	0.32	0.22	0.28	0.09	0.28
Zn	76.2	80.5	80.0	46.3	49.3	101.1	95.1	121.9	208.3	172.3	17.9	18.4	20.2	51.6	68.9	31.9	36.5	46.3	44.2
Ga	6.35	8.94	10.36	8.56	9.44	10.98	10.74	13.07	7.47	10.79	3.74	3.14	2.95	6.99	7.57	4.72	6.88	5.54	6.72
Sr	0.221	0.095	0.410	0.159	0.145	0.121	0.106	0.118	0.365	0.678	0.205	0.129	0.250	0.130	0.122	0.171	0.264	0.141	0.310
Y	0.109	0.087	0.061	0.238	0.197	0.067	0.067	0.168	0.907	0.537	0.387	0.427	0.308	0.397	0.329	0.496	0.179	0.282	0.105
Zr	0.278	0.569	0.483	0.839	0.965	0.266	0.195	1.908	2.196	1.837	0.844	0.837	1.178	1.326	1.261	1.219	1.299	1.004	1.031
Nb	0.009	0.004	0.002	0.003		0.003	0.002	0.015	0.006	0.035	0.009		0.005	0.003	0.004		0.009		0.018
Ba	0.006		0.002			0.003	0.002	0.004	0.001	0.204	0.012		0.018	0.001	0.021	0.001	0.109	0.001	0.285
La	0.004	0.003	0.043	0.006	0.006	0.002	0.002	0.005	0.014		0.012		0.040	0.014	0.014	0.024	0.047	0.018	0.032
Ce	0.014	0.027	0.140	0.018	0.020	0.009	0.008	0.025	0.058	0.044	0.025	0.016	0.121	0.100	0.102	0.143	0.202	0.110	0.137
Pr	0.004	0.007	0.018	0.003	0.003	0.002	0.002	0.005	0.010	0.009	0.004	0.003	0.019	0.023	0.022	0.030	0.036	0.027	0.027
Nd	0.013	0.042	0.081	0.016	0.020	0.012	0.009	0.032	0.063	0.065		0.031	0.072	0.167	0.150	0.203	0.227	0.163	0.177
Sm	0.006	0.015	0.015	0.017	0.010	0.008	0.009	0.016	0.036	0.061	0.021	0.022	0.032	0.056	0.059	0.077	0.064	0.065	0.057
Eu	0.005	0.007	0.006	0.007	0.007	0.004	0.003	0.008	0.016	0.017			0.009	0.019	0.018	0.024	0.019	0.018	0.018
Gd	0.011	0.018	0.022	0.029	0.019	0.011	0.010	0.033	0.060	0.063			0.028	0.066	0.066	0.088	0.066	0.070	0.059
Tb	0.003	0.003	0.002	0.005	0.005	0.002	0.002	0.007	0.014	0.012	0.009	0.008	0.007	0.011	0.010	0.013	0.008	0.010	0.006
Dy	0.018	0.021	0.012	0.045	0.040	0.013	0.014	0.040	0.133	0.095	0.065	0.067	0.041	0.071	0.060	0.090	0.048	0.052	0.027
Ho	0.004	0.003	0.002	0.009	0.008	0.002	0.002	0.008	0.037	0.023	0.016	0.023	0.012	0.015	0.012	0.019	0.007	0.011	0.004
Er	0.013	0.007	0.005	0.025	0.024	0.009	0.008	0.016	0.118	0.057	0.050	0.044	0.036	0.044	0.035	0.054	0.015	0.036	0.010
Tm	0.002	0.001	0.001	0.004	0.003	0.001	0.001	0.002	0.022	0.010	0.007		0.007	0.006	0.006	0.007	0.002	0.005	
Yb	0.012	0.007	0.006	0.024	0.022	0.009	0.012	0.013	0.187	0.056	0.056	0.056	0.039	0.044	0.034	0.050	0.013	0.024	
Lu	0.002	0.002	0.007	0.003	0.003	0.001	0.002	0.002	0.034	0.010	0.010		0.006	0.006	0.005	0.008	0.001	0.003	
Hf	0.012	0.013	0.012	0.028	0.035	0.010	0.009	0.082	0.061	0.064	0.032	0.024	0.027	0.056	0.047	0.045	0.054	0.038	0.041
Pb		0.005	0.005				0.003	0.004					0.018	0.005	0.010		0.005		0.014
Th	0.003		0.004	0.005	0.003	0.002		0.003	0.007		0.066		0.005	0.004	0.004	0.006	0.030	0.005	0.003
U	0.005	0.001	0.002	0.002	0.003	0.002		0.002	0.005	0.011	0.003		0.007	0.002	0.002	0.034	0.005		

Note: E, exsolved orthopyroxene in the lamellar zone; M1, orthopyroxene in the recrystallized zone; M2, orthopyroxene in the Sp-Gt reaction zone; H, host orthopyroxene.

Table 6-15 Trace-element compositions (ppm) of garnet in the garnet pyroxenites from Lakes Bullenmerri and Gnotuk

Sample	BM99-2	BM99-6	BM99-4		BM99-4	BME-1		BM99-2		BM99-2	BM96-3	BM99-5	DR9748	GN35			DR10165			BM99X2		
Type	C	C	E1	E2	M	E1	C	E1	M	C	C	E1	M	E1	C-core	C-rim	E1	M1	M2	E1	M	C
Li	0.31		0.65	0.45	0.28		0.33			0.16	0.38	0.52	0.48							0.44	0.38	0.40
B	1.49	2.21	12.20	16.90	12.76	1.79	1.75	1.95	2.25	2.93	1.18	1.68	0.95			10.76		9.78	10.93	6.49	6.83	3.36
Sc	88.0	63.7	89.3	82.8	84.4	58.3	53.3	90.2	83.9	112.6	87.9	153.2	110.0	135.5	130.3	130.9	78.1	97.1	100.1	74.3	70.1	101.8
Ti	557	285	368	354	321	222	271	381	423	359	889	1043	978	569	701	606	356	381	333	654	609	555
V	51.6	38.8	59.8	58.6	55.6	47.7	57.2	62.5	66.0	62.5	133.4	115.5	117.9	67.3	62.4	61.4	58.5	44.6	54.1	132.5	141.3	153.4
Cr	2943	1187	1240	1283	1302	1622	1650	1415	1431	1683	747	2908	3191	2094	2611	2091	1538	1312	1519	452	585	602
Co	75.4	58.4	43.3	46.4	42.9	75.1	74.3	69.8	71.2	72.4	75.4	69.3	73.3	47.9	48.9	49.6	51.0	51.2	46.7	79.8	84.2	77.0
Ni	48.4	46.7	21.8	22.7	20.6	44.0	40.5	45.9	45.1	38.7	56.6	37.2	54.9	37.2	36.4	37.8	30.4	29.4	25.7	35.6	39.1	34.8
Cu	0.17	1.27	0.69		0.03	0.27	0.14		0.17	0.12	0.15	0.30	0.17	0.13	0.10	0.09	0.41	0.12		0.04	0.05	0.55
Zn	17.77	6.56	14.24	18.05	14.90	18.56	19.12	23.71	24.11	22.19	29.96	41.46	38.60	7.46	6.58	6.94	6.14	6.94	6.99	41.31	43.83	40.86
Ga	6.45	4.20	3.78	3.93	3.95	4.63	4.98	6.48	6.90	6.16	8.58	7.10	7.10	2.61	5.03	3.46	2.85	1.58	2.36	6.94	7.89	6.98
Rb	0.07		0.10	0.01						0.08		0.06										
Sr	0.13	0.13	0.20	0.07	0.08	0.07	0.12	0.10	0.09	0.09	0.14	0.17	0.14	0.07	0.07	0.07	0.37	0.10	0.15	0.19	0.03	0.03
Y	12.88	7.66	35.62	33.27	35.37	14.11	13.38	13.83	12.42	14.97	26.33	57.97	46.71	49.56	27.73	43.30	24.08	34.86	59.57	17.41	20.54	36.52
Zr	4.82	13.10	9.46	9.01	10.04	7.30	7.65	3.78	3.80	4.16	25.82	18.04	16.93	9.21	10.15	9.85	11.84	12.38	13.77	1.61	1.67	2.01
Nb	0.01	0.08	0.01	0.01	0.01			0.02	0.01	0.02	0.04	0.01	0.03	0.02	0.01	0.01		0.01	0.01	0.01	0.01	0.01
Ba	0.01	0.22	0.08		0.00	0.02		0.00	0.01	0.01	0.03	0.08						0.09	0.07	0.42		0.01
La	0.02	0.02	0.03	0.01	0.01	0.02	0.01		0.01	0.01	0.02	0.03	0.01	0.02	0.01	0.01		0.02	0.07	0.01		0.01
Ce	0.04	0.11	0.06	0.07	0.07	0.12	0.11	0.03	0.03	0.03	0.09	0.10	0.08	0.08	0.07	0.08	0.19	0.20	0.22	0.02	0.02	0.02
Pr	0.02	0.02	0.03	0.03	0.03	0.06	0.05	0.02	0.01	0.02	0.04	0.05	0.04	0.02	0.02	0.02	0.06	0.09	0.07	0.01	0.01	0.01
Nd	0.18	0.18	0.34	0.40	0.36	0.78	0.58	0.18	0.19	0.14	0.38	0.65	0.52	0.30	0.29	0.31	0.70	0.94	0.69	0.07	0.09	0.09
Sm	0.29	0.28	0.52	0.58	0.54	0.67	0.59	0.24	0.22	0.28	0.70	1.08	0.79	0.43	0.46	0.52	0.61	0.79	0.69	0.37	0.30	0.35
Eu	0.22	0.23	0.46	0.48	0.47	0.34	0.33	0.20	0.20	0.21	0.42	0.69	0.52	0.36	0.36	0.38	0.38	0.47	0.45	0.30	0.31	0.29
Gd	0.92	0.85	2.21	2.27	2.28	1.37	1.37	0.87	0.89	0.91	2.60	3.82	2.80	1.89	1.72	1.90	1.51	2.12	2.21	1.69	1.93	2.04
Tb	0.24	0.19	0.63	0.66	0.65	0.29	0.27	0.25	0.22	0.25	0.56	0.96	0.73			0.60	0.46	0.55	0.65	0.43	0.48	0.59
Dy	1.98	1.33	6.39	6.74	6.74	2.37	2.10	2.11	1.96	2.17	4.65	8.94	6.94	6.17	3.64	5.60	3.48	4.92	6.88	3.39	3.96	5.64
Ho	0.49	0.30	1.68	1.95	1.84	0.51	0.50	0.55	0.48	0.58	1.03	2.27	1.83			1.40	0.92	1.10	1.97	0.69	0.80	1.43
Er	1.45	0.84	5.78	6.69	6.34	1.48	1.49	1.63	1.39	2.00	2.79	6.82	5.84	6.73	2.58	4.92	2.91	4.10	7.63	1.80	2.08	4.54
Tm	0.21	0.11	0.88	1.04	0.97	0.20	0.22	0.24	0.20	0.34	0.38	1.04	0.90			0.71	0.39	0.59	1.21	0.23	0.26	0.68
Yb	1.47	0.77	6.20	7.70	7.29	1.29	1.59	1.82	1.31	2.54	2.40	7.09	6.60	8.47	3.05	5.02	3.02	4.50	10.86	1.32	1.57	4.98
Lu	0.22	0.11	0.92	1.14	1.11	0.16	0.23	0.25	0.19	0.40	0.35	1.01	0.98	1.35	0.41	0.89	0.48	0.66	1.76	0.16	0.20	0.73
Hf	0.12	0.29	0.19	0.19	0.17	0.08	0.18	0.10	0.09	0.09	0.45	0.27	0.29	0.14	0.17	0.20	0.10	0.10	0.15	0.05	0.04	0.07
Ta	0.01	0.01				0.01	0.01			0.00		0.00								0.00		0.00
Pb		0.16			0.02		0.06					0.11								0.18		
Th	0.02		0.02		0.01		0.01				0.02	0.02										0.01
U	0.02	0.02	0.01	0.04	0.02		0.13	0.01			0.04	0.04	0.02		0.02	0.03				0.01		0.02

Continued

Sample	GN85-1	BM99-9		BM99X1		BM99-8	BM99-8	GN51	GN18	GN41	DR10162	BM90-3	BM90-3	BMC-1		BM99-7	DR11022	DR11017c			
Type	C	E1	M	E1	M	E1	M	C	C	C	C	E1	M	M1	M2	M	M	E1	M	C-core	C-rim
Li	0.30			1.08	0.43	1.16	0.50	0.42	0.37	0.44	0.15	0.66	0.77	0.44	0.40	0.32	0.87				
B	2.65	3.11	2.29	1.48	2.08	6.95	6.42	0.97	0.75	1.15	2.73	2.19	2.63	1.76	1.52	3.91	2.76	11.12	10.88	9.80	9.40
Sc	118.1	118.1	128.9	104.3	98.9	129.3	123.9	70.1	61.0	83.5	57.7	127.9	128.9	126.4	34.6	128.2	152.0	124.5	120.5	132.0	130.3
Ti	606	193	174	435	353	119	139	457	251	704	357	361	510	369	423	430	402	363	413	535	460
V	197.8	66.7	63.1	85.2	86.1	45.1	46.0	144.5	39.5	91.5	37.3	78.5	113.4	90.1	111.7	99.3	86.4	99.9	105.1	102.5	100.3
Cr	728	651	652	432	449	711	656	381	685	837	1320	824	831	523	911	685	465	652	678	920	822
Co	81.7	89.0	85.3	61.6	64.2	99.2	89.2	77.2	73.5	83.6	91.2	48.6	53.1	53.1	54.1	51.2	46.3	51.0	51.1	53.3	53.8
Ni	33.6	31.1	21.8	15.0	15.3	30.5	28.8	36.8	44.5	50.4	65.1	18.7	17.8	23.6	24.6	20.1	18.9	21.7	21.9	20.3	22.0
Cu	0.33	0.64	0.12	0.60	0.30	0.31	0.12	0.12		0.06	0.10	0.38	0.49	0.13	0.17	0.07				0.06	
Zn	39.03	37.79	32.96	26.26	29.77	29.54	26.88	38.68	27.00	41.61	24.80	11.69	11.38	9.57	10.63	7.99	6.36	7.83	8.56	8.07	8.75
Ga	8.30	5.42	5.11	5.31	5.84	4.71	4.04	6.48	5.36	7.03	5.55	3.43	5.47	3.39	3.56	4.05	2.68	4.77	4.83	4.88	4.11
Rb	0.04	0.03		0.06		0.16	0.11					0.14	0.36	0.04		0.05					0.05
Sr	0.47	0.34	0.02	0.30	0.12	0.11	0.37	0.32	0.12	0.07	0.15	0.30	0.28	0.15	0.09	0.12	0.06	0.09	0.09	0.10	0.10
Y	52.45	17.84	17.82	50.65	49.40	12.03	13.51	22.26	11.70	28.74	6.99	75.71	69.81	65.25	5.22	69.08	87.66	60.16	67.97	50.33	60.05
Zr	5.53	0.82	0.75	6.16	5.64	5.39	6.33	10.77	7.77	4.83	3.81	16.01	19.69	15.55	12.74	18.80	12.19	13.26	14.81	17.02	15.62
Nb	0.06	0.01	0.00	0.09	0.03	0.08	0.11	0.02	0.02	0.01	0.02	0.14	0.19	0.01	0.01	0.01				0.01	0.01
Ba	1.11	0.40	0.04	0.79	0.08	0.61	0.76	0.01			0.03	0.32	0.53	0.14	0.02	0.06			0.01	0.02	0.01
La	0.04	0.03	0.01	0.22	0.03	0.06	0.03	0.11	0.02	0.01	0.01	0.14	0.11	0.03	0.03	0.03	0.01	0.02	0.02	0.02	0.02
Ce	0.14	0.12	0.01	0.53	0.22	0.25	0.17	1.01	0.26	0.06	0.07	0.82	0.55	0.30	0.50	0.41	0.44	0.29	0.28	0.29	0.28
Pr	0.04	0.02		0.09	0.07	0.07	0.06	0.28	0.08	0.02	0.02	0.25	0.18	0.15	0.26	0.22	0.22	0.15	0.15	0.17	0.14
Nd	0.21	0.16	0.11	0.80	0.73	0.75	0.74	1.95	0.82	0.14	0.26	2.43	1.90	2.27	3.32	2.71	2.80	2.13	2.14	2.40	2.21
Sm	0.46	0.19	0.18	0.81	0.66	0.70	0.68	1.01	0.69	0.38	0.33	2.14	2.12	2.55	2.52	2.89	2.30	2.39	2.37	2.67	2.47
Eu	0.33	0.20	0.20	0.51	0.45	0.42	0.42	0.62	0.42	0.33	0.24	0.89	0.91	1.13	0.96	1.28	1.13	1.09	1.09	1.18	1.20
Gd	2.17	0.96	1.08	2.69	2.61	1.77	1.77	2.21	1.57	1.94	0.81	5.19	5.38	6.03	2.88	6.37	4.89	5.13	5.41	5.31	5.51
Tb	0.73	0.28	0.26	0.73	0.67	0.35	0.35	0.51	0.30	0.51	0.17	1.16	1.22	1.20	0.34	1.33	1.33	0.97	1.08	1.11	1.10
Dy	7.09	2.77	2.70	7.21	6.99	2.44	2.55	3.99	2.18	4.57	1.30	10.23	9.96	10.14	1.63	10.68	11.76	9.13	9.22	8.02	9.10
Ho	2.04	0.69	0.70	1.92	1.86	0.54	0.56	0.87	0.46	1.14	0.26	2.77	2.58	2.36	0.20	2.51	3.09	2.05	2.30	2.01	2.02
Er	7.13	2.24	2.30	6.30	6.15	1.72	1.50	2.59	1.19	3.44	0.75	9.37	8.03	7.04	0.35	7.63	10.72	6.93	6.94	5.11	6.73
Tm	1.11	0.34	0.34	0.91	0.92	0.27	0.23	0.36	0.16	0.53	0.10	1.48	1.16	1.01	0.04	1.10	1.65	1.00	1.11	0.79	0.91
Yb	8.21	2.22	2.34	6.68	6.59	2.04	1.60	2.45	1.13	3.95	0.67	10.58	8.02	6.90	0.14	7.75	12.09	7.34	8.65	4.99	7.30
Lu	1.29	0.32	0.37	0.96	1.04	0.32	0.25	0.35	0.16	0.61	0.10	1.64	1.15	0.98	0.02	1.11	1.82	1.09	1.27	0.70	1.01
Hf	0.11	0.04	0.05	0.11	0.14	0.05	0.06	0.13	0.07	0.12	0.08	0.23	0.37	0.25	0.25	0.28	0.17	0.22	0.26	0.29	0.25
Ta		0.01		0.03	0.00	0.01	0.02				0.00	0.01	0.01	0.01		0.01					0.01
Pb	0.04	0.11	0.03	0.20		0.06	0.03				0.02	0.13	0.13	0.10		0.08					
Th	0.03			0.04	0.02	0.02	0.02	0.04	0.02	0.02	0.01	0.04	0.04	0.01		0.02	0.01				0.02
U	0.04	0.02		0.04	0.03	0.02	0.04	0.05	0.04	0.05	0.02	0.02	0.03	0.01	0.02	0.02				0.02	

Note: E, garnet in the lamellar zone; M, garnet in the recrystallized granular zone; C, garnet in the coarse equant zone.

Table 6-16 Trace-element compositions (ppm) of amphibole in the garnet pyroxenites from Lakes Bullenmerri and Gnotuk

Sample	BM99-2		BM99-6	BM99-4	BME-1	BM96-3	BM99-5	DR9748		GN35	DR10165		BM99X1	GN41	GN18	BMC-1	BM90-3	BM99-7	DR11022	DR11017	
Type	Amp2	Amp3	Amp2	Amp2	Amp1	Amp2	Amp1	Amp2	Amp3	Amp2	Amp2	Amp2a	Amp2	Amp2	Amp2	Amp2	Amp1	Amp2	Amp2	Amp1	Amp2
Li	1.97	1.97	1.09	2.91	2.06	0.95	3.14	2.29	3.26	0.97	1.59	1.63	3.29	10.21	1.37	3.28	1.88	2.78	1.06	1.53	1.24
B	6.52	6.94	6.40	6.00	7.26	5.41	7.85	0.69	1.34	2.76	2.97	2.85	6.12	2.20	0.92	5.42	5.64	6.12	4.19	9.89	9.73
Sc	19.0	20.3	13.0	28.5	16.6	26.0	45.8	38.2	37.0	41.5	28.3	38.4	29.2	21.5	15.2	37.7	42.3	40.6	44.7	39.8	43.2
Ti	8856	5149	8224	14344	9551	21921	17059	20413	16530	16103	13087	12879	13203	18941	7379	9838	10250	10762	10708	9791	9536
V	265	180	248	476	336	649	468	494	386	322	294	269	543	480	240	493	487	477	462	449	429
Cr	1829	1665	1547	2644	2237	850	2866	4553	3045	2302	1944	1510	721	969	940	731	1305	634	667	706	620
Co	79.7	77.6	53.6	52.0	67.4	79.4	75.5	79.1	81.0	47.5	46.6	47.2	73.4	88.1	75.9	55.4	56.7	51.9	51.0	50.3	48.9
Ni	1212	1053	1040	613	1072	1274	782	1171	1032	773	723	704	434	1220	1070	621	471	540	560	547	525
Cu	1.71	1.81	3.31	2.00	1.55	2.04	2.08	3.91	4.56	0.88	0.81	0.75	2.14	5.37	1.70	1.63	1.80	1.51	1.04	2.56	2.58
Zn	45.0	42.9	12.8	22.8	35.1	54.7	91.3	70.9	81.7	9.7	9.1	9.3	59.1	75.1	45.4	18.3	25.8	15.5	15.9	13.4	15.3
Ga	36.06	27.06	36.40	27.39	18.54	73.03	23.65	27.92	30.83	49.49	19.09	20.86	124.28	33.10	27.02	21.78	19.39	33.41	44.19	61.26	50.01
Rb	9.35	24.35	6.25	1.57	1.01	3.17	8.88	3.88	13.06	8.77	2.14	3.02	16.58	1.51	8.06	3.80	4.19	9.05	12.06	3.32	2.43
Sr	409	327	386	493	371	359	384	525	577	311	530	556	468	217	371	580	499	700	603	561	530
Y	1.96	2.56	1.18	7.75	2.72	4.76	12.36	8.77	11.07	10.71	5.42	11.01	7.55	5.33	1.73	11.04	12.48	13.29	13.67	10.54	13.64
Zr	6.64	71.33	19.55	20.67	14.09	43.31	33.93	25.67	118.76	16.14	21.62	25.25	12.21	11.77	10.63	22.99	30.82	27.81	22.38	22.89	22.55
Nb	13.01	30.25	41.88	16.35	7.99	33.53	7.27	28.43	62.55	17.62	8.48	11.95	24.72	14.44	54.81	3.54	2.54	10.88	3.59	4.82	4.23
Ba	365	213	371	211	52	1109	109	198	193	623	130	168	2123	178	171	214	147	499	371	215	180
La	8.40	8.68	2.88	6.17	4.91	6.68	5.13	4.30	9.38	6.00	11.83	12.44	15.11	3.99	8.27	19.94	16.15	27.74	22.07	19.89	18.66
Ce	15.65	13.47	5.73	14.25	20.75	16.19	10.77	12.53	25.09	11.75	35.66	37.67	30.64	6.49	22.18	68.18	62.61	91.92	80.51	69.35	64.47
Pr	1.73	1.34	0.76	2.03	3.73	2.29	1.45	2.20	3.66	1.44	5.43	5.76	3.52	0.65	3.12	11.82	11.13	15.60	14.19	12.01	11.16
Nd	6.68	4.99	3.78	9.97	19.14	11.47	8.00	11.72	17.10	6.60	23.60	25.38	13.94	2.87	12.68	60.53	56.92	77.49	69.60	60.38	57.11
Sm	1.19	1.02	1.06	2.78	3.48	3.42	2.73	3.20	4.12	2.07	4.11	4.46	2.89	1.37	2.34	11.67	10.86	14.26	13.36	11.66	10.41
Eu	0.47	0.40	0.44	1.12	0.93	1.22	1.00	1.16	1.49	0.95	1.23	1.41	1.00	0.63	0.73	2.79	2.57	3.33	3.29	2.81	2.60
Gd	0.93	0.97	0.88	2.94	1.97	3.38	2.97	3.34	3.76	2.79	2.97	3.72	2.91	1.79	1.40	7.67	7.08	9.16	8.56	7.47	7.29
Tb	0.11	0.12	0.10	0.39	0.19	0.37	0.44	0.43	0.51	0.43	0.34	0.48	0.36	0.26	0.14	0.75	0.69	0.88	0.92	0.68	0.72
Dy	0.57	0.65	0.42	2.09	0.84	1.58	2.81	2.29	2.72	2.63	1.58	2.70	2.02	1.37	0.49	3.41	3.38	3.94	4.30	3.26	3.41
Ho	0.09	0.11	0.05	0.32	0.10	0.21	0.51	0.37	0.44	0.44	0.22	0.44	0.31	0.21	0.06	0.44	0.49	0.55	0.61	0.46	0.56
Er	0.16	0.22	0.08	0.64	0.19	0.36	1.18	0.72	1.00	0.96	0.40	0.90	0.68	0.48	0.11	0.87	0.99	1.08	1.18	0.87	1.17
Tm	0.01	0.02	0.01	0.07	0.02	0.03	0.14	0.08	0.11	0.09	0.04	0.09	0.08	0.05	0.01	0.07	0.10	0.11	0.11	0.08	0.12
Yb	0.07	0.12	0.04	0.37	0.09	0.17	0.82	0.40	0.61	0.52	0.18	0.47	0.41	0.41	0.07	0.38	0.51	0.55	0.61	0.48	0.59
Lu	0.01	0.01	0.01	0.04	0.01	0.01	0.11	0.05	0.07	0.06	0.02	0.05	0.05	0.03		0.04	0.06	0.06	0.07	0.07	0.08
Hf	0.31	1.74	0.76	0.72	0.37	1.87	1.07	1.06	2.85	0.59	0.58	0.57	0.80	0.52	0.20	0.99	1.25	1.12	1.07	0.85	0.82
Ta	0.16	1.59	2.47	0.29	0.25	0.34	0.18	0.69	2.34	0.22	0.34	0.40	0.13	0.17	2.54	0.12	0.11	0.21	0.15	0.17	0.13
Pb	1.64	1.49	1.09	2.84	2.09	1.70	0.93	2.40	2.29	1.97	2.93	2.86	6.46	2.29	1.95	5.64	3.84	7.04	5.30	4.14	4.09
Th	0.64	0.82	0.32	0.57	0.22	0.61	0.78	0.68	0.88	0.59	0.55	0.59	0.99	0.88	0.77	0.61	0.93	1.33	0.84	0.64	0.78
U	0.15	0.17	0.07	0.12	0.05	0.13	0.17	0.14	0.20	0.13	0.10	0.10	0.19	0.19	0.19	0.08	0.13	0.21	0.10	0.07	0.09

Note: Amp1, amphibole in lamellar zone; Amp2, amphibole in recrystallized granular zone; Amp3, amphibole vein.

Table 6-17 Trace-element compositions (ppm) of phlogopite (Phl), apatite (Ap) and plagioclase (Pl) in the garnet pyroxenites from Lakes Bullenmerri and Gnotuk

Mineral	Phl		Ap				Pl				
Sample	BM96-3		BM99X1	BM99-7	BMC-1		BM99X1		BM99-8		BM99-9
Type	M1	M2	M	M	M	SOG	E	M	E	M	E
Li	1.21	13.77	0.48	0.69	1.07	0.60	2.29	1.91	4.11	4.35	2.39
Be		0.10		0.08		0.02	0.12	0.13	0.23	0.33	
B	5.34	22.52	1.81	1.75	2.04	1.07	1.53	3.34	6.79	4.89	9.78
Sc	3.77	4.14	1.11	0.92	0.91	0.45	3.33	1.85	2.07	1.64	0.90
Ti	681	716	31.9	23.8	19.4	17.5	109	91.4	23.8	23.0	21.7
V	158	173	2.74	2.55	2.09	1.77	5.37	1.19	0.15	0.19	0.15
Cr	51678	52997					14.62	2.68			0.85
Co	111.3	110.9	1.79	1.22	0.94	1.00	0.63	0.44	0.30	0.30	0.21
Ni	2140	2050	1.78	3.31	1.51	1.34	3.31	2.21	0.45	0.56	0.31
Cu	2.29	14.2	0.53	0.22	0.33		1.11	1.57	1.70	1.70	2.96
Zn	73.9	74.8	1.70	1.25	1.58	0.52	1.23	1.12	1.40	0.95	0.87
Ga	814	808	3.59	0.52	0.30	0.38	35.4	47.7	39.4	40.0	14.0
Rb	87.04	91.01	0.16			0.07	1.59	1.59	3.28	3.90	0.62
Sr	128	135	3270	2904	2520	2887	3671	2991	3501	3975	221
Y	0.33	0.51	34.40	43.75	34.82	7.61	0.06	0.07	0.05	0.04	0.03
Zr	5.69	7.49	1.21	2.28	1.67	1.61	0.17	0.88	0.09	0.72	0.21
Nb	41.41	43.18	0.09	0.03				0.20	0.02	0.03	0.02
Ba	16603	16103	118	18.5	11.2	15.6	1336	1222	826	960	7.02
La	0.02	0.12	1132	1006	692	790	9.67	8.97	4.79	5.48	0.04
Ce	0.00	0.18	1146	1811	1368	1564	6.87	6.00	4.62	4.97	0.15
Pr		0.02	81.0	207	166	191	0.34	0.33	0.34	0.35	0.03
Nd		0.10	232	750	635	722	0.80	0.73	0.72	0.77	0.15
Sm	0.02	0.05	28.8	83.4	72.5	78.1	0.07	0.08	0.04	0.08	
Eu	0.20	0.21	7.75	15.4	12.9	13.2	0.45	0.37	0.27	0.28	0.06
Gd	0.03	0.06	23.8	43.9	37.6	31.1	0.06	0.10		0.05	0.12
Tb		0.01	2.33	3.40	2.65	1.68	0.01	0.01	0.01	0.01	
Dy		0.05	9.18	12.98	9.89	4.04	0.04	0.05		0.02	
Ho		0.01	1.27	1.84	1.31	0.29	0.01	0.01			0.01
Er		0.02	2.25	3.20	2.35	0.39		0.03	0.02		0.01
Tm			0.22	0.26	0.22	0.02		0.00	0.00		0.02
Yb		0.03	1.15	1.19	0.96	0.08		0.08		0.03	0.14
Lu			0.11	0.14	0.10	0.01		0.01	0.00	0.01	
Hf	0.22	0.22		0.04		0.08	0.04	0.02		0.01	
Ta	0.31	0.48		0.01				0.01	0.01	0.01	
Pb	1.83	2.21	25.30	9.82	6.64	8.26	19.89	18.80	6.82	8.44	0.44
Th			124.6	90.4	40.0	42.5	0.02	0.07	0.02	0.02	
U	0.01	0.01	24.92	18.25	6.72	7.03	0.01				

Note: E, minerals in the lamellar zone; M, minerals in the recrystallized granular zone; SOG, Sp-Gt reaction zone.

Table 6-18 Major-element compositions of the reconstructed whole rock of the garnet pyroxenites from Lakes Bullenmerri and Gnotuk

Rock type	Type I										Type II a									Type II b				
Samples:	BM99-2	BM99-6	BM99-4	BME-1	BM99-2	BM96-3	BM99-5	GN35	DR 10165	DR 9748	BM 99X2	GN85-1	BM99-9	BM 99X1	BM99-8	GN 51	GN 18	GN 41	DR 10162	BMC-1	BM90-3	BM99-7	DR 11017c	DR 11022
wt%																								
SiO_2	47.4	47.2	49.7	48.6	48.3	45.3	50.7	47.3	47.0	50.6	47.4	44.7	47.9	49.8	47.5	44.2	46.1	46.2	46.1	48.0	49.1	48.1	46.4	44.6
TiO_2	0.27	0.23	0.51	0.26	0.24	0.36	0.88	0.51	0.32	0.60	0.38	0.29	0.15	0.49	0.10	0.31	0.12	0.43	0.14	0.47	0.37	0.63	0.42	0.37
Al_2O_3	12.40	13.91	10.10	11.89	11.65	15.78	5.73	12.35	12.80	7.44	12.83	16.14	13.82	11.02	12.99	16.22	15.66	15.24	16.79	9.76	9.85	9.55	12.71	13.12
Cr_2O_3	0.36	0.19	0.26	0.22	0.20	0.11	0.29	0.55	0.33	0.37	0.09	0.11	0.12	0.08	0.11	0.00	0.11	0.09	0.19	0.14	0.11	0.10	0.14	0.15
FeO	8.68	5.63	5.83	6.84	7.62	11.11	9.88	6.10	7.06	10.21	9.63	11.90	7.70	6.66	7.42	9.65	8.55	9.74	8.78	7.20	7.45	6.34	7.59	7.02
MnO	0.20	0.16	0.18	0.12	0.19	0.30	0.19	0.18	0.10	0.21	0.22	0.31	0.21	0.16	0.19	0.17	0.16	0.19	0.14	0.15	0.22	0.15	0.16	0.11
MgO	17.46	17.06	18.75	17.81	17.90	17.40	17.68	19.62	19.64	20.80	13.68	13.51	12.08	13.53	15.21	13.21	15.20	13.95	15.87	15.71	16.02	15.69	16.31	16.02
CaO	12.58	15.24	13.39	14.03	13.44	8.40	13.72	12.29	12.25	9.94	15.81	13.13	16.90	17.79	15.76	14.28	13.38	13.89	13.04	17.70	16.33	18.16	16.22	17.72
Na_2O	0.93	0.79	1.08	0.67	0.80	0.28	0.91	0.95	0.61	0.61	1.05	0.70	1.21	1.62	0.86	0.98	0.88	1.07	0.64	0.85	0.70	1.13	0.78	0.61
K_2O	0.05	0.00	0.04	0.00	0.00	0.00	0.03	0.01	0.00	0.02	0.00	0.00	0.00	0.00	0.00	0.00	0.00	0.00	0.00	0.01	0.00	0.08	0.01	0.01
NiO	0.07	0.05	0.00	0.04	0.06	0.04	0.08	0.03	0.02	0.01	0.03	0.03	0.05	0.00	0.00	0.00	0.00	0.00	0.00	0.02	0.00	0.02	0.06	0.03
Total	100.4	100.5	99.9	100.5	100.4	99.1	100.1	99.9	100.1	100.8	101.1	100.9	100.0	101.2	100.2	99.1	100.2	100.8	101.7	100.0	100.2	99.9	100.8	99.8
Mg#	78.2	84.4	85.1	82.3	80.7	73.6	76.1	85.2	83.2	78.4	71.7	66.9	73.7	78.4	78.5	70.9	76.0	71.8	76.3	79.6	79.3	81.5	79.3	80.3

Table 6-19 Trace-element compositions (ppm) of reconstructed whole rock in the garnet pyroxenites from Lakes Bullenmerri and Gnotuk

Rock Type:	Type I										Type II a									Type II b				
Sample:	BM 99-2	BM 99-6	BM 99-4	BM E-1	BM 99-2	BM 96-3	BM 99-5	GN 35	DR 10165	DR 9748	BM 99X2	GN 85-1	BM 99-9	BM 99X1	BM 99-8	GN 51	GN 18	GN 41	DR 10162	BM C-1	BM 90-3	BM 99-7	DR 11017c	DR 11022
Li	1.86	0.97	3.53	1.58	1.53	0.95	2.70	1.63	2.01	3.25	3.96	1.61	2.14	3.06	3.01	1.87	1.98	2.30	1.10	3.73	1.55	3.07	1.72	1.36
Be	0.11	0.08	0.20	0.20	0.26	0.51	0.33	0.02	0.02	0.15	0.04	0.06	0.05	0.07	0.10	0.09	0.20	0.17	0.03	0.08	0.17	0.15	0.12	0.06
B	1.70	2.16	8.53	1.86	2.05	1.12	1.40	6.20	7.30	0.44	5.99	2.31	2.64	2.63	6.60	0.92	0.93	1.26	2.47	1.64	1.62	5.78	7.12	2.24
Sc	42.0	34.7	40.2	31.9	47.5	60.6	44.3	43.6	36.2	40.8	44.4	84.2	57.8	58.3	67.8	46.7	41.1	55.9	39.0	43.3	71.5	52.5	40.3	43.8
Ti	1685	1625	3256	1606	1459	1952	3388	2818	2105	3791	2399	1775	893	2291	665	1935	1040	3374	1072	2656	2178	3855	2685	2424
V	121	131	259	161	170	360	268	181	131	244	417	395	211	313	159	402	120	274	90	308	240	311	247	264
Cr	2264	1257	1596	1506	1312	612	1535	1248	1012	2273	544	698	704	496	730	387	736	859	1240	768	634	589	382	381
Co	52.7	41.7	38.8	55.0	56.0	104.3	34.9	36.3	37.9	82.8	58.8	67.3	60.6	42.2	64.8	59.0	56.2	63.3	71.4	45.2	37.5	37.1	25.2	23.0
Ni	370	327	262	360	346	169	267	363	309	739	256	198	185	117	218	185	231	284	314	347	163	275	200	179
Cu	0.658	1.64	1.08	0.54	1.02	154.128	1.02	1.36	0.67	2.44	0.92	1.41	1.30	1.17	0.90	1.47	0.51	0.62	0.94	0.424	0.49	0.700	0.68	0.39
Zn	50.8	13.1	21.3	26.3	33.6	25.9	37.9	9.3	14.5	102.5	44.1	41.1	36.6	29.7	26.8	37.7	25.9	42.5	26.7	60.3	13.9	22.5	7.9	5.4
Ga	10.2	9.2	10.1	8.4	10.4	27.7	8.3	5.3	3.5	11.8	13.5	12.4	12.3	13.9	8.0	12.2	9.2	13.0	8.0	13.4	5.8	12.2	7.6	5.1
Rb	0.369	0.02	0.13			2.002	0.24	0.35	0.06	0.19	0.00	0.03	0.02	0.17	0.09	0.03	0.00	0.00	0.00	0.232	0.19	1.680	0.19	0.39
Sr	90.4	84.4	109.3	72.5	63.6	24.6	79.1	65.1	83.6	80.7	8.7	25.7	10.3	204.6	124.5	77.0	73.2	34.4	72.8	138.6	92.2	249.5	138.6	128.7
Y	4.77	3.35	9.70	5.47	5.00	16.43	7.65	8.16	7.54	8.30	9.88	31.2	6.45	17.93	5.27	11.78	6.37	14.52	3.99	11.15	25.35	15.15	9.26	9.95
Zr	5.13	13.72	17.37	12.21	4.49	26.93	21.24	11.42	14.30	16.82	2.59	7.87	0.91	11.75	6.62	13.56	10.39	7.96	4.19	19.48	25.88	24.99	18.47	19.25
Nb	0.56	0.48	0.93	0.15	0.12	0.23	0.24	0.82	0.32	1.62	0.10	0.58	0.01	0.18	0.66	0.18	0.38	0.13	0.17	0.24	0.09	2.09	0.37	0.09
Ba	13.67	1.18	10.31	0.56	0.03	0.04	2.89	25.00	3.99	10.03	0.05	0.77	0.32	49.22	10.41	0.17	0.06	0.02	0.04	13.06	1.86	92.67	14.56	7.89
La	1.68	1.38	3.10	2.30	0.97	1.06	1.79	2.83	4.52	1.72	0.36	1.92	0.03	6.85	2.64	10.84	3.70	1.71	1.19	11.57	8.38	17.54	11.38	12.02
Ce	2.47	2.75	7.17	9.19	1.96	2.53	4.34	5.69	14.50	5.03	0.50	3.23	0.27	12.95	7.28	28.96	10.44	2.57	2.26	39.51	32.13	58.10	39.31	41.97
Pr	0.31	0.37	1.05	1.76	0.27	0.37	0.76	0.69	2.14	0.87	0.05	0.35	0.08	1.44	1.08	3.06	1.44	0.24	0.30	6.98	5.88	9.84	6.70	7.20
Nd	1.51	1.92	5.10	8.73	1.40	1.83	4.50	3.17	9.11	4.51	0.41	1.32	0.53	6.03	4.54	9.91	6.05	1.23	1.40	33.86	29.14	48.25	32.87	33.96
Sm	0.50	0.60	1.52	1.78	0.48	0.92	1.55	1.03	1.64	1.32	0.52	0.62	0.20	1.46	0.98	1.51	1.35	0.75	0.48	6.34	5.71	9.07	6.22	6.36
Eu	0.24	0.29	0.66	0.50	0.22	0.42	0.57	0.45	0.53	0.48	0.29	0.33	0.15	0.58	0.38	0.60	0.52	0.40	0.24	1.49	1.43	2.14	1.48	1.50
Gd	0.69	0.71	1.85	1.26	0.65	2.06	1.83	1.34	1.38	1.48	1.28	1.76	0.59	2.07	1.09	1.73	1.37	1.65	0.67	4.10	4.63	6.01	4.01	4.05
Tb	0.13	0.11	0.32	0.17	0.12	0.39	0.27	0.28	0.22	0.23	0.26	0.49	0.13	0.38	0.17	0.32	0.21	0.34	0.12	0.46	0.65	0.66	0.37	0.46
Dy	0.86	0.69	2.32	1.04	0.89	3.02	1.66	1.62	1.38	1.61	1.93	4.42	1.10	2.99	1.08	2.24	1.30	2.59	0.79	2.44	4.23	3.53	2.20	2.28
Ho	0.19	0.13	0.49	0.20	0.20	0.67	0.32	0.31	0.26	0.33	0.40	1.22	0.25	0.71	0.22	0.47	0.25	0.58	0.15	0.43	0.96	0.60	0.34	0.39
Er	0.51	0.35	1.44	0.56	0.58	1.72	0.76	0.82	0.80	0.91	1.07	4.16	0.78	2.10	0.60	1.34	0.63	1.67	0.42	1.08	2.88	1.43	0.82	0.96
Tm	0.07	0.04	0.21	0.08	0.09	0.23	0.10	0.10	0.10	0.13	0.14	0.64	0.12	0.30	0.09	0.19	0.08	0.25	0.06	0.14	0.43	0.18	0.10	0.12
Yb	0.48	0.29	1.43	0.53	0.61	1.45	0.63	0.64	0.76	0.90	0.94	4.72	0.75	2.10	0.64	1.23	0.57	1.84	0.37	0.89	2.99	1.11	0.67	0.78
Lu	0.07	0.04	0.21	0.07	0.09	0.21	0.08	0.09	0.11	0.13	0.13	0.74	0.11	0.32	0.10	0.18	0.08	0.28	0.05	0.12	0.45	0.15	0.09	0.11
Hf	0.23	0.46	0.73	0.33	0.21	0.85	0.92	0.41	0.35	0.68	0.21	0.26	0.08	0.77	0.12	0.39	0.19	0.44	0.15	0.91	1.01	1.05	0.80	0.90
Ta	0.02	0.10	0.03	0.02	0.02	0.02	0.02	0.01	0.02	0.05	0.00	0.04	0.01	0.01	0.06	0.01	0.08	0.00	0.02	0.01	0.01	0.05	0.02	0.01
Pb	0.28	0.19	0.58	0.30	0.13	0.08	0.21	0.31	0.36	0.31	0.10	0.23	0.12	1.64	0.35	0.38	0.22	0.28	0.15	1.09	0.61	2.16	0.90	0.81
Th	0.31	0.18	0.44	0.14	0.17	0.14	0.42	0.34	0.23	0.34	0.07	0.28	0.01	0.56	0.34	0.47	0.47	0.48	0.17	0.39	0.60	0.88	0.42	0.45
U	0.08	0.05	0.11	0.07	0.04	0.05	0.10	0.08	0.05	0.08	0.02	0.08	0.01	0.12	0.10	0.11	0.12	0.12	0.04	0.05	0.09	0.15	0.07	0.05

Table 6-20 Major- and Trace-element compositions of reconstructed clinopyroxene in the garnet pyroxenites from Lakes Bullenmerri and Gnotuk

Type	Type I				Type IIa			
Sample ID	BM99-4	BME-1	BM99-2	BM99-5	BM99X1	BM99-8	BM99-9	BM99X2
Exsolution phases modes (wt%)*								
Cpx	61.4	76.8	70.0	65.6	86.8	62.6	66.3	77.0
Gt	15.5	10.5	14.3	5.6	13.2	37.4	33.7	23.0
Opx	23.2	12.7	15.7	28.8				
Pl							<1	
Ilm				<1				
major element (wt%)								
SiO_2	50.27	50.93	49.96	51.27	50.38	47.36	47.56	48.83
TiO_2	0.48	0.34	0.29	0.60	0.53	0.10	0.15	0.40
Al_2O_3	9.08	7.89	8.63	5.53	9.96	12.95	13.63	10.60
Cr_2O_3	0.25	0.23	0.18	0.28	0.09	0.11	0.12	0.07
FeO	5.65	5.08	6.59	9.74	6.12	7.56	7.98	8.54
MnO	0.16	0.08	0.14	0.19	0.14	0.20	0.22	0.18
MgO	19.18	17.25	17.82	17.83	13.59	15.39	12.39	13.73
CaO	13.59	17.35	15.55	13.88	18.77	15.73	16.95	17.30
Na_2O	0.94	0.93	1.00	0.86	1.64	0.79	1.07	1.23
K_2O	0.00	0.00	0.00	0.00	0.00	0.00	0.00	0.00
NiO	0.00	0.07	0.07	0.08	0.00	0.00	0.05	0.00
Total	99.62	100.15	100.21	100.23	101.20	100.18	100.05	100.88
Mg#	85.94	85.93	82.95	76.72	79.98	78.57	73.64	74.33
Mg# in equilibrium melt	61.15	61.13	55.62	45.90	50.71	48.56	41.84	42.71
trace element (ppm)								
Li	2.94	1.70		2.70	3.80	2.94	2.12	4.97
Be	0.16	0.23	0.01	0.32		0.11	0.05	
B	8.06	2.08	1.74	1.24	1.54	6.62	2.47	6.40
Sc	36.52	22.43	32.27	44.46	50.55	68.36	60.03	35.27
Ti	2551.78	1952.61	1686.51	3035.69	3189.76	673.12	904.67	2386.75
V	224.88	183.48	179.87	263.48	406.78	160.60	214.39	443.39
Cr	1292.55	1243.77	1068.08	1506.64	545.25	731.04	720.59	463.81
Co	22.40	33.72	36.27	33.93	39.52	65.29	62.50	55.88
Ni	142.39	337.71	295.88	254.83	145.52	219.76	186.97	297.36
Cu	0.99	0.61	1.18	0.99	1.36	0.88	1.26	1.11
Zn	11.10	16.23	20.38	36.66	29.98	26.94	37.50	
Ga	7.38	8.01	9.69	7.92	14.63	7.58	12.17	13.44
Rb	0.04		0.01	0.00	0.11	0.04	0.01	
Sr	91.59	97.98	80.74	71.25	98.94	82.72	5.05	10.34
Y	8.62	2.58	2.86	7.56	11.07	5.53	6.76	4.90
Zr	17.02	13.48	4.42	21.01	14.81	6.69	0.93	2.11
Nb	0.13		0.10	0.05	0.21	0.62	0.01	0.09
Ba	0.07	0.07	0.03	0.04	0.49	0.49	0.16	0.12
La	3.06	3.14	1.17	1.71	8.40	2.53	0.03	0.41
Ce	7.21	12.62	2.42	4.19	16.04	7.03	0.27	0.55
Pr	1.06	2.41	0.35	0.75	1.84	1.05	0.08	0.06
Nd	5.14	11.68	1.75	4.43	7.23	4.39	0.54	0.42
Sm	1.50	2.15	0.57	1.52	1.80	0.95	0.21	0.53
Eu	0.63	0.59	0.20	0.56	0.63	0.37	0.15	0.26
Gd	1.76	1.28	0.56	1.81	2.11	1.08	0.60	0.99
Tb	0.28	0.13	0.09	0.27	0.33	0.17	0.13	0.17
Dy	2.08	0.66	0.58	1.64	2.20	1.12	1.15	1.12
Ho	0.41	0.09	0.12	0.31	0.45	0.23	0.26	0.20
Er	1.20	0.23	0.31	0.75	1.22	0.60	0.82	0.48
Tm	0.17	0.03	0.04	0.10	0.16	0.09	0.12	0.06
Yb	1.11	0.15	0.29	0.63	1.07	0.62	0.79	0.33
Lu	0.16		0.04	0.08	0.15	0.09	0.12	0.04
Hf	0.75	0.39	0.24	0.92	0.93	0.12	0.08	0.20
Ta	0.01	0.02	0.02	0.01	0.01	0.06	0.01	0.00
Pb	0.46	0.40	0.16	0.20	1.11	0.26	0.11	0.12
Th	0.44		0.21	0.42	0.79	0.34	0.01	
U	0.11	0.05	0.05	0.10	0.16	0.10	0.01	0.02

Table 6-21 Pressure-Temperature-Depth (P-T-D) results of re-equilibrated mineral assemblages and reconstructed clinopyroxene

Type	Sample No.	Microstructure type	EG/Wd* T (°C)	P (kb)	D (km)	CMAS§ T (°C)	P (kb)	D (km)	NT00# T (°C)	P (kb)	REE15** T (°C)	P (kb)
Type I	BM99-4	Lamelar	982	15	50							
		Recrystallized	983	15	49							
		Reconstructed				1450	23	75	1317	18		
	BM99-5	Lamelar	1047	17	57							
		Reconstructed				1460	30	97	1259	24		
	BM99-2	Lamellar	1064	17	55							
		Recrystallized	1049	17	56							
		Reconstructed				1450	24	78	1246	14		
	BM96-3	Coarse	1010	14	48							
	BME-1	Lamellar	1011	14	45							
		Coarse	997	15	49							
		Reconstructed				1420	24	78	1206	15		
	BM99-2	Recrystallized	1094	18	59							
	BM99-6	Coarse	1060	16	53							
Type IIa	BM99X1	Lamellar	980	13	42							
		Reconstructed				1280	16	53				
	BM99-9	Lamellar	1000	13	44							
		Reconstructed				1400	17	56				
	BM99-8	Lamellar	970	12	41							
		Reconstructed										
	GN85-1	Coarse	1040	15	50							
	BM99X2	Lamellar	1040	15	50						971 ± 29	12 ± 3
		Coarse	1050	17	55						1032 ± 15	21 ± 1
		Reconstructed				1400	20	66			1297 ± 45	23 ± 3
Type IIb	BM90-3	Lamellar	950	13	43							
		Recrystallized	973	14	46							
	BMC-1	Recrystallized	986	15	49							
		SOG§§	971	12	41							
	BM99-7	Recrystallized	1006	16	53							
		SOG	1002	15	51							

*Ellis and Green (1979) Cpx-Gt thermometer and Wood (1974) Al-in-Opx barometer.
§ $CaO-MgO-Al_2O_3-SiO_2$ (CMAS) system from Gasparik (2014).
# Nimis and Taylor (2000) En-in-Cpx thermometer and Cr-in-Cpx barometer.
** REE-in-garnet-clinopyroxene thermobarometer of Sun and Liang (2015).
§§ Sp-Gt reaction texture.

Table 6-22 Sr-Nd-Hf isotopes of clinopyroxene, amphibole, garnet and whole rock of garnet pyroxenites from Lakes Bullenmerri and Gnotuk

Rock type	Sample ID	Mineral	Rb (ppm)	Sr (ppm)	$^{87}Rb/^{86}Sr$	$^{87}Sr/^{86}Sr$	2 SE	Sm (ppm)	Nd (ppm)	$^{147}Sm/^{144}Nd$	$^{143}Nd/^{144}Nd$	2 SE	Lu (ppm)	Hf (ppm)	$^{176}Lu/^{177}Hf$	$^{176}Hf/^{177}Hf$	2 SE
	BHVO-2					0.703468	0.000008				0.512985	0.000003				0.283107	0.000010
Type I	BM99-4	Cpx	0.04	149	0.0008	0.705659	0.000003	2.25	7.93	0.1787	0.512607	0.000003	0.03	1.14	0.0037	0.282901	0.000003
		Amp	1.57	493	0.0090	0.705500	0.000005	2.78	9.97	0.1758	0.512699	0.000003	0.04	0.72	0.0075	0.282959	0.000007
		Gt						0.56	0.38	0.9275	0.512846	0.000005	1.13	0.18	0.8573	0.283947	0.000006
		Gt-D									0.512826	0.000014	0.20	0.71	0.0401	0.282945	0.000003
		WR*						1.48	4.88	0.1905	0.512611	0.000003					
	BME-1	Cpx		127		0.705815	0.000014	2.82	15.22	0.1167	0.512436	0.000004		0.51		0.283051	0.000005
		Cpx-R		127		0.705848	0.000003				0.512442	0.000003				0.283072	0.000026
		Gt						0.61	0.66	0.5856	0.512545	0.000012	0.35	0.09	0.5797	0.284281	0.000008
		WR*						1.77	8.71	0.1277	0.512444	0.000002	0.07	0.37	0.0262	0.283107	0.000005
	BM99-2	Cpx		114		0.704123	0.000004	0.72	2.42	0.1881	0.512833	0.000008	0.01	0.11	0.0158	0.283290	0.000011
	BM99-5	Cpx		109		0.705659	0.000003	2.23	6.69	0.2099	0.512862	0.000006	0.04	1.38	0.0040	0.282811	0.000008
	DR9748**	Cpx	0.013	116	0.0003	0.70657	0.00004	2.50	9.00	0.1685	0.512738	0.000005					
		Opx						0.29	0.94	0.1853	0.512748	0.000006					
		Gt						0.79	0.57	0.8332	0.512876	0.000050					
		WR						1.38	4.89	0.1711	0.512745	0.000016					
Type II a	BM99X2	Cpx		13.92		0.704676	0.000009	0.64	0.58	0.6872	0.513547	0.000005	0.01	0.28	0.0025	0.283580	0.000012
		Gt						0.36	0.07	3.0629	0.514189	0.000055	0.73	0.07	1.3751	0.286950	0.000015
		Gt2											0.16	0.05	0.4202	0.286720	0.000008
		WR*						0.52	0.41	0.8149	0.513582	0.000006	0.13	0.20	0.0928	0.283801	0.000012
	GN85-1	Cpx	0.03	58.72	0.0012	0.704894	0.000002	0.82	2.77	0.1867	0.513557	0.000007	0.02	0.45	0.0061	0.283963	0.000011
		Gt						0.41	0.21	1.2536	0.513997	0.000035	1.27	0.13	1.3876	0.289316	0.000006
		WR*						0.62	1.32	0.2958	0.513602	0.000010	0.73	0.27	0.3792	0.285409	0.000011
	BM99-9	Cpx	0.02	7.93	0.0068	0.704924	0.000009	0.23	0.77	0.1881	0.512964	0.000030	0.01	0.11	0.0158	0.283479	0.000042
	BM99X1	Cpx	0.12	120	0.0027	0.709112	0.000009	1.95	8.46	0.1449	0.512424	0.000003	0.03	1.07	0.0035	0.282837	0.000004
	DR10162	Cpx	0.02	155	0.0003	0.70397	0.00005	0.69	2.79	0.1500	0.51283	0.00002					
Type II b	BM90-3	Cpx	0.14	127	0.0031	0.715485	0.000004	7.41	40.84	0.1143	0.512221	0.000006	0.05	1.39	0.0050	0.282747	0.000004
	BMC-1	Cpx		138		0.714232	0.000004	7.14	39.97	0.1126	0.512218	0.000002	0.01	1.10	0.0018	0.282774	0.000011
		Amp	3.80	580	0.0185	0.715119	0.000004	11.67	60.53	0.1214	0.512216	0.000001	0.04	0.99	0.0058	0.282791	0.000005

* samples are from Griffin et al., 1988.

Table 6-23 *In situ* Sr isotopic compositions of clinopyroxene, amphibole, apatite and plagioclase from garnet pyroxenite in Lakes Bullenmerri and Gnotuk

Sample ID	Spot ID	Spot Size (um)	Texture	$^{87}Sr/^{86}Sr$	2 SE	Comments
BM99-6	BM99-6cpx1-1	155	granular	0.70462	0.00007	
	BM99-6cpx1-2	155	granular	0.70463	0.00007	
	BM99-6cpx1-3	155	granular	0.70447	0.00005	
	BM99-6cpx1-4	155	granular	0.70454	0.00005	
	BM99-6cpx1-5	155	granular	0.70445	0.00005	
	BM99-6cpx4-1	155	granular	0.70434	0.00008	
	BM99-6cpx4-2	155	granular	0.70439	0.00005	
	BM99-6cpx5-1	155	granular	0.70462	0.00007	
	BM99-6cpx5-2	155	granular	0.70445	0.00005	
	BM99-6cpx5-3	155	granular	0.70445	0.00007	
	BM99-6cpx6-1	155	granular	0.70445	0.00005	
	BM99-6amp2	85	granular	0.70460	0.00007	
	BM99-6amp3	110	granular	0.70461	0.00006	
	BM99-6amp3-1	110	granular	0.70461	0.00006	
	BM99-6amp3-2	110	granular	0.70464	0.00006	
BM96-3	BM96-3cpx5	155	granular	0.70521	0.00006	cpx with lower Sr
	BM96-3cpx7	155	granular	0.70632	0.00009	
	BM96-3cpx7-2	155	granular	0.70606	0.00009	
	BM96-3cpx3	155	granular	0.70623	0.00009	
	BM96-3cpx3-2	155	granular	0.70615	0.00011	
	BM96-3cpx4	155	granular	0.70665	0.00009	
	BM96-3cpx4-2	155	granular	0.70626	0.00010	
	BM96-3cpx4-3	155	granular	0.70603	0.00007	
	BM96-3cpx6	155	granular	0.70596	0.00007	
	BM96-3cpx6-2	155	granular	0.70628	0.00007	
	BM96-3cpx8	155	granular	0.70612	0.00029	
	BM96-3amp1-1	155	granular	0.70603	0.00004	
	BM96-3amp1-2	155	granular	0.70596	0.00002	
	BM96-3amp1-3	155	granular	0.70599	0.00002	
BM99-2	BM99-2cpx1-1	155	granular	0.70434	0.00009	
	BM99-2cpx1-2	155	granular	0.70463	0.00009	
	BM99-2cpx2	155	granular	0.70462	0.00008	
	BM99-2cpx3	155	granular	0.70472	0.00008	
BM99-2	BM99-2cpx10	155	granular	0.70423	0.00006	
	BM99-2cpx10-2	155	granular	0.70425	0.00007	
	BM99-2cpx2	155	granular	0.70430	0.00008	
	BM99-2cpx2-2	155	granular	0.70452	0.00005	
	BM99-2cpx6	155	granular	0.70450	0.00007	
	BM99-2am1	155	granular	0.70427	0.00002	
	BM99-2am1-2	155	granular	0.70439	0.00003	
	BM99-2am7	155	vein	0.70452	0.00005	
	BM99-2am9	155	vein	0.70453	0.00006	
	BM99-2am4	150	vein	0.70436	0.00017	
BM99-4	BM99-4cpx4	155	granular	0.70642	0.00009	
	BM99-4cpx4-1	155	granular	0.70650	0.00008	
	BM99-4cpx5	155	granular	0.70606	0.00008	
	BM99-4cpx5-1	155	granular	0.70605	0.00008	
	BM99-4cpx6	155	host	0.70629	0.00006	
	BM99-4cpx6-2	155	host	0.70629	0.00011	
	BM99-4cpx6-3	155	host	0.70628	0.00007	
	BM99-4am1	155	granular	0.70609	0.00004	
	BM99-4am1-2	155	granular	0.70610	0.00003	
	BM99-4am2	155	granular	0.70597	0.00004	
	BM99-4am3	155	granular	0.70601	0.00004	
BM99-5	BM99-5cpx6-1	155	host	0.70671	0.00017	
	BM99-5cpx6-2	155	host	0.70683	0.00014	
	BM99-5cpx6-3	155	host	0.70694	0.00016	
	BM99-5cpx2	155	host	0.70693	0.00015	
	BM99-5am1	155	lamellae	0.70618	0.00007	
	BM99-5am3	135	lamellae	0.70611	0.00008	
	BM99-5am5	155	lamellae	0.70611	0.00007	
	BM99-5am5-2	155	lamellae	0.70610	0.00008	
BME-1	BME-1cpx6	155	host	0.70616	0.00011	
	BME-1cpx6-2	155	host	0.70608	0.00010	

Continued

Sample ID	Spot ID	Spot Size (um)	Texture	$^{87}Sr/^{86}Sr$	2 SE	Comments
	BME-1cpx1	155	granular	0.70605	0.00018	
	BME-1cpx1-2	155	granular	0.70607	0.00013	
	BME-1cpx5	155	granular	0.70605	0.00022	
BME-1	BME-1am3	155	lamellae	0.70580	0.00007	
	BME-1am7	150	granular	0.70613	0.00007	
	BME-1am4	150	granular	0.70614	0.00008	
	BME-1am4-2	155	granular	0.70612	0.00006	
DR10165	10165-cpx3-1	150	granular	0.70761	0.00044	recrystallized zone C
	10165-cpx3-2	150	granular	0.70788	0.00042	recrystallized zone C
	10165-cpx4	180	granular	0.70887	0.00033	recrystallized zone C
	10165-cpx7	150	granular	0.70968	0.00039	
	10165-cpx7-2	150	granular	0.70781	0.00053	
	10165-cpx9	150	granular	0.70879	0.00059	
	10165-amp2	150	granular	0.70864	0.00010	recrystallized zone C
	10165-amp5	150	granular	0.70880	0.00010	recrystallized zone C
	10165-amp1-1	150	granular	0.70850	0.00009	
	10165-amp1-2	150	granular	0.70929	0.00009	
	10165-amp6-1	150	granular	0.70851	0.00011	
	10165-amp6-2	150	granular	0.70858	0.00011	
GN35	GN35-cpx4	150	host	0.70533	0.00054	
	GN35-cpx7	150	granular	0.70799	0.00065	
	GN35-cpx3	150	granular	0.70629	0.00049	
	GN35-cpx6-1	150	granular	0.70538	0.00048	
	GN35-cpx6-2	150	granular	0.70552	0.00043	
	GN35-amp1-1	150	granular	0.70544	0.00010	
	GN35-amp1-2	150	granular	0.70544	0.00015	
	GN35-amp2	150	granular	0.70546	0.00015	
	GN35-amp5	150	granular	0.70563	0.00014	
DR9748	DR9748-cpx3-1	150	granular	0.70747	0.00027	
	DR9748-cpx3-2	150	granular	0.70780	0.00025	
	DR9748-cpx4-1	150	granular	0.70736	0.00045	
	DR9748-cpx5	150	granular	0.70733	0.00043	
	DR9748-cpx9	150	amp vein	0.70570	0.00037	
	DR9748-cpx9-2	150	amp vein	0.70600	0.00042	
	DR9748-cpx10-1	150	amp vein	0.70590	0.00034	
	DR9748-cpx10-2	150	amp vein	0.70633	0.00038	
	DR9748-amp2-1	150	granular	0.70698	0.00009	
	DR9748-amp2-2	150	granular	0.70693	0.00007	
	DR9748-amp1-1	150	granular	0.70701	0.00009	
	DR9748-amp1-2	150	granular	0.70700	0.00008	
	DR9748-amp5-1	150	amp vein	0.70566	0.00009	
	DR9748-amp5-2	150	amp vein	0.70556	0.00010	
	DR9748-amp6	150	amp vein	0.70563	0.00008	
	DR9748-amp8	150	amp vein	0.70593	0.00007	
BM99-9	BM99-9pl1	110	lamellae	0.70501	0.00008	
	BM99-9pl2	110	lamellae	0.70550	0.00008	
	BM99-9pl7	110	lamellae	0.70525	0.00019	
	BM99-9pl5	110	lamellae	0.70579	0.00007	
	BM99-9pl4	135	granular	0.70532	0.00011	
	BM99-9pl6-3	135	granular	0.70545	0.00005	
	BM99-9pl6-4	135	granular	0.70574	0.00006	
GN18	GN18-cpx1-2	150	granular	0.70647	0.00060	
	GN18-cpx1-3	150	granular	0.70558	0.00050	
	GN18-cpx3	150	granular	0.70558	0.00041	
	GN18-cpx3-2	150	granular	0.70627	0.00028	
	GN18-amp2-1	150	granular	0.70677	0.00017	
	GN18-amp2-2	150	granular	0.70692	0.00015	
	GN18-amp2-3	150	granular	0.70652	0.00016	
GN41	GN41-cpx1-4	150	granular	0.70641	0.00089	
	GN41-cpx3-1	150	granular	0.70600	0.00064	
	GN41-cpx3-2	150	granular	0.70723	0.00096	
	GN41cpx2-1	150	granular	0.70626	0.00079	
	GN41cpx2-2	150	granular	0.70573	0.00079	
	GN41amp-1	150	granular	0.70599	0.00022	
GN51	GN51-cpx4	150	granular	0.71501	0.00030	
	GN51-cpx4-2	150	granular	0.71516	0.00029	
	GN51-cpx3-1	150	granular	0.71533	0.00029	

Continued

Sample ID	Spot ID	Spot Size (um)	Texture	$^{87}Sr/^{86}Sr$	2 SE	Comments
GN51	GN51-cpx3-2	150	granular	0.71557	0.00026	
	GN51-cpx1-3	150	granular	0.71570	0.00027	
	GN51-cpx1-1	150	granular	0.71590	0.00019	
	GN51-cpx1-2	150	granular	0.71413	0.00024	
DR10162	DR10162-cpx1-1	150	granular	0.70475	0.00031	
	DR10162-cpx1-2	150	granular	0.70428	0.00027	
	DR10162-cpx2-1	150	granular	0.70403	0.00032	
	DR10162-cpx2-2	150	granular	0.70400	0.00029	
	DR10162-cpx3	150	granular	0.70414	0.00023	
BM99X1	BM99X1cpx10	155	granular	0.70997	0.00010	
	BM99X1cpx10-2	155	granular	0.71007	0.00012	
	BM99X1cpx9	155	granular	0.70991	0.00010	
	BM99X1cpx9-2	155	granular	0.70977	0.00007	
	BM99X1cpx2	155	granular	0.71001	0.00006	
	BM99X1cpx6	155	host	0.70929	0.00006	
	BM99X1cpx6-2	155	host	0.70931	0.00012	
	BM99X1cpx6-3	155	host	0.70928	0.00010	
	BM99x1am5	155	amp vein	0.70954	0.00005	
	BM99x1am5-2	135	amp vein	0.70977	0.00006	
	BM99x1am3	155	amp vein	0.71026	0.00007	
	BM99X1pl6	85	lamellae	0.70865	0.00005	
	BM99X1pl7	85	lamellae	0.70880	0.00002	
	BM99X1pl7-2	85	lamellae	0.70883	0.00002	
	BM99X1pl7-3	85	lamellae	0.70882	0.00003	
	BM99X1pl7-4	85	lamellae	0.70880	0.00003	
	BM99X1pl9	110	granular	0.70924	0.00002	
	BM99X1pl10	110	granular	0.70914	0.00004	
	BM99x1ap1	50	granular	0.70930	0.00007	
BM99-8	BM99-8cpx4-2	155	granular	0.70448	0.00018	
	BM99-8cpx4-3	155	granular	0.70455	0.00018	
	BM99-8cpx8	155	host cpx	0.70488	0.00012	
	BM99-8cpx8-2	155	host cpx	0.70443	0.00010	
	BM99-8cpx3	155	host cpx	0.70458	0.00009	
	BM99-8pl7	85	lamellae	0.70439	0.00003	
	BM99-8pl6	110	granular	0.70445	0.00002	
	BM99-8pl6_2	110	granular	0.70448	0.00002	
	BM99-8pl6_2-2	110	granular	0.70443	0.00002	
	BM99-8pl6_3	110	granular	0.70442	0.00005	
BMC-1	BMC-1cpx1	155	granular	0.71600	0.00008	reaction zone B
	BMC-1cpx2	155	granular	0.71613	0.00006	cpx with sp exsolution
	BMC-1cpx2-2	155	granular	0.71604	0.00005	cpx with sp exsolution
	BMC-1cpx2-3	155	granular	0.71593	0.00009	cpx with sp exsolution
	BMC-1cpx4	155	granular	0.71609	0.00006	
	BMC-1cpx4-2	155	granular	0.71621	0.00007	
	BMC-1cpx8	135	granular	0.71590	0.00007	reaction zone C
	BMC-1cpx9	155	granular	0.71606	0.00008	
	BMC-1am6	155	granular	0.71582	0.00005	
	BMC-1amp8	155	granular	0.71592	0.00003	
	BMC-1amp10	155	granular	0.71594	0.00002	
	BMC-1amp10-2	155	granular	0.71601	0.00002	
	BMC-1ap1	50	granular	0.71575	0.00002	reaction zone B
	BMC-1ap1-2	50	granular	0.71573	0.00002	reaction zone B
	BMC-1ap7	40	granular	0.71573	0.00005	
	BMC-1ap7-2	40	granular	0.71566	0.00003	
	BMC-1ap3	25	granular	0.71525	0.00009	
BM99-7	BM99-7cpx10	155	granular	0.71553	0.00010	
	BM99-7cpx10-2	155	granular	0.71524	0.00007	
	BM99-7cpx5	155	granular	0.71523	0.00007	
	BM99-7cpx3	155	granular	0.71559	0.00009	
	BM99-7cpx3-2	155	granular	0.71543	0.00009	
	BM99-7cpx12	155	granular	0.71551	0.00013	
	BM99-7am1	155	granular	0.71565	0.00003	
	BM99-7am1-2	155	granular	0.71553	0.00003	
	BM99-7am4	155	granular	0.71556	0.00003	
	BM99-7am4-2	155	granular	0.71561	0.00003	
	BM99-7am7	155	granular	0.71559	0.00003	

Continued

Sample ID	Spot ID	Spot Size (um)	Texture	$^{87}Sr/^{86}Sr$	2 SE	Comments
BM99-7	BM99-7ap1	155	granular	0.71488	0.00016	
	BM99-7ap2	40	granular	0.71514	0.00004	
	BM99-7ap3	40	granular	0.71516	0.00025	
	BM99-7ap4	40	granular	0.71507	0.00024	
BM90-3	BM90-3cpx6	155	granular	0.71691	0.00009	
	BM90-3cpx6-2	155	granular	0.71668	0.00010	
	BM90-3cpx1	155	granular	0.71668	0.00009	
	BM90-3cpx2	155	granular	0.71659	0.00012	cpx with sp exsolution
	BM90-3cpx2-2	155	granular	0.71669	0.00014	cpx with sp exsolution
	BM90-3am3	155	cpx rim	0.71658	0.00004	amp replaced cpx
	BM90-3am3-2	155	cpx rim	0.71658	0.00004	amp replaced cpx
	BM90-3am3-3	155	cpx rim	0.71657	0.00004	amp replaced cpx
	BM90-3am5	155	lamellae	0.71659	0.00006	
	BM90-3am5-2	155	lamellae	0.71661	0.00004	
DR11017c	DR11017c-cpx6-1	150	granular	0.71628	0.00040	
	DR11017c-cpx6-2	150	granular	0.71607	0.00029	
	DR11017c-cpx1-1	150	granular	0.71657	0.00024	
	DR11017c-cpx1-2	150	granular	0.71653	0.00022	
	DR11017c-cpx3-1	150	granular	0.71603	0.00016	
	DR11017c-cpx3-2	150	granular	0.71559	0.00020	
	DR11017c-amp2-1	150	granular	0.71573	0.00006	
	DR11017c-amp2-2	150	granular	0.71576	0.00007	
	DR11017c-amp8	150	granular	0.71590	0.00007	
	DR11017c-amp5	150	granular	0.71605	0.00010	
	DR11017c-amp4	150	granular	0.71557	0.00010	
DR11022	DR11022-cpx1-1	150	granular	0.71636	0.00024	
	DR11022-cpx1-2	150	granular	0.71650	0.00022	
	DR11022-cpx2-1	150	granular	0.71641	0.00022	
	DR11022-cpx2-2	150	granular	0.71658	0.00032	
	DR11022-cpx4-1	150	granular	0.71666	0.00027	
	DR11022-cpx4-2	150	granular	0.71674	0.00025	
	DR11022-amp1-1	150	granular	0.71636	0.00024	
	DR11022-amp3-1	150	granular	0.71654	0.00009	
	DR11022-amp3-2	150	granular	0.71693	0.00008	
	DR11022-amp5-1	150	granular	0.71690	0.00009	
	DR11022-amp5-2	150	granular	0.71686	0.00007	

Note: cpx, clinopyroxene; amp, amphibole; pl, plagioclase; ap, apatite.

Table 6-24 Mean Sr isotopic compositions of clinopyroxene, amphibole, apatite and plagioclase from garnet pyroxenite in Lakes Bullenmerri and Gnotuk by LA-MC-ICPMS

Type	Sample ID	Mineral	87Sr/86Sr	1 σ
Type I	BME-1	Cpx	0.70610	0.00014
		Amp	0.70605	0.00007
	BM99-4	Cpx	0.70627	0.00008
		Amp	0.70604	0.00004
	BM99-2	Cpx	0.70447	0.00008
	BM99-5	Cpx	0.70685	0.00016
		Amp	0.70612	0.00007
	BM96-3	Cpx	0.70621	0.00009
		Amp	0.70599	0.00003
	BM99-2	Cpx	0.70444	0.00007
		Amp	0.70443	0.00004
	BM99-6	Cpx	0.70449	0.00006
		Amp	0.70461	0.00006
	DR10165	Cpx	0.70844	0.00081
		Amp	0.70872	0.00001
	GN35	Cpx	0.70563	0.00045
		Amp	0.70549	0.00009
	DR9748	Cpx	0.70749	0.00022
		Cpx-V	0.70598	0.00026
		Amp	0.70698	0.00004
		Amp-V	0.70569	0.00001
Type II a	BM99-9	Pl	0.70547	0.00007
	BM99X1	Cpx	0.70972	0.00009
		Amp	0.70986	0.00006
		Ap	0.70930	0.00007
		Pl	0.70894	0.00002
	BM99-8	Cpx	0.70457	0.00013
		Pl	0.70444	0.00003
	GN18	Cpx	0.70598	0.00046
		Amp	0.70674	0.00020
	GN41	Cpx	0.70633	0.00057
		Amp	0.70599	0.00022
	GN51	Cpx	0.71545	0.00034
	DR10162	Cpx	0.70424	0.00030
Type II b	BM99-7	Cpx	0.71540	0.00008
		Amp	0.71559	0.00003
		Ap	0.71514	0.00004
	BMC-1	Cpx	0.71604	0.00007
		Amp	0.71592	0.00003
		Ap	0.71572	0.00003
	BM90-3	Cpx	0.71666	0.00011
		Amp	0.71660	0.00004
	DR11017c	Cpx	0.71618	0.00037
		Amp	0.71580	0.00018
	DR11022	Cpx	0.71654	0.00015
		Amp	0.71672	0.00007

Note: Cpx, clinopyroxene; Amp, amphibole; Pl, plagioclase; Ap, apatite; Amp-V, amphibole vein.

Table 6-25 Mean O isotopic compositions of garnets from garnet pyroxenites in Lakes Bullenmerri and Gnotuk

Type	Sample ID	$\delta^{18}O$ (‰)	1 σ
Type I	BME-1	5.05	0.16
	BM99-4	5.58	0.21
	BM99-2	4.34	0.15
	BM99-5	6.15	0.20
Type II a	GN85-1	5.22	0.18
	BM99X2	4.89	0.14
Type II b	BMC-1	4.92	0.38

Table 6-26 The compositions of melts in equilibrium with the reconstructed clinopyroxene from garnet pyroxenites in Lakes Bullenmerri and Gnotuk

Type	Type I				Type IIa			
wt%	BM99-4	BME-1	BM99-2	BM99-5	BM99X1	BM99-8	BM99-9	BM99X2
SiO_2	50.3	50.9	50.0	51.3	50.4	47.4	47.6	48.8
TiO_2	1.31	0.93	0.79	1.63	1.44	0.27	0.41	1.09
Al_2O_3	15.4	13.4	14.6	9.4	16.9	21.9	23.1	18.0
Cr_2O_3	0.03	0.03	0.02	0.04	0.01	0.01	0.01	0.01
FeO	12.0	10.8	14.0	20.7	13.0	16.1	17.0	18.2
MnO	0.37	0.20	0.32	0.44	0.31	0.46	0.50	0.43
MgO	11.8	10.6	11.0	11.0	8.39	9.50	7.65	8.47
CaO	9.14	11.7	10.5	9.33	12.6	10.6	11.4	11.6
Na_2O	2.30	2.27	2.45	2.09	4.00	1.93	2.61	3.01
Mg#	63.7	63.7	58.3	48.6	53.4	51.3	44.5	45.4
ppm								
Li	10.9	6.3	0.0	10.0	14.1	10.9	7.8	18.4
Be	2.22	3.31	0.15	4.59	0.00	1.53	0.67	0.00
B	403	104	87.2	61.9	77.1	331	123	320
Sc	22.4	13.8	19.8	27.3	31.0	41.9	36.8	21.6
Ti	13430	10277	8876	15977	16788	3543	4761	12562
V	46.6	38.0	37.2	54.6	84.2	33.3	44.4	91.8
Cr	152	146	126	177	64.2	86.1	84.9	54.6
Co	13.58	20.44	21.98	20.56	23.95	39.57	37.88	33.87
Ni	16.75	39.73	34.81	29.98	17.12	25.85	22.00	34.98
Cu	2.11	1.30	2.52	2.12	2.90	1.87	2.67	2.36
Zn	16.08	23.53	29.53	53.13	43.45	39.05	54.35	0.00
Ga	9.59	10.40	12.59	10.29	19.00	9.85	15.80	17.45
Sr	833	891	734	648	899	752	46	94
Y	35.91	10.77	11.94	31.50	46.13	23.04	28.16	20.40
Zr	396	313	103	489	344	156	21.6	49.1
Nb	10.34	5.33	3.23	12.56	12.70	1.65	1.15	2.75
Ba	222	245	86	137	1629	1618	518	407
La	106	108	40.51	59.10	290	87.22	0.90	14.14
Ce	131.1	229.5	44.0	76.1	291.6	127.8	4.91	10.07
Pr	11.89	27.10	3.97	8.39	20.67	11.75	0.91	0.63
Nd	36.72	83.45	12.50	31.62	51.63	31.37	3.85	3.01
Sm	6.54	9.35	2.50	6.62	7.82	4.13	0.91	2.29
Eu	2.74	2.55	0.89	2.43	2.76	1.59	0.65	1.13
Gd	6.53	4.76	2.06	6.71	7.81	4.02	2.23	3.66
Tb	1.04	0.47	0.34	1.00	1.23	0.63	0.49	0.63
Dy	6.94	2.19	1.93	5.47	7.32	3.73	3.85	3.72
Ho	1.66	0.37	0.47	1.25	1.79	0.92	1.05	0.80
Er	4.99	0.95	1.28	3.12	5.08	2.48	3.40	1.99
Yb	5.02	0.70	1.32	2.86	4.88	2.82	3.58	1.51
Lu	0.89	0.00	0.20	0.45	0.84	0.53	0.65	0.24
Hf	10.34	5.33	3.23	12.56	12.70	1.65	1.15	2.75
Ta	6.70	11.10	8.90	5.75	7.21	32.06	3.85	1.78
Th	147		69.3	139	263	113	2.81	
U	36.9	16.2	16.6	34.6	54.5	35.0	3.52	6.25

BMC-1

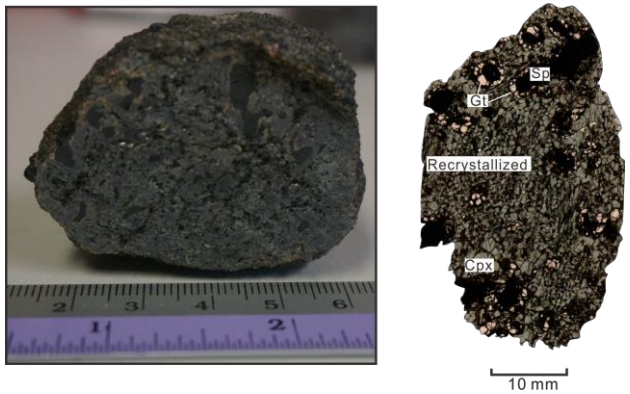

Hand specimen (left) and scanned thin section (right)

Spinel-garnet clinopyroxenite, mainly composed of Cpx (75 wt%), Gt (11 wt%), Amp (6 wt%), Sp (4 wt%) with minor Opx (2 wt%), Ol and Ap. Porphyroblastic texture.

Cpx megacryst preserves exsolution lamellae of Gt and has partially recrystallized along the boundaries to produce fine-grained Cpx and Gt, suggesting they could result from subsolidus recrystallization of primary Cpx. Sp megacryst is enveloped by Gt with/without anhedral Ol between them, and form two pyroxene +Sp +Ol +Amp clusters. Gt is subhedral or rounded and shows retrograde alteration (kelyphite rim). Amp occurs as "exsolution-like" streaks or flames within the host Cpx megacryst.

Granoblastic mosaic zone consists of recrystallized Cpx, Opx, Gt, Amp and interstitial Sp, which show well-developed granoblastic microstructures and abundant triple-point junctions. Most Amp is subhedral granular and occurs as minute grains located at triple junctions between Cpx. Minor Ap is present.

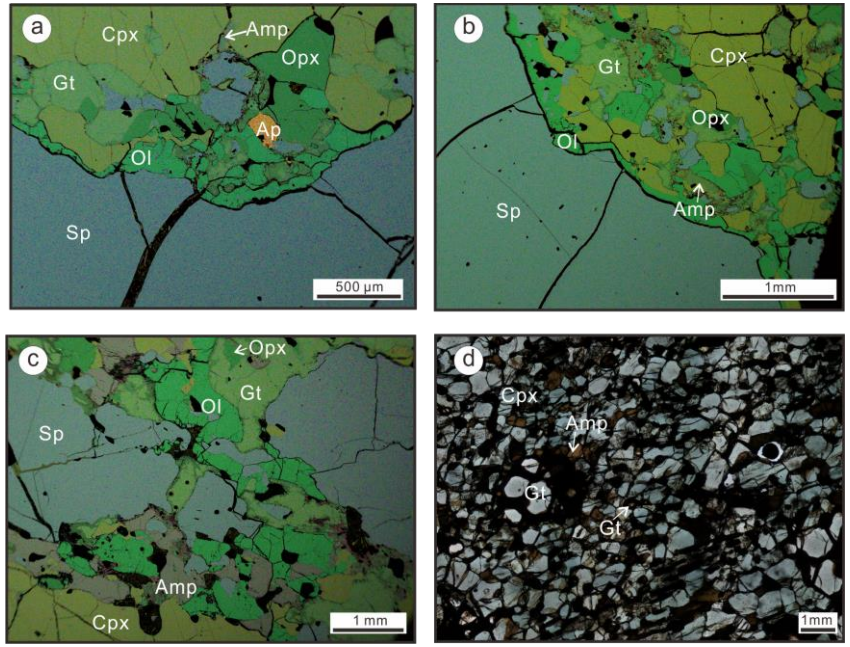

a-c: False-colour X-ray phase maps from SEM. d: Petrographic microscope, plane-polarized light

T= 986 °C

P= 15 kb

BM90-3

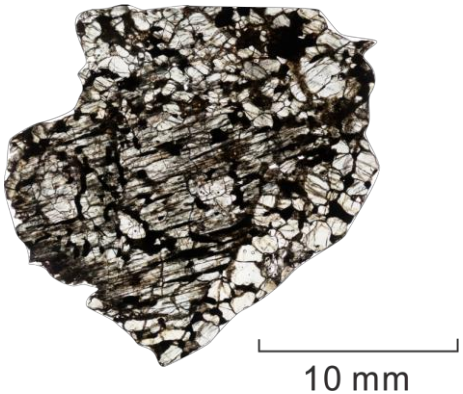

Image from petrographic microscope, plane-polarized light.

Garnet websterite, composed of Cpx (69%), Opx (5%), Gt (24%), Amp (1%) within minor Sp and Ol (1 wt%). Porphyroblastic texture.

Cpx megacryst contains exsolved Gt and Opx together with Sp. Gt occurs as lamellae and blebs within the host Cpx megacryst, but is partially/completely replaced by fine-grained symplectitic aggregate (kelyphite) associated with melt pockets comprising Ol + Pl (or Amp + Sp). Opx is enclosed by the Cpx megacryst, analogous to those of igneous cumulates containing common large oikocrysts of Ca-clinopyroxene, but is surrounded by bleb-shaped garnets. Minor Sp occurs as tiny plates in host Cpx or occurs in Amp-bearing pockets. Amp occurs as "exsolution-like" streaks or flames within the host Cpx and as rims on Cpx. Olivine is rare and occurs as irregular crystals interlocking with pyroxene or as small euhedral grains in melt pockets.

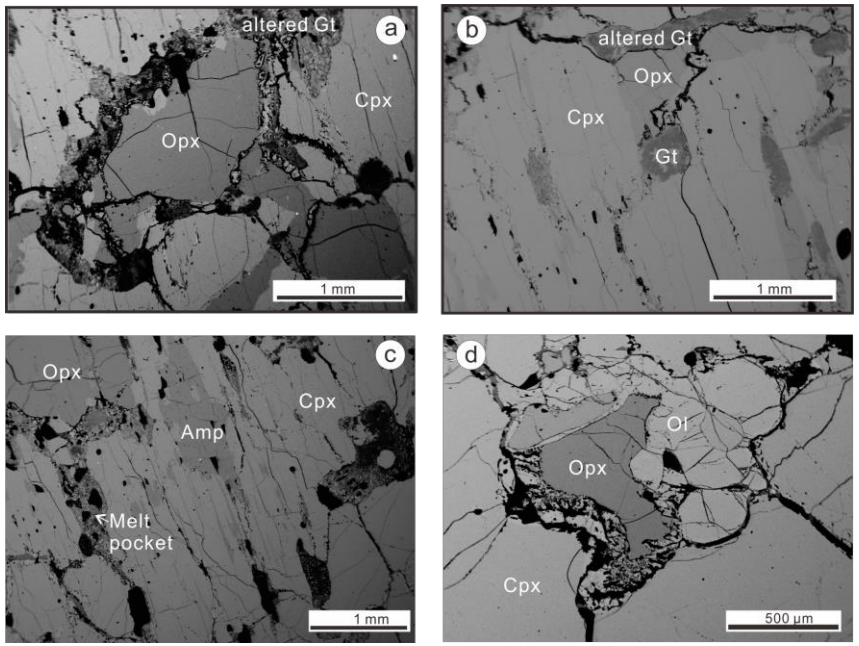

a-d: Back-scattered electron (BSE) images from SEM.

T= 950 °C

P= 13 kb

BM99-7

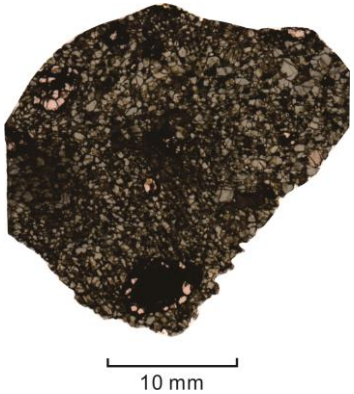

Scanned thin section

Spinel-garnet clinopyroxenite, composed of Cpx (70%), Gt (10 %), Sp (1 %), Amp (19 %) and minor Ol and Opx. Porphyroblastic textures.

Coarse Sp megacryst shows irregular shapes and disaggregated aureoles. In most cases, coarse Sp is mantled by Gt with anhedral Ol, which is succeeded by an outer layer of Cpx. Locally, small round Sp grains are enclosed by coarse Gt without other phases and these grains tend to have higher Cr_2O_3 contents than other Sp.

Granoblastic mosaic zone consists of Cpx, Gt, Amp with minor interstitial Sp, which show equilibrium texture with abundant triple-point junctions. Gt is present as blebs and shows weak foliation, suggesting it could have formed from subsolidus recrystallization of primary Cpx. Gt also shows retrograde alteration in the rim. Most Amp is subhedral or polygonal and shows textural equilibrium with the recrystallized Cpx, although they occasionally may have developed after Cpx (as rims on Cpx). Amp also forms mantles around Sp. Minor Ap is also present.

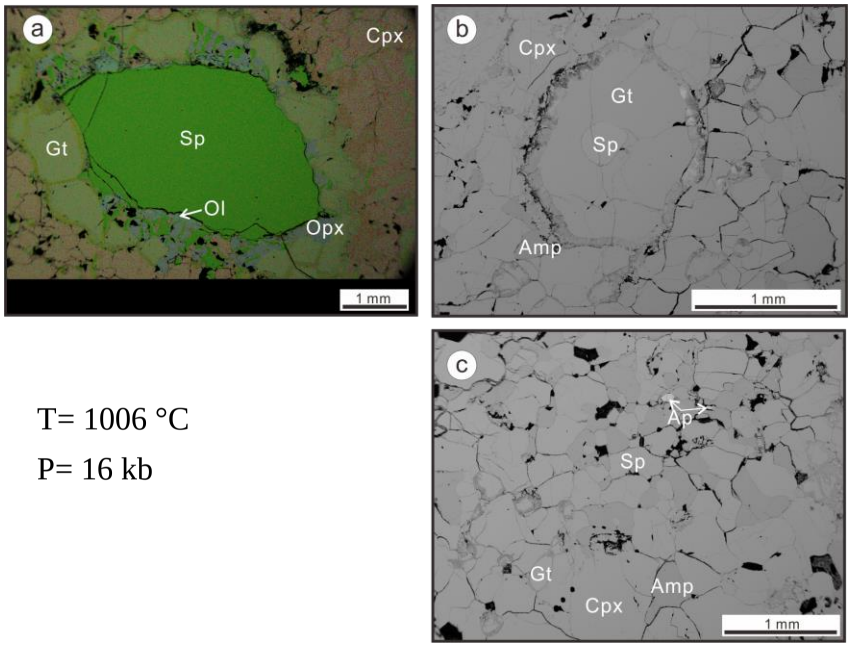

T= 1006 °C

P= 16 kb

a-c: BSE images from SEM. a, False-colour X-ray phase map.

DR11017c

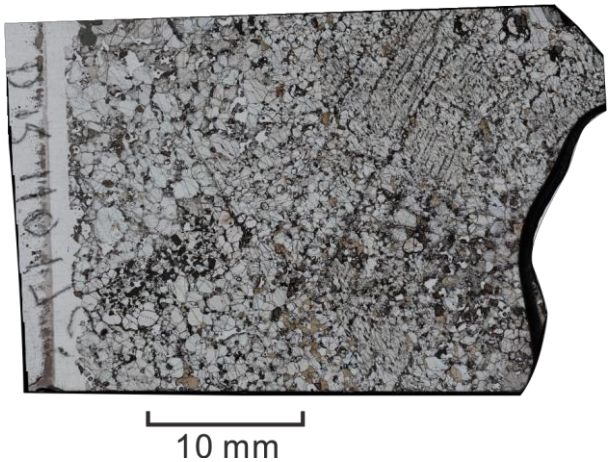

Image from petrographic microscope, plane-polarized light.

Spinel-garnet clinopyroxenite, composed of Cpx (66%), Gt (14%), Amp (8%), Sp (7%) and Opx (5%). Porphyroblastic texture.

Cpx megacryst shows exsolution lamellae of Opx and Gt. Gt occurs as blebs and lamellae and commonly shows widespread kelyphite rims. Amp occurs as “exsolution-like” streaks and flames, which replace the host Cpx.

Granoblastic mosaic zone is made up of Cpx, Gt, Amp and Sp, which show well-equilibrated textures in most cases. Garnet is partially replaced by fine-grained Sp+Opx. Locally, Sp is decomposed into small subhedral grains and intergrown with Cpx + Opx, which is surrounded by coarse Gt.

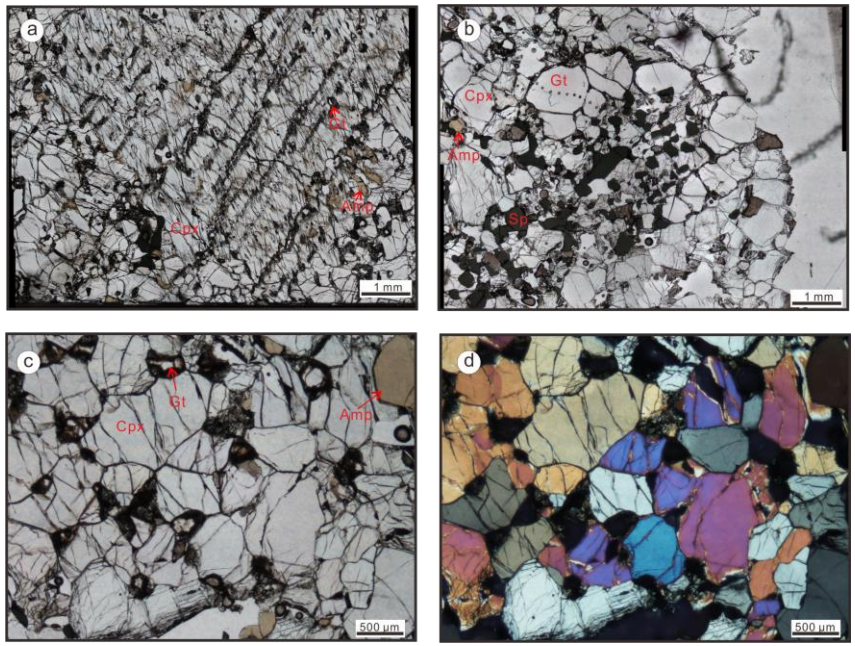

a-d: Petrographic microscrope images. a-c, plane-polarized light; d: as in c, crossed polarized light.

T= 1005 °C

P= 14 kb

DR11022

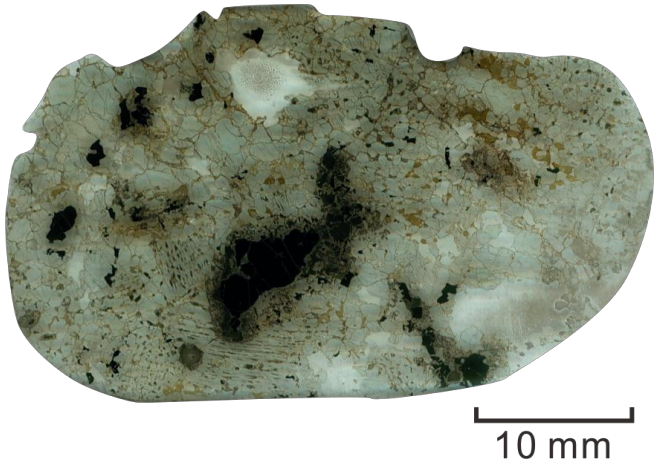

Scanned thin section

Spinel-garnet clinopyroxenite, composed of Cpx (78%), Sp (12%), Gt (4%), Amp (2%), Opx (4%) and minor Ol. Porphyroblastic texture.

Coarse Sp megacryst is irregular and amoeboid with a lobate outline and is commonly mantled by a granular assemblage of Gt, anhedral Ol, Cpx and Opx. Minor coarse Cpx megacrysts are preserved and they show exsolution lamellae of Gt which is completely replaced by fine-grained Sp + Opx (kelyphite rim).

Granoblastic mosaic zone is made up of Cpx, Gt, Amp and Sp, and they show well-equilibrated textures in most cases. Garnet is partially to completely replaced by fine-grained Sp + Opx.

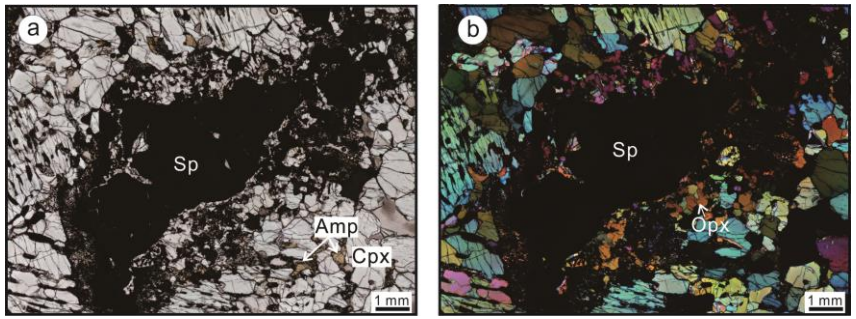

a-b: Petrographic microscope images. a, plane-polarized light; b, crossed-polarized light.

T= 973 °C

P= 13 kb

BM99X2

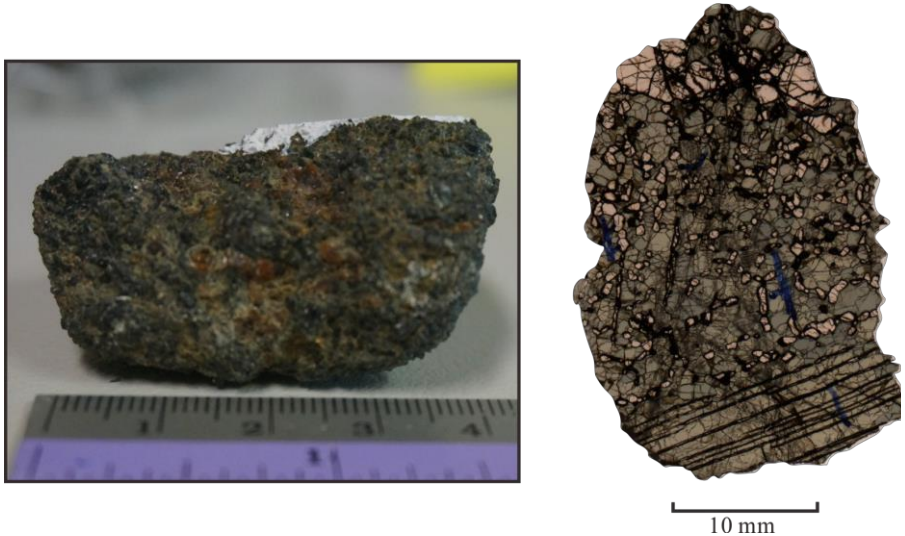

Hand specimen (left) and scanned thin section (right)

Garnet clinopyroxenite, composed of Cpx (64%) and Gt (36%). Porphyroclastic texture.

Cpx megacryst contains exsolution lamellae of garnet. The transition from lamellar to mosaic microstructure is continuous because the granular garnet still shows weak foliation parallel to the exsolution when close to the Cpx megacryst.

Gt grains in the recrystallized granular zone also preserve the original lamellar texture. However, coarse garnet grains probably represent earlier exsolution lamellae, and they are polygonal and subhedral. These garnets are also cut into several grains by zones of recrystallized fine-grained granular Cpx and also contain minor Cpx inclusions.

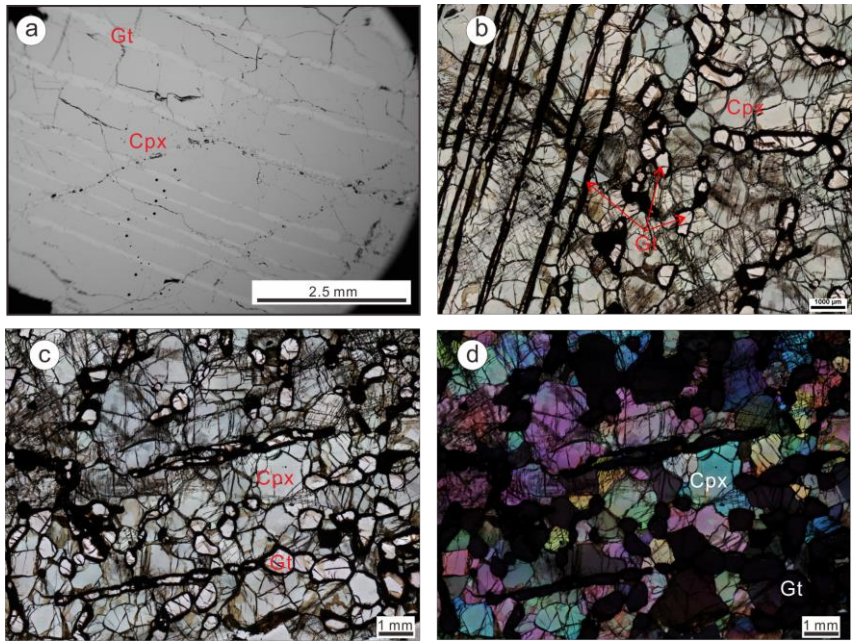

a: BSE images from SEM. b-d: Petrographic microscope images; b-c, plane-polarized light; d, crossed-polarized light.

T= 1040 °C

P= 15 kb

GN85-1

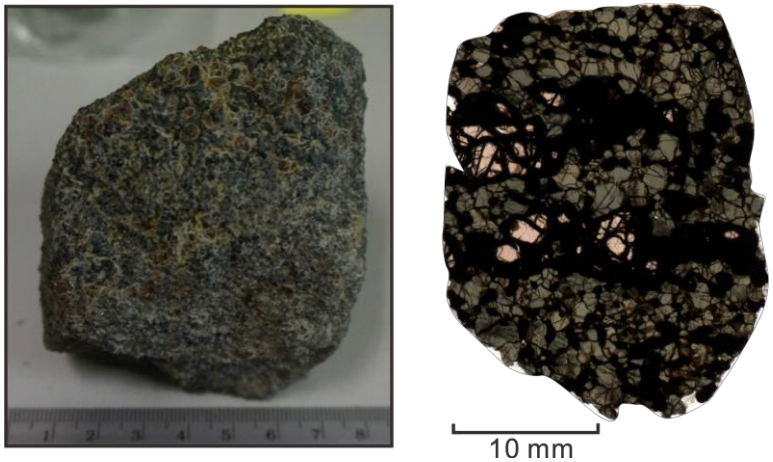

Hand specimen (left) and scanned thin section (right)

Garnet clinopyroxenite, composed of Cpx (43%) and Gt (57%). Coarse equant microstructures.

Two veins of coarse Gt cut cross the granular Cpx. Relatively small granular garnets also show weak foliation parallel to the coarse Gt veins, suggesting they originated as exsolution lamellae in the Cpx megacryst and underwent long-term subsolidus recrystallization. These garnets are partially to completely replaced by an extremely fine-grained symplectitic aggregate (kelyphite) consisting of Opx + Sp, and then infiltrated by a coarser intergrowth of Ol + Pl. Kelyphitization of Gt occurs at grain boundaries or replaces the whole grains.

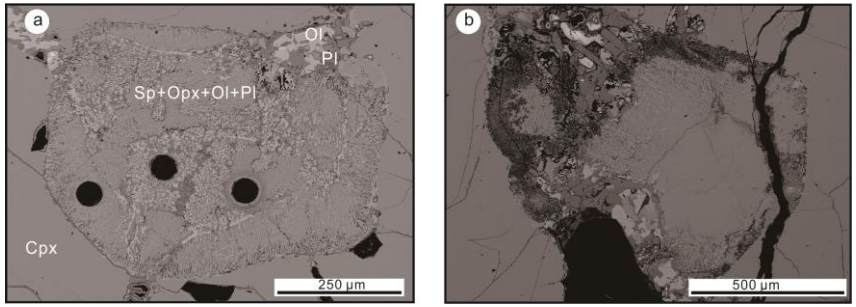

a-b: BSE image from SEM. a, showing holes from LA-ICPMS analysis.

T= 1040 °C

P= 15 kb

BM99-9

Scanned thin section

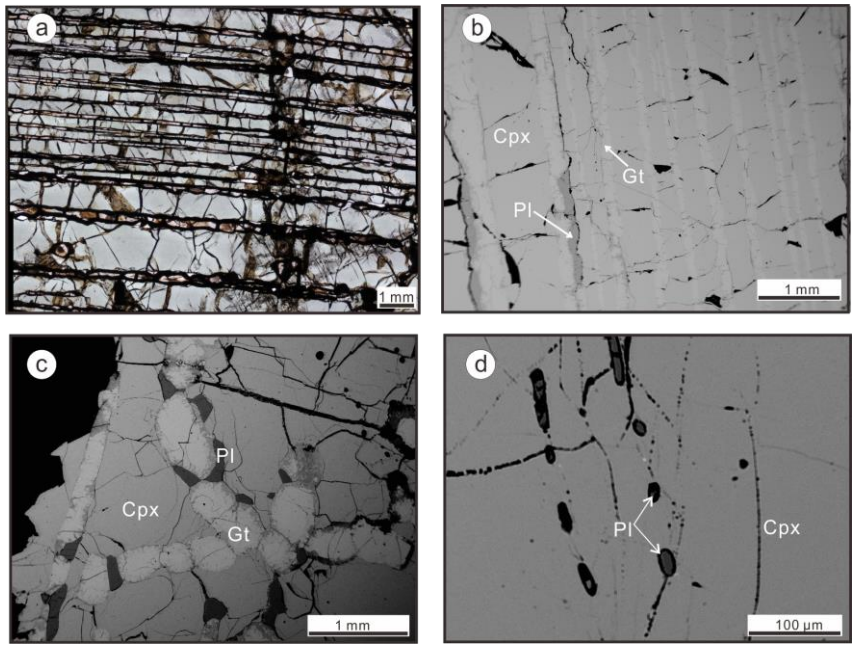

a: Petrographic microscope image, plane-polarized light. b-d: BSE images from SEM.

Garnet clinopyroxenite, composed of Cpx (66%) and Gt (32%) with minor Pl (2%). Porphyroblastic textures.

Cpx megacryst shows exsolution lamellae of Gt and Pl. The spacing between thick lamellae is always larger than that between thin lamellae. Garnet also occurs as blebs on the boundary of recrystallized fine-grained Cpx. Pl lamellae are always around garnet boundaries parallel to or crossing the Gt lamellae. Pl also occurs as blebs around recrystallized Cpx, and as drop-like inclusions in the recrystallized Cpx.

T= 1000 °C

P= 13 kb

BM99X1

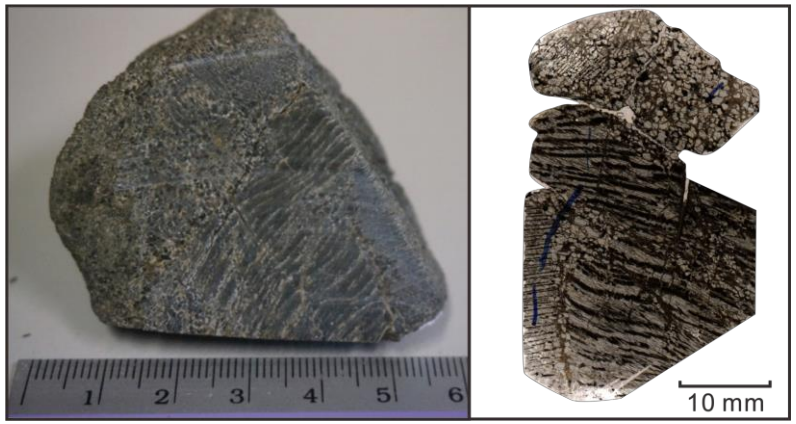

Hand specimen (left) and scanned thin section (right)

Garnet clinopyroxenite, composed of Cpx (80%) and Gt (19%) with minor Pl (1%) and Amp (<0.5%). Porphyroblastic texture.

Cpx megacryst has exsolution lamellae of Gt. The spacing between thick lamellae is always larger than that between thin lamellae. Thin Gt lamellae are aligned with each other, but thick Gt lamellae are not parallel and are completely replaced by fine-grained Opx, Sp, Ol, Pl and open cavities, which also reflect the partial melting of host Cpx (spongy rim). Locally, Amp-bearing veins infiltrate and also result in spongy rims of recrystallized Cpx close to the vein. Amp also occurs as "exsolution-like" streaks or as rims on recrystallized Cpx grains.

Granoblastic mosaic zone is made up of Cpx + Gt + Pl. Garnet is partially to completely replaced by fine-grained Sp + Opx, and even filled by Ol + Sp, melt and open vugs (melt pockets). Cpx shows obvious spongy rims with melt inclusions. Pl occurs as interstitial grains between Cpx and links with the infiltrating melt. Minor Ap is present.

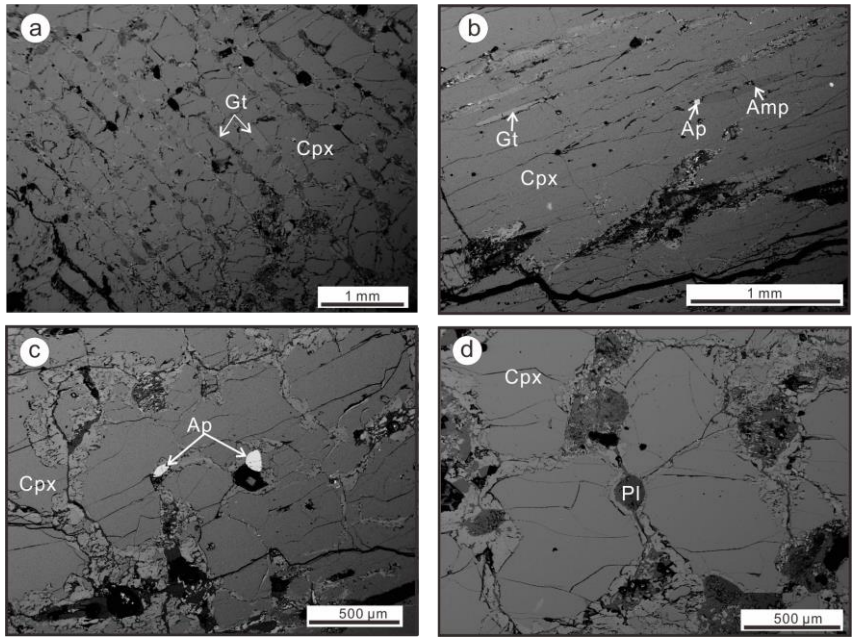

a-d: BSE images from SEM.

T= 980 °C

P= 13 kb

BM99-8

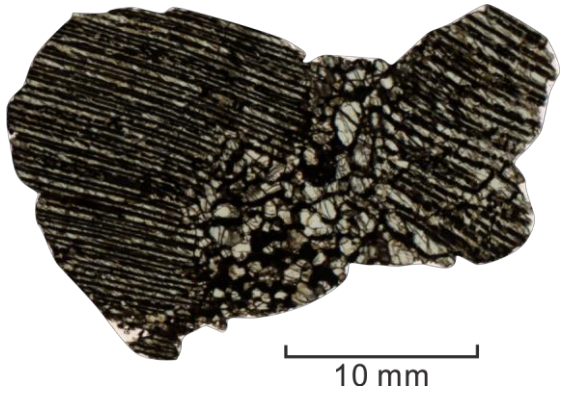

Scanned thin section

Garnet clinopyroxenite, composed of Cpx (63%) and Gt (36%) with minor Pl (1%). Porphyroblastic texture.

Cpx megacryst has exsolution lamellae of Gt. Exsolved Gt lamellae are partially to completely replaced by extremely fine-grained Pl +Opx +Sp and open cavities. Minor Pl also occurs as exsolution lamellae and links the kelyphitic Gt lamellae, which also relate to the spongy rim of the host Cpx.

Granoblastic mosaic zone is made up of Cpx + Gt + Pl, which show well-equilibrated textures in most cases, although most granular Cpx has developed spongy rims and is surrounded by completely disaggregated Gt. The replaced garnets are rounded in shape and are composed of a first, fine-grained, intergrowth of Sp + Opx and an outer symplectite rim made of a coarser intergrowth of Ol + Pl. Pl occurs not only as interstitial phases replacing garnet but also as minute grains located between Cpx and Gt.

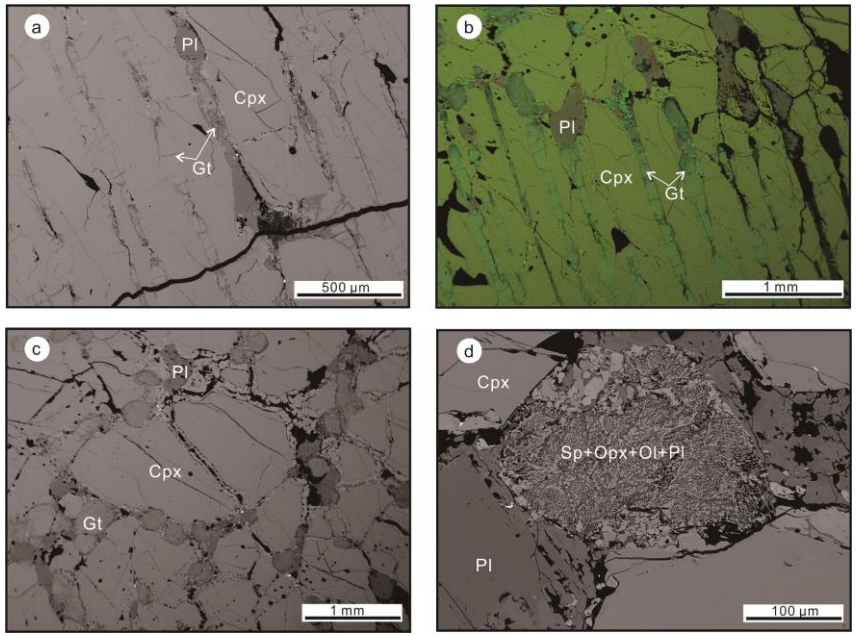

a-d: BSE images from SEM. b is false-colour phase map.

T= 970 °C

P= 12 kb

GN41

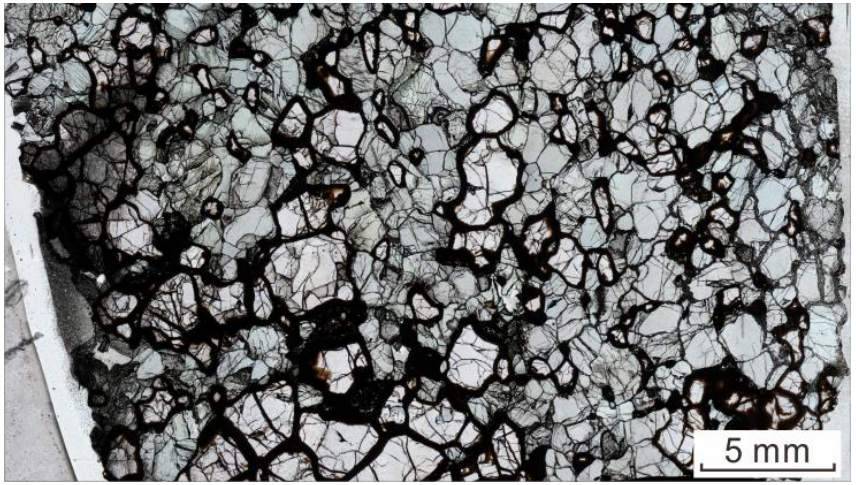

Image from petrographic microscope, plane-polarized light.

Garnet clinopyroxenite, composed of Cpx (55%) and Gt (45%). Coarse equant microstructures.

Cpx is recrystallized to fine grains. The distribution of Gt is scattered, and locally Gt is assembled to form coarse Gt aggregates with kelyphite rims.

T= 1090 °C

P= 18 kb

GN51

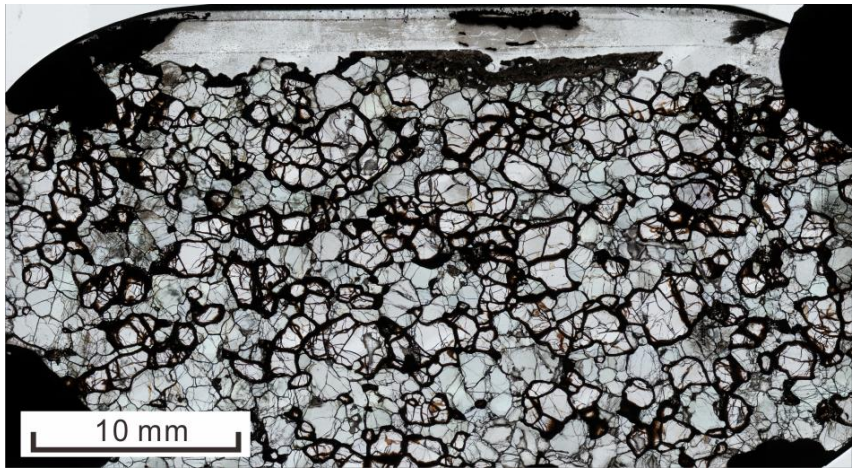

Image from petrographic microscope, plane-polarized light.

Garnet clinopyroxenite, composed of Cpx (51%) and Gt (49%). Coarse equant microstructure.

Cpx is recrystallized to fine grains. Coarse Gt preserves weak foliation.

T= 1100 °C

P= 18 kb

DR10162

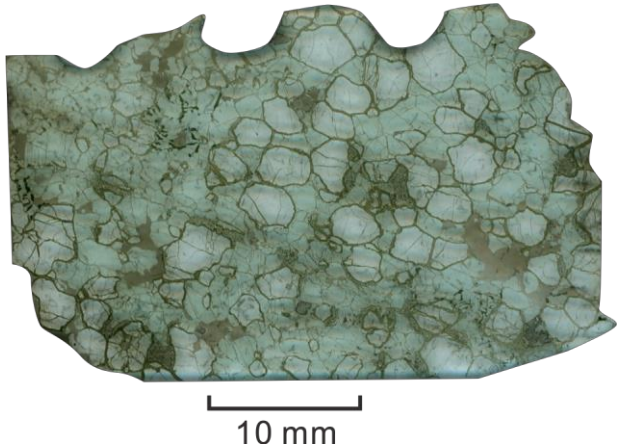

Scanned thin section

Garnet clinopyroxenite, composed of Cpx (46%), Gt (53%) and minor Sp (1%). Coarse equant microstructures.

Cpx is recrystallized to fine grains. Gt grains are coarse and are surrounded by variable thickness of kelyphite rims with visible Sp + Opx. Locally vermicular Sp is distributed along the boundaries of recrystallized Cpx.

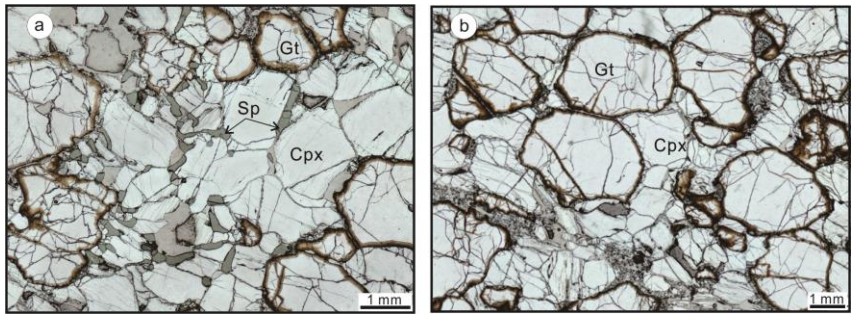

a-b: Petrographic microscope images, plane-polarized light.

T= 1063 °C

P= 14 kb

GN18

10 mm
Scanned thin section

Garnet clinopyroxenite, composed of Cpx (51%), Gt (49%) and minor Sp. Coarse equant microstructures.

Cpx is recrystallized to fine grains. Gt grains are coarse and are surrounded by variable thickness of kelyphite rims with visible Sp + Opx and brown melt. One Amp grain is also present in the thin section.

T= 1027 °C
P= 11 kb

BM99-6

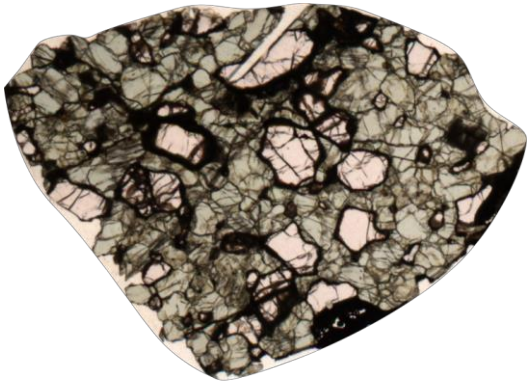

10 mm
Scanned thin section

Garnet clinopyroxenite, composed of Cpx (61%), Gt (38%) and minor Sp (1%). Coarse equant microstructure.

Garnet is subhedral and shows kelyphitic rims composed of intergrowths of Sp + Opx and minor Cpx, which is also associated with open cavities. Rare interstitial spinel is distributed among the recrystallized granular Cpx.

T= 1060 °C
P= 16 kb

BM99-4

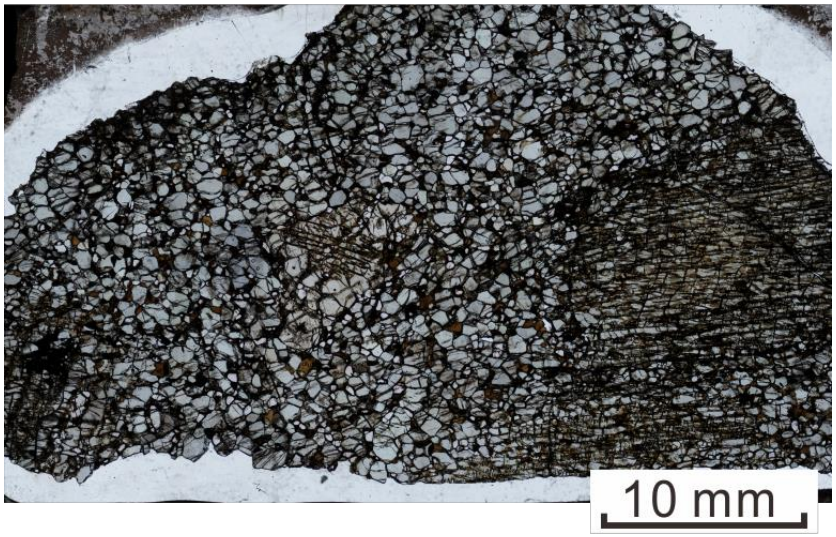

Image from petrographic microscope, plane-polarized light.

Garnet websterite, composed of Cpx (57%), Opx (20%), Gt (18%) and Amp (5%). Porphyroblastic texture.

Cpx megacryst contains exsolution lamellae of Gt and Opx. Amp forms subparallel trails oblique to exsolution lamellae in the lamellar zone. Opx megacryst has exsolution lamellae of Gt and Cpx, which are concentrated in the core of the Opx and cut by coarser granular Gt.

Granoblastic mosaic zone is mainly composed of Cpx, Gt, Amp and Opx, which show well-developed granoblastic microstructures and abundant triple-point junctions.

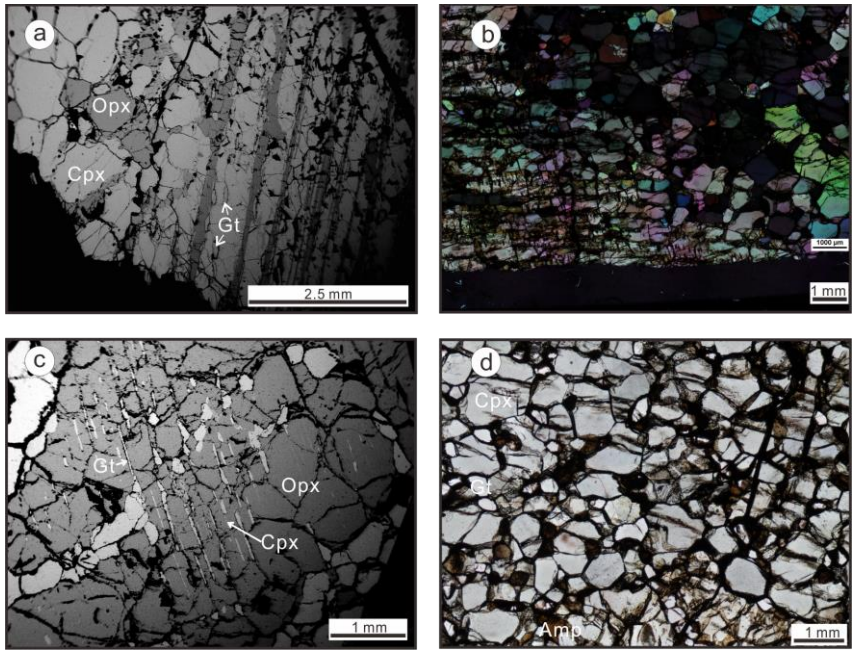

a, c: BSE images from SEM. b, d: Petrographic microscope images; b, crossed-polarized light; d, plane-polarized light.

T= 982 °C

P= 15 kb

BM99-2

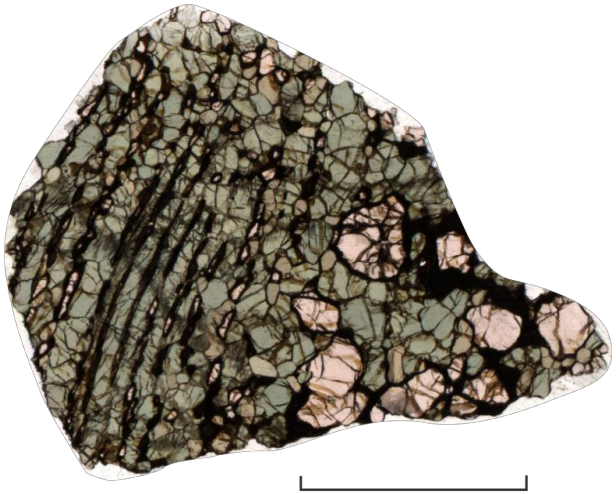

10 mm
Scanned thin section

Garnet websterite, composed of Cpx (55%), Opx (13%) and Gt (31%). Porphyroblastic texture.

Cpx megacryst contains exsolution lamellae of Gt and Opx. Opx lamellae are always formed along planes ((100), (010), (001)) of the host Cpx. When the minerals are further recrystallized, they have a random crystallographic orientation, although they still show weak foliation parallel to the exsolution structures. The transition from lamellar to mosaic microstructure is continuous.

Locally, the sample also shows coarse equant texture. Coarse Gt grains are irregular and rimmed by thick kelyphitic growths of Sp + Opx. These garnets are then surrounded by coarser mosaic Cpx and minor Opx.

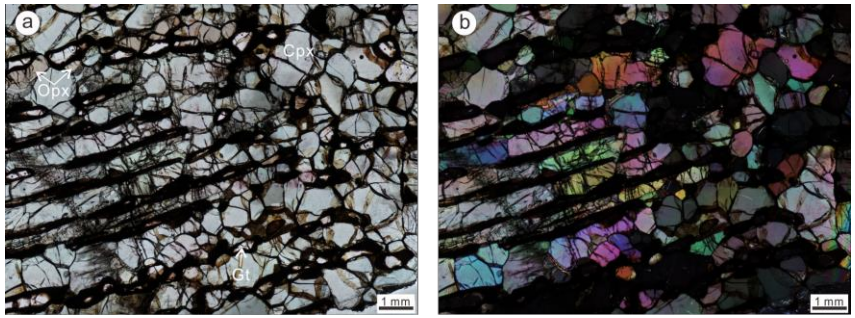

a, b: Petrographic microscope images. a, plane-polarized light; b, crossed -polarized light.

T= 1064 °C

P= 17 kb

BM96-3

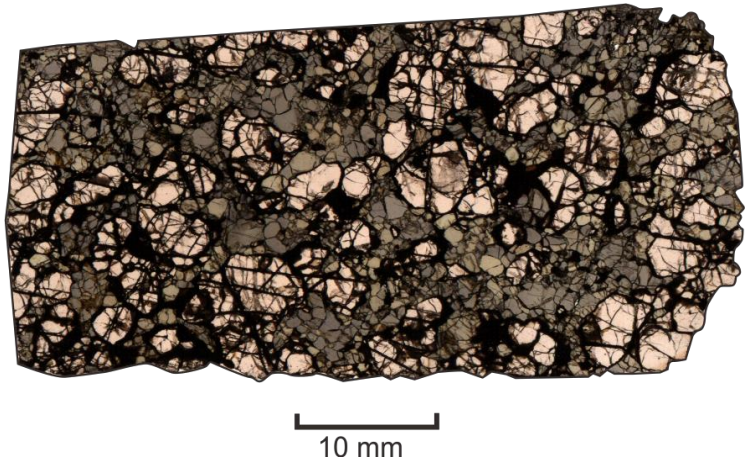

Scanned thin section

Garnet websterite, composed of Cpx (23%), Opx (15%), Gt (60%) and minor Phl (2%) and Amp. Coarse equant textures.

Polygonal coarse Gt is set in mosaic of relatively small Cpx and Opx where they have triple-point junctions and an interlocking fabric. Coarse garnets are also fractured and are replaced by the fine-grained kelyphitic rims, which are always associated with melt pockets where subhedral phlogopite and open cavities exist. Phl shows irregular Ti-rich rims close to the cavies and has minor ilmenite exsolution. When in contact with adjacent granular Cpx and Opx, Phl shows straight boundaries, but it never is in direct contact with Gt, suggesting the Phl is in equilibrium with granular Cpx and Opx but not with Gt. Only one Amp grain is present; it appears to be in equilibrium with the other minerals.

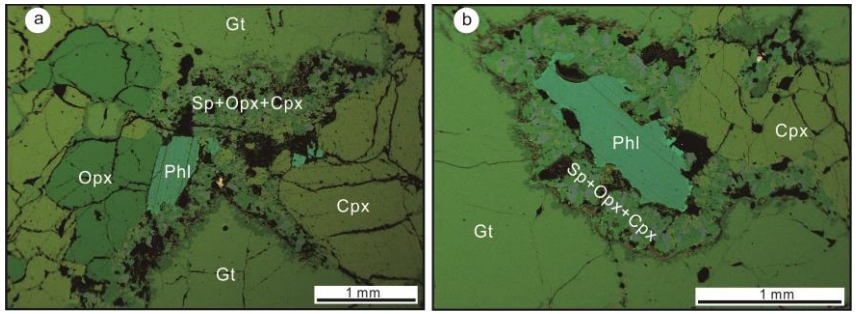

a, b: False-colour X-ray phase maps from SEM.

T= 1010 °C

P= 14 kb

BM96-2

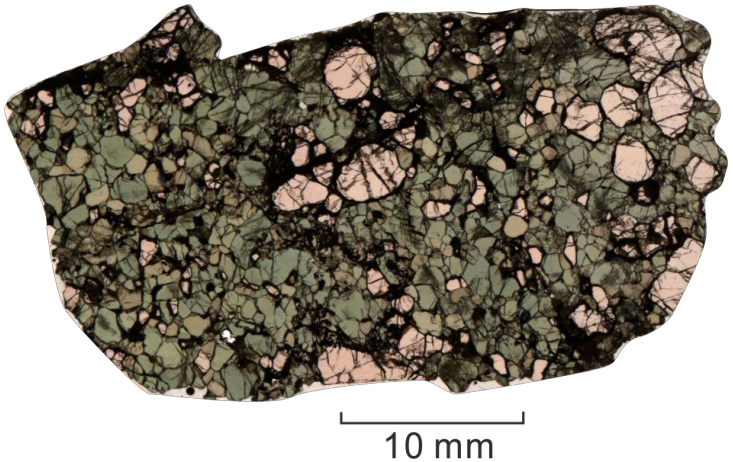

Scanned thin section

Garnet websterite, composed of Cpx (52%), Opx (13%), Gt (30%), Amp (4%), Sp (1%) and minor Ol. Coarse equant texture.

Polygonal to round coarse Gt is set in a mosaic of recrystallized fine-grained Cpx, Opx and minor Gt where they show straight grain boundaries and an interlocking fabric. In rare cases, coarse Gt include drop-like Sp with high Cr contents. Locally, Cpx, Opx, Sp, Ol and Gt form aggregates with a xenomorphic texture around coarse Gt, especially the intergrowth of Sp +Opx, suggesting that they may have been formed by breakdown of pre-existing Gt. Sp also occurs as blades, rhomboids, lamellae and rods in recrystallized Cpx.

Two sets of Amp veins infiltrate along the boundaries of coarse Gt, which causes the breakdown of Gt to thick kelyphite rims. Minor spinel grains are also enclosed by amphibole.

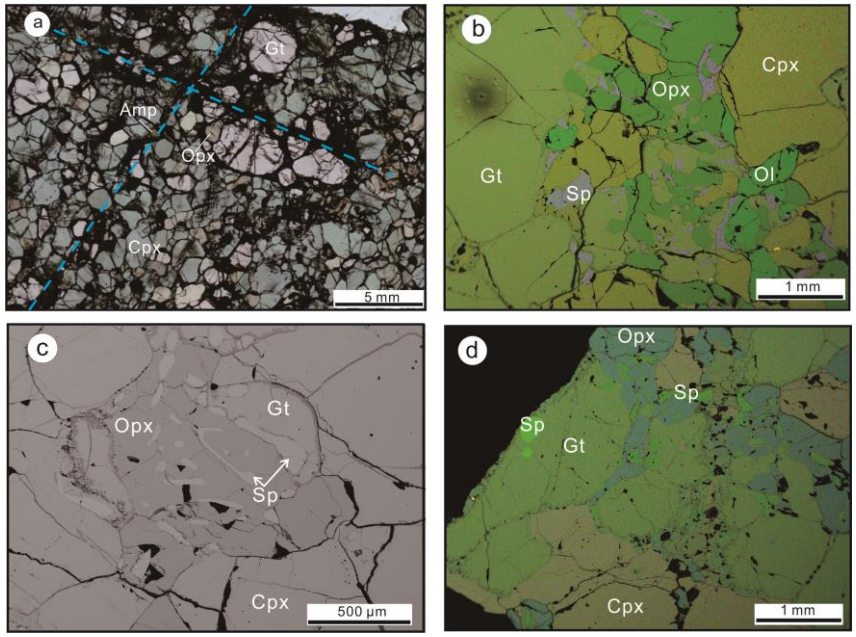

a: Petrographic microscope image, plane-polarized light. b-d: BSE images from SEM; b and d are false-colour X-ray phase maps.

T= 1094 °C

P= 18 kb

DR9748

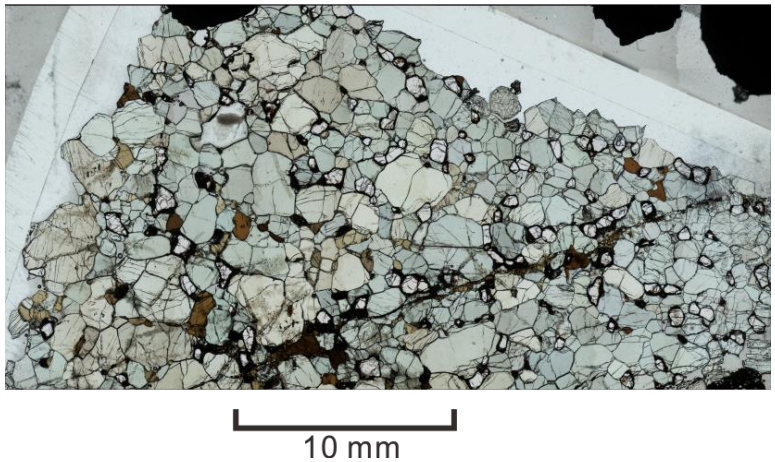

Image from petrographic microscope, plane-polarized light.

Garnet websterite, composed of Cpx (40%), Opx (44%), Gt (11%) and Amp (5%). Granoblastic mosaic zone.

Granular Cpx, Opx, Gt and Amp show well-developed granoblastic microstructures and abundant triple-point grain junctions.

One set of Amp veins crosscuts the sample along the cracks.

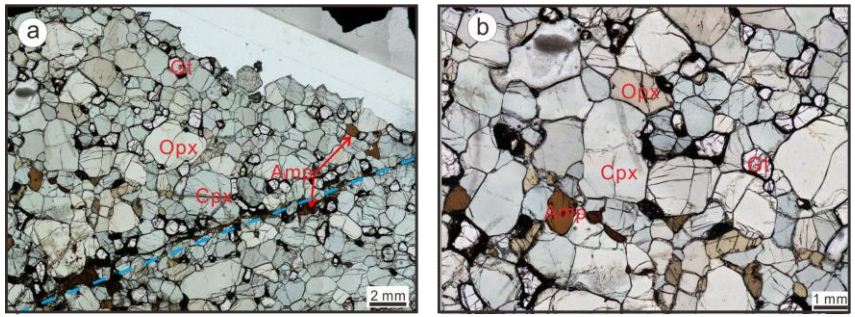

a-b: Petrographic microscrope images, plane-polarized light.

T= 1045 °C

P= 16 kb

GN35

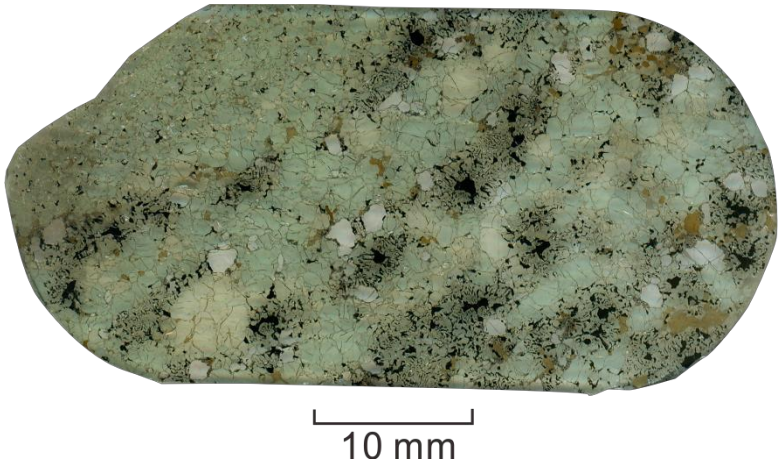

Scanned thin section

Garnet websterite, composed of Cpx (54%), Opx (27%), Gt (8%), Sp (7%) and Amp (4%). Porphyroblastic texture.

Cpx megacryst contains exsolution lamellae of Opx and Gt and they show transitional changes from the lamellar to the mosaic microstructure, due to varying degrees of recrystallization. Moreover, the intergrowth of Sp and Opx near the recrystallized Cpx is parallel to the exsolution lamellae of Gt and Opx in the Cpx megacryst, suggesting they represent breakdown of earlier Gt lamellae previously exsolved from Cpx megacryst.

Granular Cpx, Opx, Gt and Amp show well-developed granoblastic microstructures and abundant triple-point grain junctions.

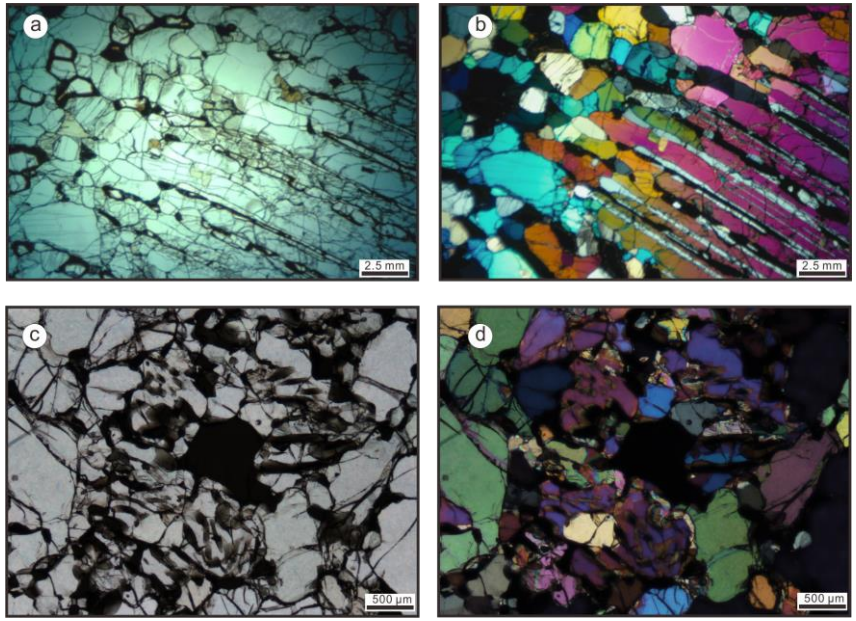

a-d: Petrographic microscope images. a and c, plane-polarized light; b and d, crossed-polarized light.

T= 1063 °C

P= 16 kb

DR10165

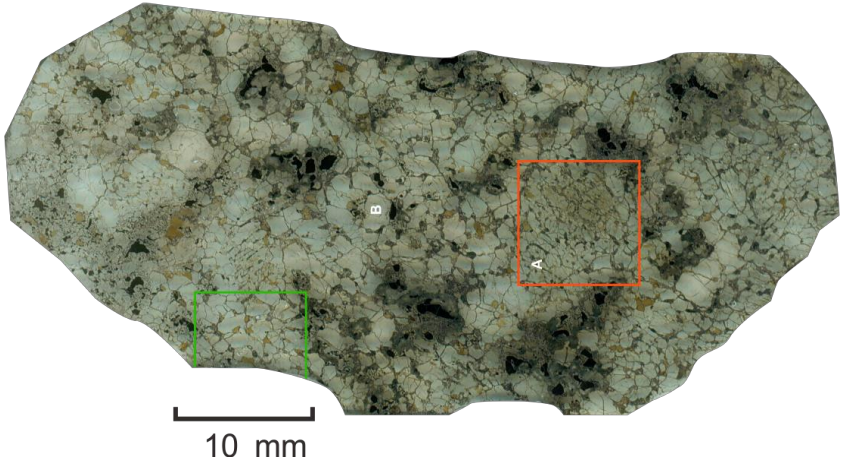

Scanned thin section

Spinel-garnet websterite, composed of Cpx (49%), Opx (25%), Sp (6%), Gt (17%) and Amp (3%). Porphyroblastic texture.

Small Cpx megacryst shows exsolution of Opx and Gt. Opx occurs as lamellae. Gt occurs as lamellae or blebs and is partially to completely replaced by kelyphite. Amp also occurs as lamellae perpendicular to Opx lamellae and replaces Cpx and Opx. Sp megacrysts are decomposed into vermicular Sp scattered in Cpx and Opx, and are surrounded by altered Gt.

Granular Cpx, Opx, Gt and Amp show well-developed granoblastic microstructures and abundant triple-point grain junctions.

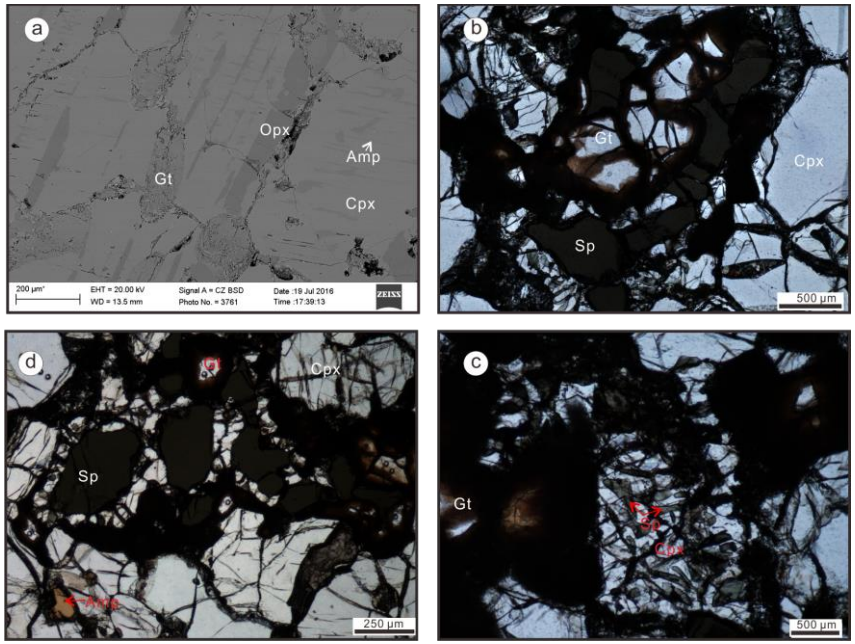

a: BSE image from SEM. b-d: Petrographic microscope images, plane-polarized light.

T= 970 °C

P= 12 kb

E-1

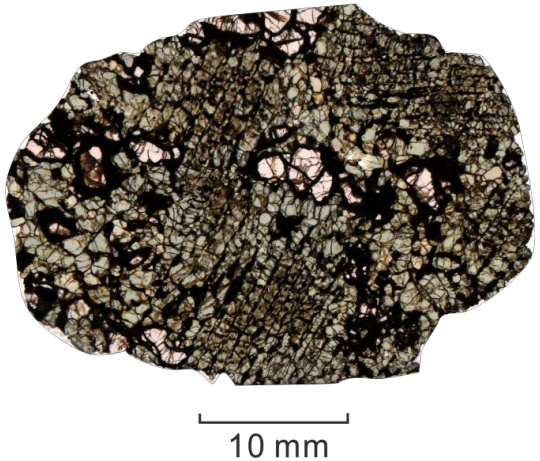

Scanned thin section

Garnet websterite, composed of Cpx (55%), Gt (33%), Opx (11%) and rare Amp and Sp. Porphyroblastic texture.

Cpx megacryst shows exsolution of Gt and Opx. Opx lamellae are parallel to the cleavage of the host Cpx. Garnet often occurs as thin, oriented rods and blebs, which are partially to completely replaced by fine-grained kelyphitic growths of Sp+Opx or Ol+Pl. Amp occurs as “exsolution-like” flames between Opx lamellae.

Gt grains in the mosaic texture are coarse and polygonal, and contain euhedral Ap inclusions, which disappear in the vicinity of fine-grained Gt. Coarse Gt also shows thick kelyphite rims composed of fine-grained Opx + Sp + Pl ± Cpx inside and an outer rim of coarser symplectitic Opx + Sp + Pl + Cpx + Ol. Rare bleb-shaped garnet aggregates occur in coronas around spinel.

The granular Cpx and Opx show well-equilibrated textures.

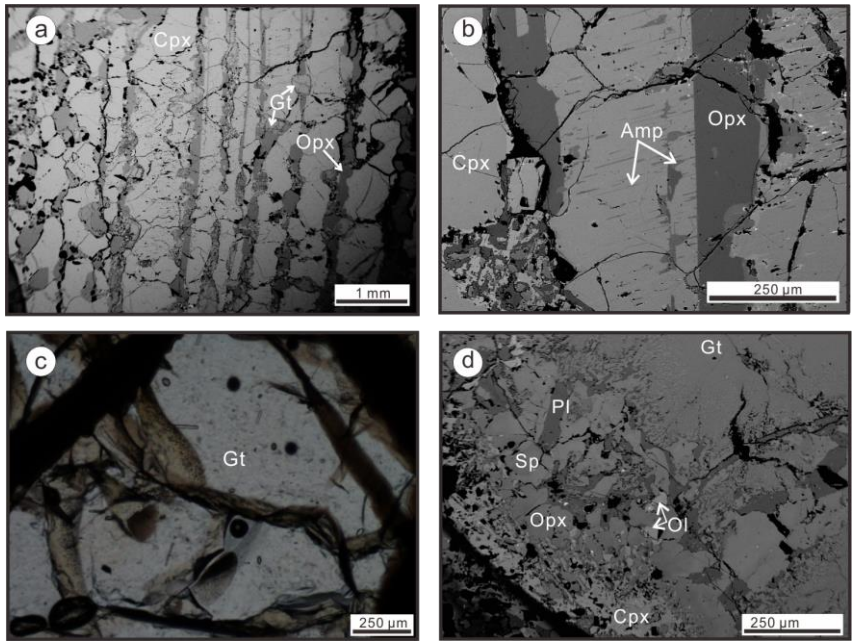

a, b and d: BSE images from SEM. c: Petrographic microscope image.

T= 1011 °C

P= 14 kb

BM99-5

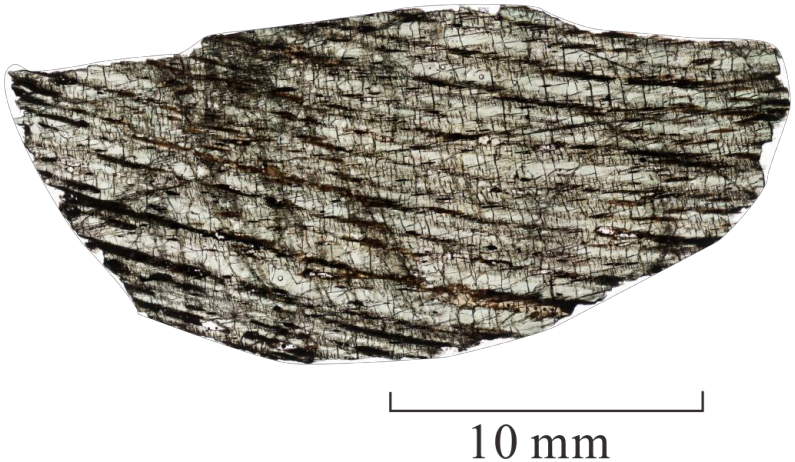

Image from petrographic microscope, plane-polarized light.

Clinopyroxene megacryst, composed of Cpx (64%), Opx (28%), Gt (5%), Amp (3%) and Ilm.

Cpx megacryst shows exsolution of Opx, Gt and Ilm. Garnet occurs as lamellae and blebs. Minor amphibole also forms pods and seams in the Cpx megacryst, parallel to Opx lamellae.

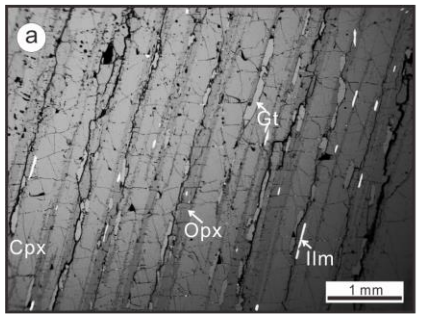

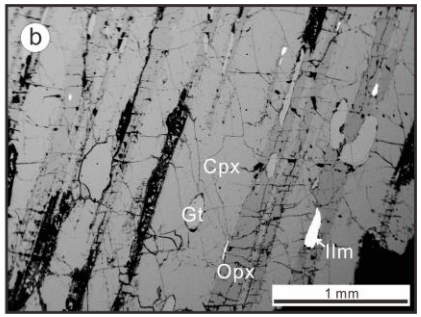

a-b: BSE images from SEM.

T= 1047 °C

P= 17 kb

Gondwana Research 23 (2013) 161–175

Contents lists available at SciVerse ScienceDirect

Gondwana Research

journal homepage: www.elsevier.com/locate/gr

Petrology and geochemistry of peridotite xenoliths from the Lianshan region: Nature and evolution of lithospheric mantle beneath the lower Yangtze block

Jianggu Lu [a], Jianping Zheng [a,b,*], William L. Griffin [b], Chunmei Yu [a,b]

[a] State Key Lab of Geological Processes and Mineral Resources, China University of Geosciences, Wuhan 430074, China
[b] GEMOC ARC National Key Centre, Department of Earth and Planetary Sciences, Macquarie University, NSW 2109, Australia

ARTICLE INFO

Article history:
Received 1 October 2011
Received in revised form 12 January 2012
Accepted 29 January 2012
Available online 13 February 2012

Keywords:
Peridotite xenoliths
Subcontinental lithospheric mantle
Mantle evolution
The lower Yangtze block

ABSTRACT

Lithospheric thinning beneath the North China Craton is widely recognized, but whether the Yangtze block has undergone the same process is a controversial issue. Based on a detailed petrographic study, a suite of xenoliths from the Lianshan Cenozoic basalts have been analyzed for the compositions of minerals and whole rocks, and their Sr–Nd isotopes to probe the nature and evolution of the subcontinental lithospheric mantle beneath the lower Yangtze block. The Lianshan xenoliths can be subdivided into two Types: the main Type 1 xenoliths (9–15% clinopyroxene and olivine-Mg#<90) and minor Type 2 peridotites (1.8–6.2% clinopyroxene and olivine-Mg#>90). Type 1 peridotites are characterized by low MgO, high levels of basaltic components (i.e., Al_2O_3, CaO and TiO_2), LREE-depleted patterns in clinopyroxenes and whole rocks, and relatively high $^{143}Nd/^{144}Nd$ (0.513219–0.513331) and low $^{86}Sr/^{87}Sr$ (0.702279–0.702789). These features suggest that Type 1 peridotites represent fragments of the newly accreted fertile lithospheric mantle that have undergone ~1% of fractional partial melting and later weak silicate–melt metasomatism, similar to Phanerozoic lithospheric mantle beneath the eastern North China Craton. Type 2 peridotites may be shallow relics of the older lithospheric mantle depleted in basaltic components, with LREE-enriched and HREE-depleted patterns, relatively low $^{143}Nd/^{144}Nd$ (0.512499–0.512956) and high $^{86}Sr/^{87}Sr$ (0.703275–0.703997), which can be produced by 9–14% partial melting and subsequent carbonatite–melt metasomatism. Neither type shows a correlation between equilibration temperatures and Mg# in olivine, indicating that the lithospheric mantle is not compositionally stratified, but both types coexist at similar depths. This coexistence suggests that the residual refractory lithospheric mantle (i.e., Type 2 peridotites) may be irregularly eroded by upwelling asthenosphere materials along weak zones and eventually replaced to create a new and fertile lithosphere mantle (i.e., Type 1 xenoliths) as the asthenosphere cooled. Therefore, the subcontinental lithospheric mantle beneath the lower Yangtze block shared a common evolutional dynamic environment with that beneath the eastern North China Craton during late Mesozoic–Cenozoic time.

© 2012 International Association for Gondwana Research. Published by Elsevier B.V. All rights reserved.

1. Introduction

Commonly, the age of the subcontinental lithospheric mantle (SCLM) is coupled with the age of the overlying crust (Boyd, 1989; Griffin et al., 1999a,b; Pearson, 1999). However, this coupling may be destroyed by asthenosphere–lithosphere and crust–mantle interactions (Griffin et al., 1998; O'Reilly et al., 2001; Zheng et al., 2001, 2007). It is generally accepted that a large thickness (more than 100 km) of old refractory lithospheric mantle beneath the eastern North China Craton was removed or strongly modified during Mesozoic–Cenozoic time (Fan and Menzies, 1992; Griffin et al., 1992; Menzies et al., 1993; Deng et al., 1996; Griffin et al., 1998; Xu, 1999; Zheng, 1999; Fan et al., 2000; Xu, 2001; Zhang, 2005), especially along the translithospheric Tanlu Fault Zone (TLFZ, i.e., Shanwang, Fig. 1a). Shallow relics of Archean lithospheric mantle have only been documented in areas away from the TLFZ (i.e., Hebi).

Xenolith-bearing basalts are widespread in the South China block which is divided by JiangShao–PingYu Fault Zone (JS–PYFZ) into the Yangtze block to the northwest and the Cathaysia block to the southeast (Fig. 1a). Both garnet and spinel-bearing peridotite xenoliths from the Cathaysia block are essentially fertile and yield Phanerozoic ages (Qi et al., 1995; Xu et al., 2000, 2003; Zheng et al., 2004a; Xu et al., 2008). The rare occurrences of refractory xenoliths from this block suggest that an older residual SCLM coexists with younger mantle beneath the block (Xu et al., 2000; Wang et al., 2003; Xu et al., 2003; Zheng et al., 2004a; Xu et al., 2008).

Relatively few studies have been carried out on the lithospheric mantle beneath the lower Yangtze block (Chen et al., 1994; Sun et al., 1998; Reisberg et al., 2005). The lack of detailed knowledge about the Mesozoic–Cenozoic SCLM of the block has constrained the overall understanding of the lithospheric evolution of eastern China. However, the eruption of xenolith-bearing basalts in the Subei basin located in

* Corresponding author at: State Key Lab of Geological Processes and Mineral Resources, China University of Geosciences, Wuhan 430074, China. Tel.: +86 27 67885100 8301; fax: +86 27 67883873.
E-mail addresses: jpzheng@cug.edu.cn, jpzheng2003@yahoo.com (J. Zheng).

1342-937X/$ – see front matter © 2012 International Association for Gondwana Research. Published by Elsevier B.V. All rights reserved.
doi:10.1016/j.gr.2012.01.008

Lithos 232 (2015) 111–123

Contents lists available at ScienceDirect

Lithos

journal homepage: www.elsevier.com/locate/lithos

Microscale effects of melt infiltration into the lithospheric mantle: Peridotite xenoliths from Xilong, South China

Jianggu Lu [a,b], Jianping Zheng [a,*], William L. Griffin [b], Suzanne Y. O'Reilly [b], Norman J. Pearson [b]

[a] State Key Laboratory of Geological Processes and Mineral Resources, School of Earth Sciences, China University of Geosciences, Wuhan 430074, China
[b] ARC Centre of Excellence for Core to Crust Fluid Systems and GEMOC, Department of Earth and Planetary Sciences, Macquarie University, NSW 2109, Australia

ARTICLE INFO

Article history:
Received 16 April 2015
Accepted 26 June 2015
Available online 3 July 2015

Keywords:
Mantle peridotite mineral reactions
Na-rich mantle melts
K-rich mantle melts
Mantle metasomatism
Xilong basaltic rocks

ABSTRACT

Melting and reactions between minerals and melts are important processes in the evolution of the lithospheric mantle, and are usually inferred from their geochemical fingerprints in mantle samples. However, a suite of mantle-derived peridotite xenoliths from the Xilong area, South China, records the reaction of successive silicate melts of different compositions with mineral assemblages in the mantle, preserved by quenching during entrainment. These xenoliths form two groups and record a compositionally layered mantle. Group 1 has olivine Mg# ~91, (and is thus relatively refractory), is derived from depths of ~50–65 km, and shows the trace-element geochemical signature of "old" carbonatitic metasomatism. Group 2 is more fertile with olivine Mg# mainly ~89–90, is derived from ~40 to 55 km and has ubiquitous modal spinel. Xenoliths of both groups then show sequential infiltration by two compositionally distinct melts (Na-rich and K-rich) not long before eruption.

The Na-rich melts are enclosed in spongy clinopyroxene and spinel rims and are inferred to have triggered the reactions that formed the spongy rims, which have lower Al_2O_3, Na_2O and Mg#, but higher FeO, TiO_2 and Cr# than the primary phases. The undersaturated Na-rich mafic melts were probably formed in the asthenosphere by low-degree melting.

The K-rich melts occur mainly in reaction zones around orthopyroxene and in reaction patches containing fine-grained secondary olivine, clinopyroxene and minor spinel. The melts have high contents of SiO_2, K_2O (mean 14.3 wt.%), Rb, Ba, and LREE but very low Na_2O/K_2O (0.01–0.29), positive anomalies in Eu and Sr, and variable HFSE anomalies. These compositional characteristics are consistent with an origin as low-degree partial melts of pre-existing phlogopite-bearing rocks.

The K-rich melts also react with primary olivine, and the spongy-textured secondary clinopyroxene and spinel inferred to have formed by reaction with the Na-rich melts, yielding secondary olivine, vermicular clinopyroxene and spinel compositionally similar to that in the reaction patches. This observation suggests that the infiltration of K-rich melt occurred after the percolation of Na-rich melts.

This study demonstrates the complexity of metasomatic processes in the lithospheric mantle, and emphasizes the caution required when interpreting the geochemical signatures of mantle-derived xenoliths in which multiple overprinting by compositionally diverse fluid and melt interactions with mantle minerals cannot be so clearly observed and characterized as in these samples.

© 2015 Elsevier B.V. All rights reserved.

1. Introduction

Quenched melts in the form of glasses have been reported in mantle xenoliths from many locations worldwide; they commonly occur in veins and patches, as intergranular films, or as inclusions in primary mantle minerals (e.g., Beccaluva et al., 2001; Bonadiman et al., 2005, 2011; Carpenter et al., 2002; Coltorti et al., 1999; Ionov et al., 1995; Miller et al., 2012; Ryabchikov et al., 1995; Scambelluri et al., 2009; Schiano and Bourdon, 1999; Shaw et al., 2006; Su et al., 2010, 2011; Varela et al., 1999; Xu et al., 1996; Yaxley and Kamenetsky, 1999; Yaxley et al., 1997; Zhu, 2008; Zinngrebe and Foley, 1995). Various explanations for their origin have been proposed on the basis of mineralogical observations, geochemical datasets and experimental results. Such melts have been interpreted as either the agents or the products of mantle metasomatism (e.g., Beccaluva et al., 2001; Bonadiman et al., 2001, 2005, 2011; Coltorti et al., 1999; Hauri et al., 1993; Ionov et al., 2005; Neumann et al., 2002; Varela et al., 1999; Xu et al., 1996), or the products of in situ incongruent melting of pre-existing minerals (e.g., Aliani et al., 2009; Erlank et al., 1987; Su et al., 2010, 2011; Yaxley et al., 1997; Zhu, 2008) prior to or during entrainment of the

* Corresponding author at: State Key Laboratory of Geological Processes and Mineral Resources, China University of Geosciences, Wuhan 430074, China. Tel.: +86 27 67885100 8301; fax: +86 27 67883873.
E-mail address: jpzheng@cug.edu.cn (J. Zheng).

http://dx.doi.org/10.1016/j.lithos.2015.06.013
0024-4937/© 2015 Elsevier B.V. All rights reserved.

The Geological Society of America
Special Paper 526

Uplift of the southeastern Australian lithosphere: Thermal-tectonic evolution of garnet pyroxenite xenoliths from western Victoria

Jiang-Gu Lu*
State Key Laboratory of Geological Processes and Mineral Resources, School of Earth Sciences, China University of Geosciences, Wuhan 430074, China, and *ARC Centre of Excellence for Core to Crust Fluid Systems and Geochemical Evolution and Metallogeny of Continents (GEMOC), Department of Earth and Planetary Sciences, Macquarie University, Sydney, NSW 2109, Australia*

Qing Xiong*
William L. Griffin
ARC Centre of Excellence for Core to Crust Fluid Systems and Geochemical Evolution and Metallogeny of Continents (GEMOC), Department of Earth and Planetary Sciences, Macquarie University, Sydney, NSW 2109, Australia

Jian-Ping Zheng*
State Key Laboratory of Geological Processes and Mineral Resources, School of Earth Sciences, China University of Geosciences, Wuhan 430074, China, and *ARC Centre of Excellence for Core to Crust Fluid Systems and Geochemical Evolution and Metallogeny of Continents (GEMOC), Department of Earth and Planetary Sciences, Macquarie University, Sydney, NSW 2109, Australia*

Jin-Xiang Huang
Suzanne Y. O'Reilly
ARC Centre of Excellence for Core to Crust Fluid Systems and Geochemical Evolution and Metallogeny of Continents (GEMOC), Department of Earth and Planetary Sciences, Macquarie University, Sydney, NSW 2109, Australia

Takako Satsukawa
Department of Geophysics, Graduate School of Science, Kyoto University, Kyoto 606-8502, Japan

Norman J. Pearson
ARC Centre of Excellence for Core to Crust Fluid Systems and Geochemical Evolution and Metallogeny of Continents (GEMOC), Department of Earth and Planetary Sciences, Macquarie University, Sydney, NSW 2109, Australia

ABSTRACT

Detailed petrography, microstructure, and geochemistry of garnet pyroxenite xenoliths in Holocene basanite tuffs from maars at Lakes Bullenmerri and Gnotuk (western Victoria, southeastern Australia) have been used to track their igneous and

*Corresponding author e-mail: jianggu.lu@students.mq.edu.au; qing.xiong@mq.edu.au; jpzheng@cug.edu.cn.

Lu, J.-G., Xiong, Q., Griffin, W.L., Zheng, J.-P., Huang, J.-X., O'Reilly, S.Y., Satsukawa, T., and Pearson, N.J., 2017, Uplift of the southeastern Australian lithosphere: Thermal-tectonic evolution of garnet pyroxenite xenoliths from western Victoria, *in* Bianchini, G., Bodinier, J.-L., Braga, R., and Wilson, M., eds., The Crust-Mantle and Lithosphere-Asthenosphere Boundaries: Insights from Xenoliths, Orogenic Deep Sections, and Geophysical Studies: Geological Society of America Special Paper 526, doi:10.1130/2017.2526(02). © 2017 The Geological Society of America. All rights reserved. For permission to copy, contact editing@geosociety.org.